UC Davis

UC Davis Electronic Theses and Dissertations

Title

Study on Particle Shape, Size and Gradation Effects on the Mechanical Behavior of Coarse-Grained Soils

Permalink

https://escholarship.org/uc/item/4gz1z4fs

Author

Ahmed, Sheikh Sharif

Publication Date

2021

Peer reviewed|Thesis/dissertation

eScholarship.org Powered by the California Digital Library
University of California

Study on Particle Shape, Size and Gradation Effects on the Mechanical Behavior of Coarse-Grained Soils

By

SHEIKH SHARIF AHMED

DISSERTATION

Submitted in partial satisfaction of the requirements for the degree of

DOCTOR OF PHILOSOPHY

in

Civil and Environmental Engineering

in the

OFFICE OF GRADUATE STUDIES

of the

UNIVERSITY OF CALIFORNIA

DAVIS

Approved:

Alejandro Martinez, Chair

Jason T. DeJong

Katerina Ziotopoulou

Committee in Charge

2021

To my parents, my brother and my wife

STUDY ON PARTICLE SHAPE, SIZE AND GRADATION EFFECTS ON THE MECHANICAL BEHAVIOR OF COARSE-GRAINED SOILS

Abstract

Inherent particle properties such as size, shape, gradation, surface roughness and constituent material (i.e. mineralogy) control the particle-scale contact response of particles which in turn determines the global mechanical behavior of coarse-grained soils observed in both laboratory tests and full-scale geosystems. This dissertation presents a series of studies as part of two separate projects aimed to characterize the effects of particle shape and gradation on the mechanical behavior of coarse-grained soils.

Systematic investigation of the effects of an individual particle property on the mechanical behavior of granular soils is a pervasive challenge in experimental studies with naturally occurring soils because it requires careful control over the remaining particle properties. Due to this challenge, conflicting interpretations of the effect of different particle properties on the behavior of soils exist in literature. By taking advantage of state-of-the-art additive manufacturing (i.e. 3D printing) technology, artificial sand analog particles can be manufactured with independent control over different particle properties such as size, shape and gradation. The first part of this dissertation investigates the feasibility of 3D printing technology to model the mechanical behavior of coarse-grained soils. The results of this study show that 3D printing technology can be used successfully to create artificial sand analogs with different sizes and shapes using either X-ray CT scans of natural sands or synthetic shape generating algorithms based on spherical harmonics. Although the 3D printed analogs exhibited greater compressibility compared to that of natural sands, the shear wave transmission behavior of 3D printed sands, measured using piezoelectric bender

elements, exhibited dependencies on mean effective stress, void ratio and particle shape that are quantitatively similar to those previously reported for natural sands. By analyzing the shear wave transmission data, equations to predict the shear wave velocity taking into account the particle shape and void ratio were developed. The triaxial compression behavior of the 3D printed sands was investigated in both drained and undrained conditions, which exhibited a stress-dilatancy response typical of natural sands, and the interpretation of their shear response can be captured within the critical state soil mechanics framework. The results of tests on 3D printed sands show that changes in particle shape produce changes in friction angles and critical state parameters that are similar to those observed in natural sands. However, the greater compressibility of the 3D printed material and the smaller inter-particle friction coefficient should be considered in the interpretation of results.

The use of methods based on poorly-graded sand data to characterize the strength and stress-dilatancy behavior of widely-graded soils is a common practice in geotechnical engineering; however, many naturally-occurring soils encountered in the field are widely-graded as evidenced by case studies. The second part of this dissertation examines the effect of gradation and particle size on the strength and stress-dilatancy behavior of widely-graded coarse-grained soils. A well-graded natural sand sourced from the Cape May Formation near Mauricetown, New Jersey was selectively sieved to produce different sands with similar particle shape parameters but with different gradation and median particle size. The results of a series of isotropically consolidated drained and undrained triaxial tests exhibited dependency on the peak strength, dilatancy and critical state parameters of the gradation and median particle size. The analysis of the results also showed that capturing the effects of gradation and particle size depends on the definition of soil state, where the state parameter provides more robust trends than the relative density. The results indicate that for any given state parameter, more widely-graded soils exhibit greater peak friction angles, maximum dilation angles, and differences between the peak and critical state friction angles.

The research efforts presented in this dissertation show that the individual effects of particle shape, size and gradation on the soil behavior can be investigated using new experimental techniques (i.e. creating artificial sand particles using 3D printing) or selective sieving of naturally occurring soils. This can bring benefits in improved understanding of soil behavior aiding increased efficiency and robustness of geotechnical site characterization and design methodologies and in the advancement of constitutive models.

Table of Contents

List of Tables

List of Figures

Chapter 1

Introduction

1.1 Background

The mechanical behavior of coarse-grained soils is determined by the particle-scale contact response resulting from the applied boundary stresses and the geometric arrangement of particles, contacts, and pores. Inherent particle properties such as size, shape, gradation, surface roughness and mineralogy control the normal and shear deformation response of the contacts. These particle-scale interactions govern the global-scale mechanical behavior of granular soils observed in both laboratory tests and in the field. The research efforts presented in this dissertation are part of two separate projects aimed to characterize the effects of particle shape and gradation on the behavior of coarse-grained soils.

The first project is broadly focused on extending the understanding of the effects of individual particle properties on the behavior of soils that could aid in the advancement of constitutive models as well as in the increased efficiency and robustness of geotechnical site characterization and design methodologies. The investigation of individual particle properties on the behavior of coarse-grained soils requires careful control over other properties, which poses a significant challenge in experimental studies with naturally occurring soils because they tend to vary in particle sizes, shapes, surface roughness, and mineralogy. Several previous studies attempted to examine the effects of different particle properties on the engineering properties of coarse-grained soils, such as friction angle [e.g. Kirkpatrick, 1965; Marschi et al., 1972; Wang et al., 2013; Vangla and Latha, 2015; Xiao

et al., 2019; Altuhafi et al., 2016], and shear wave velocity and small-strain modulus [e.g. Iwasaki and Tatsuoka, 1977; Chang and Ko, 1982; Menq, 2003; Cho et al., 2006; Bui, 2009; Patel et al., 2009; Wichtmann and Triantafyllidis, 2009; Senetakis et al., 2012; Yang and Gu, 2013; Altuhafi et al., 2016; Liu and Yang, 2018; Dutta et al., 2020; Liu et al., 2021] often reporting contradicting trends likely due to the aforementioned challenge. Recent advances in 3D printing technology provides the ability to create artificial soil analogs with independent control over particle size, shape, and gradation [e.g. Hanaor et al., 2016; Adamidis et al., 2020].

In recent years, researchers have used 3D printing technology to generate analog particles of different sizes and shapes [e.g. Hanaor et al., 2016; Adamidis et al., 2020; Miskin and Jaeger, 2013; Athanassiadis et al., 2014], and showed that these analogs can successfully replicate the morphology of natural particles [e.g. Adamidis et al., 2020]. The results of triaxial tests on 3D printed analogs show that 3D printed particles exhibit stress-dilatancy behavior similar to that typical of natural coarse-grained soils [e.g. Hanaor et al., 2016; Adamidis et al., 2020; Matsumura et al., 2017]. Some other applications of 3D printed analogs include examining the effect of particle shape on clogging and discharge [e.g. Hafez et al., 2021], calibration of DEM simulations [e.g. Kittu et al., 2019; Peerun et al., 2021], permeability of uniformly graded soil [e.g. Adamidis et al., 2020; Wei et al., 2021], and development of transparent soil surrogates [e.g. Li et al., 2021]. These studies highlight the usefulness of 3D printing technology to create artificial soils with a precise control over their properties and indicate further research possibilities to investigate the effects of individual particle properties.

The second project is aimed to characterize the effects of gradation and particle size on the strength and stress-dilatancy behavior of coarse-grained soils. Soil strength is a fundamental parameter for geotechnical engineering design. Dilatancy of a granular soil is the change in volume due to shear deformations [Reynolds, 1885]. The stress-dilatancy relationships capture the dependence of soil strength on the dilative tendency of

coarse-grained soils. However, a number of knowledge gaps and limitations to estimate the soil strength with existing studies remain due to the challenges associated with sampling and testing of widely-graded coarse-grained soils [e.g. Daniel et al., 2004; Goto et al., 1994; Kokusho, 1994; Yoshimi et al., 1994; Singh et al., 1982]. Particularly, the effects of gradation on the strength and stress-dilatancy behavior of coarse-grained soils are complex because they depend on the soil state which can be characterized using different parameters such as void ratio, relative density, and the difference in void ratio between a given state and the critical state (termed as the state parameter by Been and Jefferies [1985]). Since the early work of Taylor [1948], several stress-dilatancy frameworks have been proposed based on either theoretical [e.g. Skempton and Bishop, 1950; Bishop, 1954; Newland and Allely, 1957; De Josselin de Jong, 1976; Rowe, 1962, 1969; Schofield and Wroth, 1968] or experimental [e.g. Vaid and Sasitharan, 1992; Lee and Seed, 1967; Bolton, 1986; Chakraborty and Salgado, 2010; Negussey et al., 1988] studies. Bolton [1986] derived stress-dilatancy correlations based on direct simple shear and triaxial compression test results on poorly-graded sands, and proposed a relative density index that accounted for the effects of both relative density and confining effective stress. Further stress-dilatancy relations clearly demonstrated the effects of particle shape, stress history, density, fabric and confinement [e.g. Vermeer and De Borst, 1984; Pradhan et al., 1989; Houlsby, 1991; Gudehus, 1996; Nakai, 1997; Wan and Guo, 1998, 1999; Vaid and Sivathayalan, 2000; Guo and Su, 2007]. However, assessing the applicability of exiting stress-dilatancy relations to widely-graded materials which are developed mostly based on experiments on poorly-graded sands warrants further systematic investigation.

1.2 Scope

The first part of this dissertation focuses on the effects of particle shape on the mechanical behavior of coarse-grained soils. 3D printing technology is used to create analog particles with different shapes while maintaining similar particle size and gradation. These 3D printed analogs are used to characterize the uniaxial inter-particle compression, oedometric

compression, shear wave transmission and triaxial compression behaviors, and compared to those of glass and steel spheres and natural sand particles.

The second part of this dissertation focuses on systematically examining the effects of particle size and gradation on the strength and stress-dilatancy behavior of widely-graded coarse-grained soils. A widely-graded natural sand sourced from a single deposit is selectively sieved to produce different sand samples with similar particle shapes but different gradations and median particle sizes. A series of isotropically-consolidated drained and undrained triaxial tests are performed with a range of initial void ratios and confining stresses to define their critical state lines and to interpret the results as a function of the initial state parameters. The applicability of using poorly-graded sand-based method with widely-graded coarse-grained soils is evaluated through Bolton's [1986] empirical framework.

1.3 Organization

This dissertation is organized into seven chapters and can be principally divided into two parts based on their topical focus. The first part of the dissertation (Chapter 2-5) focuses on the generation, characterization and mechanical behavior of 3D printed particle analogs. The second part (Chapter 6) focuses on the insights gained from the triaxial compression tests conducted on widely-graded coarse-grained soils.

Chapter 2 evaluates the feasibility of two different 3D printing technologies (i.e. Stereolithography and Polyjet) to create analog sand particles that can simulate the behavior of natural coarse-grained soils. 3D printing technology is used to generate equal-sized spheres and analog sand particles from 3D X-ray CT scans of natural angular and rounded sand particles. The uniaxial inter-particle compression, oedometric compression and shear wave transmission behaviors of the 3D printed particles are examined and compared to those of glass and steel spheres and natural angular and rounded sand particles.

Chapter 3 investigates the triaxial compression behavior of angular and rounded 3D printed analog particles and compares to those of natural angular and rounded sands. Also,

the existence of critical states for the 3D printed sands is examined.

Chapter 4 examines the effect of particle shape on the shear wave transmission behavior of 3D printed sands generated with different shapes but similar size and gradation.

Chapter 5 investigates the effect of particle shape on the triaxial compression behavior of 3D printed sands generated with different shapes but similar size and gradation.

Chapter 6 evaluates the effect of gradation and median particle size on the strength and stress-dilatancy behavior of widely-graded coarse-grained soils by conducting a series of drained and undrained triaxial compression tests on soils with different size and gradation sourced from a single deposit. The applicability of Bolton's [1986] stress-dilatancy framework that was developed from poorly-graded clean river sands, on widely-graded coarse-grained sands, is also investigated.

Chapter 7 summarizes the primary conclusions of this dissertation and provides general ideas and recommendations for future work.

Bibliography

Adamidis, O., Alber, S., and Anastasopoulos, I. (2020). Assessment of three-dimensional printing of granular media for geotechnical applications. *Geotechnical Testing Journal*, 43(3).

Altuhafi, F. N., Coop, M. R., and Georgiannou, V. N. (2016). Effect of particle shape on the mechanical behavior of natural sands. *Journal of Geotechnical and Geoenvironmental Engineering*, 142(12):04016071.

Athanassiadis, A. G., Miskin, M. Z., Kaplan, P., Rodenberg, N., Lee, S. H., Merritt, J., Brown, E., Amend, J., Lipson, H., and Jaeger, H. M. (2014). Particle shape effects on the stress response of granular packings. *Soft Matter*, 10(1):48–59.

Been, K. and Jefferies, M. G. (1985). A state parameter for sands. *Géotechnique*, 35(2):99–112.

Bishop, A. W. (1954). The use of pore-pressure coefficients in practice. *Géotechnique*, 4(4):148–152.

Bolton, M. (1986). The strength and dilatancy of sands. *Géotechnique*, 36(1):65–78.

Bui, M. T. (2009). *Influence of some particle characteristics on the small strain response of granular materials*. PhD thesis, University of Southampton.

Chakraborty, T. and Salgado, R. (2010). Dilatancy and shear strength of sand at low confining pressures. *Journal of Geotechnical and Geoenvironmental Engineering*, 136(3):527–532.

Chang, N.-Y. and Ko, H.-Y. (1982). Effects of grain size distribution on dynamic properties and liquefaction potential of granular soils. *NASA STI/Recon Technical Report N*, 83:18966.

Cho, G.-C., Dodds, J., and Santamarina, J. C. (2006). Particle shape effects on packing density, stiffness, and strength: Natural and crushed sands. *Journal of Geotechnical and Geoenvironmental Engineering*, 132(5):591–602.

Daniel, C., Howie, J., Campanella, R., and Sy, A. (2004). Characterization of spt grain size effects in gravels. In *Proc., 2nd Int. Conf. on Site Characterization (ISC'2), Millpress, Rotterdam, Netherlands*.

De Josselin de Jong, G. (1976). Rowe's stress—dilatancy relation based on friction. *Géotechnique*, 26(3):527–534.

Dutta, T., Otsubo, M., Kuwano, R., and O'Sullivan, C. (2020). Evolution of shear wave velocity during triaxial compression. *Soils and Foundations*, 60(6):1357–1370.

Goto, S., Nishio, S., and Yoshimi, Y. (1994). Dynamic properties of gravels sampled by ground freezing. In *Ground Failures under Seismic Conditions*, pages 141–157. ASCE.

Gudehus, G. (1996). A comprehensive constitutive equation for granular materials. *Soils and Foundations*, 36(1):1–12.

Guo, P. and Su, X. (2007). Shear strength, interparticle locking, and dilatancy of granular materials. *Canadian Geotechnical Journal*, 44(5):579–591.

Hafez, A., Liu, Q., Finkbeiner, T., Alouhali, R. A., Moellendick, T. E., and Santamarina, J. C. (2021). The effect of particle shape on discharge and clogging. *Scientific Reports*, 11(1):1–11.

Hanaor, D., Gan, Y., Revay, M., Airey, D., and Einav, I. (2016). 3d printable geomaterials. *Géotechnique*, 66(4):323–332.

Houlsby, G. T. (1991). How the dilatancy of soils affects their behaviour. In *Tenth European Conference on Soil Mechanics and Foundation Engineering*, volume 4, pages 1189–1202. University of Oxford, Department of Engineering Science Oxford.

Iwasaki, T. and Tatsuoka, F. (1977). Effects of grain size and grading on dynamic shear moduli of sands. *Soils and Foundations*, 17(3):19–35.

Kirkpatrick, W. (1965). Effects of grain size and grading on the shearing behaviour of granular materials. In *Proceedings of the sixth International Conference on Soil Mechanics and Foundation Engineering*, pages 273–277.

Kittu, A., Watters, M., Cavarretta, I., and Bernhardt-Barry, M. (2019). Characterization of additive manufactured particles for dem validation studies. *Granular Matter*, 21(3):1–15.

Kokusho, T. (1994). Dynamic properties of gravel layers investigated by in-situ freezing sampling. *Ground Failure under Seismic Condition*, pages 121–140.

Lee, K. L. and Seed, H. B. (1967). Drained strength characteristics of sands. *Journal of the Soil Mechanics and Foundations Division*, 93(6):117–141.

Li, Y., Zhou, H., Liu, H., Ding, X., and Zhang, W. (2021). Geotechnical properties of 3d-printed transparent granular soil. *Acta Geotechnica*, 16(6):1789–1800.

Liu, X. and Yang, J. (2018). Shear wave velocity in sand: effect of grain shape. *Géotechnique*, 68(8):742–748.

Liu, X., Zou, D., Liu, J., Zheng, B., Zhou, C., and Bai, J. (2021). A gradation-dependent particle shape factor for characterizing small-strain shear modulus of sand-gravel mixtures. *Transportation Geotechnics*, 28:100548.

Marschi, N. D., Chan, C. K., and Seed, H. B. (1972). Evaluation of properties of rockfill materials. *Journal of the Soil Mechanics and Foundations Division*, 98(1):95–114.

Matsumura, S., Kobayashi, T., Mizutani, T., and Bathurst, R. J. (2017). Manufacture of bonded granular soil using x-ray ct scanning and 3d printing. *Geotechnical Testing Journal*, 40(6):1000–1010.

Menq, F.-Y. (2003). *Dynamic properties of sandy and gravelly soils*. The University of Texas at Austin.

Miskin, M. Z. and Jaeger, H. M. (2013). Adapting granular materials through artificial evolution. *Nature materials*, 12(4):326–331.

Nakai, T. (1997). Dilatancy characteristics of geomaterials.

Negussey, D., Wijewickreme, W., and Vaid, Y. (1988). Constant-volume friction angle of granular materials. *Canadian Geotechnical Journal*, 25(1):50–55.

Newland, P. and Allely, B. (1957). Volume changes in drained taixial tests on granular materials. *Géotechnique*, 7(1):17–34.

Patel, A., Bartake, P., and Singh, D. (2009). An empirical relationship for determining shear wave velocity in granular materials accounting for grain morphology. *Geotechnical Testing Journal*, 32(1):1–10.

Peerun, M., Ong, D. E. L., Desha, C., Oh, E., and Choo, C. S. (2021). Advances in the study of micromechanical behaviour for granular materials using micro-ct scanner and 3d printing. In *International Conference of the International Association for Computer Methods and Advances in Geomechanics*, pages 911–918. Springer.

Pradhan, T. B., Tatsuoka, F., and Sato, Y. (1989). Experimental stress-dilatancy relations of sand subjected to cyclic loading. *Soils and Foundations*, 29(1):45–64.

Reynolds, O. (1885). Lvii. on the dilatancy of media composed of rigid particles in contact. with experimental illustrations. *The London, Edinburgh, and Dublin Philosophical Magazine and Journal of Science*, 20(127):469–481.

Rowe, P. (1969). The relation between the shear strength of sands in triaxial compression, plane strain and direct. *Géotechnique*, 19(1):75–86.

Rowe, P. W. (1962). The stress-dilatancy relation for static equilibrium of an assembly of particles in contact. *Proceedings of the Royal Society of London. Series A. Mathematical and Physical Sciences*, 269(1339):500–527.

Schofield, A. N. and Wroth, P. (1968). *Critical state soil mechanics*, volume 310. McGraw-hill London.

Senetakis, K., Anastasiadis, A., and Pitilakis, K. (2012). The small-strain shear modulus and damping ratio of quartz and volcanic sands. *Geotechnical Testing Journal*, 35(6):964–980.

Singh, S., Seed, H. B., and Chan, C. K. (1982). Undisturbed sampling of saturated sands by freezing. *Journal of the Geotechnical Engineering Division*, 108(2):247–264.

Skempton, A. and Bishop, A. (1950). The measurement of the shear strength of soils. *Géotechnique*, 2(2):90–108.

Taylor, D. W. (1948). *Fundamentals of soil mechanics*. John Wiley & Sons, New York, NY.

Vaid, Y. and Sasitharan, S. (1992). The strength and dilatancy of sand. *Canadian Geotechnical Journal*, 29(3):522–526.

Vaid, Y. P. and Sivathayalan, S. (2000). Fundamental factors affecting liquefaction susceptibility of sands. *Canadian Geotechnical Journal*, 37(3):592–606.

Vangla, P. and Latha, G. M. (2015). Influence of particle size on the friction and interfacial shear strength of sands of similar morphology. *International Journal of Geosynthetics and Ground Engineering*, 1(1):6.

Vermeer, P. A. and De Borst, R. (1984). Non-associated plasticity for soils, concrete and rock. *Heron, 29 (3), 1984*.

Wan, R. and Guo, P. (1998). A simple constitutive model for granular soils: modified stress-dilatancy approach. *Computers and Geotechnics*, 22(2):109–133.

Wan, R. and Guo, P. (1999). A pressure and density dependent dilatancy model for granular materials. *Soils and Foundations*, 39(6):1–11.

Wang, J.-J., Zhang, H.-P., Tang, S.-C., and Liang, Y. (2013). Effects of particle size distribution on shear strength of accumulation soil. *Journal of Geotechnical and Geoenvironmental Engineering*, 139(11):1994–1997.

Wei, D., Wang, Z., Pereira, J.-M., and Gan, Y. (2021). Permeability of uniformly graded 3d printed granular media. *Geophysical Research Letters*, 48(5).

Wichtmann, T. and Triantafyllidis, T. (2009). Influence of the grain-size distribution curve of quartz sand on the small strain shear modulus g max. *Journal of Geotechnical and Geoenvironmental Engineering*, 135(10):1404–1418.

Xiao, Y., Long, L., Matthew Evans, T., Zhou, H., Liu, H., and Stuedlein, A. W. (2019). Effect of particle shape on stress-dilatancy responses of medium-dense sands. *Journal of Geotechnical and Geoenvironmental Engineering*, 145(2):04018105.

Yang, J. and Gu, X. (2013). Shear stiffness of granular material at small strains: does it depend on grain size? *Géotechnique*, 63(2):165–179.

Yoshimi, Y., Tokimatsu, J., and Ohara, A. (1994). In situ liquefaction resistance of clean sands over a wide density range. *Géotechnique*, 44(3):479–494.

Chapter 2

Modeling the Mechanical Behavior of Coarse-Grained Soil Using Additive Manufactured Particle Analogs

Author's Note: This chapter was published in the Acta Geotechnica under the following citation and is presented here with minor edits.

Ahmed, S. S., & Martinez, A. (2020). Modeling the mechanical behavior of coarse-grained soil using additive manufactured particle analogs. *Acta Geotechnica*, 15(10), 2829-2847.

2.1 Abstract

Systematic investigation of the effects of individual particle properties, such as shape, size, surface roughness, and constituent materials stiffness, on the behavior of coarse-grained soils requires careful control over the other particle properties. Achieving this control is a pervasive challenge in investigations with naturally occurring soils. The rapid advance of modern additive manufacturing (AM) technology provides the ability to create analog particles with independent control over particle size and shape. This work evaluates the feasibility of the Stereolithography (SLA) and polyjet technologies to generate analog particles that can model the mechanical behavior of coarse-grained soils. AM is used to generate equal-sized spheres and analog sand particles from 3D X-ray CT scans of natural rounded and angular sand particles. The uniaxial inter-particle compression, oedometer compression, and shear wave

transmission behaviors of the AM particles are investigated and compared to those of glass and steel spheres and natural rounded and angular sand particles. The results indicate that AM can successfully reproduce the shape of natural coarse sand particles. The deformation of micro-asperities was found to influence the contact response of the polyjet AM particles, thus affecting their inter-particle uniaxial compression and oedometer compression response. The contact response of the SLA AM particles was closer to that of glass spheres. Both AM particle types exhibit a dependency of shear wave velocity and shear modulus on mean effective stress that is consistent with that of natural sands.

2.2 Introduction

Skeletal forces transmitted at the particle-particle contacts resulting from applied boundary stresses control the mechanical behavior of coarse-grained soil [Santamarina, 2003]. The inherent properties of the particles, such as their shape, size, surface roughness, and the stiffness of their constituent materials, control the normal and shear deformation response of the contacts. These particle-scale interactions govern the global-scale response observed in both laboratory and field tests.

Several researchers have examined the effects of different inherent particle properties on the engineering properties of coarse-grained soils, such as the friction angle, shear wave velocity, and small-strain shear modulus, often reporting contradicting trends. In triaxial compression tests on specimens of uniformly-graded sand and glass beads, Kirkpatrick [1965] and Marschi et al. [1972] observed an increase in both friction angle (ϕ') and dilatancy with a decrease in particle size. On the contrary, an increase in ϕ' with an increase in particle size has also been reported based on direct shear test results [Islam et al., 2011; Wang et al., 2013; Kara et al., 2013; Vangla and Latha, 2015]. Xiao et al. [2019] observed an increase in both peak and critical state friction angles with a decrease in particle regularity at a given confining stress from triaxial compression tests. Casini et al. [2011] also observed similar trends from direct shear tests. Contradictory observations on the effects that particle size and shape

have on the shear wave velocity (V_s) and small-strain modulus (G_{max}) of coarse-grained soils have also been reported in literature. For instance, Patel et al. [2009] and Bartake and Singh [2007] reported that the V_s of sand increases as the mean particle size (D_{50}) decreases. In contrast, Iwasaki and Tatsuoka [1977], Wichtmann and Triantafyllidis [2009], and Yang and Gu [2013] observed no significant effect of D_{50} on V_s, whereas Sharifipour et al. [2004] and Bui [2009] reported an increase in V_s with increasing D_{50}. In addition, while Iwasaki and Tatsuoka [1977] reported no significant influence of particle shape on G_{max}, an increase in G_{max} has been reported both with increasing particle roundness (i.e. decreasing angularity) by Bui [2009] and Cho et al. [2006] and decreasing particle roundness by Altuhafi et al. [2016] and Liu and Yang [2018]. These types of contradictory observations likely result from the pervasive challenge to experimentally control individual particle properties in natural soils.

Additive manufacturing (AM) or 3D printing technology has advanced rapidly in the last decade. This technology can be used to generate artificial soil analogs with independent control over particle size, shape, and gradation [Hanaor et al., 2016; Adamidis et al., 2020]. In recent years, researchers have used AM technology to generate particles of different sizes and shapes [Hanaor et al., 2016; Adamidis et al., 2020; Miskin and Jaeger, 2013; Athanassiadis et al., 2014]. A morphological comparison study conducted by Adamidis et al. [2020] on Hostun sand particles and AM analogs showed that these analogs can successfully replicate morphology of natural particles. Authors have also performed triaxial tests on specimens of AM particles of different shapes and sizes [Adamidis et al., 2020; Miskin and Jaeger, 2013; Athanassiadis et al., 2014]. Some of these results show that the assemblies of AM particles exhibit stress-dilatancy behavior similar to that typical of frictional granular materials [Hanaor et al., 2016; Adamidis et al., 2020; Matsumura et al., 2017]. Other studies have revealed that AM particles qualitatively exhibit key aspects of 1D compression behavior of natural soils, such as different compression and recompression indices [Gupta et al., 2019]. These findings qualitatively suggest that AM particle analogs can emulate the macro-scale behavior of coarse-grained soil.

Despite the similarities in mechanical behavior of assemblies composed of natural and additive manufactured particles, further insight requires the understanding of inter-particle contact behavior, which depends on particle morphology as well as the mechanical properties of the particle constituent material [Cavarretta et al., 2010]. The force-displacement response of particle contacts under compression indicates a transition from an approximately linear relationship at lower forces to a Hertzian response at higher forces [Cavarretta et al., 2010; Cole and Peters, 2007, 2008; Cavarretta et al., 2012, 2017]. The threshold force at which the behavior changes depends on the particle morphology and material stiffness [Cavarretta et al., 2010]. Kittu et al. [2019] characterized the contact behavior of AM spheres of two different materials and showed that the Hertzian behavior is observed after a threshold force, and suggest that AM materials can feasibly be used for applications such as validation of discrete element modeling (DEM) simulations.

The current study presents a methodology to generate additive manufactured particles with similar size and morphology to natural soil particles. Three behaviors of these AM particles are then investigated: inter-particle uniaxial compression, oedometric compression of assemblies, and shear wave transmission and small-strain shear moduli of assemblies. For each behavior investigation, the response of the AM particles is compared to that of particles and specimens of glass and stainless-steel spheres and rounded and angular natural sand particles.

2.3 Inter-Particle Contact Response

Hertz theory describes the force-deformation relationship for two elastic spheres in contact. The contact stress is a function of the applied normal force (F), particle radii ($R_{1,2}$), Young's moduli ($E_{1,2}$), and Poisson's ratios ($\nu_{1,2}$) of the spheres. According to Hertz theory, the contact deformation, δ, can be calculated as:

$$\delta = \left(\frac{9}{16} \frac{F^2}{RE^{*2}} \right)^{1/3} \tag{2.1}$$

where R is the effective radius of curvature expressed as: $1/R = 1/R_1 + 1/R_2$, and E^* is the effective Young's modulus defined as: $1/E^* = (1 - \nu_1^2)/E_1 + (1 - \nu_2^2)/E_2$.

Hertz theory assumes that the strains are small and elastic, the surfaces of the bodies are continuous and non-conforming, each body can be considered as elastic half space, the surfaces are frictionless, and the contact is non-adhesive. Prior research shows that the normal force-displacement response of two spheres pressed against each other usually follows the behavior predicted by Hertz theory within a certain force interval. Antonyuk et al. [2005] describes four stages of the force-displacement relationship as shown in Fig. 2.1: (I) plastic deformation of micro-asperities on the contact surface, (II) elastic deformation predicted by Hertz theory, (III) elasto-plastic deformation, and (IV) breakage.

Initial plastic response due to the deformation of micro-asperities was reported by Cavarretta et al. [2010], who observed plastic yielding (stage I in Fig. 2.1) until the contact normal force F reached a threshold force, N_{GT}. The threshold force depends on a given particle's surface roughness, surface radius at the contact point, and Young's modulus [Greenwood and Tripp, 1967]. Once F exceeds N_{GT}, the force-displacement response follows that predicted by Hertz theory (stage II in Fig. 2.1). Point N in Fig. 2.1 represents a transition between stage II and stage III, where elastic deformations give way to plastic yielding and deformations accumulate at a larger rate than predicted by Hertz theory. With further increase in force, the first breakage point is reached and the particle begins to suffer significant breakage as shown in stage IV.

2.4 Hertz-Based Normalization of Contact Deformation

Important insight into the small- and medium-strain behavior of coarse-grained soil can be achieved with elastic contact mechanics theories, such as Hertz theory [Santamarina, 2003]. Development of an interpretation framework based on Hertz theory would thus capture the stage II behaviors shown in Fig. 2.1, which is described with the particle's Young's modulus and size.

For a contact between spheres of the same material to undergo the same deformation as another contact composed of spheres of different radius and constituent material, the following condition must be met:

$$\left(\frac{F_1^2}{R_1 E_1^{*2}}\right)^{1/3} = \left(\frac{F_2^2}{R_2 E_2^{*2}}\right)^{1/3} \tag{2.2}$$

The average normal force at inter-particle contacts in an assembly of mono-sized spheres with a random packing is related to the effective stress within the assembly (σ'), radius of the spheres (R), and void ratio of the assembly (e) [Santamarina, 2003], as follows:

$$F = C\sigma' R^2 \tag{2.3}$$

where C is a coefficient that describes the particle tributary area and can be expressed as $C = \pi(1+e)^{2/3}$ [Santamarina, 2003]. Considering assemblies of particles to undergo the same average contact deformation, Eq. 2.2 can be written as:

$$\left(\frac{C_1 \sigma_1' R_1}{E_1^{*2}}\right)^{1/3} = \left(\frac{C_2 \sigma_2' R_2}{E_2^{*2}}\right)^{1/3} \tag{2.4}$$

For assemblies with the same void ratio and particle size, Eqs. 2.2 and 2.4 lead to

the following relationship:

$$\frac{F_1}{E_1^*} = \frac{F_2}{E_2^*} \qquad \text{or} \qquad \frac{\sigma_1'}{E_1^*} = \frac{\sigma_2'}{E_2^*} \tag{2.5}$$

This relationship indicates that the same average deformation will be experienced at the particle contacts if the ratio of the contact force to the constituent material's Young's modulus is equal for the two assemblies. For assemblies, an additional requirement of an equal void ratio must also be met.

Figure 2.2a shows the Hertzian force-displacement relationship for contacts between particles composed of steel, glass, and polymer. The curves correspond to equal-sized spheres with a diameter of 3.175 mm and show that a greater force is required to obtain a given deformation for contacts between particles with higher Young's modulus. Figure 2.2b presents curves in terms of normalized force (F/E^*) for the same materials. The three curves overlap, indicating that the normalized force required to produce a given contact deformation is independent of the Young's modulus. This normalization, however, ignores plastic deformation of micro-asperities and contact yielding.

2.5 Materials and Methods

Experiments were performed on eight different types of particles to characterize their contact- and element-scale responses. This section describes the AM technology employed in this investigation, the materials tested, and the experimental procedures used to characterize their mechanical response.

2.5.1 Additive Manufacturing Technology

Advances in AM technology have developed different methods and materials that enable modern 3D printers to generate objects with a wide range of precision and cost. Large-scale, specialized 3D printers can generate highly complex geometries using materials such as

metals, polymers, ceramics, and concrete with high accuracy. Some of those printers can mix different materials on demand to achieve desired mechanical properties [Jiménez et al., 2019; Najmon et al., 2019]. Desktop 3D printers are typically constrained to printing polymers; however, even these printers can print layers with thickness in the order of 10 to 30 μm [Ngo et al., 2018]. These fast-paced advances offer design freedom and production flexibility which have established 3D printers as a conventional tool in many science and engineering research laboratories [Tofail et al., 2018].

Different AM methods provide certain advantages and drawbacks. The Stereolithography (SLA) and polyjet AM methods are popular in research and prototyping to manufacture small, detailed parts because they are relatively inexpensive and quick [Hanaor et al., 2016; Adamidis et al., 2020; Kittu et al., 2019]. Hence, this study uses these two AM methods to evaluate differences in the responses of the manufactured AM particles and their implications in modeling of coarse-grained soil behavior. Stereolithography uses an ultraviolet (UV) laser to cure and harden thin layers of liquid photopolymer resin contained in a reservoir (Fig. 2.3a). After a layer solidifies, the build platform moves up by a distance equivalent to one layer, and this process is repeated to produce a 3D object. A support structure attached to the printed object prevents deflection and warping. After printing and washing the object with alcohol to clean off uncured resin from its surface, the support structure is removed by cutting and the printed object further cures under UV light at temperatures between 40° and 80° C to increase the polymer stiffness and strength. The second method considered here is the polyjet technology, which also uses a UV laser to harden liquid photopolymer resin (Fig. 2.3b). However, polyjet printers have two print heads that deposit different resins, where one resin creates the desired object while the other resin acts as the support structure. The support structure is then removed from the finished 3D object either by water jetting or treatment using a 2% sodium hydroxide solution.

2.5.2 Equal Sized Spheres

This study examined eight different particle types (Fig. 2.4). Four types were spheres with a diameter of 3.175 mm composed of 304 stainless steel, borosilicate glass, SLA photopolymer, and polyjet acrylate-based polymer. Table 2.1 lists selected properties of these materials. The SLA spheres were generated using a *Form 2* printer from Formlabs with clear photopolymer resin (FKGPCL02). The print layer thickness was 25 μm, requiring a total of 127 layers to print one sphere. The polyjet spheres were generated using an *Objet Eden 260V* printer from Stratasys with *VeroWhitePlus* rigid acrylate-based polymer resin with a printing resolution of 30 μm.

Figure 2.5 shows X-ray CT scans of the SLA and polyjet spheres. Both the direction of the SLA sphere layers as well as the asperity left by the support structure are visible. The scans also show that the polyjet spheres have a greater surface roughness compared to the SLA spheres. Table 2.1 includes the measured angle of repose (ϕ_{rep}) of all the spheres. Results indicate that the glass spheres have the smallest ϕ_{rep} whereas the polyjet spheres have the largest ϕ_{rep}. Since all the spheres have the same particle shape and size, the differences in ϕ_{rep} suggest that the glass spheres have the smallest surface roughness and the polyjet spheres have the largest surface roughness. The specific gravity values indicate that steel is the densest material and both 3D printing resins are the least dense materials.

2.5.3 Natural and Additive Manufactured Sand Particles

Natural quartz particles were separated by sieving a well-graded sand to obtain samples passing through the #6 (3.36 mm) and retained by the #8 (2.38 mm) sieves. This resulted in a poorly-graded sandy soil composed of both angular and rounded particles. The particles were then manually separated to create two sand samples: one with angular particles and one with rounded particles (Fig. 2.4). This methodology offers the advantage of ensuring that both natural sand samples have the same gradation and mineralogy, and only differ in

particle morphology. To generate the additive manufactured particle analogs, 90 angular and 70 rounded natural sand particles were first chosen randomly for X-ray CT scanning with a resolution of 10 μm (Fig. 2.6a). These scans were reduced in resolution to increase the speed of the AM process (Fig. 2.6b), which were used to generate the analog particles using the polyjet technology (Fig. 2.6c). The AM particles appear significantly rougher than the natural particles due to the polyjet printing procedure. The influence of the larger surface roughness can be appreciated in the ϕ_{rep} measurements, with consistently larger values for both angular and rounded analog particles than for the natural particles.

The similarity between the natural and additive manufactured particles was assessed through comparison of particle morphology. Typically, roundness and sphericity are used to quantify particle shape. Roundness is a measure of the sharpness of a particle's edges and corners, whereas sphericity is a measure of the similarity of the particle shape to a circle or sphere. The roundness of a particle is defined as the ratio of the average radius of curvature of the particle corners to the radius of the largest inscribed circle [Wadell, 1932]. The sphericity of a particle can be defined in a number of ways [Mitchell et al., 2005; Guida et al., 2020]; here, the following parameters were considered: area sphericity (ratio of the projected area of a particle to the area of the minimum circumscribing circle), perimeter sphericity (ratio of the perimeter of the particle to the perimeter of a circle having the same projected area as the particle), and width-to-length ratio. The shape parameters were obtained from image analysis of photographs of particles using the code by Zheng and Hryciw [2015]. As Fig. 2.7 shows, all the shape parameters of the AM particle analogs compare well with those of the natural particles, indicating that morphology is successfully reproduced.

2.5.4 Particle-Particle Compression Test

A uniaxial compression loading frame was built to characterize the normal contact force-displacement behavior of spherical particles. Figure 2.8a shows a schematic of the testing setup, which consists of two custom-made pedestals fabricated with 316 stainless

steel and two 18-8 stainless steel holders, each of which has a machined 3.185 mm diameter circular hole. The spheres were attached to the holes with Ethyl Cyanoacrylate glue. An electric actuator was used to apply the displacement-controlled compression. Three linear variable differential transformers (LVDT) with a range of ± 1.27 mm were used to measure the contact displacement. The LVDTs were attached to the top pedestal with three custom-made aluminum clamps, and differences in the readings were used to identify any tilting of the particles during testing. Two different load cells with capacities of 100 N and 1000 N were used to measure the applied load on the SLA and polyjet particles, and glass and steel particles, respectively. An initial investigation indicated no significant effect of the displacement rate on the force-displacement response for values between 0.03 and 0.003 mm/s. Thus, a displacement rate of 0.003 mm/s was used in all tests. The force-displacement response for the steel, glass, SLA, and polyjet spheres was measured with three cycles of subsequently increasing load. Load levels applied to the different materials were determined so that the normalized force, F/E^*, was 0.008 N/MPa for glass and steel and 0.06 N/MPa for the SLA and polyjet polymers.

2.5.5 Oedometer Compression Test

One-dimensional oedometer compression tests were performed on assemblies of spherical sand (natural and AM) particles to characterize their stress-strain response. Figure 2.8b shows a schematic of the oedometer testing setup. A custom-made mold made of 316 stainless steel with an inside diameter and height of 63.5 mm was used to contain the specimens. An electric actuator was used to apply displacement-controlled compression at a rate of 0.02 mm/sec to each specimen. Vertical displacements were measured with an LVDT and the load was measured with a load cell. Specimens were prepared by pouring the particles in the testing mold in three lifts. After pouring each lift, the specimen side was tapped with a rubber mallet to densify the specimen to its target void ratio. Specimens were prepared at initial void ratios of 0.55 ± 0.02, 0.60 ± 0.02, and 0.65 ± 0.02 for all materials except the glass spheres,

as their maximum attainable void ratio was 0.60. The maximum applied normalized vertical stress (σ'_v/E^*) was 4×10^{-5} for all the specimens, which was selected based on experience to prevent breakage or significant yielding of the particle contacts according to Ahmed et al. [2019].

2.5.6 Bender Element Test

The small-strain response of spherical and sand (natural and AM) particle assemblies was examined by means of bender element tests. Figure 2.8c shows a schematic of the bender element test setup. Specimens with a diameter of 70 mm and a height between 58 and 70 mm were contained within a latex membrane. Bender elements with 12.7 mm in length, 8 mm in width, and 0.66 mm in thickness were attached to the top and bottom caps, which were used to send and receive the S-waves. The shear wave velocity was calculated using the travel time from the transmitter to the receiver bender. The wave arrival time was taken as the initial rise of the signal, defined as the time when a signal first crossed the x-axis, as described by Yamashita et al. [2009]. Shear wave velocity measurements were obtained for specimens with initial void ratios of 0.55 ± 0.02, 0.60 ± 0.02, and 0.65 ± 0.02. The specimens were prepared following the same procedure as stated above. Isotropic confining pressures between 10 kPa and 70 kPa were applied to all the specimens using a vacuum pump.

2.6 Results

This section presents results from the uniaxial particle-particle compression, oedometer compression, and bender element tests aimed at characterizing the behavior of the additive manufactured particles and comparing it to that of other particle types. Individual particle tests provide information about the contact response whereas tests on assemblies enable an evaluation of the element-level stress-strain and stiffness behavior.

2.6.1 Uniaxial Particle-Particle Compression

The contact force-displacement response of equal-sized spheres of stainless steel, glass, SLA polymer, and polyjet polymer was investigated. Figure 2.9 provides force-displacement results for each material, along with the response predicted by Hertz theory. Figure 2.10 presents results in terms of the normalized contact force (F/E^*) and the force ratio (F/N_{GT}). Although five tests were conducted for each material, the results of only one representative test are shown here for brevity.

The contact force-displacement response of the glass and SLA spheres is mostly elastic at lower loads, as shown in Fig. 2.9. The threshold force N_{GT} is about 4 N for the glass spheres and about 6 N for the SLA spheres. The response of the glass spheres begins to deviate from the Hertz prediction at a normal force (F) of about 30 N, corresponding to an F/E^* of about 0.0009 N/MPa (Fig. 2.10a) and an F/N_{GT} of about 7.5 (Fig. 2.10b). Deviation from the Hertz prediction begins at about 20 N for the SLA particles, corresponding to an F/E^* of about 0.01 N/MPa (Fig. 2.10c) and an F/N_{GT} of 3.4 (Fig. 2.10d). The contact plastic deformation (δ_{pm}) after unloading is significantly lower for the glass spheres than for the SLA particles (Figs. 2.10b and 2.10d), indicating that the SLA spheres underwent a larger amount of plastic deformation either due to deformation of micro-asperities or contact yielding. However, under a similar applied normalized contact force, both the glass and SLA 3D printed spheres have similar contact displacements (Fig. 2.10a). The plastic deformation of micro-asperities (i.e. stage I in Fig. 2.1) is strongly pronounced in the response of the polyjet AM particles, as shown in Fig. 2.9d, where the second dotted line represents the Hertz solution with a constant offset in the initial constant displacement. For these particles, N_{GT} has a magnitude of about 12 N. After stage I, the force-displacement response is somewhat elastic as predicted by Hertz theory as shown in the offset Hertzian relationships in Figs. 2.10a, 2.10e, and 2.10f. However, the response begins to deviate from the Hertz theory at a normal force of about 22 N, corresponding to an F/E^* of

0.017 N/MPa. The polyjet spheres exhibit a higher δ_{pm} than the glass and SLA spheres. In addition, under similar applied F/E^*, the polyjet contact displacement is higher than that for glass and SLA due to the larger deformations accumulated during stage I. The steel spheres exhibited yielding starting from a very small normal force of about 10 N ($F/E^* \approx 0.0001$ N/MPa). The stage I regime (i.e. plastic deformation of micro-asperities) and stage III regime (i.e. elasto-plastic deformation) appear to govern the force-displacement response, resulting in a large deviation from the Hertzian prediction, in accordance with Goldsmith and Lyman [1960] and Kagami et al. [1983].

2.6.2 Oedometer Compression

Results from the 1D oedometer compression tests highlight the effects of constituent material stiffness on the compression response of particle assemblies. Figure 2.11 shows the results of spherical particle tests in terms of vertical strain ($\Delta H/H_0$) versus effective vertical stress (σ'_{v}) for specimens with e_0 of 0.55, 0.60, and 0.65. Results of two tests per material are presented here denoted by "Test 1" and "Test 2" in the legend (Fig. 2.11). Both types of AM sphere specimens require the lowest stress to achieve a certain vertical strain, followed by the glass spheres and then by the steel spheres with the highest stress, as shown in Figs. 2.11a to 2.11c, due to differences in Young's moduli where $E_{\text{polyjet}} < E_{\text{SLA}} < E_{\text{glass}} < E_{\text{steel}}$. The assemblies of polyjet spheres are more compressible than the other assemblies for all e_0, and especially appreciable for $e_0 = 0.65$. In terms of normalized stress (σ'_{v}/E^*), the compression responses of all the specimens aggregate in a tighter band as depicted in Figs. 2.11d to 2.11f. However, the curves for both the AM spheres lie to the right of the curves for the steel and glass spheres. The results indicate that the Hertz-based normalization does not account for other effects that influence the compression behavior of granular assemblies, such as yielding of micro-asperities and plastic yielding at particle contacts (stages I and III in Fig. 2.1). The compression curves collapse to a more compact band when plotted using a modified normalization, as shown in Figs. 2.11g to 2.11i, where the Young's modulus is

raised to an empirically determined power $n = 0.70$ as follows:

$$\frac{\sigma'_{v1}}{E_1^{*0.7}} = \frac{\sigma'_{v2}}{E_2^{*0.7}} \tag{2.6}$$

Similar to the observation in Fig. 2.11, the specimens of additive manufactured angular and rounded sand particles require a lower stress to undergo a given amount of vertical strain than the specimens of natural sand, as shown in Figs. 2.12a to 2.12c and 2.13a to 2.13c, respectively. The compression curves aggregate in a tighter band when plotted in terms of normalized stress using Eq. 2.6 (Figs. 2.12d to 2.12f and 2.13d to 2.13f), although the polyjet assemblies of both angular and rounded particles are more compressible than the natural particles at larger normalized stresses.

Differences in compressibility for the specimens of different constituent materials but of similar particle shape and void ratio can be due to different amounts of either contact plastic deformation or particle rearrangement. Ahmed et al. [2019] investigated the distribution of contact normal forces within an assembly of spheres with an $e_0 = 0.60$ using 3D Discrete Element Modeling simulations. The authors found that for an applied normalized stress of $\sigma'_{\mathrm{v}}/E^* = 4 \times 10^{-5}$, the average and 95$^{\mathrm{th}}$ percentile contact forces were 20 N and 62 N for assemblies of glass spheres, respectively, and 1.0 N and 3.5 N for assemblies of polyjet polymer, respectively. Comparing these values to the results from uniaxial particle compression tests suggests the contact forces in the glass sphere assemblies largely remain in the elastic regime (stage II in Fig. 2.1) bounded by an N_{GT} of about 4 N and an onset of contact yielding of about 30 N. On the other hand, the contact forces in the polyjet sphere assemblies remain in the micro-asperity yielding regime (stage I in Fig. 2.1), where $F < N_{\mathrm{GT}}$, with an N_{GT} of about 12 N. This comparison indicates that the larger compressibility of the polyjet assemblies is likely due to the larger initial compressibility of the rougher inter-particle contacts.

All sphere assemblies exhibit larger compression indices (C_{c}) as e_0 is increased, as

shown in Fig. 2.14a, likely due to the larger contact forces transferred at the contacts and more pronounced rearrangement of particles with increasing σ'_v. The polyjet spheres exhibit higher C_c at each e_0 compared to the other sphere types. Figure 2.14b shows that C_c values for the SLA, glass, and steel specimens are relatively independent of the constituent material Young's modulus (E). Figure 2.14c shows that, similar to the spherical particles, the natural particles and 3D printed analogs exhibit higher C_c as e_0 is increased, although C_c is systematically larger for the polyjet specimens. In addition, the rounded particle specimens have a slightly larger compressibility than the angular particle specimens for both natural and AM particles. These results indicate that while the AM analogs can qualitatively model the compression behavior of natural soils, some AM materials and processes, such as polyjet, can result in exaggeration of certain behaviors such as 1D compression.

2.6.3 Shear Wave Velocity and Small-Strain Modulus

The shear wave velocity (V_s) for assemblies of spheres and sand (natural and AM) particles were obtained using bender elements. The corresponding shear moduli or small-strain moduli (G_{max}) were then determined using the relationship $G_{max} = \rho V_s^2$, where ρ is the specimen density. Figure 2.15 shows typical transmitter and receiver bender signals for glass and polyjet sphere assemblies at different isotropic stresses.

The effect of the constituent material stiffness on the shear wave velocity is examined through V_s measurements on specimens of steel, glass, SLA, and polyjet spheres with similar initial void ratio (e_0), as shown in Figs. 2.16a to 2.16c. The V_s decreases as e_0 is increased for any given p'. The steel spheres exhibit higher V_s for all e_0 compared to the glass and AM spheres due to the steel's larger stiffness. The SLA and polyjet specimens have similar V_s values, which are greater than those for glass. Since the particle shape and void ratio are similar between the specimens, the likely cause of higher V_s in the AM specimens relative to the glass specimens is a larger inter-particle contact area facilitated by the softer polymer material, especially considering the high surface roughness that leads to significant plastic

contact deformation.

A comparison of the V_s measurements on specimens of angular and rounded natural and AM particles shows similar trends as the tests on spheres, where V_s decreases as e_0 is increased for both the natural and analog particles (Figs. 2.16d to 2.16f). The AM particles exhibit a higher V_s compared to the natural particles; similarly, the AM spheres have larger V_s measurements than the glass spheres. The rounded particles exhibit slightly larger V_s values than the angular particles for both natural and 3D printed specimens, consistent with trends reported in the literature [Cho et al., 2006].

The shear wave velocities for the AM materials are larger during unloading than during loading for any given p', as shown in Figs. 2.17a, 2.17c, and 2.17d. The polyjet spheres display a stronger difference than the SLA spheres, which is likely due to the larger plastic contact deformation as observed in the uniaxial particle-particle compression tests. This greater deformation leads to a larger contact area, which increases the stiffness of the contact. The V_s measured on assemblies of glass and steel, shown in Fig. 2.17b, indicate that the values are only slightly larger during unloading than during loading, suggesting a small amount of contact plastic deformation. The sand particle tests reveal similar trends, with significantly larger V_s values measured during unloading for the polyjet specimens and almost similar values measured during loading and unloading for the natural sand specimens.

A comparison of the dependency of the shear wave velocity on the mean effective stress for the different materials can be made based on a power-law equation of the following form:

$$V_s = \alpha(p')^{\beta} \tag{2.7}$$

where α is the shear wave velocity (m/s) at an effective stress of 1 kPa and β reflects the evolution of the particle as a function of mean effective stress [Cha et al., 2014]. The values of α-coefficients and β-exponents of all the specimens were obtained from fitted relationships

as shown in Fig. 2.16. Figures 2.18a and 2.18b provide the α and β values for specimens composed of spheres and sand particles, respectively. As the void ratio is decreased, the α-coefficient generally increases and the β-exponent generally decreases. For the tests on spheres, the α-coefficients are similar for the SLA and polyjet specimens, and higher for the steel specimens. The α-coefficients obtained from sand specimens indicate larger values for the polyjet particles than for the natural particles (Fig. 2.18b). The values of the β-exponents for the sphere specimens range between 0.1553 and 0.1913. For these tests, the β-exponent generally decreases with increasing constituent material stiffness such that steel has the lowest values and the AM polymers have the larger values. The β-exponents for the natural and analog sand specimens range between 0.2060 and 0.2480, and the values for the AM specimens are generally slightly higher than those for the natural particle specimens at any given initial void ratio.

As indicated by Cascante and Santamarina [1996], the β-exponent values can range between 0 and 0.75 depending on the type of contact (e.g. curved or cone-to-plane) and contact response (e.g. Hertzian elastic or elasto-plastic). Theoretical β values for Hertzian inter-sphere contacts (i.e. stage II in Fig. 2.1) are equal to 0.167 and for elastic cone-to-plane contacts and spheres experiencing contact yield are equal to 0.25 [Cascante and Santamarina, 1996]. Since the β-exponents obtained from the test results on sphere specimens are generally larger than 0.167, they indicate that the contacts do not exhibit a pure Hertzian response possibly due to contact yielding and particle rearrangement. This effect is more pronounced for the natural and analog sand particles, which yielded larger β-exponents in agreement with trends reported in the literature [Cha et al., 2014]. Figure 2.18c presents a comparison of α and β values of the specimens of natural and AM sand particles with those from natural sands reported by Cha et al. [2014]. As shown, the values from this investigation are within the range for sands reported in the literature, suggesting that the AM analogs can reproduce the relationship between V_s and p' for coarse-grained soils.

The small-strain shear moduli (G_{max}) of the spherical particles specimens show similar

trends, where $G_{\max}$ increases with decreasing e_0 and increasing p' (Figs. 2.19a to 2.19c). The steel spheres exhibit significantly higher $G_{\max}$ compared to other materials due to the greater stiffness and density of steel. Both types of AM spheres exhibit similar $G_{\max}$, which are smaller than those for glass. Figures 2.19d to 2.19f present $G_{\max}$ measurements for specimens of angular and rounded natural and AM particles, which increase with decreasing e_0 and increasing p', similar to the spherical specimens. The natural particles exhibit higher $G_{\max}$ compared to the AM particles due to the sand specimens' greater density. Also, both the natural and AM rounded particles had larger $G_{\max}$ values than the angular particles.

The shear modulus of a particle assembly under an effective isotropic stress, p', can be represented by the following power equation [Hardin and Richart Jr, 1963]:

$$G_{\max} = AF(e)(p')^{\mathrm{n}} \tag{2.8}$$

where A is a coefficient that depends on the fabric and the constituent materials' elastic properties, $F(e)$ is a function of the void ratio, and n is an exponent that describes the sensitivity of $G_{\max}$ to changes in p'. The parameters A, $F(e)$, and n can be determined empirically [Hardin and Richart Jr, 1963; Hardin and Black, 1966] or analytically for an assembly with an isotropic stress state using Hertz contact theory or rough contact theory [Chang et al., 1991; Yimsiri and Soga, 2000].

Figures 2.20a and 2.20b show the values of A-coefficients and n-exponents for the sphere and sand particle specimens, respectively. In the same manner as the results shown in Figs. 2.18a and 2.18b, the A-coefficients generally increase as e_0 is decreased. Relative to the other sphere specimens, the steel spheres have significantly higher A-coefficients and the AM spheres have the smallest. The n-exponents for all spheres range between 0.3114 and 0.4027, with the smaller values of the range representing the steel sphere specimens and the larger values representing the AM sphere specimens. The A-coefficients for the natural particle specimens are larger than those for the analog particle specimens, and the

n-exponents range between 0.421 and 0.458 for natural sand and between 0.432 and 0.529 for analog sand. These values are in agreement with those reported in literature [Hardin and Black, 1966; Chung et al., 1984]. These observations also indicate that the SLA and polyjet analog particles can be used to model the relationship between $G_{\max}$ and p' for coarse-grained soils.

2.7 Implication on Experimental and Numerical Studies

The results presented in this paper highlight several aspects of both the SLA and polyjet additive manufacturing technologies related to the ability of AM analogs to model the behavior of natural soils. Both the SLA and polyjet technologies have their own advantages and limitations. From a manufacturing perspective, polyjet technology is better equipped to successfully and more efficiently reproduce the shape of natural sand particles (Figs. 2.6 and 2.7). This is because the support structure in polyjet AM is composed of a gel-like material that does not alter the surface of the 3D printed particles. SLA technology, on the other hand, requires solid support structures that must be removed from each individual particle, resulting in a slower production and an asperity on the particle surface (Fig. 2.5).

From a modeling perspective, the contact deformation response of SLA particles was similar to that of glass, which is typically used as an analog for quartz particles (Fig. 2.10a). In comparison, the polyjet spheres accumulated larger contact plastic deformations (Fig. 2.10a), likely due to the significantly larger surface roughness produced by the printing procedure (Figs. 2.5 and 2.6). The 1D compression response of assemblies of AM particles suggests that normalization of the applied stresses by the constituent material stiffness may provide a viable framework for modeling the compression behavior. However, assemblies of spherical and analog sand polyjet particles indicate that their compressibility is larger than that of assemblies of glass and natural soil particles, likely due to plastic deformation of the polyjet particles' micro-asperities (Figs. 2.11, 2.12, 2.13, and 2.14). Shear wave velocity and shear modulus measurements indicate that the AM analogs have a similar dependency on

mean effective stress as natural sands, suggesting that this behavior is appropriately modeled by the analogs (Figs. 2.18 and 2.20).

The results presented herein highlight the potential benefits that additive manufacturing technology can provide for the study of the behavior of granular materials. Possibly the greatest advantage of the AM technology is the ability to systematically control individual particle properties, such as particle size, shape, and constituent material stiffness. In addition, as pointed out by Kittu et al. [2019], AM particle analogs may enhance validation procedures for DEM models against experimental data. Namely, use of AM could ensure that the same particle shape and sizes are being tested in both numerical and experimental tests. However, this requires DEM models to accurately capture the normal and shear force-displacement response of the AM material, which can deviate from Hertz theory for materials such as the polyjet polymer.

2.8 Conclusions

This paper provides the results of an investigation into the feasibility of using additive manufacturing technology to generate particle analogs to model the mechanical behavior of coarse-grained soils. The behaviors investigated include uniaxial inter-particle compression, oedometric compression, and shear wave transmission. The materials tested were stainless steel, borosilicate glass, and SLA and polyjet AM spheres, as well as natural and AM sand particles. The main findings are summarized as follows:

- The SLA and polyjet AM technologies can accurately reproduce the shape of natural coarse sand particles. However, the surface texture of the AM particles is determined by the specific manufacturing procedure, resulting in different surface roughnesses that can affect the inter-particle contact behavior.

- The results from uniaxial inter-particle compression tests on spheres of different constituent materials indicate that the contact normal force-displacement response

of the SLA AM particles can closely model the contact behavior of glass particles using a Hertz-based normalization where the contact force is scaled by the material Young's modulus (F/E^*). However, the contact response of the polyjet particles was significantly influenced by the deformation of micro-asperities at small loads, which led to an initially softer response. The contact force at which the micro-asperities are fully deformed (N_{GT}) is larger for the polyjet particles than the SLA particles due to the larger surface roughness of the former.

- The results from oedometer tests indicate that compressive stress-strain response is influenced by the constituent material stiffness, yielding at inter-particle contacts, and densification caused by particle rearrangements. Overall, the results indicate that the 1D compression behavior can be modeled more accurately with the SLA particles with a modified Hertz-based normalization. However, the polyjet method offers the ability to reproduce a wider range of particle shapes.

- Shear wave velocity and shear modulus measurements obtained with bender elements indicate that the dependency with mean effective stress for the AM materials is similar to that of natural sands. This is confirmed by measurements on assemblies of steel, glass, and AM SLA and polyjet spheres, as well as natural and polyjet rounded and angular sand particles.

Additive manufacturing technology is rapidly evolving. Manufacturing processes are becoming faster and more precise, allowing for better representation of particle shapes. In addition, new materials are being developed, some of which have properties that are closer to natural minerals such as quartz. While the technology is readily available to manufacture analog sand particles, there is a need to carefully evaluate each manufacturing process and material for its ability to model the behavior of natural soils.

2.9 Acknowledgment

This material is based upon work supported in part by the National Science Foundation (NSF) under award No. 1735732. Any opinions, findings, and conclusions or recommendations expressed in this material are those of the author(s) and do not necessarily reflect those of the NSF.

Bibliography

Adamidis, O., Alber, S., and Anastasopoulos, I. (2020). Assessment of three-dimensional printing of granular media for geotechnical applications. *Geotechnical Testing Journal*, 43(3).

Ahmed, S. S., Singh, M., and Martinez, A. (2019). Particle-scale contact response of 3d printed particle analogs. In *Engineering mechanics institute conference. Pasadena, CA*.

Altuhafi, F. N., Coop, M. R., and Georgiannou, V. N. (2016). Effect of particle shape on the mechanical behavior of natural sands. *Journal of Geotechnical and Geoenvironmental Engineering*, 142(12):04016071.

Antonyuk, S., Tomas, J., Heinrich, S., and Mörl, L. (2005). Breakage behaviour of spherical granulates by compression. *Chemical Engineering Science*, 60(14):4031–4044.

Athanassiadis, A. G., Miskin, M. Z., Kaplan, P., Rodenberg, N., Lee, S. H., Merritt, J., Brown, E., Amend, J., Lipson, H., and Jaeger, H. M. (2014). Particle shape effects on the stress response of granular packings. *Soft Matter*, 10(1):48–59.

Bartake, P. and Singh, D. (2007). Studies on the determination of shear wave velocity in sands. *Geomechanics and Geoengineering*, 2(1):41–49.

Bui, M. T. (2009). *Influence of some particle characteristics on the small strain response of granular materials*. PhD thesis, University of Southampton.

Cascante, G. and Santamarina, J. C. (1996). Interparticle contact behavior and wave propagation. *Journal of Geotechnical Engineering*, 122(10):831–839.

Casini, F., Brauchli, S., Herzog, R., and Springman, S. (2011). Grain size distribution and particle shape effects on shear strength of sand–gravel mixtures. In *Proceedings of the 15th European conference on soil mechanics and geotechnical engineering*, pages 149–154. GR.

Cavarretta, I., Coop, M., and O'SULLIVAN, C. (2010). The influence of particle characteristics on the behaviour of coarse grained soils. *Géotechnique*, 60(6):413–423.

Cavarretta, I., O'sullivan, C., and Coop, M. (2017). The relevance of roundness to the crushing strength of granular materials. *Géotechnique*, 67(4):301–312.

Cavarretta, I., O'Sullivan, C., Ibraim, E., Lings, M., Hamlin, S., and Wood, D. M. (2012). Characterization of artificial spherical particles for dem validation studies. *Particuology*, 10(2):209–220.

Cha, M., Santamarina, J. C., Kim, H.-S., and Cho, G.-C. (2014). Small-strain stiffness, shear-wave velocity, and soil compressibility. *Journal of Geotechnical and Geoenvironmental Engineering*, 140(10):06014011.

Chang, C. S., Misra, A., and Sundaram, S. S. (1991). Properties of granular packings under low amplitude cyclic loading. *Soil Dynamics and Earthquake Engineering*, 10(4):201–211.

Cho, G.-C., Dodds, J., and Santamarina, J. C. (2006). Particle shape effects on packing density, stiffness, and strength: Natural and crushed sands. *Journal of Geotechnical and Geoenvironmental Engineering*, 132(5):591–602.

Chung, R. M., Yokel, F. Y., and Drnevich, V. (1984). Evaluation of dynamic properties of sands by resonant column testing. *Geotechnical Testing Journal*, 7(2):60–69.

Cole, D. M. and Peters, J. F. (2007). A physically based approach to granular media mechanics: grain-scale experiments, initial results and implications to numerical modeling. *Granular Matter*, 9(5):309–321.

Cole, D. M. and Peters, J. F. (2008). Grain-scale mechanics of geologic materials and lunar simulants under normal loading. *Granular Matter*, 10(3):171.

Goldsmith, W. and Lyman, P. T. (1960). The penetration of hard-steel spheres into plane metal surfaces. *Journal of Applied Mechanics*, 27(4):717–725.

Greenwood, J. A. and Tripp, J. H. (1967). The elastic contact of rough spheres. *Journal of Applied Mechanics*, 34(1):153–159.

Guida, G., Viggiani, G. M., and Casini, F. (2020). Multi-scale morphological descriptors from the fractal analysis of particle contour. *Acta Geotechnica*, 15(5):1067–1080.

Gupta, R., Salager, S., Wang, K., and Sun, W. (2019). Open-source support toward validating and falsifying discrete mechanics models using synthetic granular materials—part i: Experimental tests with particles manufactured by a 3d printer. *Acta Geotechnica*, 14(4):923–937.

Hanaor, D., Gan, Y., Revay, M., Airey, D., and Einav, I. (2016). 3d printable geomaterials. *Géotechnique*, 66(4):323–332.

Hardin, B. O. and Black, W. L. (1966). Sand stiffness under various triaxial stresses. *Journal of the Soil Mechanics and Foundations Division*, 92(2):27–42.

Hardin, B. O. and Richart Jr, F. (1963). Elastic wave velocities in granular soils. *Journal of the Soil Mechanics and Foundations Division*, 89(1):33–65.

Islam, M. N., Siddika, A., Hossain, M. B., Rahman, A., and Asad, M. A. (2011). Effect of particle size on the shear strength behavior of sands. *Australian Geomechanics Journal*, 46(3):75–86.

Iwasaki, T. and Tatsuoka, F. (1977). Effects of grain size and grading on dynamic shear moduli of sands. *Soils and Foundations*, 17(3):19–35.

Jiménez, M., Romero, L., Domínguez, I. A., Espinosa, M. d. M., and Domínguez, M. (2019). Additive manufacturing technologies: an overview about 3d printing methods and future prospects. *Complexity*, 2019.

Kagami, J., Yamada, K., and Hatazawa, T. (1983). Contact between a sphere and rough plates. *Wear*, 87(1):93–105.

Kara, E. M., Meghachou, M., and Aboubekr, N. (2013). Contribution of particles size ranges to sand friction. *Engineering, Technology & Applied Science Research*, 3(4):497–501.

Kirkpatrick, W. (1965). Effects of grain size and grading on the shearing behaviour of granular materials. In *Proceedings of the sixth International Conference on Soil Mechanics and Foundation Engineering*, pages 273–277.

Kittu, A., Watters, M., Cavarretta, I., and Bernhardt-Barry, M. (2019). Characterization of additive manufactured particles for dem validation studies. *Granular Matter*, 21(3):1–15.

Liu, X. and Yang, J. (2018). Shear wave velocity in sand: effect of grain shape. *Géotechnique*, 68(8):742–748.

Marschi, N. D., Chan, C. K., and Seed, H. B. (1972). Evaluation of properties of rockfill materials. *Journal of the Soil Mechanics and Foundations Division*, 98(1):95–114.

Matsumura, S., Kobayashi, T., Mizutani, T., and Bathurst, R. J. (2017). Manufacture of bonded granular soil using x-ray ct scanning and 3d printing. *Geotechnical Testing Journal*, 40(6):1000–1010.

Miskin, M. Z. and Jaeger, H. M. (2013). Adapting granular materials through artificial evolution. *Nature Materials*, 12(4):326–331.

Mitchell, J. K., Soga, K., et al. (2005). *Fundamentals of Soil Behavior*, volume 3. John Wiley & Sons New York.

Miura, K., Maeda, K., and Toki, S. (1997). Method of measurement for the angle of repose of sands. *Soils and Foundations*, 37(2):89–96.

Najmon, J. C., Raeisi, S., and Tovar, A. (2019). Review of additive manufacturing technologies and applications in the aerospace industry. *Additive Manufacturing for the Aerospace Industry*, pages 7–31.

Ngo, T. D., Kashani, A., Imbalzano, G., Nguyen, K. T., and Hui, D. (2018). Additive manufacturing (3d printing): A review of materials, methods, applications and challenges. *Composites Part B: Engineering*, 143:172–196.

Otsubo, M., O'sullivan, C., Sim, W. W., and Ibraim, E. (2015). Quantitative assessment of the influence of surface roughness on soil stiffness. *Géotechnique*, 65(8):694–700.

Patel, A., Bartake, P., and Singh, D. (2009). An empirical relationship for determining shear wave velocity in granular materials accounting for grain morphology. *Geotechnical Testing Journal*, 32(1):1–10.

Santamarina, J. C. (2003). Soil behavior at the microscale: particle forces. In *Soil Behavior and Soft Ground Construction*, pages 25–56.

Santamarina, J. C., Klein, K. A., and Fam, M. A. (2001). *Soils and waves*, volume 316. J. Wiley & Sons New York.

Sharifipour, M., Dano, C., and Hicher, P.-Y. (2004). Wave velocities in assemblies of glass beads using bender-extender elements. In *17th ASCE Engineering Mechanics Conference*.

Tofail, S. A., Koumoulos, E. P., Bandyopadhyay, A., Bose, S., O'Donoghue, L., and Charitidis, C. (2018). Additive manufacturing: scientific and technological challenges, market uptake and opportunities. *Materials Today*, 21(1):22–37.

Vangla, P. and Latha, G. M. (2015). Influence of particle size on the friction and interfacial shear strength of sands of similar morphology. *International Journal of Geosynthetics and Ground Engineering*, 1(1):6.

Wadell, H. (1932). Volume, shape, and roundness of rock particles. *The Journal of Geology*, 40(5):443–451.

Wang, J.-J., Zhang, H.-P., Tang, S.-C., and Liang, Y. (2013). Effects of particle size distribution on shear strength of accumulation soil. *Journal of Geotechnical and Geoenvironmental Engineering*, 139(11):1994–1997.

Wichtmann, T. and Triantafyllidis, T. (2009). Influence of the grain-size distribution curve of quartz sand on the small strain shear modulus g max. *Journal of Geotechnical and Geoenvironmental Engineering*, 135(10):1404–1418.

Xiao, Y., Long, L., Matthew Evans, T., Zhou, H., Liu, H., and Stuedlein, A. W. (2019). Effect of particle shape on stress-dilatancy responses of medium-dense sands. *Journal of Geotechnical and Geoenvironmental Engineering*, 145(2):04018105.

Yamashita, S., Kawaguchi, T., Nakata, Y., Mikami, T., Fujiwara, T., and Shibuya, S. (2009). Interpretation of international parallel test on the measurement of gmax using bender elements. *Soils and Foundations*, 49(4):631–650.

Yang, J. and Gu, X. (2013). Shear stiffness of granular material at small strains: does it depend on grain size? *Géotechnique*, 63(2):165–179.

Yimsiri, S. and Soga, K. (2000). Micromechanics-based stress–strain behaviour of soils at small strains. *Géotechnique*, 50(5):559–571.

Zheng, J. and Hryciw, R. D. (2015). Traditional soil particle sphericity, roundness and surface roughness by computational geometry. *Géotechnique*, 65(6):494–506.

2.10 Tables and Figures

Table 2.1: Properties of the experimental materials

Material	Young's Modulus, E (GPa)	Poisson's Ratio, ν	Specific Gravity, G_s	*Angle of Repose, ϕ_{rep} (deg)	N_{GT} (N)
Steel spheres	[1]190	[1]0.30	[1]7.82	26.3	-
Glass spheres	[1]63	[2]0.20	[1]2.23	23.4	4
SLA 3DP spheres	[1]3.6	[3]0.27	[6]1.15	27.3	6
Polyjet 3DP spheres	[1]2.4	[4]0.30	[6]1.18	31.8	12
Quartz (angular)	[5]76	[5]0.31	[5]2.65	36.3	-
Quartz (rounded)	[5]76	[5]0.31	[5]2.65	32.2	-
Polyjet 3DP (angular)	2.4	0.30	1.18	39.2	-
Polyjet 3DP (rounded)	2.4	0.30	1.18	36.5	-

[1]Material specification sheet; [2]Otsubo et al. [2015]; [3]Kittu et al. [2019]; [4]Assumed; [5]Santamarina et al. [2001]; [6]Measured in lab; *Measured using the method by Miura et al. [1997]

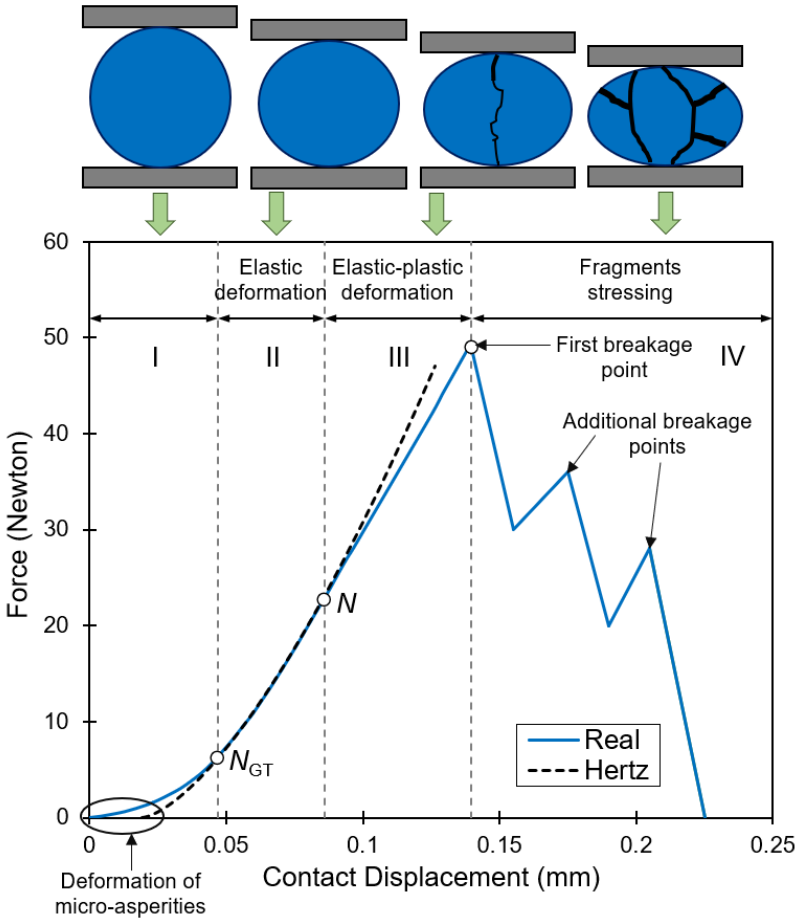

Figure 2.1: Typical contact force-displacement curve up to failure [redrawn after Antonyuk et al., 2005]

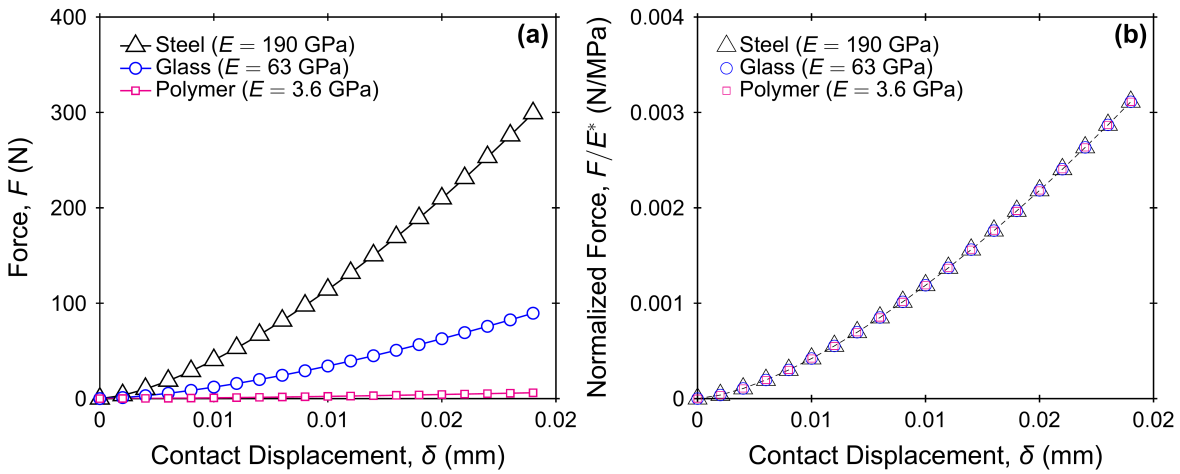

Figure 2.2: Hertzian relationships for steel, glass, and polymer particle contacts in terms of (a) contact force vs. displacement and (b) normalized contact force vs. displacement

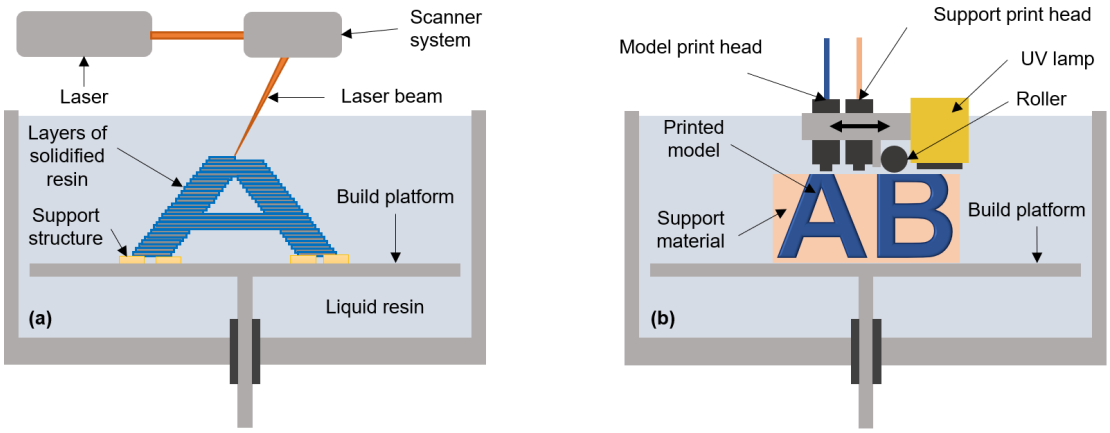

Figure 2.3: Schematics of additive manufacturing technologies used to generate the spheres and particle analogs: (a) stereolithography (SLA) and (b) polyjet

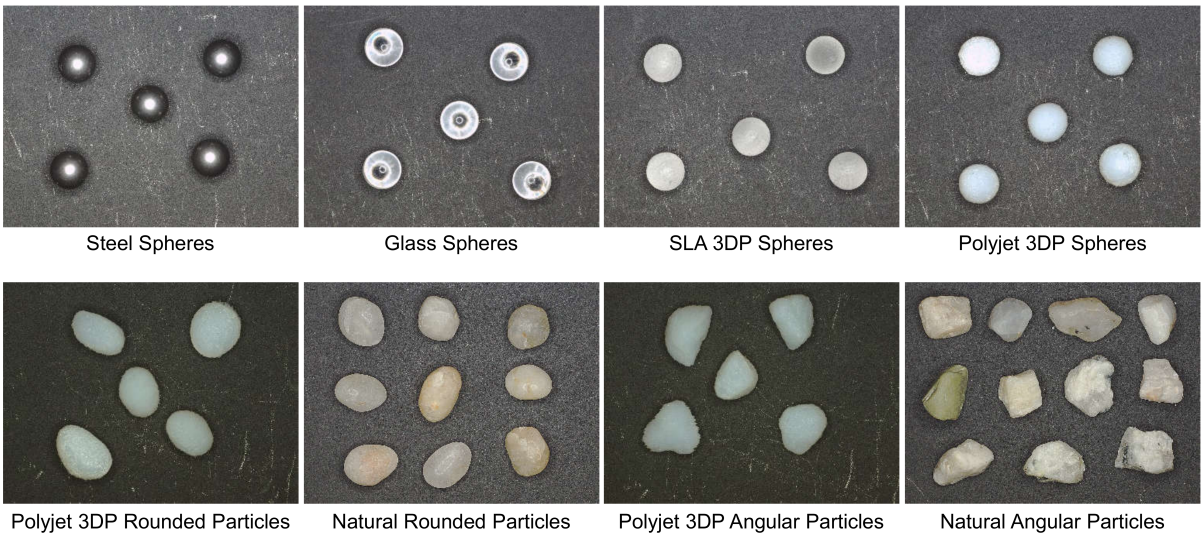

Figure 2.4: Spherical, angular, and rounded particles of different materials used in this study

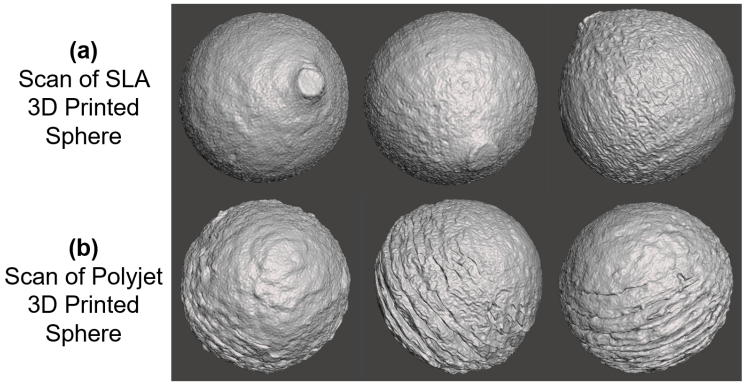

Figure 2.5: X-ray CT scans of additive manufactured spheres: (a) SLA and (b) polyjet

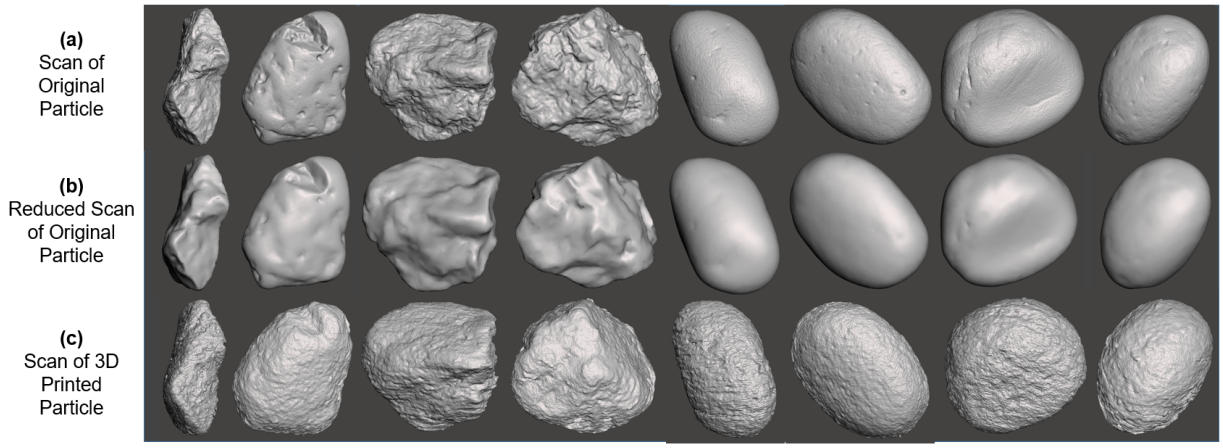

Figure 2.6: Comparison of X-ray CT scans of (a) natural particles, (b) reduced scans for 3D printing, and (c) of additive manufactured particle analogs

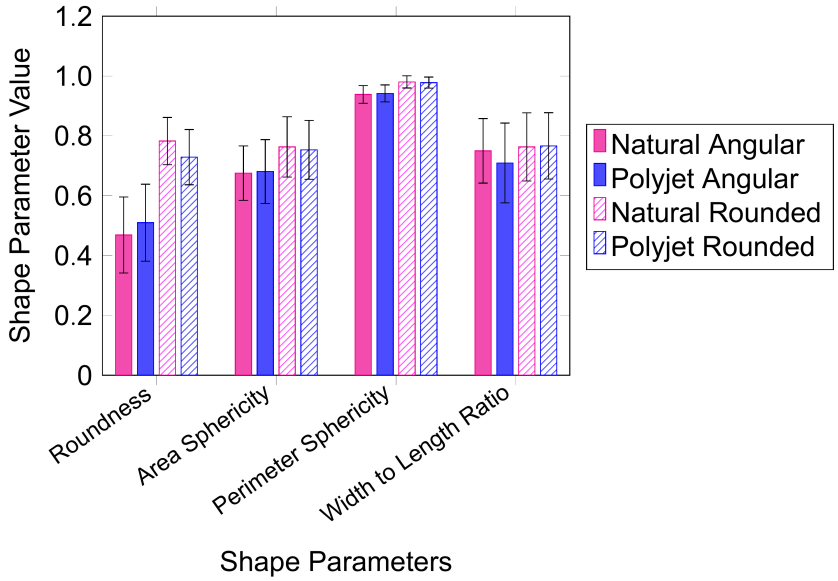

Figure 2.7: Comparison of shape parameters for natural and additive manufactured particles (note: standard deviation shown by error bars)

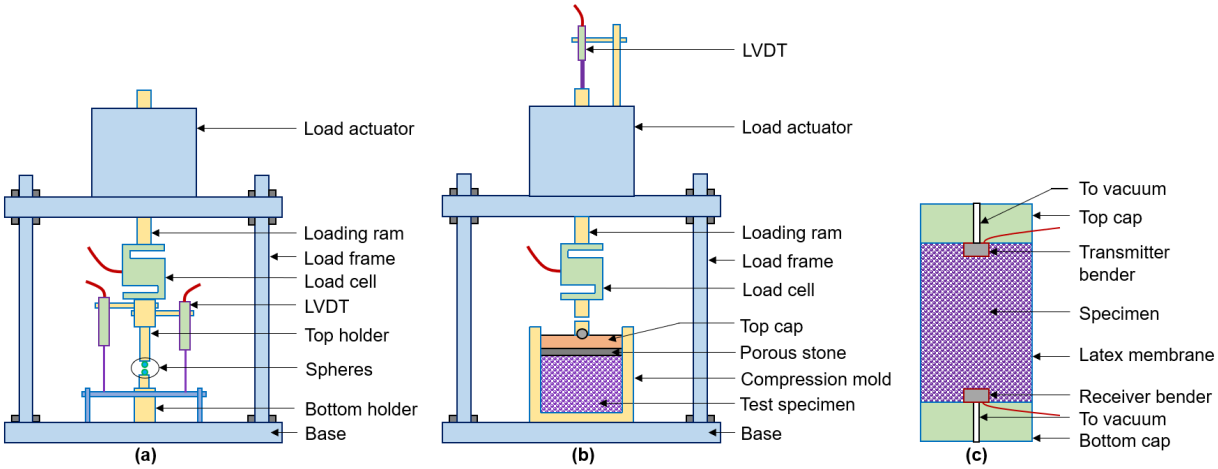

Figure 2.8: Schematics of devices for (a) uniaxial particle-particle compression, (b) oedometer compression, and (c) bender element tests

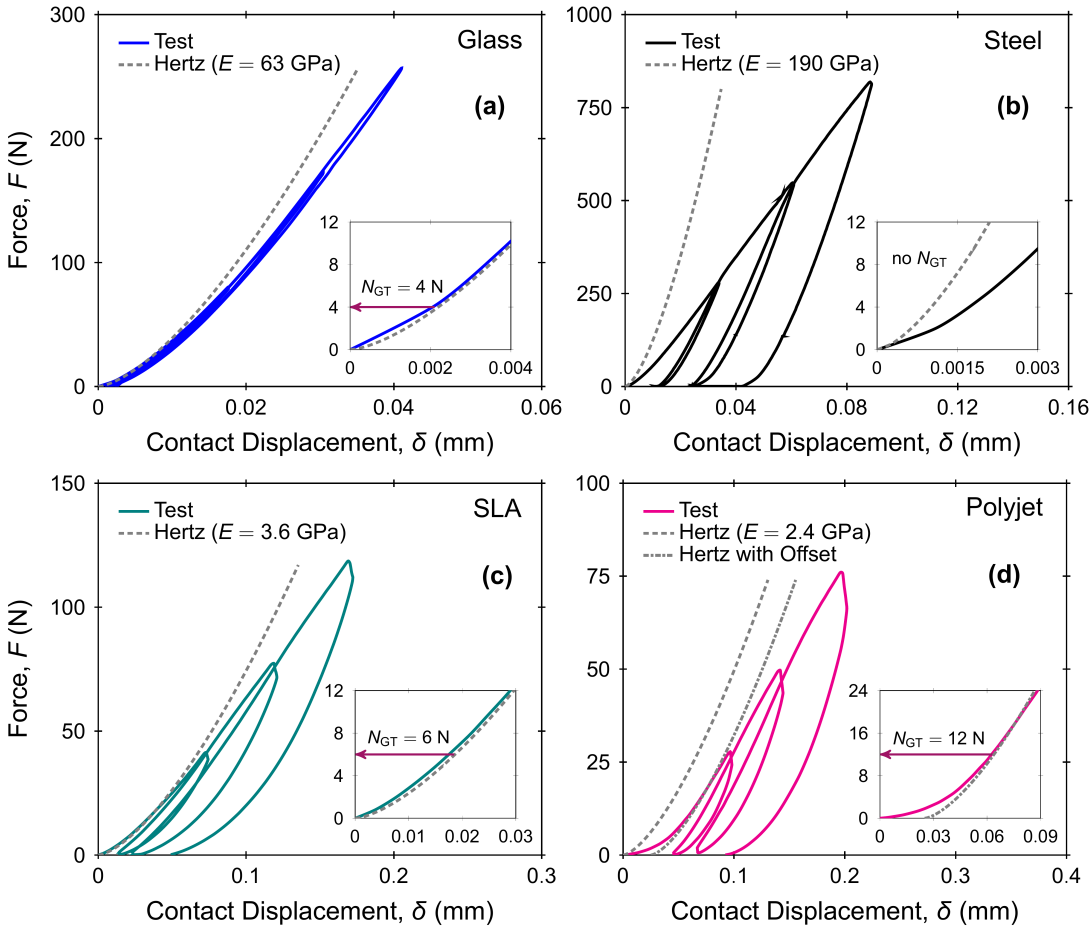

Figure 2.9: Force-displacement response from uniaxial particle-particle compression tests for spheres of (a) glass, (b) steel, (c) SLA 3D printing resin, and (d) polyjet 3D printing resin

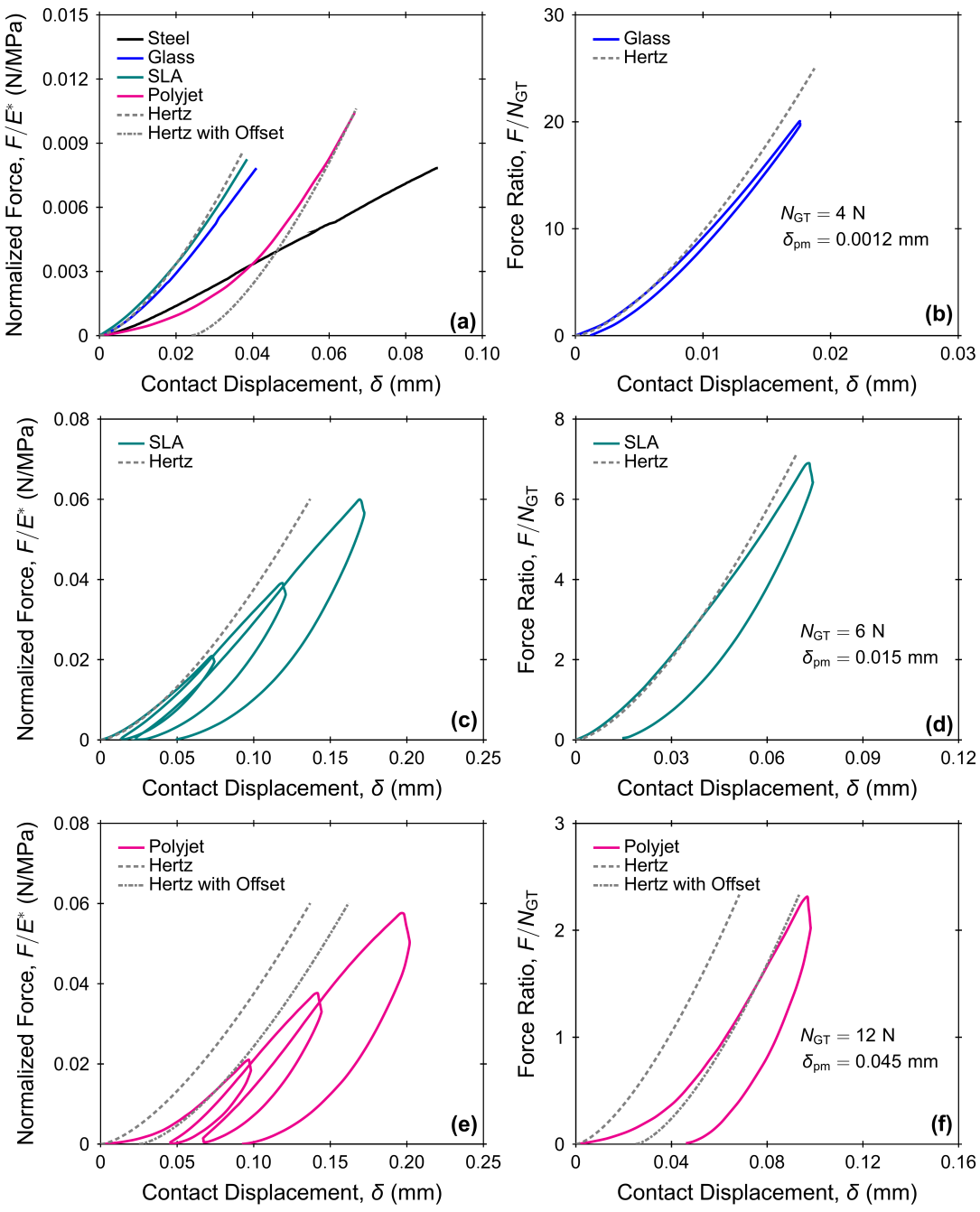

Figure 2.10: Normalized force (F/E^*)−displacement response for (a) all spheres, (c) SLA AM spheres, and (e) polyjet AM spheres and force ratio (F/N_{GT})−displacement plots for (b) glass spheres, (d) SLA AM spheres, and (f) polyjet AM spheres

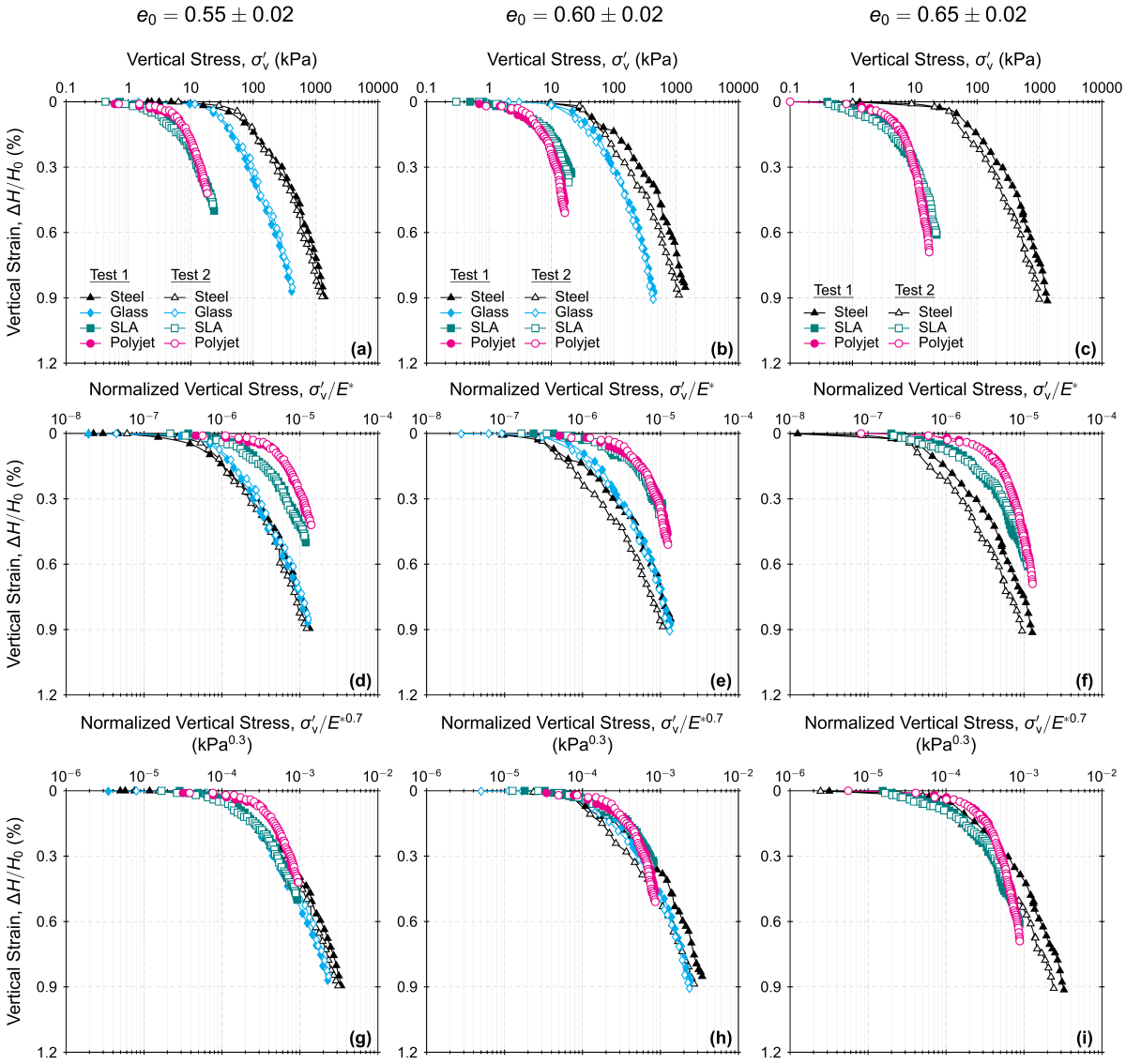

Figure 2.11: Oedometric compression test results for spheres: (a, b, c) strain vs. stress, (d, e, f) strain vs. normalized stress (σ'_v/E^*), and (g, h, i) strain vs. normalized stress ($\sigma'_v/E^{*0.7}$)

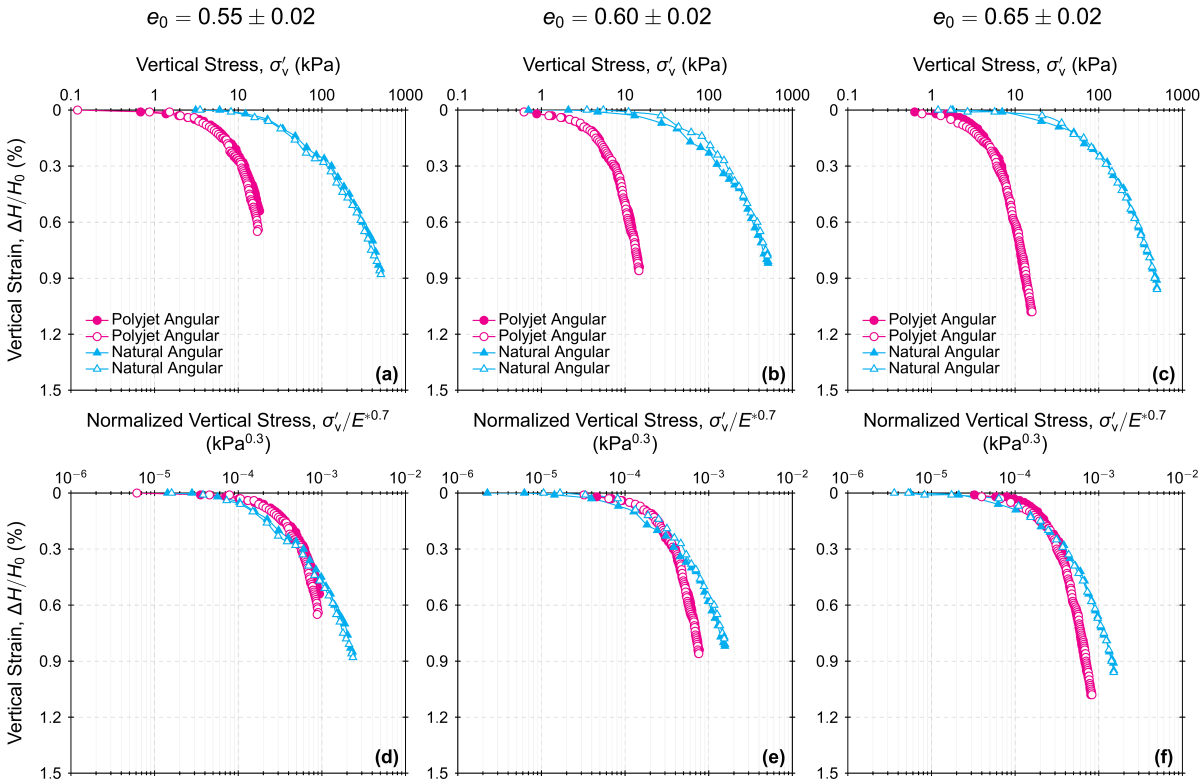

Figure 2.12: Oedometric compression test results for angular natural and additive manufactured particles: (a, b, c) strain vs. stress and (d, e, f) strain vs. normalized stress ($\sigma'_v/E^{*0.7}$)

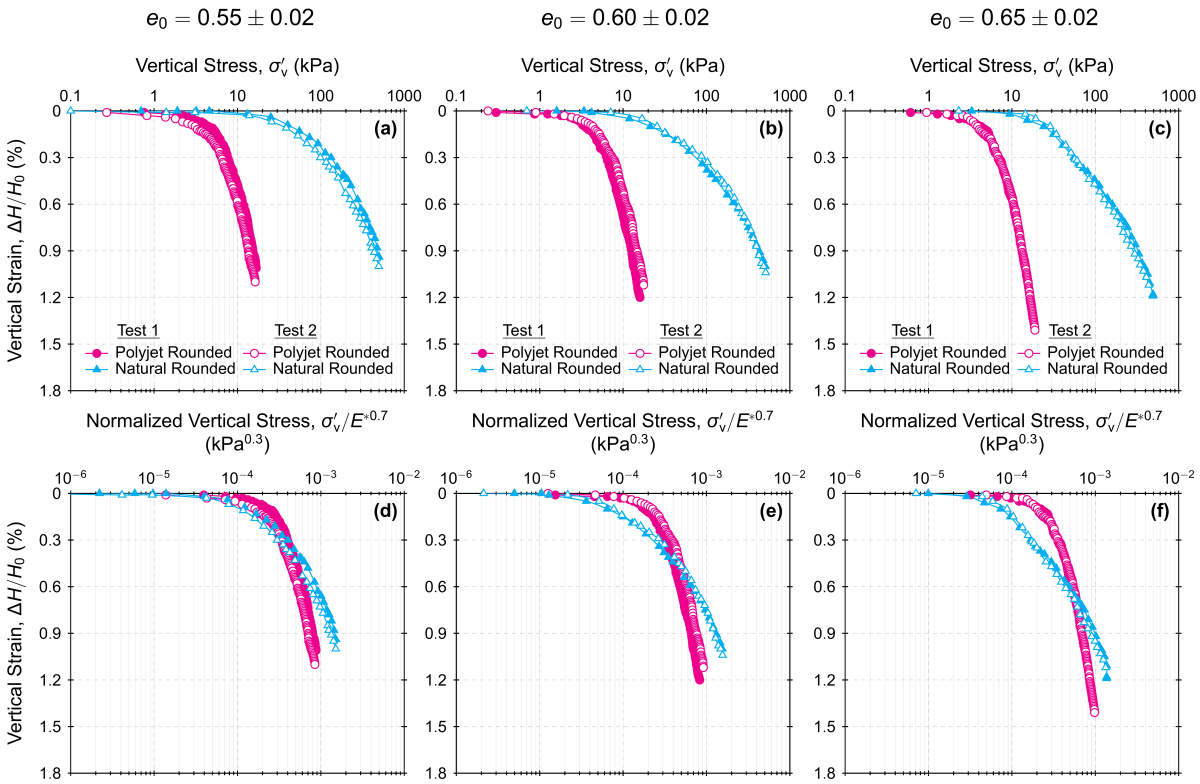

Figure 2.13: Oedometric compression test results for rounded natural and additive manufactured particles: (a, b, c) strain vs. stress and (d, e, f) strain vs. normalized stress ($\sigma'_v/E^{*0.7}$)

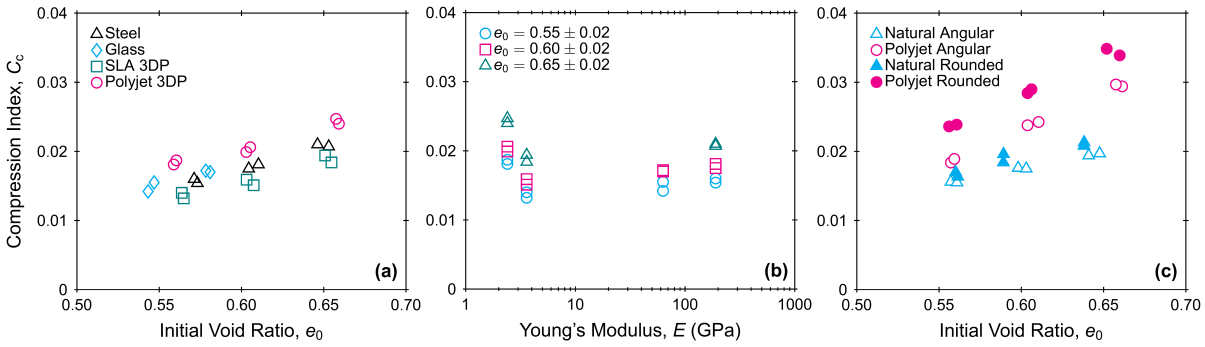

Figure 2.14: Compressibility indices from oedometric compression tests: (a) C_c vs. e_0 for spheres, (b) C_c vs. E for spheres, and (c) C_c vs. e_0 for additive manufactured and natural sand particles

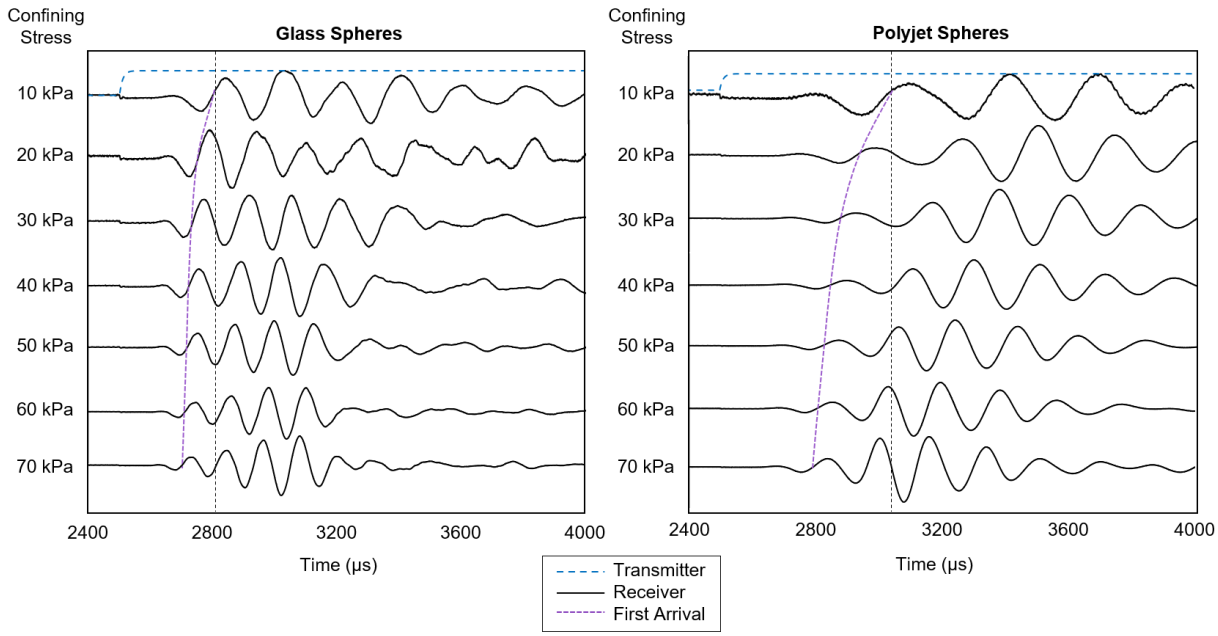

Figure 2.15: Receiver bender element signals for glass and polyjet spheres at different isotropic stresses. Note that the initial height of glass sphere specimen was 59.7 mm whereas the initial height of polyjet sphere specimen was 68.6 mm

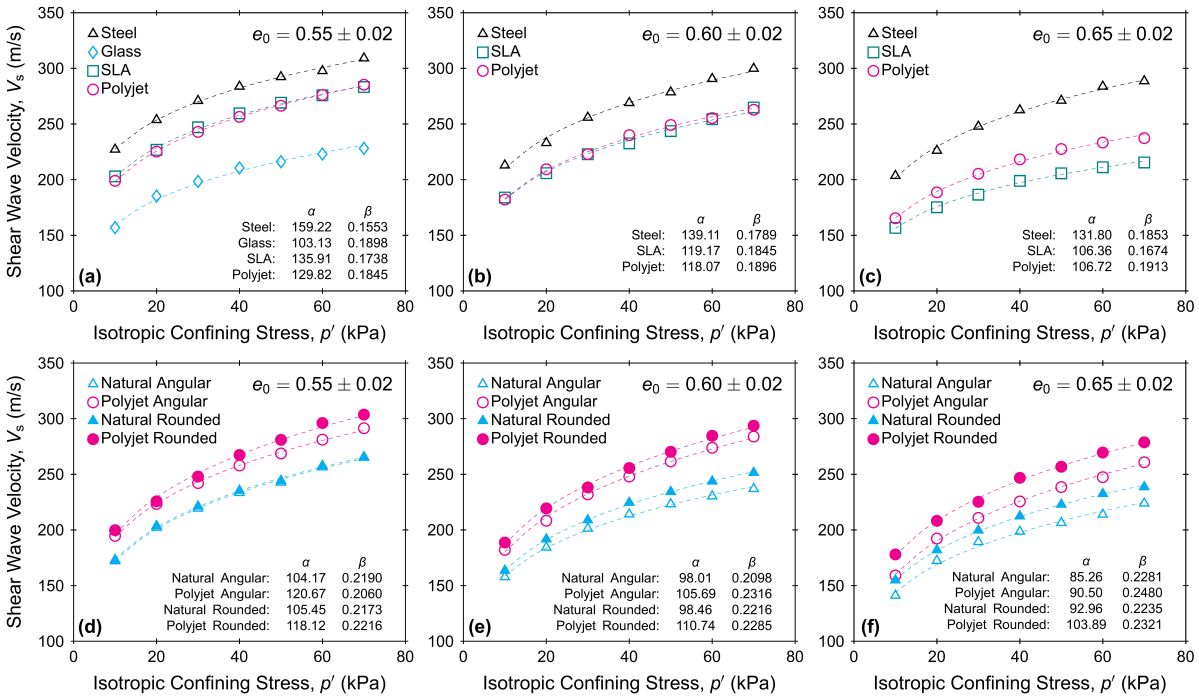

Figure 2.16: Shear wave velocities for specimens of (a, b, c) spheres and (d, e, f) natural and polyjet angular and rounded particles

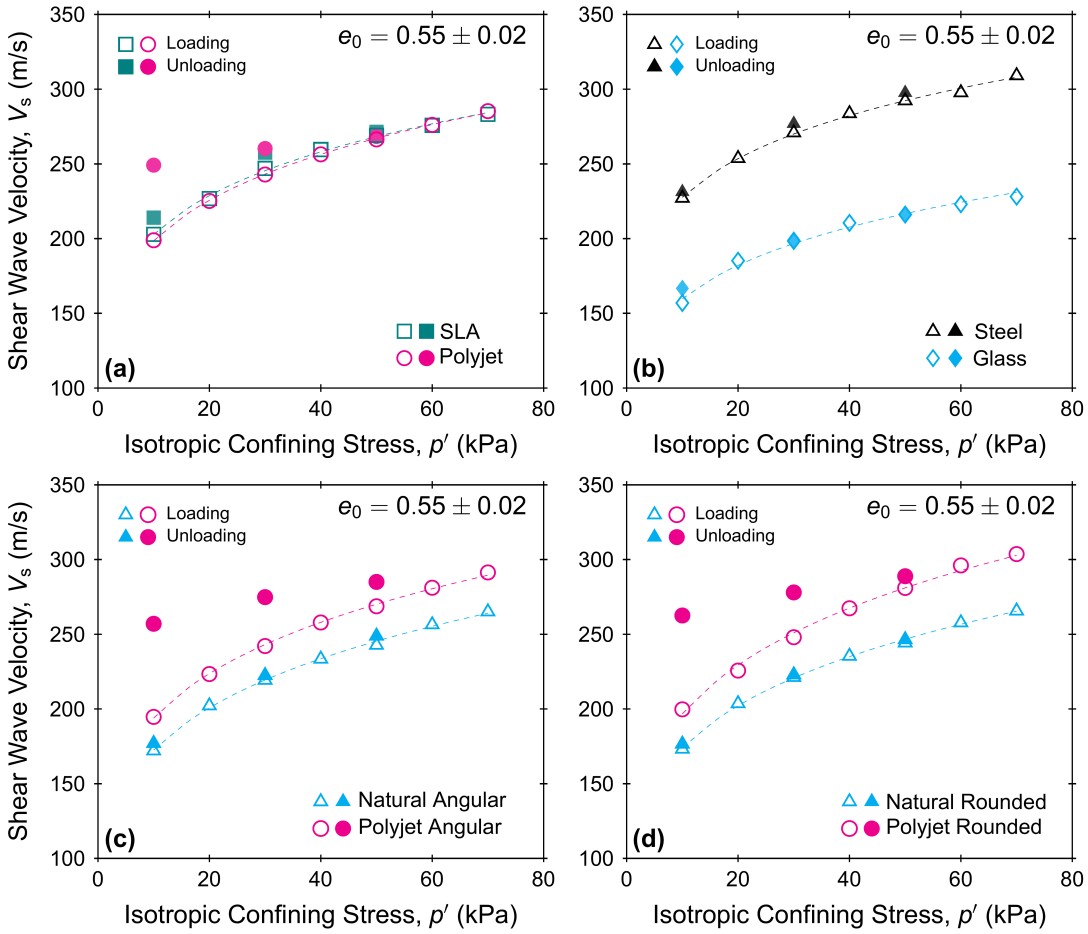

Figure 2.17: Shear wave velocities during loading and unloading for (a, b) spheres and (c, d) natural and polyjet angular particles

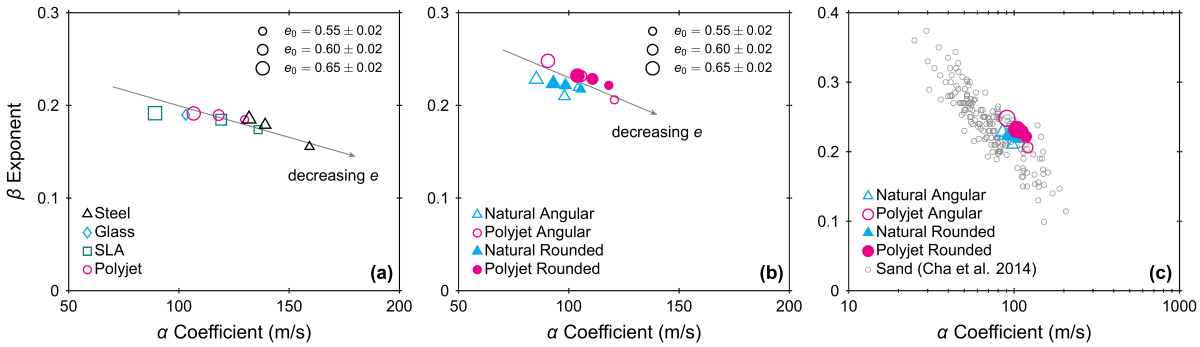

Figure 2.18: β-exponent vs. α-coefficient for specimens of (a) spheres, (b) angular and rounded natural particles, and (c) comparison of β-exponent vs. α-coefficient with values from literature

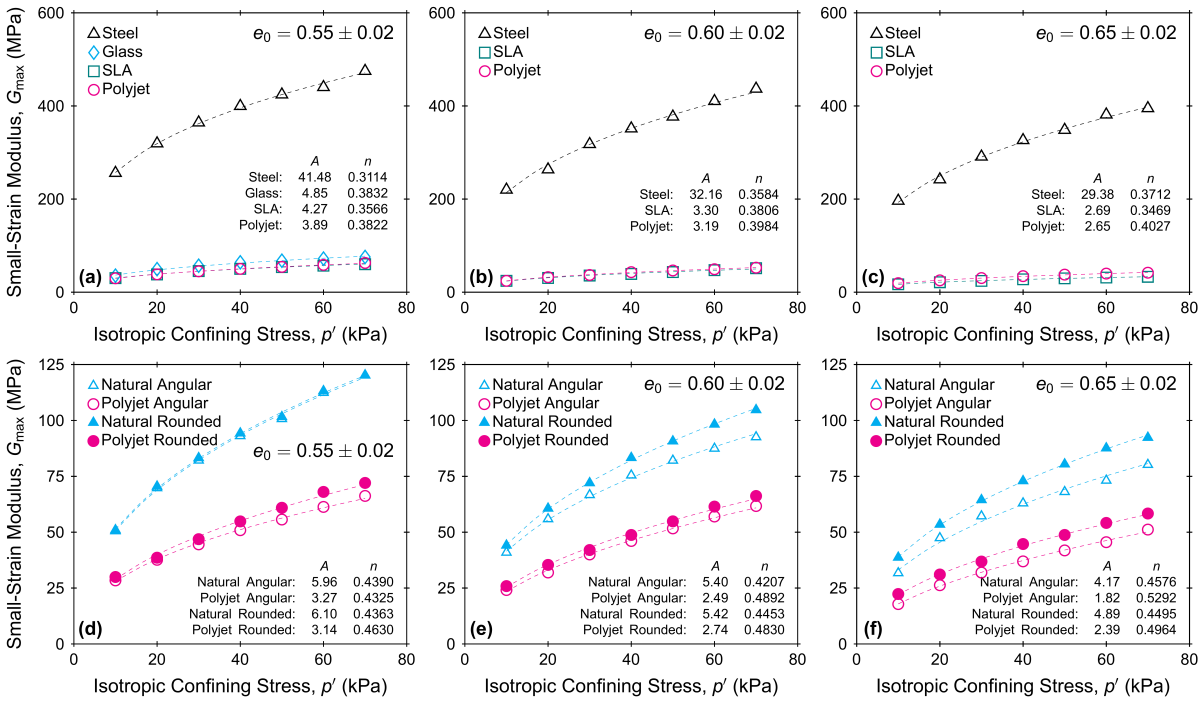

Figure 2.19: Small-strain moduli for specimens of (a, b, c) spheres and (d, e, f) angular and rounded natural and additive manufactured particles

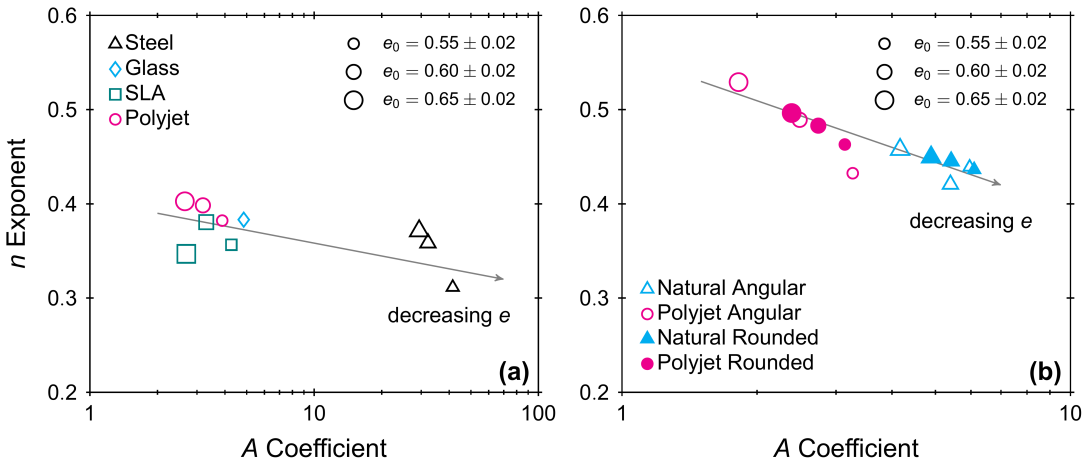

Figure 2.20: n-exponent vs. A-coefficient for specimens of (a) spheres and (b) angular and rounded natural and additive manufactured particles

Chapter 3

Triaxial Compression Behavior of 3D Printed and Natural Sands

This paper was published in the Granular Matter under the following citation and is presented herein with minor edits.

Ahmed, S. S., & Martinez, A. (2021). Triaxial compression behavior of 3D printed and natural sands. *Granular Matter*, 23(4), 1–21.

3.1 Abstract

Different particle properties, such as shape, size, surface roughness, and constituent material stiffness, affect the mechanical behavior of coarse-grained soils. Systematic investigation of the individual effects of these properties requires careful control over other properties, which is a pervasive challenge in investigations with natural soils. The rapid advance of 3D printing technology provides the ability to produce analog particles with independent control over particle size and shape. This study examines the triaxial compression behavior of specimens of 3D printed sand particles and compares it to that of natural sand specimens. Drained and undrained isotropically-consolidated triaxial compression tests were performed on specimens composed of angular and rounded 3D printed and natural sands. The test results indicate that the 3D printed sands exhibit stress−dilatancy behavior that follows well-established flow rules, the angular 3D printed sand mobilizes greater critical state friction angle than that of

rounded 3D printed sand, and analogous drained and undrained stress paths can be followed by 3D printed and natural sands with similar initial void ratios if the cell pressure is scaled. The results suggest that some of the fundamental behaviors of soils can be captured with 3D printed soils, and that the interpretation of their mechanical response can be captured with the critical state soil mechanics framework. However, important differences in response arise from the 3D printing process and the smaller stiffness of the printed polymeric material.

3.2 Introduction

The mechanical behavior of coarse-grained soils is governed by the skeletal forces that develop at the particle-particle contacts resulting from applied boundary stresses [Santamarina, 2003]. The distribution and magnitude of these skeletal forces, along with the resulting normal and shear deformation at the particle contacts, are influenced by the inherent properties of the particles, such as gradation, shape, surface roughness, and mechanical properties of the constituent materials. These particle-scale interactions control the global-scale behavior observed in laboratory tests and field conditions. Previous studies have employed experimental and numerical methods to expand our understanding regarding the effects of different inherent particle properties on the engineering properties of coarse-grained soils, such as friction angle [Casini et al., 2011; Islam et al., 2011; Kara et al., 2013; Kirkpatrick, 1965; Marschi et al., 1972; Vangla and Latha, 2015; Wang et al., 2013; Xiao et al., 2019] and shear wave velocity and small-strain modulus [Bartake and Singh, 2007; Bui, 2009; Cho et al., 2006; Iwasaki and Tatsuoka, 1977; Liu and Yang, 2018; Patel et al., 2009; Sharifipour et al., 2004; Wichtmann and Triantafyllidis, 2009; Yang and Gu, 2013]. However, contradicting trends regarding the effect of particle properties have been reported, likely due to challenges associated with the isolation of individual particle properties for their systematic investigation in natural soils.

3D printing technology has advanced rapidly in the last decade. This technology can be used to generate parts composed of different materials such as polymers, metals, and

ceramics. 3D printing has been previously used to generate artificial soil analog particles with independent control over particle shape and gradation [Adamidis et al., 2020; Hanaor et al., 2016]. Morphological comparison studies on natural sand particles and 3D printed analogs have shown that these analogs can replicate the morphology of natural sand particles successfully [Adamidis et al., 2020; Matsumura et al., 2017]. Triaxial tests on 3D printed particles of different shapes and sizes have demonstrated that the analog assemblies exhibit a stress-dilatancy behavior that is similar to that typical of coarse-grained soils [Adamidis et al., 2020; Hanaor et al., 2016; Matsumura et al., 2017] and revealed the dependence of the assembly stiffness on the particle shape [Adamidis et al., 2020; Athanassiadis et al., 2014; Miskin and Jaeger, 2013]. However, 3D printed particles exhibited a more initial contractive response during shearing compared to natural particles [Hanaor et al., 2016], and time-dependent compressibility during consolidation [Adamidis et al., 2020]. Comparison of 1D compression test results on natural and 3D printed particles showed that 3D printed particles qualitatively exhibit key aspects of 1D compression behavior of natural soils, such as different compression and recompression indices [Ahmed and Martinez, 2020; Gupta et al., 2019]. However, the 3D printed assemblies exhibited greater compressibility than the natural sand assemblies [Ahmed and Martinez, 2020]. Bender element test results on 3D printed particles revealed the dependency of shear wave velocity and shear modulus on mean effective stress similar to that of natural sands [Ahmed and Martinez, 2020]. A characterization study of the contact behavior of 3D printed spheres of different materials indicated that 3D printed particles may be used to validate discrete element method (DEM) simulations against experimental results [Kittu et al., 2019]. The above findings demonstrate the ability of 3D printed particle analogs to emulate the macro-scale behavior of coarse-grained soil. However, the research to date also indicates important differences in the behavior of 3D printed and natural sand assemblies, particularly with regards to the compressibility at medium and large strain regimes.

Although assemblies of natural and 3D printed particles exhibit similarities in their

mechanical behavior, further insight requires understanding of the particle-scale contact response. The normal force-deformation behavior of two spheres in contact can be described using Hertz theory, which relates the contact deformation, δ, to an applied normal force, F, as follows:

$$\delta = \left(\frac{9}{16} \frac{F^2}{R E^{*2}} \right)^{1/3} \tag{3.1}$$

where R is given by: $1/R = 1/R_1 + 1/R_2$, and R_1 and R_2 are the radii of the contacting spheres. The effective Young's modulus, E^*, is defined as: $1/E^* = (1-\nu_1^2)/E_1 + (1-\nu_2^2)/E_2$, where ν_1 and ν_2 are the Poisson's ratios of the contacting spheres. As shown, δ is proportional to $E^{*1/6}$; thus, it follows that particles with smaller stiffness will undergo greater deformations under any given F.

Figure 3.1 shows a subset of the results of uniaxial particle-particle compression tests by Ahmed and Martinez [2020]. The force-displacement responses correspond to equal-sized spheres (3.175 mm diameter) of borosilicate glass and 3D printed polyjet polymer. As shown, the contact force-displacement response of the glass spheres is mostly elastic and follows Hertz solution at loads smaller than 100 N. In contrast, the response of the 3D printed polyjet polymer deviates considerably from Hertz solution at contact deformations smaller than about 0.04 mm due to initial plastic deformation of micro-asperities, as shown in Fig. 3.1b. This initial plastic response due to the deformation of micro-asperities has been reported by a number of researchers [Cavarretta et al., 2010; Cole, 2015; Greenwood and Tripp, 1967; Senetakis et al., 2013], who observed plastic yielding until the contact normal force, F, reached a threshold force, N_{GT}. The threshold force depends on the particle's surface roughness, surface radius at the contact point, and the constituent material's stiffness [Greenwood and Tripp, 1967]. Once F exceeds N_{GT}, the force-displacement response follows that predicted by Hertz theory. This is shown in Fig. 3.1b by a second dotted line that represents the Hertz solution with a constant offset in the initial constant displacement.

Although a Hertzian model with an offset appears to provide a reasonable approximation over the range shown, the 3D printed particle exhibits a response that is more complex possibly due to the coupling of elastic and plastic deformations.

Table 3.1 summarizes Young's modulus, E, and N_{GT} values for a natural sand, glass spheres, and polyjet 3D printing polymer spheres. The N_{GT} values are smallest for glass ballotini and borosilicate glass spheres, followed by the polyjet 3D printing polymer spheres, and highest for the Leighton Buzzard sands. Since the normal contact deformation depends on E (Eq. 3.1), the N_{GT}/E ratio can give insight into the relative magnitude of plastic to elastic deformations that can be expected at a given contact. The glass spheres have the smallest N_{GT}/E ratio, indicating that their response is likely to be dominated by elastic deformations as shown in Fig. 3.1a. In contrast, the polyjet 3D printing polymer has the highest N_{GT}/E ratio, highlighting the important role of the plastic deformation of micro asperities as shown in Fig. 3.1b. These differences in particle-level response are likely to be responsible for differences in the response of granular assemblies tested in a laboratory setting.

While a number of researchers have investigated the similarities in mechanical behavior of natural and 3D printed particles, there is need to characterize the shearing behavior across a range of effective stresses, void ratios, and imposed boundary conditions. The current study investigates the triaxial compression behavior of angular and rounded 3D printed sands. In addition, the analysis presented here examines the existence of critical states for the 3D printed sands in the stress and compression planes. Both drained and undrained behaviors of 3D printed analogs are investigated and compared to those of natural angular and rounded particles.

3.3 Materials and Methods

Drained and undrained isotropically-consolidated triaxial compression tests were performed on specimens of two types of 3D printed sand and two types of natural sand to evaluate their

shear response and stress-dilatancy behavior and make comparisons between the materials. The 3D printed particles were generated from X-ray CT scans of the natural particles with the goal of reproducing their shape and size, leaving the constituent material as the main difference between them. This section provides an overview of the 3D printing technology used in this study, the materials tested, and the experimental procedures used to characterize the triaxial compression behavior.

3.3.1 3D Printing Technology

3D printing technology has advanced rapidly in last few years, and several 3D printing methods have been developed to generate parts composed of different materials. Different methods and materials have enabled the availability of modern 3D printers in a wide spectrum of precision, capability, and cost. Large-scale and specialized 3D printers are capable of printing highly complex geometries using materials such as polymers, metals, ceramics, concrete, and even clay with high accuracy. Some of those printers can mix different materials with different colors on demand to achieve the desired mechanical properties and aesthetics [Jiménez et al., 2019; Najmon et al., 2019]. More economic desktop 3D printers are typically constrained to printing polymers that can print layers with thickness as low as 10 μm [Ngo et al., 2018]. Contemporary 3D printing technology affords greater design freedom and production flexibility in both research and industrial applications [Tofail et al., 2018].

A given 3D printing method offers certain advantages and drawbacks. This study uses the polyjet 3D printing technology because it provides relatively inexpensive and fast manufacturing of small, detailed parts. Usually, polyjet printers have two print heads that deposit different resins. The resins are liquid photopolymers and are hardened by an ultraviolet laser. One resin creates the desired object while the other resin acts as a support structure. Once the printing is complete, the support structure is removed from the finished 3D object by water jetting and chemical treatment using a 2% sodium hydroxide solution.

The inter-particle uniaxial compression test result shown in Fig. 3.1b was performed on two spheres of polyjet-printed polymer.

The polyjet polymer has a Young's Modulus of 2.4 GPa and a Poisson's ratio of 0.3, as shown in Table 3.2. As reported in the literature, both the printing direction and printing material can significantly affect the strength and surface properties of polyjet printed objects [Cazón et al., 2014; Stansbury and Idacavage, 2016]. Specifically, the fracture stress and strain, and tensile toughness are affected by the printing orientation [Cazón et al., 2014; Hong et al., 2018], which may affect the fracture and breakage of 3D printed objects. However, it should be noted that no significant breakage of particles was observed during any of the tests reported here. On the other hand, the contact deformation response of 3D printed particles is not expected to have an anisotropic behavior based on literature reporting that the printing orientation has no significant effect on the modulus of elasticity, and the ultimate tensile and compressive strengths [Hong et al., 2018; Tee et al., 2020; Wang et al., 2017].

3.3.2 Natural and 3D Printed Sand Particles

The natural sand particles used in this study were obtained by sieving a well-graded quartz sand. The particles that passed through the #6 (3.36 mm) and were retained by the #8 (2.38 mm) sieves were separated to obtain a poorly-graded soil. This soil consisted of both angular and rounded particles, which were then manually separated to create two separate soil samples: one with angular particles and one with rounded particles (Fig. 3.2). This approach ensured similarity in the gradation and mineralogy of the two samples, and allowed isolating particle shape as the only difference between them.

The 3D printed particles were generated from X-ray CT scans of a set of randomly chosen angular and rounded natural sand particles (90 for the former, 70 for the latter). The particles were printed using an *Objet Eden 260V* printer from Stratasys with *VeroWhitePlus* rigid acrylate-based polymer resin with a printing resolution of 30 μm. The X-ray CT scans

had a resolution of 10 μm, which were reduced to expedite the 3D printing process. The scans of reduced resolution were used to generate the 3D printed particles. A comparison of natural particle scans, scans with reduced resolution, and scans of 3D printed particles are presented in Figs. 3.3a, 3.3b, and 3.3c, respectively.

The morphology of a particle can be characterized at different scales: shape (medium scale), and surface texture or roughness (small scale) [Berrezueta et al., 2019]. This study considers the particle shape to compare the similarity between the natural and 3D printed particles. A particle shape is typically quantified by roundness and sphericity, both of which can be described in a number of ways [Berrezueta et al., 2019; Guida et al., 2020; Mitchell et al., 2005]. The shape parameters are usually estimated from 2D projection of a particle [Berrezueta et al., 2019]. Roundness is a measure of the smoothness of the angles or corners of a particle, whereas sphericity is a measure of how closely the particle shape approaches that of a circle (in 2D) or sphere. This study considers Wadell roundness [Wadell, 1932], area sphericity, and width-to-length ratio sphericity [Mitchell et al., 2005; Zheng and Hryciw, 2015] to describe the particle shape. The shape parameters were obtained by image analysis of 2D projections of particles using the code by Zheng and Hryciw [2015] and are shown in Fig. 3.4 and summarized in Table 3.2. The shape parameters of the 3D printed particles compare well with those of the natural particles, indicating the successful reproduction of particle shape.

3.3.3 Coefficient of Friction Test

Differences in the friction coefficient can lead to differences in the stiffness and strength behavior of granular assemblies [Huang et al., 2014; Otsubo et al., 2015; Santamarina and Cascante, 1998]. The frictional resistance between polyjet 3D printed materials was measured by shearing two equal-sized blocks (63 mm length, 25 mm width, and 19 mm thickness) against each other in a modified direct shear test apparatus. Anisotropy in the frictional resistance due to the direction of material layer deposition was examined by shearing the

blocks in the directions perpendicular and parallel to the printing direction (Fig. 3.5a). Every test used newly printed blocks. Five tests in each direction were performed under normal stresses (σ_v) ranging from 50 kPa to 400 kPa.

3.3.4 Triaxial Test

Drained and undrained isotropically-consolidated triaxial compression tests were performed to characterize the shear behavior and stress-dilatancy response of specimens of 3D printed and natural sands. This study used an automatic triaxial testing system with digital data acquisition capabilities. Cell and pore pressure and volume change were controlled using two digital pressure volume controllers. The measured volume changes are used to determine the specimen volumetric strain, ε_v. Axial load was measured by an external load cell mounted on the load frame. Axial displacement was measured by an external linear variable differential transducer which is used to determine the specimen axial strain, ε_a. Pore pressure transducers were used to measure the specimen pore pressure as well as the triaxial confining pressure. The changes in void ratio, e, of the specimens is computed based on the measured volumetric changes following the equation: $\Delta e = \varepsilon_v(1 + e_0)$.

Tests were performed on specimens of 70 mm diameter and 150 mm height. The dense specimens were prepared by pouring the particles in the mold in three lifts. After pouring each lift, a tamping rod was used to densify the layer to the target void ratio. The loose specimens were prepared by pouring the particles from a small height into the mold in a single lift without any tamping. Once prepared, a small vacuum was applied to stabilize the specimen. The specimen was then placed in the triaxial cell and the cell was filled with de-aired water. The specimen was saturated by applying back-pressure while maintaining a constant small difference between the cell and the back-pressure. The back-pressure was increased slowly until a B-value of 0.95 was obtained. After saturation, the specimen was consolidated isotropically to the target confining pressure; once the consolidation phase finished, the shearing phase commenced. All the specimens exhibited a bulging failure with

no visible shear bands, with the exception of two tests on dense 3D printed rounded sand which exhibited shear bands (tests "6-3DPR-30" and "7-3DPR-30" in Table 3.3). While a membrane penetration correction was attempted for the volume changes, the effect was insignificant (less than 2%); thus, correction was ignored for all the tests.

Table 3.3 summarizes the 34 triaxial compression tests performed. The testing ID convention is such that ID "x-AB-y" corresponds to test number "x" of particular sand "AB" at an effective confining pressure (σ'_{3c}) of "y" kPa. For example, "4-NR-530" corresponds to test number "4" on natural rounded sand at σ'_{3c} of "530" kPa. Given the greater stiffness of quartz as compared to the 3D printed polymer (Table 3.2), the tests on natural sand were performed at greater confining pressures than the tests on 3D printed sand. Initially, a series of five drained tests were performed on angular and rounded 3D printed sands (σ'_{3c} range of 20 to 90 kPa) and natural sands (σ'_{3c} range of 90 to 742 kPa) to characterize their triaxial compression behavior. Then, five triaxial tests were performed on angular 3D printed and natural sand specimens with similar initial void ratios with the objective of shearing them along specific drained or undrained stress paths to compare their response. Two similar tests were performed on rounded 3D printed and natural sand specimens subjected to undrained shearing. These tests on natural sands were performed at confining pressures that were about 22 times greater than those used for the 3D printed particles (i.e. 650 kPa for the natural sands and 30 kPa for the 3D printed sands). This ratio was chosen to be somewhat close to the ratio of the Young's moduli of quartz and polyjet 3D printing polymer while minimizing the possibility for particle breakage in the natural sands by maintaining the mean effective stress, p', to values smaller than about 2000 kPa throughout the triaxial tests. It is noted that both natural and 3D printed sands showed no visible particle crushing. Figure 3.4 presents particle shape parameters for the 3D printed sands obtained after being subjected to 15 triaxial compression tests under cell pressures varying from 20 to 90 kPa. As shown, no significant changes in roundness, area sphericity, and width-to-length ratio were observed, implying that damage to the 3D printed particles was not significant.

3.4 Results

This section first discusses the friction coefficient measurements of 3D printed polymer and compares it with published values from natural quartz sand particles to provide insight into differences in the inter-particle frictional interactions. Then, the results of drained triaxial tests performed on angular and rounded 3D printed and natural sands are presented to explore the stress-dilatancy behavior and make comparisons between the different materials. Finally, tests along analogous drained or undrained stress paths are presented to compare the mechanical response of the 3D printed and natural sands, and to provide insight regarding the feasibility of modeling the behavior of coarse-grained soils with 3D printed analogs. The next section includes a comparison of the response of 3D printed and natural sands along analogous stress paths, along with an estimation of the critical state lines (CSLs) in $e - \log p'$ space.

3.4.1 Friction of Polyjet 3D Printing Resin

The results of frictional resistance tests between equal-sized blocks printed with polyjet 3D printing polymer revealed dependence of the friction coefficient, μ, on the orientation of the printing layers and the magnitude of normal stress, σ_{v}, as shown in Figs. 3.5b and 3.5c. The measured μ was significantly greater (2.9 times on average) for the direction parallel to layer deposition as compared to the μ values measured in the direction perpendicular to layer deposition. Also, μ decreased as σ_{v} was increased in both shearing directions. This may be related to the plastic deformation of the micro-asperities on the polymer surface. Namely, as the σ_{v} is increased the normal contact force increased, yielding the micro-asperities shown in Fig. 3.1b. As plastic strains accumulate at the contact, the micro-asperities flatten, likely resulting in a smaller surface roughness that leads to a decrease in interlocking interactions between the asperities. While in reality the failure envelope is curved, the data can be reasonably fitted with two separate linear envelopes for different σ_{v} ranges where the slopes

correspond to the average friction coefficient (Fig. 3.5c). As shown, the average μ for $\sigma_v < 200$ kPa is 0.44 in the parallel direction and 0.15 in the perpendicular direction, whereas the average μ for $\sigma_v > 200$ kPa is 0.35 in the parallel direction and 0.11 in the perpendicular direction. Average μ values for Leighton Buzzard and ASTM 20-30 sand particles range between 0.17 and 0.36 (Table 3.1). While not reported in the literature, these values are likely not direction-dependent. Thus, the results of the block friction tests reported here suggest that the μ in the parallel direction for 3D printed polymer are greater than those expected between natural sand particles; however, the μ in the perpendicular for 3D printed polymer are smaller than those expected between natural sand particles.

3.4.2 Triaxial Compression Behavior

Five drained triaxial compression tests were performed on specimens of natural and 3D printed angular and rounded particles to characterize their consolidation and shearing behavior. Figures 3.6a through 3.6d show the isotropic consolidation curves of natural angular, natural rounded, 3D printed angular, and 3D printed rounded particles, respectively. As shown, the decrease in void ratio with increasing mean effective stress is greater for the angular and rounded 3D printed particles (Figs. 3.6c and 3.6d) than for the corresponding natural particles (Figs. 3.6a and 3.6b), highlighting the greater skeleton compressibility of the 3D printed soils. The average slopes of the consolidation curves for natural angular and rounded particles are 0.032 and 0.036, respectively, while the corresponding values for 3D printed angular and rounded particles are 0.116 and 0.138, respectively. The greater compressibility of 3D printed sand is likely due to the initial plastic yielding of micro-asperities of the rougher inter-particle contacts, as shown in Fig. 3.1b and discussed by Ahmed and Martinez [2020]. The results presented herein also highlight that the natural and 3D printed rounded particles exhibit a slightly greater compressibility than the natural and 3D printed angular particles, respectively.

The consolidation results from the natural sands indicate that the curves that start at

different void ratios remain roughly parallel to each other in the range of mean effective stress considered. This is particularly evident in Fig. 3.6b and is in agreement with Altuhafi and Coop [2011] and Yamamuro et al. [1996] for mean effective stresses at which no significant particle crushing takes place. In contrast, the consolidation results from the 3D printed soils indicate that the curves tend to converge; this is particularly evident in Fig. 3.6c. This difference in behavior between the natural and 3D printed sands could be explained by the limiting compression curve (LLC) concept. Namely, the compression curves for natural cohesionless soils with different initial densities tend to converge to a unique curve at high mean effective stress levels, referred to as the LCC [Coop and Lee, 1992; Pestana and Whittle, 1995]. At low stress levels, the volume changes of soils are due to elastic compression of the soil skeleton and particle rearrangement, while the LCC response is controlled by particle damage (i.e. asperity breakage and particle crushing) [Roberts, 1958]. The damage of particles is affected by particle shape, gradation and mineralogy. In this study, no crushing was observed in the specimens of natural sand and 3D printed sand. However, damage of the 3D printed particles during consolidation likely took place in the form of plastic yielding of the micro-asperities, which could be analogous to the breakage of asperities in natural sands. For the 3D printed sands, the results suggest that a mean effective stress of about 50 kPa causes this convergence of the compression curves.

The deviatoric stress and volumetric change responses for the natural and 3D printed sands during drained shearing correspond to those expected for coarse-grained soils. As shown in Fig. 3.7 for the angular sands, greater deviatoric stresses were developed at higher confining pressure for both natural (Fig. 3.7a) and 3D printed (Fig. 3.7e) sands. The $q - \varepsilon_a$ curves for the natural angular sand tests performed at confining pressures of 90, 200, and 318 kPa show a slight peak followed by strain softening (Fig. 3.7a) accompanied by dilative volumetric strains (Fig. 3.7b). On the other hand, the $q - \varepsilon_a$ curves for the tests at confining pressures of 530 and 742 kPa exhibit strain hardening along with overall contractive volumetric strains (Figs. 3.7a and 3.7b). The $q - \varepsilon_a$ curves for the tests on

angular 3D printed sand exhibit strain hardening and an overall contractive behavior (Figs. 3.7e and 3.7f). However, the specimens exhibited slight dilation at axial strains greater than about 15%.

The points at the end of shearing for the natural and 3D printed sand specimens were taken as the critical state points to estimate the critical state line in the $q - p'$ plane (Figs. 3.7c and 3.7g). The tests on natural angular sand yielded CS points in the $q - p'$ plane that can be fitted with a straight line passing through the origin with a slope, M, of 1.35, corresponding to a critical state friction angle, ϕ'_{cs}, of 33.4°. In contrast, the CS points of the tests on 3D printed sand cannot be fitted with a straight line in the $q - p'$ plane. While the CSL may be curved, two straight lines are used here to define average friction angles for two σ'_{3c} ranges. A straight line fitted to the tests with a confining pressure smaller than 50 kPa has a M of 0.936 (ϕ'_{cs} of 23.9°), while a line fitted to the tests with confining pressures greater than 50 kPa has a slope of 0.792 (ϕ'_{cs} of 20.6°). The reason for the decrease in M and ϕ'_{cs} with increasing σ'_{3c} could be due to the decrease in inter-particle friction coefficient of the 3D printed polymer as the normal stress is increased, as shown in Figs. 3.5b and 3.5c. The results also indicate that the M and ϕ'_{cs} values obtained for the 3D printed angular sand are smaller than those for natural angular sand. One possible reason for this is the smaller inter-particle friction coefficient of the 3D printed polymer in the direction perpendicular to layer deposition (between 0.12 and 0.19) compared to that of natural sands (between 0.17 and 0.36) (Table 3.1). Another reason could be plastic deformation of the particles' asperities, which would decrease the interlocking between particles. However, further research is required to determine the reason for the differences in M and ϕ'_{cs} values. Note that, post-test assessment of particle shapes shows no statistically significant changes in particle shape parameters (Fig. 3.4). The stress paths in the $e - \log p'$ plane in Figs. 3.7d and 3.7h show the dilation of the natural sand observed during tests at confining pressures of 90, 200, and 318 kPa and the contraction observed during tests at greater confining pressures. In contrast, the stress paths show the overall contraction during all the tests on 3D printed

sands. Due to this continued contraction, the 3D printed sand specimens reach lower void ratios (0.581 to 0.683) than the natural sand specimens (0.627 to 0.750). It is noted that the difference in final void ratios is likely due to a combination of the greater compressibility of the 3D printed skeleton as well as the differences in volume change tendencies dictated by the specific void ratio and mean effective stress of each specimen.

Similar to the angular natural and 3D printed sands, the drained shear behavior of rounded natural and 3D printed sands agrees with that expected for coarse-grained soils (Fig. 3.8). The $q - \varepsilon_a$ plots indicate that both natural and 3D printed particles develop higher shear stress at higher confining pressure (Figs. 3.8a and 3.8e). All the $q - \varepsilon_a$ curves for the natural rounded sand exhibit a peak followed by slight strain softening (Fig. 3.8a) accompanied by dilative volumetric strains (Fig. 3.8b). The tests on 3D printed rounded sand exhibit strain hardening (Fig. 3.8e) accompanied by an overall contractive behavior. However, in a similar way as the 3D printed angular sand, slight dilative volumetric strains take place at axial strains greater than about 15% (Fig. 3.8f). The trends shown in the $q-p'$ plane (Figs. 3.8c and 3.8g) are similar to those described for the angular sand. Namely, a straight line passing through the origin can be fitted for the natural rounded sand in the $q - p'$ plane with an M of 1.29 ($\phi'_{cs} = 32.1°$), which is slightly smaller than the M for the natural angular sand ($M = 1.35$, $\phi'_{cs} = 33.4°$). This difference reflects the greater roundness and sphericity of the rounded particles (Fig. 3.4). The CS points from the tests on 3D printed rounded sand can be fitted with two different straight lines in the $q - p'$ plane (Fig. 3.8g). The fitted M slope for the tests at $\sigma'_{3c} < 50$ kPa is 0.887 ($\phi'_{cs} = 22.7°$) while the slope for the tests at $\sigma'_{3c} > 50$ kPa is 0.742 ($\phi'_{cs} = 19.3°$). Both M values obtained for 3D printed rounded particles are lower than those obtained for 3D printed angular particles due to the greater roundness and sphericity of the former. The stress paths in the $e - \log p'$ plane shown in Figs. 3.8d and 3.8h indicate similar trends as described for the angular sands. Namely, they show net dilation for the natural sand and contraction for the 3D printed sand as well as smaller void ratios for the 3D printed sand at the end of the tests.

The drained triaxial compression results indicate that the 3D printed sands exhibit stress-dilatancy behavior in agreement with that of natural coarse-grained soils. The stress-dilatancy ($R - D$) relationships for the tests on the natural and 3D printed angular and rounded sands are shown in Fig. 3.9, where $R = \sigma'_1/\sigma'_3$ is the stress ratio, σ'_1 is the major principal effective stress and σ'_3 is the minor principal effective stress, and $D = 1 - d\varepsilon_{\mathrm{v}}/d\varepsilon_{\mathrm{a}}$ is the dilatancy. The test data is compared to Rowe's flow rule [Rowe, 1962], which is expressed as:

$$R = D \tan^2 \left(\frac{\pi}{4} + \frac{\phi'_{\mathrm{cs}}}{2} \right) \tag{3.2}$$

Figures 3.9a and 3.9b show that the stress-dilatancy data for natural angular and rounded sands, respectively, closely follow Rowe's flow rule. Figures 3.9c and 3.9d show a similar result for 3D printed angular and rounded sands, respectively, although two different flow rule lines are included corresponding to the different ϕ'_{cs} values obtained for tests with confining pressures greater and smaller than 50 kPa.

3.5 Comparison of the Behavior of 3D Printed and Natural Sands along Analogous Stress Paths

Triaxial test pairs were performed on natural and 3D printed sands at confining pressures of 650 and 30 kPa, respectively. The tests pairs were performed with void ratios at the beginning of shearing (e_{c}) that were within 0.02 from each other. This section discusses the similarities in triaxial response for drained and undrained tests on the angular sands and undrained test pairs on the rounded sands.

3.5.1 Drained Behavior of Natural and 3D Printed Angular Sands

The effect of the void ratio at the beginning of shearing on the natural and 3D printed angular particles was investigated by conducting test pairs on specimens with larger and

smaller void ratios. The results of drained tests on natural angular and 3D printed angular sands with e_c values of 0.705 ± 0.01 and 0.645 ± 0.01 are shown in Figs. 3.10a through 3.10h. As shown in the $q - \varepsilon_a$ curves (Figs. 3.10a and 3.10e), the specimens with smaller e_c yielded greater deviatoric stresses than the specimens with greater e_c for both natural and 3D printed sands. The natural angular sand specimen with smaller e_c exhibited an initially contractive response followed by strong dilation (Fig. 3.10b); the continued dilation at the end of the test indicates that the specimen did not reach a constant-volume state (i.e. critical state). The specimen with the greater e_c exhibited overall contractive volumetric strains throughout the entire test. The 3D printed angular sand specimens with both larger and smaller e_c exhibit an initial contractile response up to an axial strain of about 15% followed by some dilation (Fig. 3.10f). The specimen with smaller e_c exhibited a smaller amount of initial contraction followed by greater rate of dilation, as compared to the specimen with the larger e_c. The initial contraction observed in all the tests on 3D printed sand specimens may be indicative of skeleton compression due to the increase in p' during the initial 15% of axial strains. This suggests an agreement with the consolidation results shown in Figs. 3.6c and 3.6d and with 1D compression results presented by Ahmed and Martinez [2020], which indicate greater compressibility of the 3D printed sand skeleton in comparison with the natural sand skeleton.

In the $q - p'$ plane, the stress paths for the natural angular sand specimens appear to evolve towards the CSL (Fig. 3.10c) even though it appears that neither test reached critical state. The stress paths of the tests on 3D printed angular sand also appear to evolve towards the CSL (Fig. 3.10g), with the test with an initially greater e_c converging to the CSL and the test with the smaller e_c still above the CSL due to the larger rate of dilation. The stress paths in the $e - \log p'$ plane are qualitatively similar between the tests on natural and 3D printed natural sands. Namely, both tests with larger e_c show net contraction and both tests with smaller e_c show initial contraction follow by dilation (Figs. 3.10d and 3.10h).

3.5.2 Undrained Behavior of Natural and 3D Printed Angular and Rounded Sands

The undrained triaxial compression behavior of natural and 3D printed angular particles with different void ratios at the beginning of shearing was investigated by performing test pairs at e_c of 0.705 ± 0.01, 0.650 ± 0.01, and 0.590 ± 0.01 (Fig. 3.11). The $q - \varepsilon_a$ curves (Figs. 3.11a and 3.11e) indicate that the specimens of both natural and 3D printed particles with an e_c of 0.590 ± 0.01 mobilized the greatest deviatoric stresses while the specimens with an e_c of 0.705 ± 0.01 mobilized the smallest deviatoric stresses. The natural angular sand specimen with the highest e_c exhibited positive Δu that increased to about 310 kPa and then decreased to about 210 kPa, while the specimen with an e_c of 0.649 exhibit initial positive Δu and decreased to slightly negative values by the end of shearing (Fig. 3.11b). The densest natural sand specimen generated negative Δu that reached a value of about -330 kPa at the end of shearing. The trends exhibited by the angular 3D printed sand specimens follow a similar trend where the specimen with the greatest e_c (0.714) generated the greatest magnitude of Δu, followed by the specimen with an e_c of 0.654 and then by the specimen with the lowest e_c of 0.591 (Fig. 3.11f). The Δu of the 3D printed sand specimens during the tests increased rapidly at axial strains smaller than 5%, after which the magnitudes tended to decrease slowly throughout the end of the tests. These trends are in agreement with the rapid rate of contraction observed in the drained tests in Figs. 3.7f and 3.10f at small axial strains followed by the slight dilation at greater axial strains.

In the $q - p'$ plane, the end-of-test points for the natural angular sand specimens converged towards the CSL (Fig. 3.11c). The stress paths of the angular 3D printed specimens evolve towards the CSL; however, the points are above the CSL at the end of the test, indicating that critical state has not been reached (Fig. 3.11g). In the $e - \log p'$ plane, the end-of-test points for the natural particles show the increase in p' which is greatest for the specimen with the smallest e_c (Fig. 3.11h). The stress paths of the 3D printed sand

specimens follow similar paths; however, the increase in mean stress is considerably smaller than for the tests on natural angular sand.

The results of the undrained triaxial tests on natural and 3D printed rounded sands show similar trends as described for the angular sands (Fig. 3.12). Namely, the specimens with smaller e_c mobilize greater deviatoric stresses (Figs. 3.12a and 3.12e) due to the greater magnitude of negative excess pore pressures (Figs. 3.12b and 3.12f) than the specimens with greater e_c. All the $q-\varepsilon_a$ curves exhibit a hardening response, which is characteristic of dilative undrained sand. The tendency of the 3D printed sands to contract at axial strains smaller than about 5% to 10% is evident in the results; however, this tendency is stronger for the specimen with the greater e_c. In the $q-p'$ plane, the end-of-test points for the natural sand specimens converge toward the CSL (Fig. 3.12c) whereas they are above the CSL for the 3D printed sands, indicating that critical state has not been reached (Fig. 3.12g). In the $e-\log p'$ plane, all the stress paths of the tests on both natural and 3D printed sands show a net increase in the p' (Figs. 3.12d and 3.12h).

The change in mean effective stress with axial strain during undrained shearing is typically associated with the volumetric deformations of the specimen. Constant p' during undrained shearing indicates volumetric deformation of the soil skeleton itself while skeleton shear deformations in the form of dilation or contraction due to particle rearrangement have not yet taken place [Wood, 1990]. Figure 3.13 shows the $p'-\varepsilon_a$ plots of the undrained tests on natural and 3D printed sands. As shown, p' for both angular and rounded natural sands (Figs. 3.13a and 3.13b) begins to change at very small ε_a (smaller than 0.5%), indicating that skeleton shear deformation starts at a very small ε_a. However, p' remains relatively constant for ε_a up to about 3% for the 3D printed angular sand (Fig. 3.13c) and about 7% for the loose 3D printed rounded sand (Fig. 3.13d), indicative of the initial volumetric contraction of the skeleton observed up to a larger ε_a compared to the natural sands. This suggests that skeletal shear deformation for the 3D printed sands initiates after higher initial skeleton volumetric contraction and at a greater ε_a compared to the natural sands. This

observation for the 3D printed sands is in agreement with the initial contraction up to a larger ε_a observed in drained tests (Figs. 3.7f, 3.8f, and 3.10f).

3.5.3 Estimation of Critical State Lines in *e*–log *p*' Space

The critical state lines in $e - \log p'$ space for both the natural and 3D printed sands are approximated by best fitting the critical state points obtained from both drained and undrained tests. The CS points for CD and CU tests were obtained by extrapolating the end-of-test results following methods described in Zhang et al. [2018] and Torres-Cruz and Santamarina [2020], respectively. Examples of the extrapolation procedures are presented in Supplementary Information, which consist of extrapolating the dilatancy to a value of 1.0 in drained tests and the rate of pore pressure change to a value of zero in undrained tests.

The end-of-test points in the $e-\log p'$ plane for natural angular and rounded sands are shown in Figs. 3.14a and 3.14b, separated into specimens that were deemed to reach critical state and those that did not. A curved form of the critical state line (CSL) is considered here to better capture the shape across a wide range of p' values. Hence, the CSL is presented by a power function [Wang et al., 2002] as:

$$e_f = e_\Gamma - \lambda \left(\frac{p'}{p_a} \right)^\xi \tag{3.3}$$

where e_f is the critical state void ratio, e_Γ is the critical state void ratio at $p' = 0$ kPa, p_a is the atmospheric pressure (≈ 100 kPa), and λ and ξ are material constants describing the material compressibility and the non-linearity of the CSL, respectively. The CSL equations obtained for both natural angular and rounded sands are provided in Figs. 3.14a and 3.14b, respectively, showing a greater e_Γ intercept for the angular sand, a slightly greater λ for the rounded sand, and similar ξ exponents. Similar to the natural sand, the CS points in $e - \log p'$ plane obtained for the 3D printed sand can be approximated by Eq. 3.3 as shown in Figs. 3.14c and 3.14d for the angular and rounded sands, respectively. Comparison of the

equations for angular and rounded 3D printed sands indicates similar trends as the natural sand. Namely, the e_Γ intercept is greater for the angular sand and λ is slightly greater for the rounded sand. However, the ξ exponent is slightly smaller for the rounded sand.

Comparison of the CSL equations for the natural and 3D printed sands reveals important trends. The e_Γ intercepts are relatively close in value albeit slightly greater for the natural sands: 0.785 to 0.746 for natural sands and 0.745 to 0.725 for 3D printed sands. The λ values, which are related to the material compressibility, are considerably greater for the 3D printed sands: 0.0215 to 0.024 for natural sands and 0.148 to 0.165 for 3D printed sands. These differences agree with the greater compressibility during isotropic and 1D compression shown in Figs. 3.6a through 3.6d and by Ahmed and Martinez [2020]. Finally, the ξ exponents were smaller for the 3D printed sands: 0.78 for natural sands and 0.70 to 0.65 for 3D printed sands. This indicates a greater non-linearity of the CSL of the 3D printed soils. The estimation of the CSLs for the 3D printed soils suggests that their behavior can be captured within the critical state framework in the same way as for natural soils. It can be envisioned that the behavior of natural soils could be modeled with 3D printed analogs using critical state concepts. For example, tests could be performed at a combination of void ratio and initial mean effective stress such that the state at the beginning of shearing for the natural and 3D printed sand specimens have the same state parameter with respect to their corresponding CSLs [as described by Been and Jefferies, 1985].

3.6 Discussion on the Modeling of Soil Behavior with 3D Printed Particle Analogs

One of the greatest potential benefits offered by the 3D printed sands is the ability to systematically control different particle properties, such as the shape, size, and constituent material. Additionally, 3D printed particles may also enhance validation procedures for discrete element modeling simulations against experimental data by ensuring the use of particles with similar morphology in both experimental and numerical investigations [Kittu

et al., 2019]. The results presented here indicate that polyjet 3D printing technology can be used to successfully reproduce the shape of natural sand particles (Figs. 3.3 and 3.4). It can thus be envisioned how synthetic particles could be generated with methods such as spherical harmonics [Wei et al., 2018] and 3D printing to systematically investigate differences in strength and stiffness of granular assemblies due to changes in particle shape or particle size distribution alone. The triaxial compression tests indicate that the 3D printed sands exhibit many of the fundamental behaviors that characterize sands and gravels, suggesting that they can be used to model the behavior of natural soils. Namely, the stress-dilatancy behavior conformed to established flow rules (Fig. 3.9), loose specimens contracted and dense specimens dilated during drained shearing (Figs. 3.7, 3.8, and 3.10), loose specimens developed positive excess pore pressures and dense developed negative ones during undrained shearing (Figs. 3.11 and 3.12), sands with more rounded particles had smaller critical state friction angles (Figs. 3.7 and 3.8), and critical state lines appear to exist in the $q - p'$ and $e - \log p'$ planes (Figs. 3.7, 3.8, and 3.14).

There are important differences in the response of 3D printed sands with respect to that of natural sands. The polyjet 3D printed particles employed in this study exhibit greater plastic deformation at inter-particle contacts compared to that observed between glass or sand particles due to the greater surface roughness of the particles resulting from the layer deposition process (Fig. 3.1). In addition, greater elastic deformation is also experienced at the contact due to the lower Young's modulus of the 3D printed polymer. These are likely the reasons for the greater compressibility of the 3D printed sands (Figs. 3.6 and 3.14), along with the greater skeleton compressive deformation observed at small axial strains during triaxial testing (Figs. 3.7, 3.8, and 3.13). The layer deposition process also results in direction-dependency of the friction coefficient of the 3D printed material (Fig. 3.5), which is likely not the case for natural soil particles. The smaller friction coefficient in the direction perpendicular to layer deposition may be responsible for the smaller friction angles of the 3D printed soils (Figs. 3.7 and 3.8). Understanding of these differences is required for assessing

how closely the macro-scale behavior of natural soils can be modeled or reproduced by the 3D printed soil analogs.

The micro-scale behavior of 3D printed particles is determined by the surface created by the printing process and by the mechanical properties of the printed material. Multiple types of 3D printing technology exist (e.g. stereolithography, fused deposition modeling, selective laser sintering), and new technologies are being developed rapidly. Because each technology is capable of printing different materials and each one employs a different manufacturing process, the possible effects on the response of individual particles (i.e. contact normal stiffness, friction coefficient) and granular assemblies should be evaluated and understood if the behavior of soils and other granular materials is to be modeled in a quantitative manner.

3.7 Conclusions

This paper investigates the feasibility of using 3D printing technology to generate analog particles to model the triaxial compression behavior of coarse-grained soils. A total of 34 drained and undrained triaxial compression tests on specimens of natural and 3D printed angular and rounded particles were performed. The main findings of this study are summarized as follows:

- The polyjet 3D printing technology can accurately reproduce the shape and size of natural coarse sand particles. However, the surface texture of the polyjet 3D printed particles is dependent on the printing layer direction, which results in different surface roughness that affects the inter-particle frictional coefficient. The friction coefficient of the polyjet polymer was also observed to be dependent on the magnitude of applied normal stress.

- The 3D printed sands are more compressible compared to the natural sands, which is likely due to lower Young's Modulus of the polymer and to plastic yielding of

micro-asperities on the surface of the 3D printed material. During shearing, this greater compressibility likely causes larger initial volumetric contraction (or positive excess pore pressure generation) followed by skeletal shear deformation that begins at a higher axial strain compared to that of natural sand.

- The drained test results show that the 3D printed sands follow Rowe's flow rule, demonstrating that they can replicate the stress−dilatancy behavior observed in natural sands. Also, the angular 3D printed sand mobilizes greater critical state friction angle than that of rounded 3D printed sand, in agreement with the results on the natural sands.

- The results from test pairs performed at similar void ratios but different confining pressures (30 kPa for 3D printed sand, 650 kPa for the natural sand) indicate that analogous drained and undrained stress paths are followed by the test pairs in both the $q - p'$ and $e - \log p'$ planes. This included contractive volumetric changes and generation of positive excess pore pressures in loose specimens, and dilative volumetric changes and generation of negative excess pore pressures in dense specimens.

- The critical state line in the $q-p'$ plane is curved for the polyjet 3D printed sands, with a slope that decreases as p' is increased. The critical state line in the $e - \log p'$ space can be described with a power-law function. Owing to the greater compressibility of the 3D printed sands, their critical state void ratios are smaller than those for the natural sands.

- The stress paths followed by the 3D printed and natural sands are similar. Also, the curved CSLs approximated for the 3D printed particles are similar to those of natural particles.

3.8 Acknowledgment

This material is based upon work supported in part by the National Science Foundation (NSF) under award No. 1735732. Any opinions, findings, and conclusions or recommendations expressed in this material are those of the author(s) and do not necessarily reflect those of the NSF.

Bibliography

Adamidis, O., Alber, S., and Anastasopoulos, I. (2020). Assessment of three-dimensional printing of granular media for geotechnical applications. *Geotechnical Testing Journal*, 43(3).

Ahmed, S. S. and Martinez, A. (2020). Modeling the mechanical behavior of coarse-grained soil using additive manufactured particle analogs. *Acta Geotechnica*, 15(10):2829–2847.

Altuhafi, F. and Coop, M. R. (2011). Changes to particle characteristics associated with the compression of sands. *Géotechnique*, 61(6):459–471.

Athanassiadis, A. G., Miskin, M. Z., Kaplan, P., Rodenberg, N., Lee, S. H., Merritt, J., Brown, E., Amend, J., Lipson, H., and Jaeger, H. M. (2014). Particle shape effects on the stress response of granular packings. *Soft Matter*, 10(1):48–59.

Bartake, P. and Singh, D. (2007). Studies on the determination of shear wave velocity in sands. *Geomechanics and Geoengineering*, 2(1):41–49.

Been, K. and Jefferies, M. G. (1985). A state parameter for sands. *Géotechnique*, 35(2):99–112.

Berrezueta, E., Cuervas-Mons, J., Rodríguez-Rey, Á., and Ordóñez-Casado, B. (2019). Representativity of 2d shape parameters for mineral particles in quantitative petrography. *Minerals*, 9(12):768.

Bui, M. T. (2009). *Influence of some particle characteristics on the small strain response of granular materials*. PhD thesis, University of Southampton.

Casini, F., Brauchli, S., Herzog, R., and Springman, S. (2011). Grain size distribution and particle shape effects on shear strength of sand–gravel mixtures. In *Proceedings of the 15th European conference on soil mechanics and geotechnical engineering*, pages 149–154. GR.

Cavarretta, I., Coop, M., and O'SULLIVAN, C. (2010). The influence of particle characteristics on the behaviour of coarse grained soils. *Géotechnique*, 60(6):413–423.

Cazón, A., Morer, P., and Matey, L. (2014). Polyjet technology for product prototyping: Tensile strength and surface roughness properties. *Proceedings of the Institution of Mechanical Engineers, Part B: Journal of Engineering Manufacture*, 228(12):1664–1675.

Cho, G.-C., Dodds, J., and Santamarina, J. C. (2006). Particle shape effects on packing density, stiffness, and strength: Natural and crushed sands. *Journal of Geotechnical and Geoenvironmental Engineering*, 132(5):591–602.

Cole, D. M. (2015). Laboratory observations of frictional sliding of individual contacts in geologic materials. *Granular Matter*, 17(1):95–110.

Coop, M. and Lee, I. (1992). The behaviour of granular soils at elevated stresses. In *Predictive soil mechanics: Proceedings of the Wroth Memorial Symposium held at St Catherine's College, Oxford, 27-29 July 1992*, pages 186–198. Thomas Telford Publishing.

Greenwood, J. A. and Tripp, J. H. (1967). The elastic contact of rough spheres. *Journal of Applied Mechanics*, 34(1):153–159.

Guida, G., Viggiani, G. M., and Casini, F. (2020). Multi-scale morphological descriptors from the fractal analysis of particle contour. *Acta Geotechnica*, 15(5):1067–1080.

Gupta, R., Salager, S., Wang, K., and Sun, W. (2019). Open-source support toward validating and falsifying discrete mechanics models using synthetic granular materials—part i: Experimental tests with particles manufactured by a 3d printer. *Acta Geotechnica*, 14(4):923–937.

Hanaor, D., Gan, Y., Revay, M., Airey, D., and Einav, I. (2016). 3d printable geomaterials. *Géotechnique*, 66(4):323–332.

Hong, S. Y., Kim, Y. C., Wang, M., Kim, H.-I., Byun, D.-Y., Nam, J.-D., Chou, T.-W., Ajayan, P. M., Ci, L., and Suhr, J. (2018). Experimental investigation of mechanical properties of uv-curable 3d printing materials. *Polymer*, 145:88–94.

Huang, X., Hanley, K. J., O'Sullivan, C., and Kwok, C. Y. (2014). Exploring the influence of interparticle friction on critical state behaviour using dem. *International Journal for Numerical and Analytical Methods in Geomechanics*, 38(12):1276–1297.

Islam, M. N., Siddika, A., Hossain, M. B., Rahman, A., and Asad, M. A. (2011). Effect of particle size on the shear strength behavior of sands. *Australian Geomechanics Journal*, 46(3):75–86.

Iwasaki, T. and Tatsuoka, F. (1977). Effects of grain size and grading on dynamic shear moduli of sands. *Soils and Foundations*, 17(3):19–35.

Jiménez, M., Romero, L., Domínguez, I. A., Espinosa, M. d. M., and Domínguez, M. (2019). Additive manufacturing technologies: an overview about 3d printing methods and future prospects. *Complexity*, 2019.

Kara, E. M., Meghachou, M., and Aboubekr, N. (2013). Contribution of particles size ranges to sand friction. *Engineering, Technology & Applied Science Research*, 3(4):497–501.

Kirkpatrick, W. (1965). Effects of grain size and grading on the shearing behaviour of granular materials. In *Proceedings of the sixth International Conference on Soil Mechanics and Foundation Engineering*, pages 273–277.

Kittu, A., Watters, M., Cavarretta, I., and Bernhardt-Barry, M. (2019). Characterization of additive manufactured particles for dem validation studies. *Granular Matter*, 21(3):1–15.

Liu, X. and Yang, J. (2018). Shear wave velocity in sand: effect of grain shape. *Géotechnique*, 68(8):742–748.

Marschi, N. D., Chan, C. K., and Seed, H. B. (1972). Evaluation of properties of rockfill materials. *Journal of the Soil Mechanics and Foundations Division*, 98(1):95–114.

Matsumura, S., Kobayashi, T., Mizutani, T., and Bathurst, R. J. (2017). Manufacture of bonded granular soil using x-ray ct scanning and 3d printing. *Geotechnical Testing Journal*, 40(6):1000–1010.

Miskin, M. Z. and Jaeger, H. M. (2013). Adapting granular materials through artificial evolution. *Nature Materials*, 12(4):326–331.

Mitchell, J. K., Soga, K., et al. (2005). *Fundamentals of soil behavior*. John Wiley & Sons New York.

Najmon, J. C., Raeisi, S., and Tovar, A. (2019). Review of additive manufacturing technologies and applications in the aerospace industry. *Additive Manufacturing for the Aerospace Industry*, pages 7–31.

Ngo, T. D., Kashani, A., Imbalzano, G., Nguyen, K. T., and Hui, D. (2018). Additive manufacturing (3d printing): A review of materials, methods, applications and challenges. *Composites Part B: Engineering*, 143:172–196.

Otsubo, M., O'sullivan, C., Sim, W. W., and Ibraim, E. (2015). Quantitative assessment of the influence of surface roughness on soil stiffness. *Géotechnique*, 65(8):694–700.

Patel, A., Bartake, P., and Singh, D. (2009). An empirical relationship for determining shear wave velocity in granular materials accounting for grain morphology. *Geotechnical Testing Journal*, 32(1):1–10.

Pestana, J. M. and Whittle, A. (1995). Compression model for cohesionless soils. *Géotechnique*, 45(4):611–631.

Roberts, J. (1958). The compressibility of sand. *Proc., Am. Soc. for Testing Mat.*, 58:1269–1277.

Rowe, P. W. (1962). The stress-dilatancy relation for static equilibrium of an assembly of particles in contact. *Proceedings of the Royal Society of London. Series A. Mathematical and Physical Sciences*, 269(1339):500–527.

Santamarina, C. and Cascante, G. (1998). Effect of surface roughness on wave propagation parameters. *Géotechnique*, 48(1):129–136.

Santamarina, J. C. (2003). Soil behavior at the microscale: particle forces. In *Soil Behavior and Soft Ground Construction*, pages 25–56.

Santamarina, J. C., Klein, K. A., and Fam, M. A. (2001). *Soils and Waves*. J. Wiley & Sons New York.

Senetakis, K., Coop, M. R., and Todisco, M. C. (2013). The inter-particle coefficient of friction at the contacts of leighton buzzard sand quartz minerals. *Soils and Foundations*, 53(5):746–755.

Sharifipour, M., Dano, C., and Hicher, P.-Y. (2004). Wave velocities in assemblies of glass beads using bender-extender elements. In *17th ASCE Engineering Mechanics Conference*.

Stansbury, J. W. and Idacavage, M. J. (2016). 3d printing with polymers: Challenges among expanding options and opportunities. *Dental Materials*, 32(1):54–64.

Tee, Y. L., Peng, C., Pille, P., Leary, M., and Tran, P. (2020). Polyjet 3d printing of composite materials: experimental and modelling approach. *Jom*, 72(3):1105–1117.

Tofail, S. A., Koumoulos, E. P., Bandyopadhyay, A., Bose, S., O'Donoghue, L., and Charitidis, C. (2018). Additive manufacturing: scientific and technological challenges, market uptake and opportunities. *Materials Today*, 21(1):22–37.

Torres-Cruz, L. A. and Santamarina, J. C. (2020). The critical state line of nonplastic tailings. *Canadian Geotechnical Journal*, 57(10):1508–1517.

Vangla, P. and Latha, G. M. (2015). Influence of particle size on the friction and interfacial shear strength of sands of similar morphology. *International Journal of Geosynthetics and Ground Engineering*, 1(1):6.

Wadell, H. (1932). Volume, shape, and roundness of rock particles. *The Journal of Geology*, 40(5):443–451.

Wang, J.-J., Zhang, H.-P., Tang, S.-C., and Liang, Y. (2013). Effects of particle size distribution on shear strength of accumulation soil. *Journal of Geotechnical and Geoenvironmental Engineering*, 139(11):1994–1997.

Wang, L., Ju, Y., Xie, H., Ma, G., Mao, L., and He, K. (2017). The mechanical and photoelastic properties of 3d printable stress-visualized materials. *Scientific Reports*, 7(1):1–9.

Wang, Z.-L., Dafalias, Y. F., Li, X.-S., and Makdisi, F. I. (2002). State pressure index for modeling sand behavior. *Journal of Geotechnical and Geoenvironmental Engineering*, 128(6):511–519.

Wei, D., Wang, J., and Zhao, B. (2018). A simple method for particle shape generation with spherical harmonics. *Powder Technology*, 330:284–291.

Wichtmann, T. and Triantafyllidis, T. (2009). Influence of the grain-size distribution curve of quartz sand on the small strain shear modulus g max. *Journal of Geotechnical and Geoenvironmental Engineering*, 135(10):1404–1418.

Wood, D. M. (1990). *Soil Behaviour and Critical State Soil Mechanics*. Cambridge University Press.

Xiao, Y., Long, L., Matthew Evans, T., Zhou, H., Liu, H., and Stuedlein, A. W. (2019). Effect of particle shape on stress-dilatancy responses of medium-dense sands. *Journal of Geotechnical and Geoenvironmental Engineering*, 145(2):04018105.

Yamamuro, J. A., Bopp, P. A., and Lade, P. V. (1996). One-dimensional compression of sands at high pressures. *Journal of Geotechnical Engineering*, 122(2):147–154.

Yang, J. and Gu, X. (2013). Shear stiffness of granular material at small strains: does it depend on grain size? *Géotechnique*, 63(2):165–179.

Zhang, J., Lo, S.-C. R., Rahman, M. M., and Yan, J. (2018). Characterizing monotonic behavior of pond ash within critical state approach. *Journal of Geotechnical and Geoenvironmental Engineering*, 144(1):04017100.

Zheng, J. and Hryciw, R. D. (2015). Traditional soil particle sphericity, roundness and surface roughness by computational geometry. *Géotechnique*, 65(6):494–506.

3.9 Table and Figures

Table 3.1: Inter-particle friction coefficient and N_{GT} for various granular materials

Material	Young's Modulus, E (GPa)	N_{GT} (N)	N_{GT}/E (N/GPa)	Inter-particle Friction Coefficient, μ
Leighton Buzzard Sand	70[1]	9-29[1]	0.13-0.41	0.173[1], 0.27-0.36[2]
ASTM 20-30 Sand	–	–	–	0.27±0.093[3]
Glass Ballotini	70[1]	4.5	0.06	0.176[1]
Borosilicate Glass Spheres	63[4]	4[4]	0.06	–
Polyjet 3D Printing Polymer	2.4[4]	12[4]	5.00	0.11-0.44[5]

[1]Cavarretta et al. [2010], [2]Senetakis et al. [2013], [3]Cole [2015], [4]Ahmed and Martinez [2020], [5]this study

Table 3.2: Properties of the materials tested. Note that mean values are reported for roundness, area sphericity, and width-to-length ratio, while standard deviations are reported inside parentheses

Material	Young's Modulus, E (GPa)	Poisson's Ratio	Roundness	Area Sphericity	Width to Length Ratio
Natural angular quartz particles	76[1]	0.31[1]	0.47 (0.13)	0.68 (0.09)	0.75 (0.11)
Natural rounded quartz particles			0.78 (0.08)	0.76 (0.10)	0.76 (0.11)
3D printed angular particles	2.4[2]	0.30[2]	0.51 (0.13)	0.68 (0.11)	0.71 (0.13)
3D printed rounded particles			0.73 (0.09)	0.75 (0.10)	0.77 (0.11)

[1]Santamarina et al. [2001], [2]Ahmed and Martinez [2020]

Table 3.3: Summary of triaxial testing program for natural and 3D printed particles

Material	Test ID	Test Type	σ'_{3c} (kPa)	e_0	e_c	e_f	q_{peak} (kPa)	q_{end} (kPa)	p'_{peak} (kPa)	p'_{end} (kPa)
Natural Angular	1-NA-90	CD	90	0.681	0.671	0.750	336	278	201	179
	2-NA-200	CD	200	0.684	0.663	0.715	610	554	401	385
	3-NA-318	CD	318	0.686	0.659	0.687	882	840	610	601
	4-NA-530	CD	530	0.691	0.648	0.651	1348	1324	975	968
	5-NA-742	CD	742	0.686	0.639	0.627	1774	1739	1331	1321
Natural Angular	6-NA-650	CD	650	0.691	0.647	0.643	1711	1661	1217	1201
	7-NA-650	CD	650	0.754	0.702	0.680	1440	1425	1127	1110
	8-NA-650	CU	650	0.617	0.585	0.585	2604	2584	1835	1832
	9-NA-650	CU	650	0.696	0.649	0.649	1600	1559	1211	1193
	10-NA-650	CU	650	0.747	0.699	0.699	971	946	771	759
Natural Rounded	1-NR-90	CD	90	0.655	0.646	0.714	267	237	178	168
	2-NR-200	CD	200	0.650	0.631	0.682	521	459	372	351
	3-NR-318	CD	318	0.638	0.611	0.649	818	743	589	568
	4-NR-530	CD	530	0.631	0.591	0.615	1237	1144	940	908
	5-NR-742	CD	742	0.627	0.579	0.586	1734	1666	1318	1289
Natural Rounded	6-NR-650	CU	650	0.545	0.515	0.515	2592	2567	1910	1905
	7-NR-650	CU	650	0.623	0.582	0.582	1830	1819	1438	1435
3DP Angular	1-3DPA-20	CD	20	0.733	0.703	0.683	29	29	29	28
	2-3DPA-30	CD	30	0.731	0.688	0.662	37	36	41	41
	3-3DPA-50	CD	50	0.707	0.651	0.627	52	52	66	67
	4-3DPA-70	CD	70	0.718	0.628	0.601	79	78	95	95
	5-3DPA-90	CD	90	0.718	0.609	0.581	90	90	119	119
3DP Angular	6-3DPA-30	CD	30	0.699	0.652	0.638	48	47	45	45
	7-3DPA-30	CD	30	0.757	0.708	0.682	40	39	42	41
	8-3DPA-30	CU	30	0.652	0.591	0.591	42	41	40	40
	9-3DPA-30	CU	30	0.711	0.654	0.654	34	34	33	33
	10-3DPA-30	CU	30	0.775	0.714	0.714	32	32	32	31
3DP Rounded	1-3DPR-20	CD	20	0.700	0.667	0.654	27	26	27	27
	2-3DPR-30	CD	30	0.707	0.653	0.634	34	34	40	40
	3-3DPR-50	CD	50	0.695	0.624	0.599	51	50	66	66
	4-3DPR-70	CD	70	0.688	0.590	0.571	69	68	92	91
	5-3DPR-90	CD	90	0.671	0.556	0.539	83	81	116	116
3DP Rounded	6-3DPR-30	CU	30	0.560	0.528	0.528	54	54	57	56
	7-3DPR-30	CU	30	0.641	0.591	0.591	37	37	39	38

Note: σ'_{3c} = effective confining pressure; e_0 = initial void ratio; e_c = void ratio after consolidation; e_f = void ratio at the end of test; q_{peak} and q_{end} = peak and end of test deviatoric stress, respectively; p'_{peak} and p'_{end} = peak and end of test mean effective stress, respectively; NA = natural angular; NR = natural rounded; 3DPA = 3D printed angular; 3DPR = 3D printed rounded; CD = consolidated drained; CU= consolidated undrained.

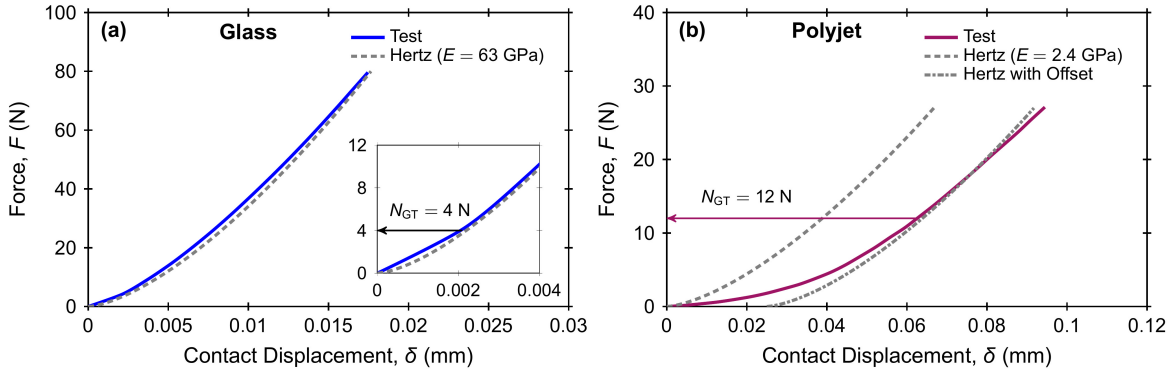

Figure 3.1: Uniaxial particle-particle test results for equal-sized spheres of (a) borosilicate glass and (b) polyjet 3D printing polymer [data from Ahmed and Martinez, 2020]

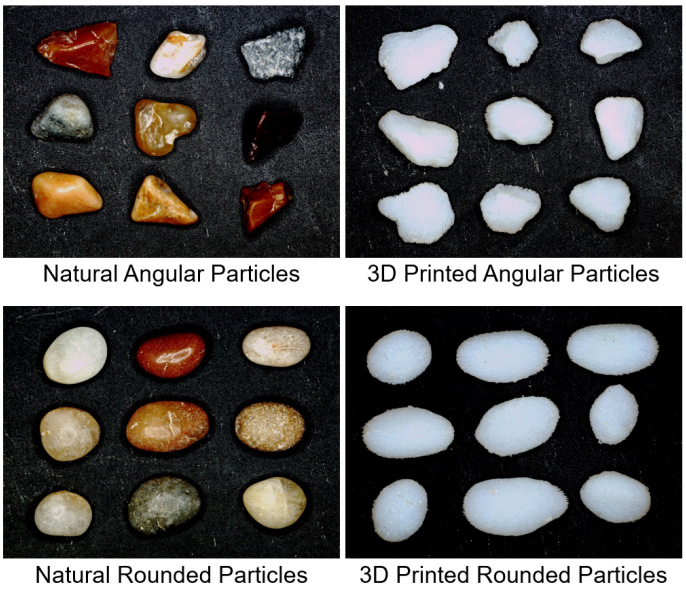

Figure 3.2: Natural and 3D printed angular and rounded particles used in this study

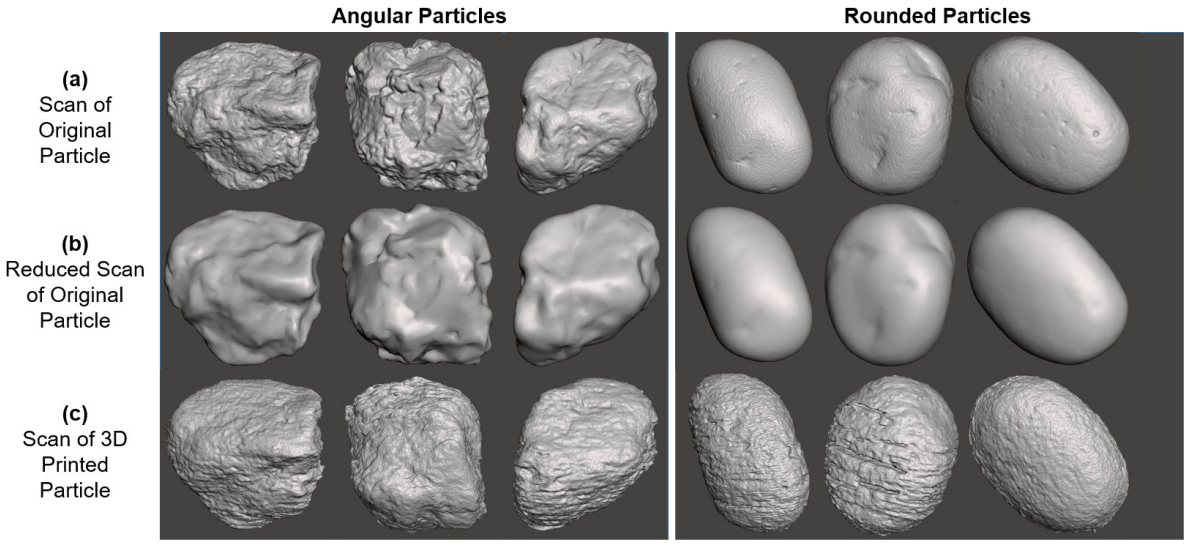

Figure 3.3: Comparison of X-ray CT scans of (a) natural particles, (b) reduced scans for 3D printing, and (c) 3D printed particle analogs

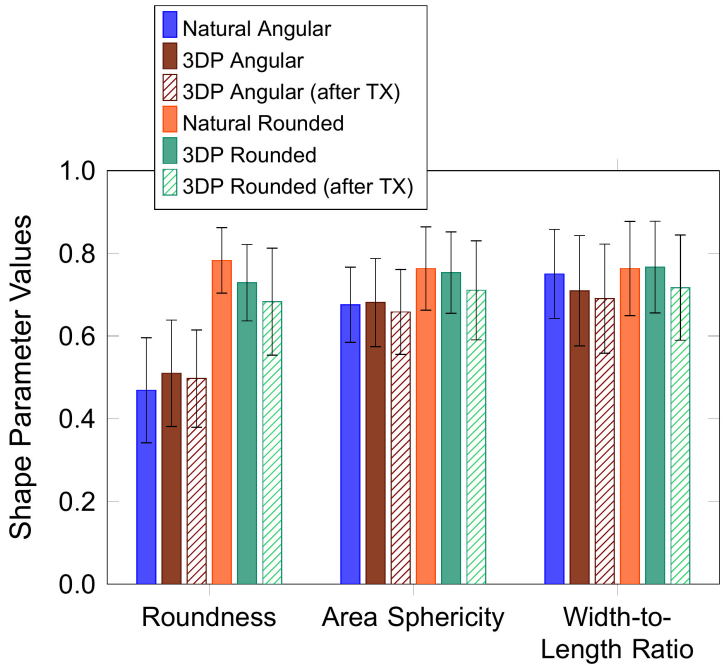

Figure 3.4: Comparison of shape parameters for natural and 3D printed particles. Note that standard deviation in shape parameter values is shown by the error bars and the "after TX" parameters were obtained after performing over 15 triaxial tests on the 3D printed particles

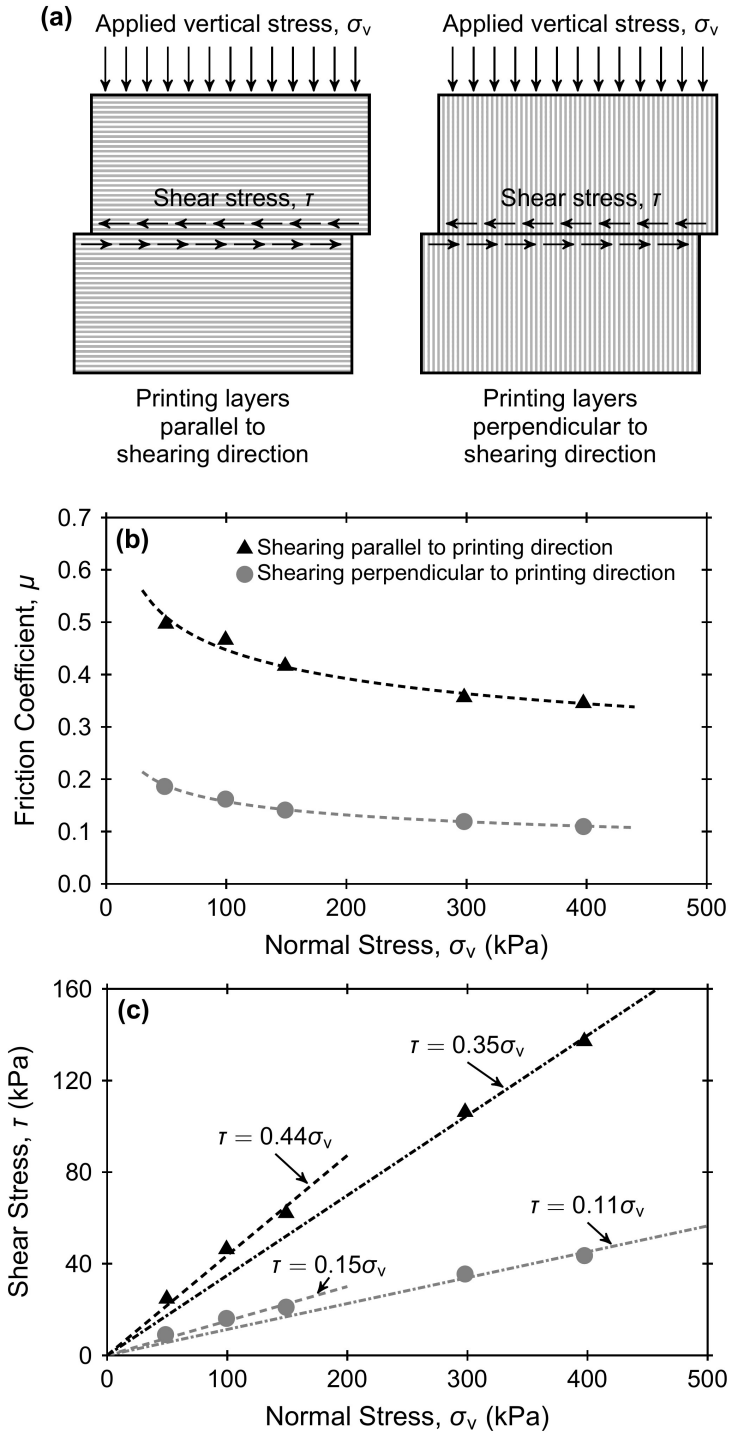

Figure 3.5: (a) Schematic of friction test used to determine printed material friction coefficient with different printed layer orientations, (b) friction coefficient of polyjet 3D printed blocks for different applied vertical stresses, and (c) relationship between shear stress and applied vertical stress

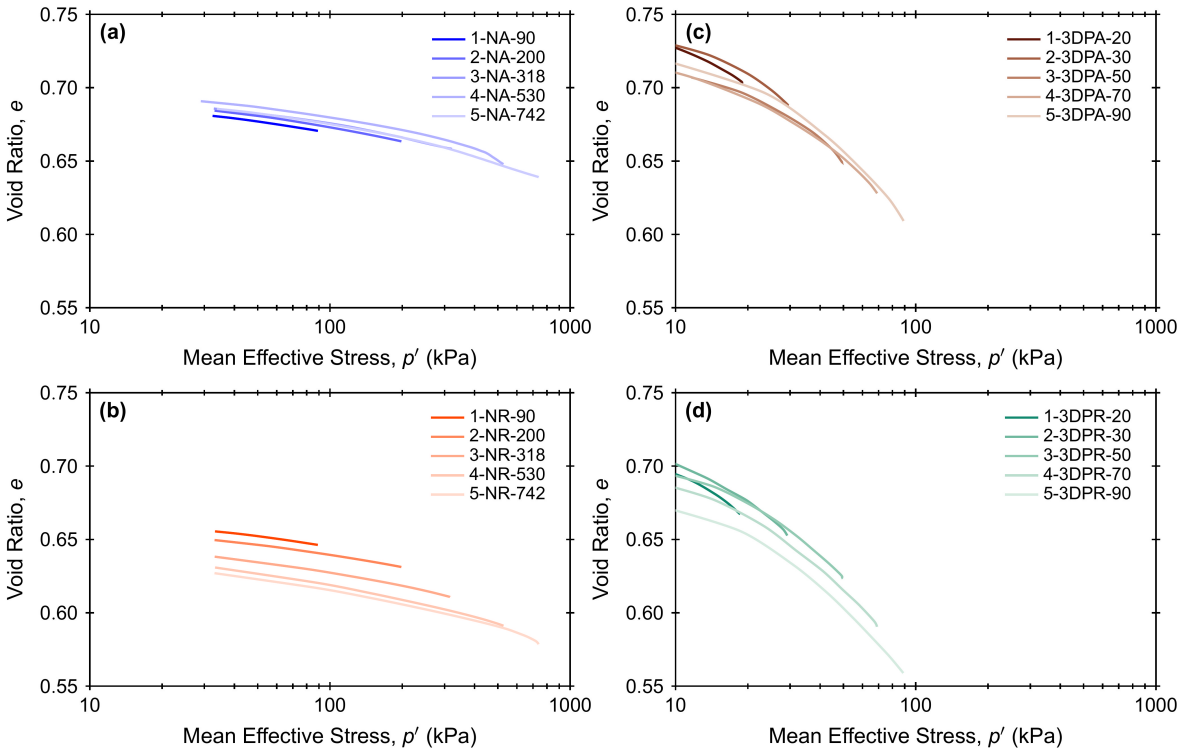

Figure 3.6: Isotropic consolidation curves for (a) natural angular sand, (b) natural rounded sand, (c) 3D printed angular sand, and (d) 3D printed rounded sand

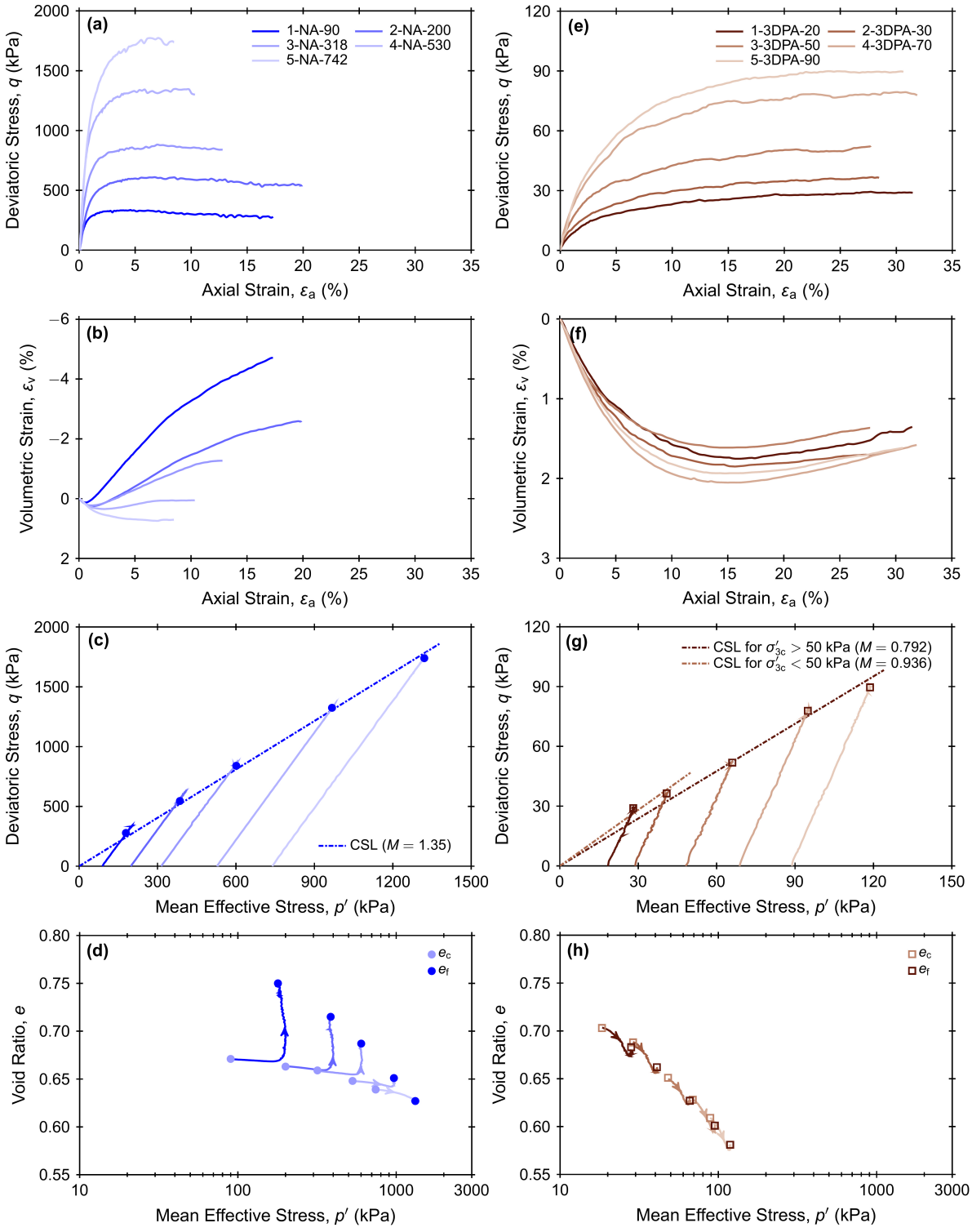

Figure 3.7: Drained triaxial test results on (a-d) natural angular sand and (e-h) 3D printed angular sand

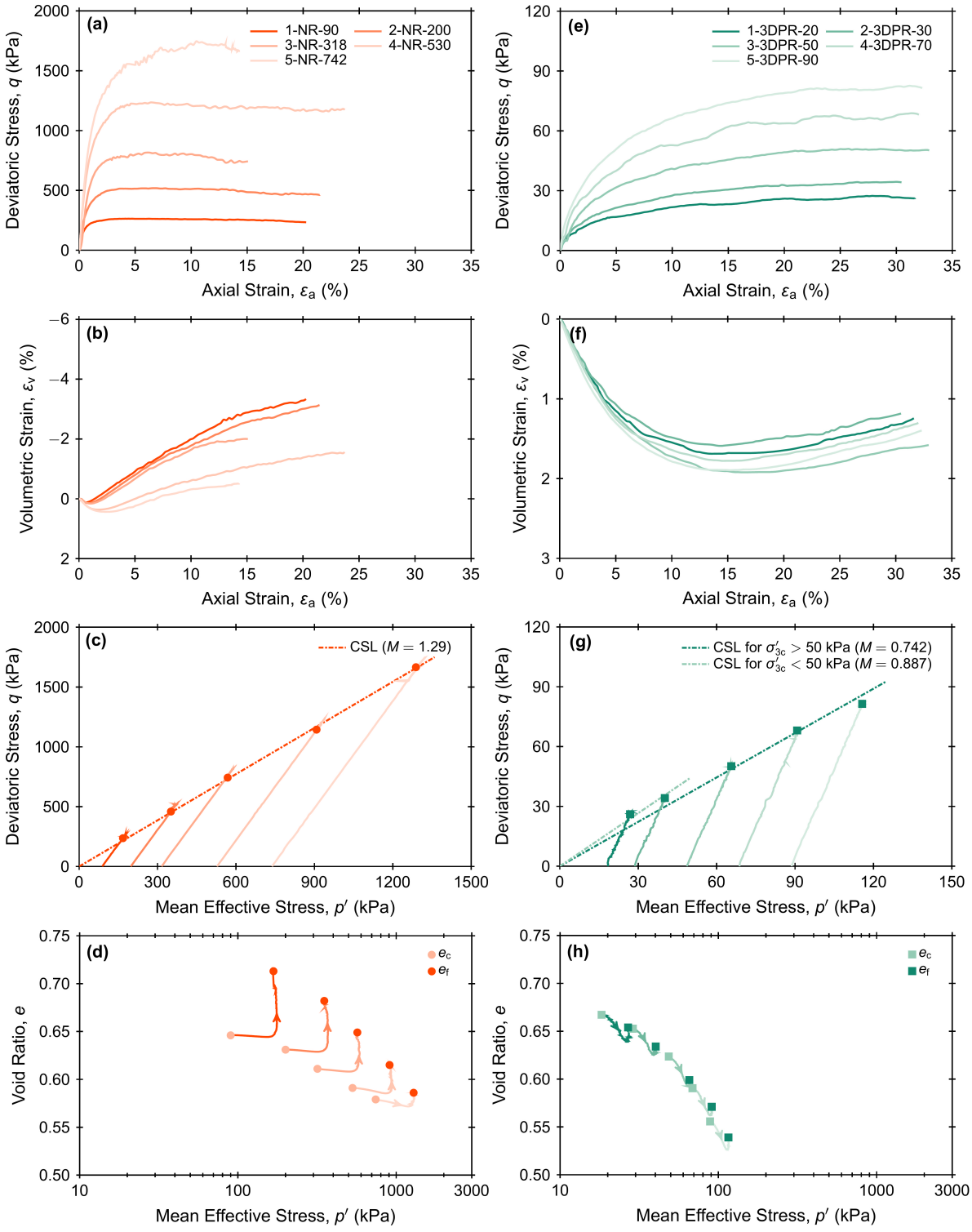

Figure 3.8: Drained triaxial test results on (a-d) natural rounded sand and (e-h) 3D printed rounded sand

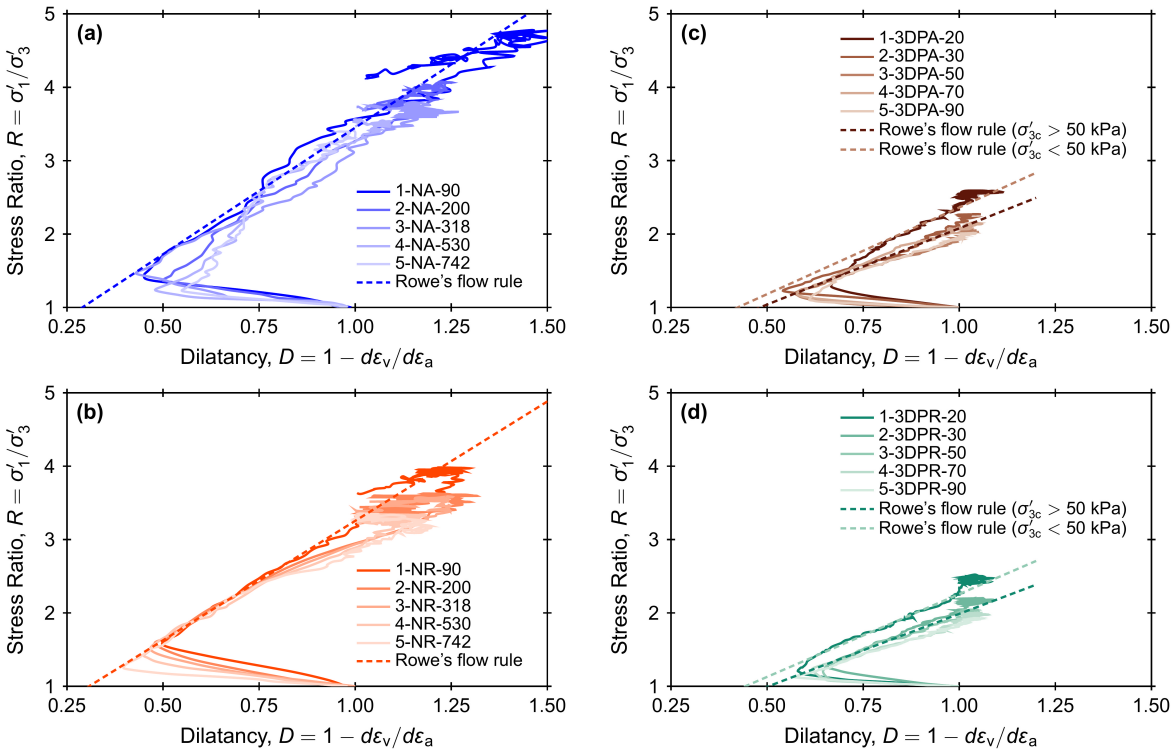

Figure 3.9: Dilatancy behavior of (a) natural angular sand, (b) natural rounded sand, (c) 3D printed angular sand, and (d) 3D printed rounded sand

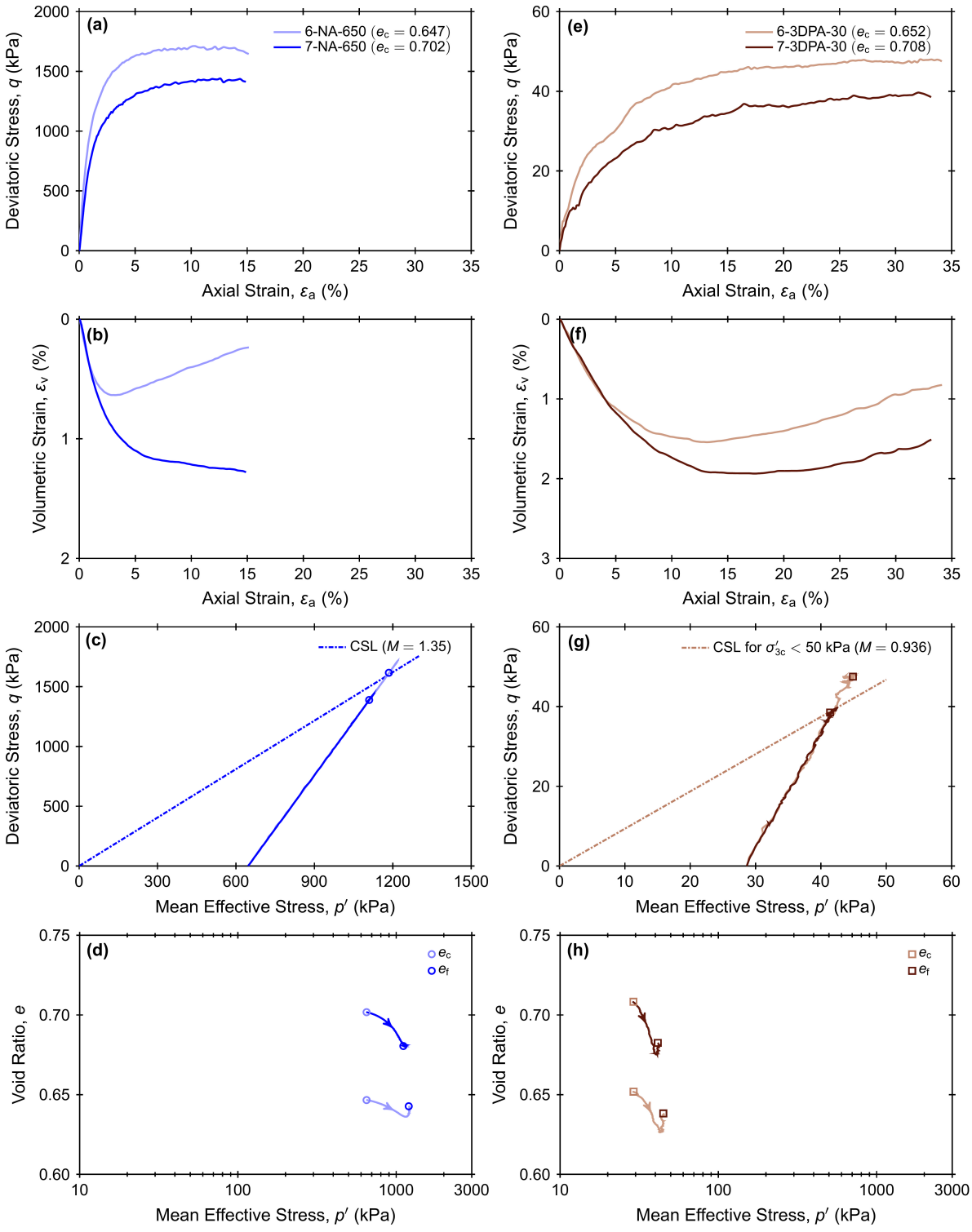

Figure 3.10: Drained behavior of (a-d) natural angular sand and (e-h) 3D printed angular sand

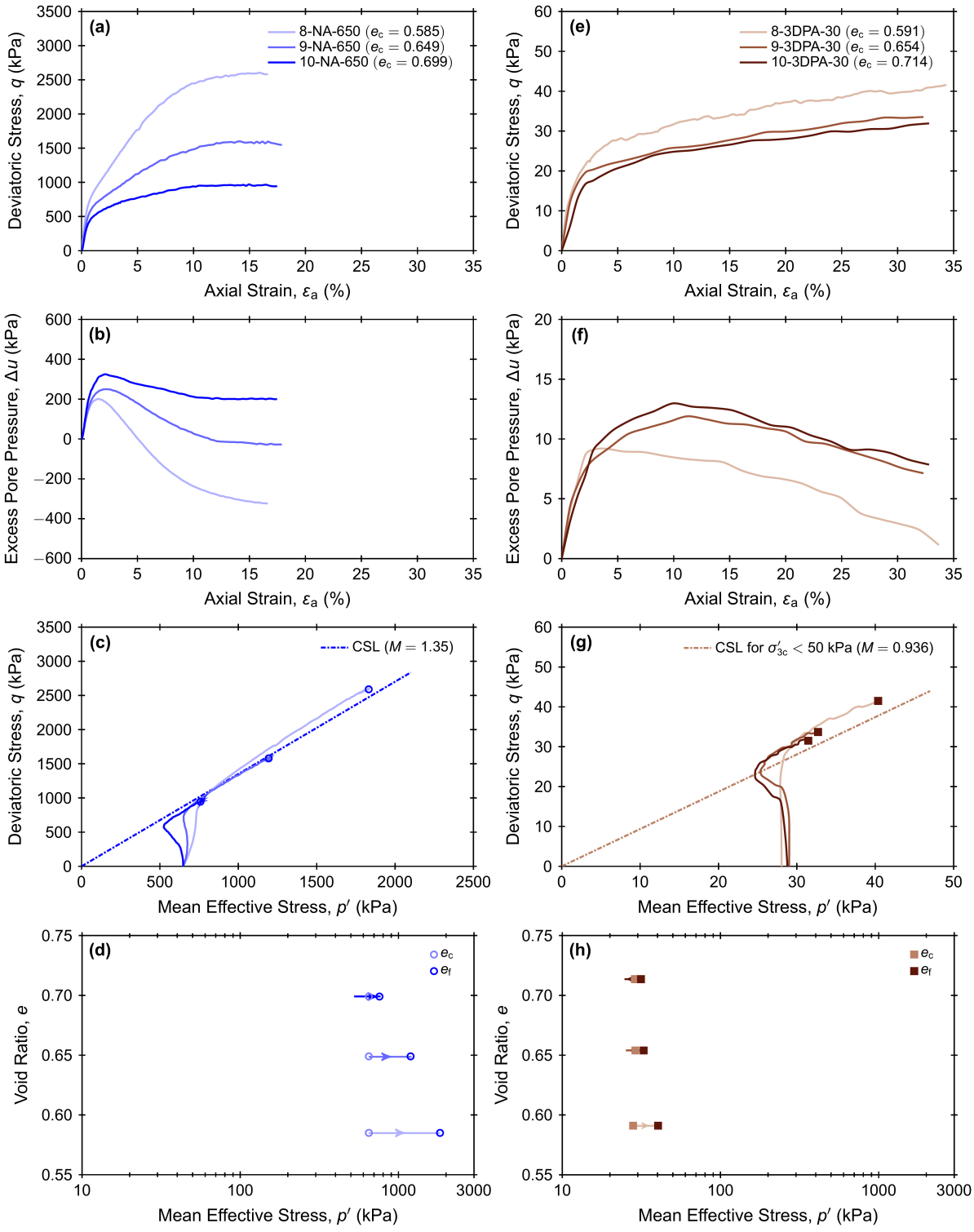

Figure 3.11: Undrained behavior of (a-d) natural angular sand and (e-h) 3D printed angular sand

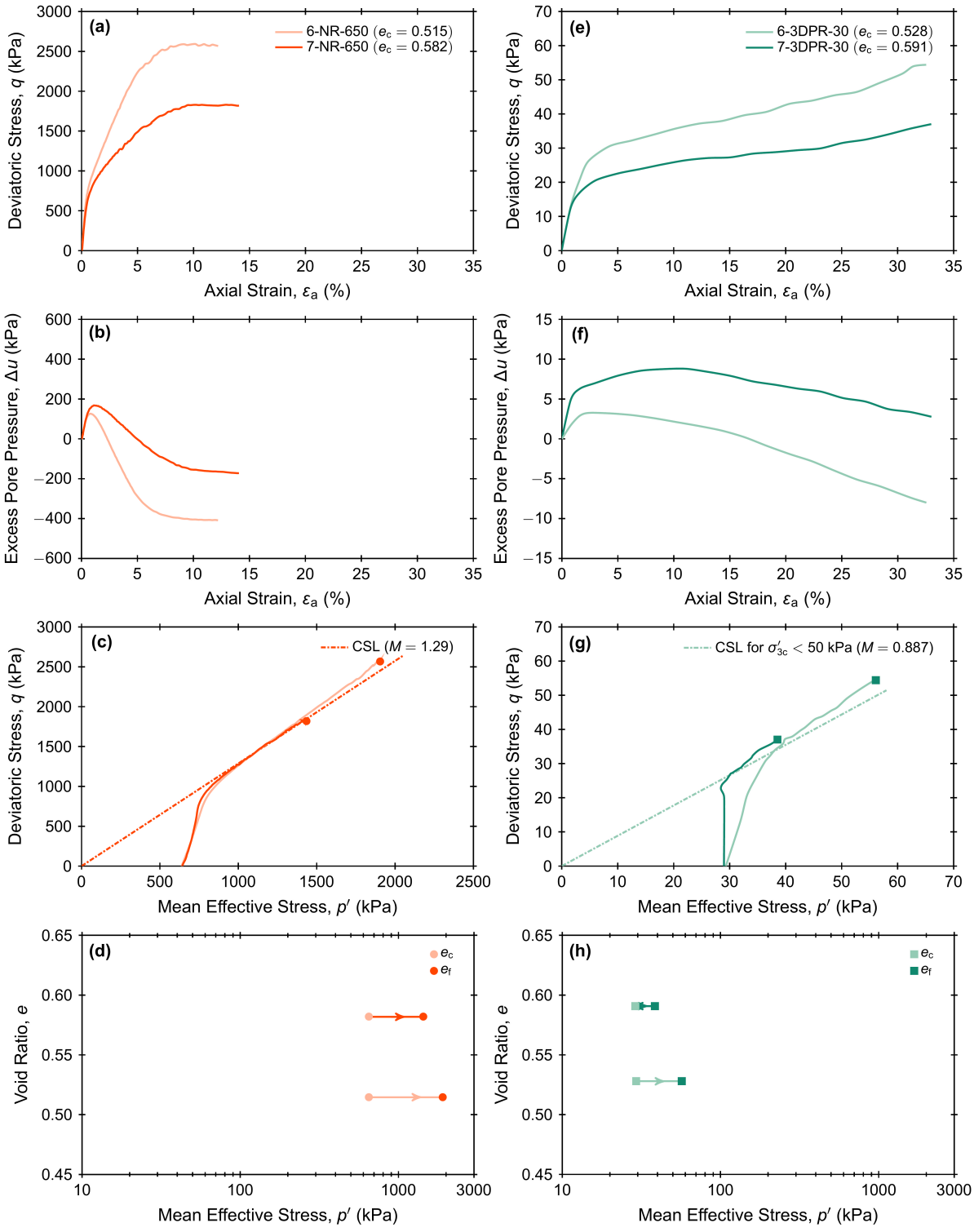

Figure 3.12: Undrained behavior of (a-d) natural rounded sand and (e-h) 3D printed rounded sand

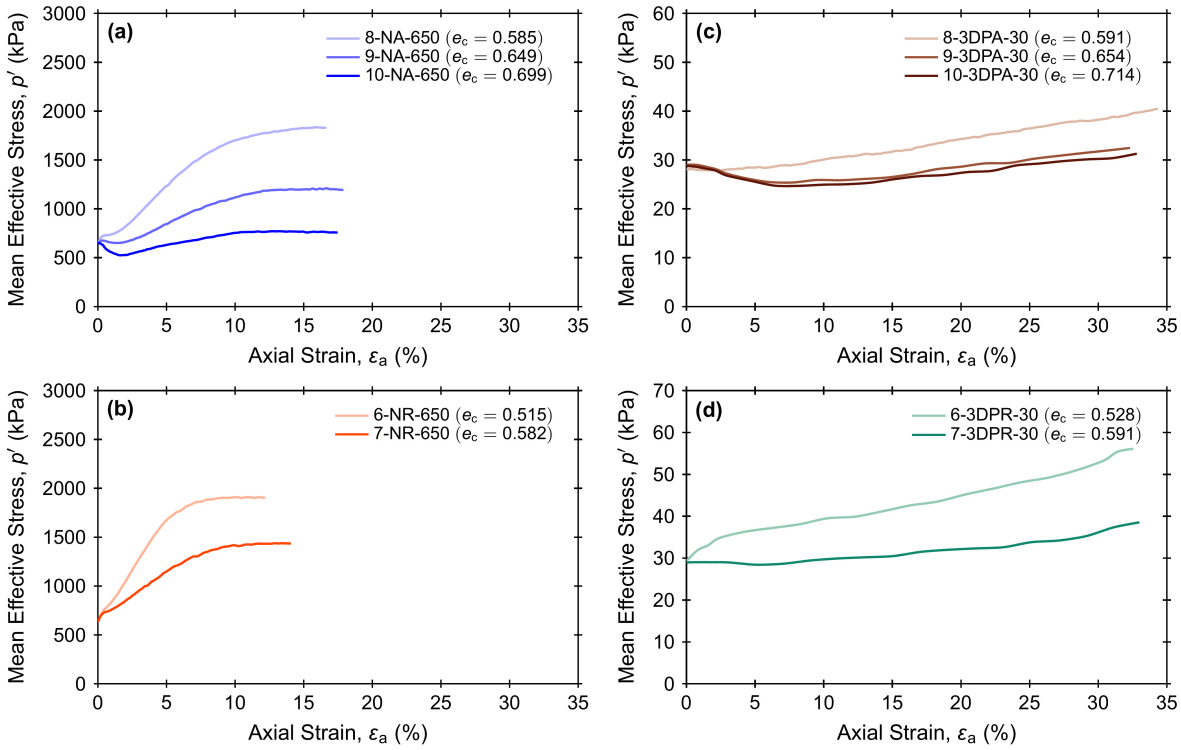

Figure 3.13: Mean effective stress evolution during undrained triaxial tests on (a) natural angular sand, (b) natural rounded sand, (c) 3D printed angular sand, and (d) 3D printed rounded sand

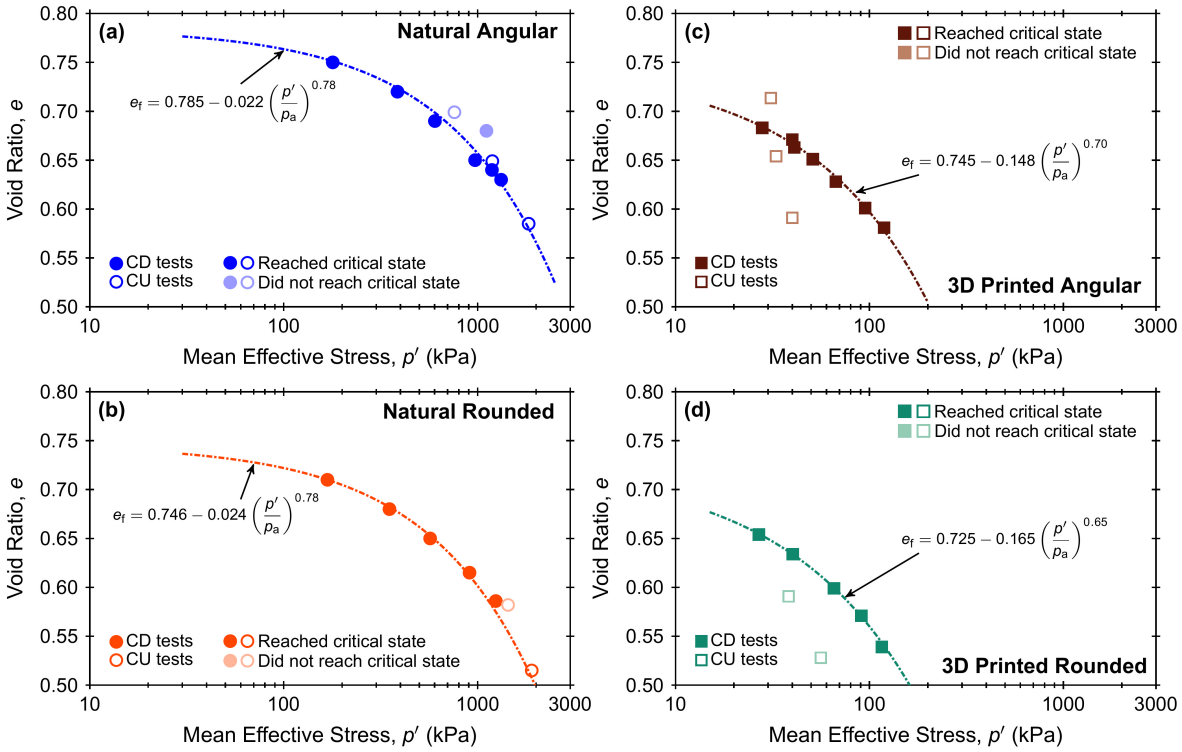

Figure 3.14: Critical state lines in $e - \log p'$ plane approximated for (a) natural angular sand, (b) natural rounded sand, (c) 3D printed angular sand, and (d) 3D printed rounded sand

3.10 Supplementary Information and Figures

The extrapolation procedure to obtain the critical state (CS) parameters (final void ratio, e_{f}, and stress ratio, R_{f}) from drained (CD) tests is based on the assumption that dilatancy, D, converges to a value of 1 at the critical state [Zhang et al., 2018]. The procedure is exemplified taking test "2-NA-200" as the reference. First, void ratio, e, and stress ratio, R, are plotted against dilatancy, D, as shown in Figs. 3.15a and 3.15b, respectively. Then, the $e - D$ and $R - D$ curves are extrapolated linearly to a value of $D = 1$, and the intercepts are considered as e_{f} and R_{f}, respectively. Since σ'_3 remains constant in drained tests, $q_{\mathrm{f}}$and p'_{f} can be calculated from the extrapolated R_{f}. The extrapolated CS data of "2-NA-200" are $e_{\mathrm{f}} = 0.715$, $R_{\mathrm{f}} = 3.77$, $q_{\mathrm{f}} = 554$ kPa, and $p'_{\mathrm{f}} = 385$ kPa.

The CS points from the undrained (CU) tests are obtained assuming that the rate of change of excess pore pressure ($\delta u/\delta\varepsilon_{\mathrm{a}}$) converges to 0 at the critical state [Torres-Cruz and Santamarina, 2020]. As shown in Fig. 3.15c, stress ratio ($\eta = q/p'$) is plotted against $\delta u/\delta\varepsilon_{\mathrm{a}}$ for the test "8-NA-650", and $\eta_{\mathrm{f}} = 1.41$ by linear extrapolation when $\delta u/\delta\varepsilon_{\mathrm{a}} = 0$. Then, the data obtained from the test are plotted in $q - p'$ plane space and, assuming that the critical state stress ratio $\eta_{\mathrm{f}} = 1.41 = M$, the critical state line (CSL) is plotted. The $q - p'$ curve is then extrapolated to the CSL (Fig. 3.15d), and values of $q_{\mathrm{f}} = 2586$ kPa and $p'_{\mathrm{f}} = 1835$ kPa are obtained with $e_{\mathrm{f}} = 0.585$, which remains constant during undrained shearing.

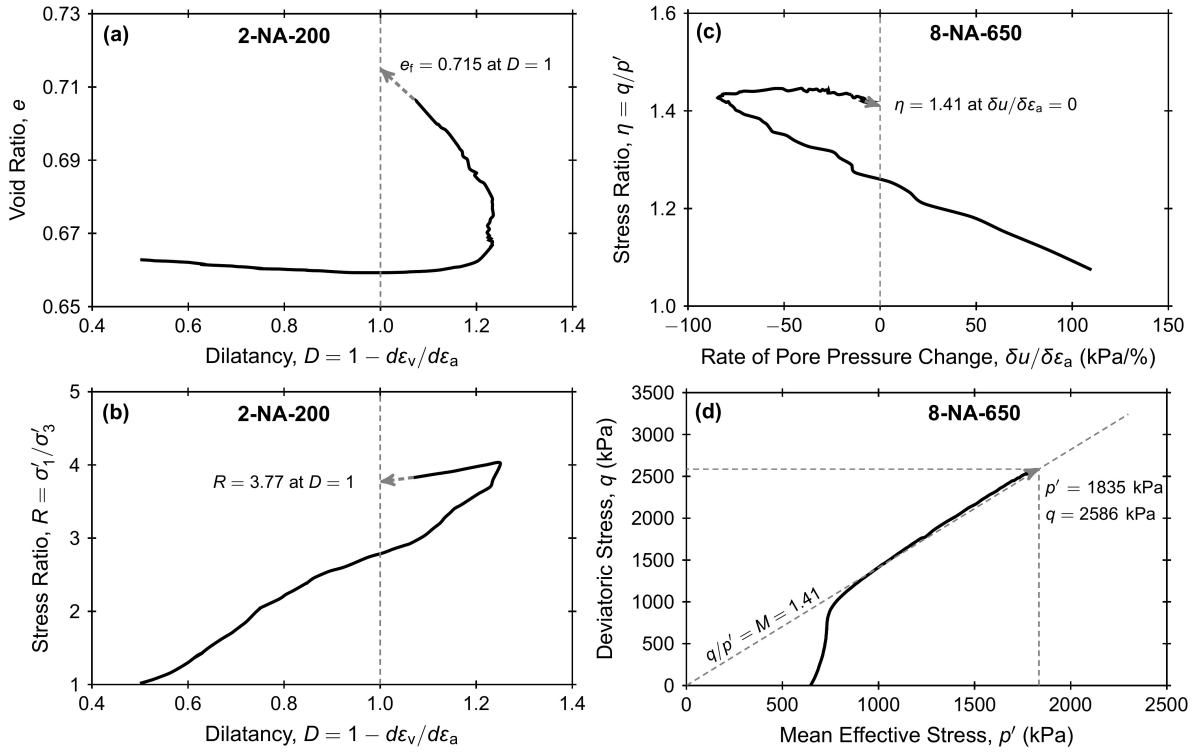

Figure 3.15: Example of extrapolation procedure employed to obtain the final void ratio and stress ratio from (a, b) CD tests and (c, d) CU tests

Chapter 4

Effects of Particle Shape on the Shear Wave Velocity and Shear Modulus of 3D Printed Sand Analogs

Author's Note: At the time of the present Dissertation, this paper is under review in the *Open Geomechanics* Journal under the following citation and is presented herein with minor edits.

Ahmed, S. S., & Martinez, A. (2021). Effects of Particle Shape on the Shear Wave Velocity and Shear Modulus of 3D Printed Sand Analogs. *Open Geomechanics*, Under Review.

4.1 Abstract

Isolating the effects of individual particle properties (e.g. shape, size, mineralogy, surface roughness) on the mechanical behavior of naturally occurring coarse-grained soils is a significant challenge in experimental studies. This challenge can be addressed by recent advances in 3D printing technology which enable generation of artificial sand-sized particles with independent control over particle size and shape. In this study, bender element tests are conducted to examine the isolated effects of particle shape on the shear wave velocity and shear modulus of 3D printed sand analogs. The experimental results show that the shear wave velocity and shear modulus of the 3D printed sand specimens exhibit a relationship with mean effective stress that is in agreement to that reported for natural sands. The

specimens composed of 3D printed sands with greater particle roundness and sphericity exhibit greater shear wave velocity and shear modulus for a given void ratio, relative density, and mean effective stress. The changes in shear wave velocity can be captured in terms of differences in individual particle shape parameters such as roundness and sphericity as well as combined particle shape parameters such as regularity. Regression analysis is used to develop relationships between shear wave velocity and particle shape parameters and void ratio, which are shown to be in agreement with previously-published relationships and to reliably predict the shear wave velocity of natural sands. The results presented herein highlight the usefulness of testing 3D printed soils to identify functional trends and dependencies between soil response parameters and intrinsic properties. However, this requires verification of the results against published trends and assessment of the possible effects of the differences in constituent material between the 3D printed and the natural soils.

4.2 Introduction

Inherent particle properties such as shape, gradation, surface texture and constituent material stiffness control the global mechanical behavior of granular soils [Santamarina, 2003]. Extending the understanding of the effects of individual particle properties on the behavior of soils could aid in the advancement of constitutive models as well as in the increased efficiency and robustness of geotechnical site characterization and design methodologies. A number of previous investigations have examined the effects of different particle properties on the engineering properties of coarse-grained soils, such as friction angle [e.g. Kirkpatrick, 1965; Marschi et al., 1972; Wang et al., 2013; Vangla and Latha, 2015; Xiao et al., 2019; Altuhafi et al., 2016] and shear wave velocity (V_s) and small-strain modulus (G_{max}) [e.g. Iwasaki and Tatsuoka, 1977; Chang and Ko, 1982; Menq, 2003; Sharifipour et al., 2004; Cho et al., 2006; Bartake and Singh, 2007; Bui, 2009; Patel et al., 2009; Wichtmann and Triantafyllidis, 2009; Senetakis et al., 2012; Yang and Gu, 2013; Hussien and Karray, 2015; Altuhafi et al., 2016; Payan et al., 2016b,a; Liu and Yang, 2018; Dutta et al., 2020; Liu

et al., 2021]. Regarding the small-strain behavior, some studies have reported increases in V_s with decreases in the median particle size (D_{50}) [Bartake and Singh, 2007; Patel et al., 2009]. Conversely, other studies such as Iwasaki and Tatsuoka [1977], Wichtmann and Triantafyllidis [2009], and Yang and Gu [2013] observed no significant effect of D_{50} on V_s, whereas Chang and Ko [1982], Menq [2003], Sharifipour et al. [2004], Bui [2009], and Hussien and Karray [2015] reported an increase in V_s with increasing D_{50}. Regarding the effects of particle shape, Cho et al. [2006], Bui [2009], Patel et al. [2009], and Lee et al. [2017] reported an increase in V_s and G_{max} with increasing particle roundness. However, Altuhafi et al. [2016], Liu and Yang [2018], and Liu et al. [2021] observed a decrease in small strain stiffness with increasing particle roundness.

These conflicting observations highlight the significant challenges in isolating the effects of individual particle properties and state on the response of natural soils. For instance, V_s has been shown to depend on particle size, shape, surface roughness, mineralogy, and void ratio [e.g. Cho et al., 2006; Otsubo et al., 2015]. Also, there are different parameters that have been used to characterize a given particle properties, and it is often unclear which one better caputre the aspects of soil behavior that govern the properties of interest. For example, particle shape can be characterized in terms of roundness, sphericity, and regulatity. Despite the aforementioned challenges, several studies have used synthetic soils or natural soil mixtures to isolate the effect of individual particle properties on soil response [e.g. Xiao et al., 2019].

3D printing technology has advanced rapidly in the last decade, offering a solution for the individual control of particle properties. The current technological capabilities can be used to generate artificial soil analogs with independent control over particle size, shape, and gradation [e.g. Hanaor et al., 2016; Adamidis et al., 2020]. Recent studies have used 3D printing technology to generate analog particles of different sizes and shapes, and showed that these analogs can successfully replicate the morphology of natural particles [e.g. Miskin and Jaeger, 2013; Athanassiadis et al., 2014; Hanaor et al., 2016; Adamidis et al., 2020;

Ahmed and Martinez, 2020; Su et al., 2020]. Results of triaxial tests on 3D printed particles show that they exhibit stress-dilatancy behavior similar to that typical of natural soils [e.g. Hanaor et al., 2016; Adamidis et al., 2020; Matsumura et al., 2017; Ahmed and Martinez, 2021], and the interpretation of their mechanical response can be captured with the critical state soil mechanics framework [Ahmed and Martinez, 2021]. However, the 3D printed sands have a greater compressibility owing to the smaller stiffness of their polymeric constituent material. The V_s and G_{max} of 3D printed particles obtained by bender element tests have also show a dependency on mean effective stress similar to that of natural sands [Ahmed and Martinez, 2020]. Other applications of 3D printed analogs include investigation of the frictional behavior of faults [Braun et al., 2021], effect of particle shape on clogging and discharge [Hafez et al., 2021], calibration of DEM simulations [Kittu et al., 2019; Peerun et al., 2021], permeability of uniformly graded soil [Adamidis et al., 2020; Wei et al., 2021], and development of transparent soil surrogates [Li et al., 2021]. These results highlight the usefulness of 3D printed synthetic soils as soil analogs that provide accurate control of their properties. Further, the conclusions of some of these studies show that they exhibit many of the similar behaviors and functional trends as natural soils despite of the smaller stiffness of the 3D printed soils.

The goal of this investigation is to examine the isolated effects of various particle shape parameters on the V_s and G_{max} of coarse-grained soils. To do so, seven 3D printed sands with different particle shape parameters but similar particle size distributions were generated. Then, measurements of V_s and G_{max} were obtained in specimens composed of the 3D printed particles subjected to different magnitudes of isotropic confining effective stress. The trends obtained in this investigation are then compared to published relationships to assess consistency in the results.

4.3 Materials and Methods

4.3.1 3D Printing Technology

Rapid advances in 3D printing technology have developed different methods and materials in recent years. Modern 3D printers can be used to create complex objects using methods such as fused deposition modeling (FDM), stereolithography (SLA), digital light processing (DLP), and selective laser sintering (SLS) using polymeric, metallic, or ceramic materials, resulting in a wide range of precision and cost. While specialized 3D printers can mix materials on demand to achieve the desired mechanical properties and aesthetics to produce highly complex models [Najmon et al., 2019; Jiménez et al., 2019], typical desktop 3D printers are limited to printing polymeric materials. These more economic printers typically print layers with a thickness as low as 10 μm and have a lateral resolution in the order of 20 to 40 μm [Ngo et al., 2018].

This study used the polyjet 3D printing technology that offers relatively economical and fast manufacturing of small parts with high accuracy [Ahmed and Martinez, 2020; Kittu et al., 2019; Adamidis et al., 2020; Wei et al., 2021]. A polyjet printer has two print heads that deposit different liquid photopolymer resins. One resin generates the desired object while the other acts as the support structure, and both resins are hardened by ultraviolet laser. Once the printing is completed, the support structure is removed by water jetting and chemical treatment using a 2% sodium hydroxide solution. Detailed description of the polyjet technology and its use to generate sand particles is provided in Ahmed and Martinez [2020, 2021] (Chapters 2 and 3).

4.3.2 3D Printed Sands

Particle shape can be described by roundness and sphericity parameters, which can be defined in different ways [Mitchell et al., 2005; Guida et al., 2020]. This study considers the Wadell roundness (R) [Wadell, 1932], circle ratio sphericity (S_{C}), perimeter sphericity

(S_{P}), width-to-length ratio sphericity (S_{WL}) and convexity (C) [Mitchell et al., 2005; Altuhafi et al., 2016]. For this investigation, four materials were generated using the method proposed by Wei et al. [2018] that uses spherical harmonics to create random 3D shapes based on the desired shape features (mixes 3, 6, 7, and 8 in Fig. 4.1a, Tables 4.1 and 4.2). These four materials were designed to have a D_{50} of 2.5 mm and a C_{u} of 1.26 (Table 4.2). To extend the range of particle shape parameters considered in this investigation, the three 3D printed mixes used by Ahmed and Martinez [2020, 2021] were also tested. Two of these mixes (mix 2 and 4) were generated from the X-ray CT scans of representative rounded and angular natural sand particles, respectively, as described by Ahmed and Martinez [2020] (Fig. 4.1b, Tables 4.1 and 4.2). The D_{50} and C_{u} of these materials are 3.2 mm and 1.47, respectively. The last mix (mix 1) consisted of spheres with a D_{50} of 3.2 mm and a C_{u} 1.0.

All the particles were generated using an *Objet Eden 260V* printer from Stratasys with *VeroWhitePlus* rigid acrylate-based polymer resin with a horizontal printing resolution of 30 μm. The hardened polymer resin has a Young's modulus of 2.4 GPa, Poisson's ratio of 0.3, and specific gravity of 1.18. The polyjet 3D printing process produces a surface roughness that is greater than that typical of natural soil particles [Ahmed and Martinez, 2021] (Chapter 3). Due to the smaller Young's modulus and the greater surface roughness, the stiffness of the interparticle contacts between 3D printed particles is smaller compared to that for natural sands. Figure 4.2 shows the results of interparticle uniaxial compression tests performed on spherical polyjet particles by Ahmed and Martinez [2020] (Chapter 2). The results show that initial increases in force result in a soft contact response due to plastic yielding of the particles' micro-asperities. As the load is increased, the contact becomes stiffer and follows the Hertzian solution more closely. Another important difference between the polyjet particles and natural sand particles is the magnitude and anisotropy of the friction coefficient of the former. Ahmed and Martinez [2020, 2021] (Chapters 2 and 3) provide a detailed description of the compressive and frictional contact response of polyjet particles.

The roundness and sphericities of the printed particles were obtained from image

analysis using the code by Zheng and Hryciw [2015], and the convexity was obtained using the solidity function in Matlab. The analysis of results also considered three combined shape parameters: regularity (R_{G}), overall regularity (OR) and shape-angularity group indicator ($SAGI$). Regularity of a particle is the average of R and S_{C} [Cho et al., 2006], overall regularity is the average of R, S_{P}, S_{WL} and C [Liu and Yang, 2018] and $SAGI$ is defined by the relationship $SAGI = 5.4(1 - S_{\mathrm{WL}}) - 67.8(1 - C) - 77.9(1 - S_{\mathrm{P}})$ [Altuhafi et al., 2016]. The maximum and minimum void ratios of all the mixes were determined using the methods outlined in Carey et al. [2020] and are provided in Table 4.2. Figure 4.3 shows the variation of $e_{\max}$ and $e_{\min}$ with particle R, S_{P}, and R_{G}. These parameters were selected to allow for comparison with published relationships from Youd [1973] and Cho et al. [2006]. As shown, the measurements indicate a decrease in $e_{\max}$ and $e_{\min}$ as roundness, circle ratio sphericity and regularity are increased, which is consistent with the trends from literature. For the relationship with R, the $e_{\max}$ and $e_{\min}$ measurements fall in between the relationships from Youd [1973] and Cho et al. [2006] (Fig. 4.3a); however, the trends reported by Cho et al. [2006] indicate a steeper decrease as S_{C} and R_{G} are increased (Figs. 4.3b and 4.3c).

4.3.3 Bender Element Test

Bender element (BE) tests were conducted on specimens with a diameter of 70 mm and a height between 65 and 76 mm contained in a latex membrane of 0.3 mm in thickness. Specimens with initial void ratios (e_0) of 0.55 ± 0.02, 0.60 ± 0.02 and 0.65 ± 0.02 were prepared for the seven sand mixes, which corresponded to relative densities (D_{R}) between 80% and 30%. The BE tests were performed under isotropic confining pressures (p') from 10 to 80 kPa applied by vacuum. BEs attached to the specimen top and bottom caps were used to send and receive S-waves. V_{s} values were calculated using the travel time of the S-waves and the distance between the BEs. The initial rise of the signal (i.e. the time when a signal first crosses the x-axis) was taken as the wave arrival time [Yamashita et al., 2009]. Ahmed and Martinez [2020] provide further information on the testing setup and results

interpretation methodology. Figure 4.4 shows typical transmitter and receiver BE signals at different p'.

4.4 Results

4.4.1 Shear Wave Velocity and Small-Strain Modulus Measurements

The V_s of the specimens composed of all seven materials increased as p' was increased and e_0 was decreased, in agreement with trends for natural soils [e.g. Hardin and Richart Jr, 1963; Cho et al., 2006] as shown in Figs. 4.5a, 4.5b and 4.5c for e_0 of 0.55 ± 0.02, 0.60 ± 0.02 and 0.65 ± 0.02, respectively. The V_s for any given p' and e_0 combination increased as the particle roundness and sphericity were increased. For example, the mix with the greatest roundness and sphericity (mix 1) has the greatest V_s whereas the mix with the smallest roundness and sphericity (mix 7) has the smallest V_s. The dependency of V_s on particle shape is discussed in more detail in the following section.

The dependency of V_s on p' can be expressed by the following power-law equation [Lee and Stokoe, 1986]:

$$V_s = \alpha \left(\frac{p'}{1 \text{ kPa}} \right)^{\beta} \tag{4.1}$$

where α is the shear wave velocity (m/s) at p' of 1 kPa and β reflects the sensitivity to changes in p'. Values of α-coefficients and β-exponents for all the 3D printed sands were obtained by fitting power functions (Fig. 4.6a). As shown, the α-coefficient generally increased and the β-exponent generally decreased as the e_0 decreased, in agreement with trends reported by Cha et al. [2014]. The values of the α-coefficients ranged between 90 and 124 m/s whereas the values of the β-exponents ranged between 0.2025 and 0.2216. The α-coefficient and β-exponent obtained in this study are within the range of those for natural sands (Fig. 4.6b) [Cha et al., 2014]. Analytical relationships for the β-exponents indicate values of 0.167

for a Hertzian contact and of 0.25 for particles experiencing contact yield. The β-exponents obtained in this investigation are within this range possibly due to local asperity yielding and particle rearrangement caused by the increases in p', as expected for natural sands [Cascante and Santamarina, 1996].

Small-strain shear modulus values were calculated using the relation $G_{\max} = \rho V_s^2$, where ρ is the specimen total density (Figs. 4.5d, 4.5e and 4.5f). It is noted that the $G_{\max}$ values reported are smaller than those typical of natural sands due to the smaller specific gravity of the 3D printed sands (1.18 compared to 2.65 to 2.7 for silica sands). The relationship between $G_{\max}$ and p' can be represented by the following power-law equation [Hardin and Richart Jr, 1963]:

$$G_{\max} = AF(e)\left(\frac{p'}{1\text{ kPa}}\right)^n \tag{4.2}$$

where A is a coefficient that depends on the particle arrangement and elastic properties of constituent material, $F(e)$ is the function of e_0 as described by Hardin and Richart Jr [1963], and n describes the sensitivity to changes in p'. Figure 4.6c shows the A and n values obtained by fitting power functions. As shown, the A-coefficient generally increased and the n-exponent generally decreased as e_0 was decreased. The n-exponents for all the specimens range between 0.4235 and 0.4630, which are greater than the value of 0.33 for the Hertz solution, in agreement with those reported in literature [e.g. Chung et al., 1984; Hardin and Black, 1966].

The V_s of the specimens composed of all seven mixes are also evaluated for specimens of similar relative density to account for differences in $e_{\max}$ and $e_{\min}$ and state, as shown in Fig. 4.7. The results indicate the same trends as previously described in Figs. 4.5a, 4.5b, and 4.5c. Namely, V_s increased as p' and D_R were increased. For any given combination of p' and D_R , V_s increased as the particle roundness and sphericity were increased.

4.4.2 Effect of Particle Shape on Shear Wave Velocity and Small-Strain Modulus

The results presented in Fig. 4.5 allow for examination of the effects of particle shape on V_s for specific combinations of e_0 (or D_R) and p'. Such results are presented in Fig. 4.8 for a p' of 50 kPa and e_0 of 0.55 and 0.65. It is noted that the trends reported here are true for all other combinations of p' and e_0, which are not shown here for brevity. The results show that V_s increased as R (Figs. 4.8a and 4.8e), S_{WL} (Figs. 4.8b and 4.8f), S_C (Figs. 4.8c and 4.8g) and S_P (Figs. 4.8d and 4.8h) were increased for any given e_0. The correlation with V_s is strongest with the R parameter (R^2 between 0.89 and 0.90), followed by that with S_P and S_C (R^2 between 0.75 and 0.84) and weakest with S_{WL} (R^2 between 0.66 and 0.75). These differences imply that the R parameter is a stronger predictor of V_s, likely because this parameter reflects the radii of the particle asperities which in turn determine the stiffness of the inter-particle contact. This contrasts with the S_P, S_C, and S_{WL} parameters which capture the overall particle shape. Similar trends as reported for V_s were observed for G_{max} (shown in Fig. 4.13 in Supplementary Information), with an increase in G_{max} with increasing shape parameters and a stronger correlation between G_{max} and R. The shear wave velocity results can also be grouped according to their relative density, as shown in Fig. 4.14 in Supplementary Information. The results reveal similar trends, with V_s increasing with increasing R, S_{WL}, S_C and S_P and with increasing D_R for all stress levels.

The effects of particle shape on V_s are further examined using the combined shape parameters R_G, OR and $SAGI$. The results shown in Fig. 4.9 correspond to a p' of 50 kPa. As shown, V_s increased as R_G and OR were increased, and decreased as $SAGI$ was increased, in agreement with the trends in Fig. 4.8. Stronger correlations are observed between V_s and the combined shape parameters (R^2 between 0.90 and 0.98 for R_G, OR and $SAGI$) than between V_s and the individual shape parameters (R^2 between 0.66 and 0.90 for R, S_{WL}, S_C and S_P). These trends likely reflect the complex relationship between contact stiffness (and

thus V_s) and different aspects of particle shape; the combined shape parameters seem to better capture this complexity, at least phenomenologically. The G_{max} values show similar trends as described for V_s (shown in Fig. 4.15 in Supplementary Information), consisting of an increase of G_{max} with increases in R_G and OR and decreases in $SAGI$. The trends between V_s and the combined shape parameters are also true for specimens of similar D_R, as shown in Fig. 4.16 in the Supplementary Information, with R^2 values between 0.81 and 0.95.

The variation of α-coefficient and β-exponent values obtained from power-law fits (Eq. 4.1) with several of the shape parameters are presented in Figs. 4.10a to 4.10h. As shown, the α-coefficient increased as R, R_G and OR were increased, and decreased as $SAGI$ was increased for any given e_0 (Figs. 4.10a to 4.10d). This indicates an increase in the contact stiffness at a p' of 1 kPa as R, R_G and OR increase and as $SAGI$ decreases. Additionally, the α-coefficient increased as e_0 was decreased, as expected. Figures 4.10e, 4.10f, 4.10g and 4.10h indicate no clear trend between the β-exponent and the shape parameters; the β values appear to depend only on e_0. Comparison of these trends with published relationships is discussed in the following section. A similar analysis for the A-coefficient and n-exponent for the power-law fits for G_{max} (Eq. 4.2) are presented in Fig. 4.17 in the Supplementary Information. These results indicate similar trends, with increases in A as R, R_G and OR increase and as $SAGI$ decreases, and no clear influence of the shape parameters on n. However, both parameters show dependence on e_0.

Several published studies show an increase in V_s and α, and a decrease in β as particle roundness, sphericity, and regularity are increased [Cho et al., 2006; Bui, 2009; Patel et al., 2009; Lee et al., 2017]. However, other studies report a decrease in small-strain stiffness with increases in roundness, sphericity, and regularity [Shin and Santamarina, 2013; Altuhafi et al., 2016; Liu and Yang, 2018; Liu et al., 2021]. A reason that may lead to these conflicting observations include differences in testing configurations and interpretation methods used to obtain shear wave velocity measurements. Another reason is the intertwined effects of

different particle and soil properties and whether these were considered in the aforementioned studies. In particular, the latter may be an important consideration as D_{50}, C_{u}, e_0, and mineralogy have all been shown to affect shear wave velocity magnitudes [e.g. Menq, 2003; Sharifipour et al., 2004; Hussien and Karray, 2015]. For example, Cho et al. [2006] does not recognize the effect of e_0 in the V_{s}, α, and β values. While Altuhafi et al. [2016] found an increase in G_{max} with increasing $SAGI$, the authors also report a weak increase in G_{max} with increasing particle surface roughness (S_{q}), which in turn increases with $SAGI$. This is, however, in contrast with results from analytical solutions and other experimental results, indicating a decrease in G_{max} with increasing S_{q} [e.g. Otsubo et al., 2015]. Indeed, Liu and Yang [2018] discuss aspects leading to uncertainty in establishing relationships between particle shape parameters and G_{max} associated with the aforementioned inter-relationships. These inter-dependencies among particle shape parameters, their influence on soil void ratio and density, and their aggregated effects on V_{s} further highlight the usefulness of allowing for individual control of particle properties, as enabled by the 3D printing technology.

4.5 Discussion

4.5.1 Relationships Between Shear Wave Velocity and Shape Parameters

The results of bender element tests indicate a dependency of the shear wave velocity on the different particle shape parameters and the initial void ratio. To quantify these interrelationships and to compare to published equations developed based on natural sands, a linear regression analysis was performed to determine an empirical relationship between V_{s} and a specific shape parameter and e_0. Here, the R parameter is considered due to its widespread use in literature and the R_{G}, OR and $SAGI$ parameters are considered due to their stronger correlations with V_{s} (i.e. Fig. 4.9). It is noted that the regression analysis can also consider D_{R} instead of e_0; the former would capture the effect of state in relation to the extreme void ratios of a given soil while the latter captures the effects of absolute

density and coordination number. In the regression analysis, V_s (m/s) was defined according to Eq. 4.1. Based on the results presented in Figs. 4.10a to 4.10h, α can be defined in terms of different particle shape parameters and e_0, and β is a function of e_0 only. α and β are expressed as:

$$\alpha = 26.8(R) - 210(e_0) + 220 \tag{4.3}$$

$$\alpha = 34.5(R_G) - 210(e_0) + 213 \tag{4.4}$$

$$\alpha = 61.7(OR) - 210(e_0) + 185 \tag{4.5}$$

$$\alpha = -2.2(SAGI) - 210(e_0) + 243 \tag{4.6}$$

$$\beta = 0.25(e_0) + 0.0724 \tag{4.7}$$

The equations reflect linear relationships between α and the different shape parameters and e_0, and a linear relationship between β and e_0. The following discussion is limited to the R and R_G shape parameters due to their widespread use in the literature. Correlations between α and β with R and R_G have been previously published by Cho et al. [2006]; a comparison of these relationships with those provided in Eqs. 4.3, 4.4 and 4.7 are shown in Figs. 4.11a to 4.11f. While Cho et al. [2006] did not consider the effect of e_0 on α, the predicted values are generally consistent with one another. Namely, the values predicted by the Cho et al. [2006] equation are smaller than those predicted by Eqs. 4.3 and 4.4 for e_0 of 0.55 and 0.65. If a greater e_0 value of 0.80 is considered, the predictions between the Cho et al. [2006] equation and Eqs. 4.3 and 4.4 are close to one another (Figs. 4.11a and 4.11b). However, it is noted that this falls outside of the range of e_0 values considered in the experiments on 3D printed sands. Cha et al. [2014] indicated an increase in α with decreases in e_0, which is in agreement with Eqs. 4.3 and 4.4 and the results shown in Figs. 4.10a, 4.10b, 4.10c and 4.10d. While Cha et al. [2014] did not provide an equation between in α and e_0, they suggest so by their relationship between α and the coefficient of compression (C_c), which is known to have a strong dependency on e_0 [Vesić and Clough, 1968].

Cho et al. [2006] also provided an equation between the β-exponent and R and R_G without consideration of the effect of void ratio. However, Cha et al. [2014] report a decrease in β with decreases in void ratio, in agreement with Eq. 4.7. Figures 4.11c and 4.11d shows that the values predicted by Eq. 4.7 are within the range of the values predicted by the Cho et al. [2006] equation, with closer agreement at greater void ratios for small roundness values and at smaller void ratios with larger roundness values. Considering the decrease in limiting void ratios of sand with increasing particle roundness and regularity (i.e. as reported by Youd [1973] and Cho et al. [2006] and shown in Fig. 4.3), it is possible that the Cho et al. [2006] equation and Eq. 4.7 highlight similar trends. Namely, an increase in roundness causes a decrease in the void ratio values that a soil can take. This decrease in e_0 may cause a concomitant decrease in the β-exponent. Indeed, Patel et al. [2009] provided an equation for V_s that explicitly considers e_{max} and e_{min} in addition to other particle shape and size parameters. Equations 4.3, 4.4 and 4.7 can be manipulated to write the following :

$$\beta = 0.032R - 0.0012\alpha + 0.335 \tag{4.8}$$

$$\beta = 0.041R_G - 0.0012\alpha + 0.327 \tag{4.9}$$

As shown, the equations are independent of e_0 but dependent on the particle shape parameters. Figures 4.11e and 4.11f shows inverse relationship between α and β. The figures also provide the relationships presented by Cha et al. [2014] and Lee et al. [2017]. The predictions based on Eqs. 4.8 and 4.9 are in general agreement with the previously-published relationships, with slightly greater predicted β values likely due to the greater compressibility of the contacts of the 3D printed particles.

To further assess the applicability of Eqs. 4.1, 4.3, 4.4 and 4.7 to measurements on natural sands, values predicted using these equations are compared to those reported in the literature in Fig. 4.12. As shown, there is a close agreement between the predicted values and the experimental values reported by the authors, with the bulk of the data falling within the

±15% lines. This agreement, along with the comparisons between Eqs. 4.3, 4.4, 4.7, 4.8, and 4.9 provided in Fig. 4.11, suggests that relationships developed based on tests on 3D printed soils can capture the effects of particle shape and void ratio on the shear wave velocity of natural sands for the range of mean effective stresses considered in this investigation (i.e. 10 to 80 kPa).

4.5.2 Considerations on the Modeling of Sand Behavior with 3D Printed Particle Analogs

A significant advantage in using 3D printed soils is the ability to control particle shape while the remaining properties (i.e. particle size, constituent material, surface roughness) are maintained constant, which expand the experimental capabilities available to researchers. A similar procedure can be used to isolate the effects of particle size, as shown by Adamidis et al. [2020]. Despite this benefit, it is important to consider the possible effects of the smaller contact stiffness and greater bulk compressibility of the 3D printed particles in comparison to natural sands on the conclusions drawn from such studies. Comparisons of the measurements on 3D printed analogs with experimental data on natural soils and established relationships can help validate the conclusions drawn from such studies. However, it should be considered how inherent differences caused by the materials and layer deposition process used in 3D printing may affect different aspects of the behavior of granular materials. One such example is the direction-dependency of the friction coefficient of 3D printed particles [Ahmed and Martinez, 2021], which may affect properties such as the sand friction angle. It is envisioned that such differences in inherent properties will be addressed as the additive manufacturing technology enables generating objects with a broader suite of materials and processes.

4.6 Conclusion

An investigation on the effects of particle shape on the small-strain behavior of sands using seven 3D printed soils is presented. The synthetic particles were designed based on

spherical harmonics and on X-ray CT images from natural sands, allowing for careful control of the materials' particle shape parameters. The same polymeric material and additive manufacturing process was used to generate all the 3D printed materials, thus minimizing the differences in constituent material properties and particle surface roughness. Measurements based on bender element tests indicate an increase in V_s and G_{max} with increasing mean effective stress and decreasing void ratio, in agreement with trends reported for natural sands. The results also show an increase in V_s and G_{max} with increases in particle roundness, sphericity, and regularity for a given e_0, D_R, and p'.

Fitting the relationship between V_s and p' with a power law (i.e. Eq. 4.1) shows an increase in the α-coefficient with increases in the particle shape partameters R, S_P, S_C, S_{WL}, R_G, and OR and decreases in $SAGI$, as well as an increase in α with decreases in e_0. In contrast, the β-exponent was found to depend on e_0 but to be independent of the particle shape parameters. The correlations between V_s and the combined shape parameters R_G, OR, and $SAGI$ was shown to be stronger than with the individual shape parameters R, S_P, S_C and S_{WL}, likely because the former parameters better capture the effects of different aspects of particles (i.e. the shape of the corners as well as the overall particle shape). The results of this study are used to develop equations for the α-coefficient and β-exponent that consider their dependency on particle shape and e_0. These equations are shown to agree with published relationships and to predict the V_s values of natural sands with an error smaller than or equal to 15%. This close agreement suggests that 3D printed soils can be reliably used to model the small-strain behavior of natural sands. However, it is important to consider differences in the inherent behaviors of 3D printed and natural sands, such as the smaller contact stiffness of the 3D printed soils owing to the smaller Young's modulus of the polymer material.

4.7 Acknowledgment

This material is based upon work supported in part by the National Science Foundation (NSF) under award No. 1735732. Any opinions, findings, and conclusions or recommendations expressed in this material are those of the author(s) and do not necessarily reflect those of the NSF.

Bibliography

Adamidis, O., Alber, S., and Anastasopoulos, I. (2020). Assessment of three-dimensional printing of granular media for geotechnical applications. *Geotechnical Testing Journal*, 43(3).

Ahmed, S. S. and Martinez, A. (2020). Modeling the mechanical behavior of coarse-grained soil using additive manufactured particle analogs. *Acta Geotechnica*, 15(10):2829–2847.

Ahmed, S. S. and Martinez, A. (2021). Triaxial compression behavior of 3d printed and natural sands. *Granular Matter*, 23(4):1–21.

Altuhafi, F. N., Coop, M. R., and Georgiannou, V. N. (2016). Effect of particle shape on the mechanical behavior of natural sands. *Journal of Geotechnical and Geoenvironmental Engineering*, 142(12):04016071.

Athanassiadis, A. G., Miskin, M. Z., Kaplan, P., Rodenberg, N., Lee, S. H., Merritt, J., Brown, E., Amend, J., Lipson, H., and Jaeger, H. M. (2014). Particle shape effects on the stress response of granular packings. *Soft Matter*, 10(1):48–59.

Bartake, P. and Singh, D. (2007). Studies on the determination of shear wave velocity in sands. *Geomechanics and Geoengineering*, 2(1):41–49.

Braun, P., Tzortzopoulos, G., and Stefanou, I. (2021). Design of sand-based, 3-d-printed analog faults with controlled frictional properties. *Journal of Geophysical Research: Solid Earth*, 126(5):e2020JB020520.

Bui, M. T. (2009). *Influence of some particle characteristics on the small strain response of granular materials*. PhD thesis, University of Southampton.

Carey, T. J., Stone, N., and Kutter, B. L. (2020). Grain size analysis and maximum and minimum dry density testing of ottawa f-65 sand for leap-ucd-2017. In *Model tests and numerical simulations of liquefaction and lateral spreading*, pages 31–44. Springer.

Cascante, G. and Santamarina, J. C. (1996). Interparticle contact behavior and wave propagation. *Journal of Geotechnical Engineering*, 122(10):831–839.

Cha, M., Santamarina, J. C., Kim, H.-S., and Cho, G.-C. (2014). Small-strain stiffness, shear-wave velocity, and soil compressibility. *Journal of Geotechnical and Geoenvironmental Engineering*, 140(10):06014011.

Chang, N.-Y. and Ko, H.-Y. (1982). Effects of grain size distribution on dynamic properties and liquefaction potential of granular soils. Research Report R82-103, University of Colorado at Denver.

Cho, G.-C., Dodds, J., and Santamarina, J. C. (2006). Particle shape effects on packing density, stiffness, and strength: Natural and crushed sands. *Journal of Geotechnical and Geoenvironmental Engineering*, 132(5):591–602.

Chung, R. M., Yokel, F. Y., and Drnevich, V. (1984). Evaluation of dynamic properties of sands by resonant column testing. *Geotechnical Testing Journal*, 7(2):60–69.

Dutta, T., Otsubo, M., Kuwano, R., and O'Sullivan, C. (2020). Evolution of shear wave velocity during triaxial compression. *Soils and Foundations*, 60(6):1357–1370.

Guida, G., Viggiani, G. M., and Casini, F. (2020). Multi-scale morphological descriptors from the fractal analysis of particle contour. *Acta Geotechnica*, 15(5):1067–1080.

Hafez, A., Liu, Q., Finkbeiner, T., Alouhali, R. A., Moellendick, T. E., and Santamarina, J. C. (2021). The effect of particle shape on discharge and clogging. *Scientific Reports*, 11(1):1–11.

Hanaor, D., Gan, Y., Revay, M., Airey, D., and Einav, I. (2016). 3d printable geomaterials. *Géotechnique*, 66(4):323–332.

Hardin, B. O. and Black, W. L. (1966). Sand stiffness under various triaxial stresses. *Journal of the Soil Mechanics and Foundations Division*, 92(2):27–42.

Hardin, B. O. and Richart Jr, F. (1963). Elastic wave velocities in granular soils. *Journal of the Soil Mechanics and Foundations Division*, 89(1):33–65.

Hussien, M. N. and Karray, M. (2015). Shear wave velocity as a geotechnical parameter: an overview. *Canadian Geotechnical Journal*, 53(2):252–272.

Iwasaki, T. and Tatsuoka, F. (1977). Effects of grain size and grading on dynamic shear moduli of sands. *Soils and Foundations*, 17(3):19–35.

Jiménez, M., Romero, L., Domínguez, I. A., Espinosa, M. d. M., and Domínguez, M. (2019). Additive manufacturing technologies: an overview about 3d printing methods and future prospects. *Complexity*, 2019.

Kirkpatrick, W. (1965). Effects of grain size and grading on the shearing behaviour of granular materials. In *Proceedings of the sixth International Conference on Soil Mechanics and Foundation Engineering*, pages 273–277.

Kittu, A., Watters, M., Cavarretta, I., and Bernhardt-Barry, M. (2019). Characterization of additive manufactured particles for dem validation studies. *Granular Matter*, 21(3):1–15.

Lee, C., Suh, H. S., Yoon, B., and Yun, T. S. (2017). Particle shape effect on thermal conductivity and shear wave velocity in sands. *Acta Geotechnica*, 12(3):615–625.

Lee, S. and Stokoe, K. (1986). Investigation of low-amplitude shear wave velocity in anisotropic material. Geotechnical Engineering Report GR86-6, The University of Texas at Austin.

Li, Y., Zhou, H., Liu, H., Ding, X., and Zhang, W. (2021). Geotechnical properties of 3d-printed transparent granular soil. *Acta Geotechnica*, 16(6):1789–1800.

Liu, X. and Yang, J. (2018). Shear wave velocity in sand: effect of grain shape. *Géotechnique*, 68(8):742–748.

Liu, X., Zou, D., Liu, J., Zheng, B., Zhou, C., and Bai, J. (2021). A gradation-dependent particle shape factor for characterizing small-strain shear modulus of sand-gravel mixtures. *Transportation Geotechnics*, 28:100548.

Marschi, N. D., Chan, C. K., and Seed, H. B. (1972). Evaluation of properties of rockfill materials. *Journal of the Soil Mechanics and Foundations Division*, 98(1):95–114.

Matsumura, S., Kobayashi, T., Mizutani, T., and Bathurst, R. J. (2017). Manufacture of bonded granular soil using x-ray ct scanning and 3d printing. *Geotechnical Testing Journal*, 40(6):1000–1010.

Menq, F.-Y. (2003). *Dynamic properties of sandy and gravelly soils*. PhD thesis, The University of Texas at Austin.

Miskin, M. Z. and Jaeger, H. M. (2013). Adapting granular materials through artificial evolution. *Nature Materials*, 12(4):326–331.

Mitchell, J. K., Soga, K., et al. (2005). *Fundamentals of soil behavior*. John Wiley & Sons New York.

Najmon, J. C., Raeisi, S., and Tovar, A. (2019). Review of additive manufacturing technologies and applications in the aerospace industry. *Additive Manufacturing for the Aerospace Industry*, pages 7–31.

Ngo, T. D., Kashani, A., Imbalzano, G., Nguyen, K. T., and Hui, D. (2018). Additive manufacturing (3d printing): A review of materials, methods, applications and challenges. *Composites Part B: Engineering*, 143:172–196.

Otsubo, M., O'sullivan, C., Sim, W. W., and Ibraim, E. (2015). Quantitative assessment of the influence of surface roughness on soil stiffness. *Géotechnique*, 65(8):694–700.

Patel, A., Bartake, P., and Singh, D. (2009). An empirical relationship for determining shear wave velocity in granular materials accounting for grain morphology. *Geotechnical Testing Journal*, 32(1):1–10.

Payan, M., Khoshghalb, A., Senetakis, K., and Khalili, N. (2016a). Effect of particle shape and validity of gmax models for sand: A critical review and a new expression. *Computers and Geotechnics*, 72:28–41.

Payan, M., Khoshghalb, A., Senetakis, K., and Khalili, N. (2016b). Small-strain stiffness of sand subjected to stress anisotropy. *Soil Dynamics and Earthquake Engineering*, 88:143–151.

Peerun, M., Ong, D. E. L., Desha, C., Oh, E., and Choo, C. S. (2021). Advances in the study of micromechanical behaviour for granular materials using micro-ct scanner and 3d printing. In *International Conference of the International Association for Computer Methods and Advances in Geomechanics*, pages 911–918. Springer.

Santamarina, J. C. (2003). Soil behavior at the microscale: particle forces. In *Soil behavior and soft ground construction*, pages 25–56.

Senetakis, K., Anastasiadis, A., and Pitilakis, K. (2012). The small-strain shear modulus and damping ratio of quartz and volcanic sands. *Geotechnical Testing Journal*, 35(6):964–980.

Sharifipour, M., Dano, C., and Hicher, P.-Y. (2004). Wave velocities in assemblies of glass beads using bender-extender elements. In *17th ASCE Engineering Mechanics Conference*.

Shin, H. and Santamarina, J. C. (2013). Role of particle angularity on the mechanical behavior of granular mixtures. *Journal of Geotechnical and Geoenvironmental Engineering*, 139(2):353–355.

Su, Y. F., Lee, S. J., and Sukumaran, B. (2020). Influence of particle morphology

simplification on the simulation of granular material behavior. *Granular Matter*, 22(1):1–12.

Vangla, P. and Latha, G. M. (2015). Influence of particle size on the friction and interfacial shear strength of sands of similar morphology. *International Journal of Geosynthetics and Ground Engineering*, 1(1):6.

Vesić, A. S. and Clough, G. W. (1968). Behavior of granular materials under high stresses. *Journal of the Soil Mechanics and Foundations Division*, 94(3):661–688.

Wadell, H. (1932). Volume, shape, and roundness of rock particles. *The Journal of Geology*, 40(5):443–451.

Wang, J.-J., Zhang, H.-P., Tang, S.-C., and Liang, Y. (2013). Effects of particle size distribution on shear strength of accumulation soil. *Journal of Geotechnical and Geoenvironmental Engineering*, 139(11):1994–1997.

Wei, D., Wang, J., and Zhao, B. (2018). A simple method for particle shape generation with spherical harmonics. *Powder Technology*, 330:284–291.

Wei, D., Wang, Z., Pereira, J.-M., and Gan, Y. (2021). Permeability of uniformly graded 3d printed granular media. *Geophysical Research Letters*, 48(5).

Wichtmann, T. and Triantafyllidis, T. (2009). Influence of the grain-size distribution curve of quartz sand on the small strain shear modulus g max. *Journal of Geotechnical and Geoenvironmental Engineering*, 135(10):1404–1418.

Xiao, Y., Long, L., Matthew Evans, T., Zhou, H., Liu, H., and Stuedlein, A. W. (2019). Effect of particle shape on stress-dilatancy responses of medium-dense sands. *Journal of Geotechnical and Geoenvironmental Engineering*, 145(2):04018105.

Yamashita, S., Kawaguchi, T., Nakata, Y., Mikami, T., Fujiwara, T., and Shibuya, S. (2009). Interpretation of international parallel test on the measurement of gmax using bender elements. *Soils and Foundations*, 49(4):631–650.

Yang, J. and Gu, X. (2013). Shear stiffness of granular material at small strains: does it depend on grain size? *Géotechnique*, 63(2):165–179.

Youd, T. (1973). Factors controlling maximum and minimum densities of sands. In *Evaluation of Relative Density and its Role in Geotechnical Projects Involving Cohesionless Soils*, pages 98–112. ASTM International.

Zheng, J. and Hryciw, R. D. (2015). Traditional soil particle sphericity, roundness and surface roughness by computational geometry. *Géotechnique*, 65(6):494–506.

4.8 Tables and Figures

Table 4.1: Average and standard deviation (in parenthesis) of shape parameters of the 3D printed sand mixes

Soil specimen	Roundness, R	Circle ratio sphericity, S_{C}	Perimeter sphericity, S_{P}	Width-to-length ratio sphericity, S_{WL}	Convexity, C	Regularity, R_{G} [Cho et al., 2006]	Overall regularity, OR [Liu and Yang, 2018]	$SAGI$ [Altuhafi et al., 2016]
Mix 1	0.90 (0.09)	0.94 (0.01)	1.00 (0.00)	0.96 (0.02)	0.99 (0.00)	0.92 (0.05)	0.96 (0.02)	0.31 (0.30)
Mix 2	0.73 (0.09)	0.75 (0.10)	0.98 (0.02)	0.77 (0.11)	0.99 (0.00)	0.74 (0.08)	0.87 (0.04)	1.09 (0.99)
Mix 3	0.61 (0.12)	0.75 (0.04)	0.98 (0.01)	0.77 (0.04)	0.99 (0.00)	0.68 (0.07)	0.84 (0.04)	1.56 (0.57)
Mix 4	0.52 (0.13)	0.66 (0.10)	0.94 (0.03)	0.69 (0.13)	0.98 (0.01)	0.59 (0.08)	0.78 (0.05)	4.70 (1.93)
Mix 6	0.55 (0.13)	0.65 (0.05)	0.95 (0.01)	0.67 (0.06)	0.98 (0.01)	0.60 (0.07)	0.79 (0.04)	3.39 (1.23)
Mix 7	0.48 (0.12)	0.53 (0.04)	0.90 (0.02)	0.53 (0.04)	0.98 (0.01)	0.50 (0.06)	0.72 (0.03)	6.49 (1.96)
Mix 8	0.54 (0.11)	0.84 (0.04)	0.98 (0.01)	0.92 (0.05)	0.98 (0.00)	0.69 (0.07)	0.86 (0.03)	2.09 (0.95)

Table 4.2: Average and standard deviation (in parenthesis) of shape parameters of the 3D printed sand mixes.

Soil specimen	$e_{\max}$	$e_{\min}$	D_{50}	C_{u}	C_{c}
Mix 1	0.732 (0.037)	0.471 (0.016)	3.2	1.00	1.00
Mix 2	0.787 (0.036)	0.490 (0.004)	3.2	1.47	1.02
Mix 3	0.776 (0.008)	0.483 (0.008)	2.5	1.26	0.95
Mix 4	0.825 (0.008)	0.507 (0.006)	3.2	1.47	1.02
Mix 6	0.812 (0.013)	0.499 (0.011)	2.5	1.26	0.95
Mix 7	0.861 (0.012)	0.513 (0.005)	2.5	1.26	0.95
Mix 8	0.849 (0.027)	0.501 (0.009)	2.5	1.26	0.95

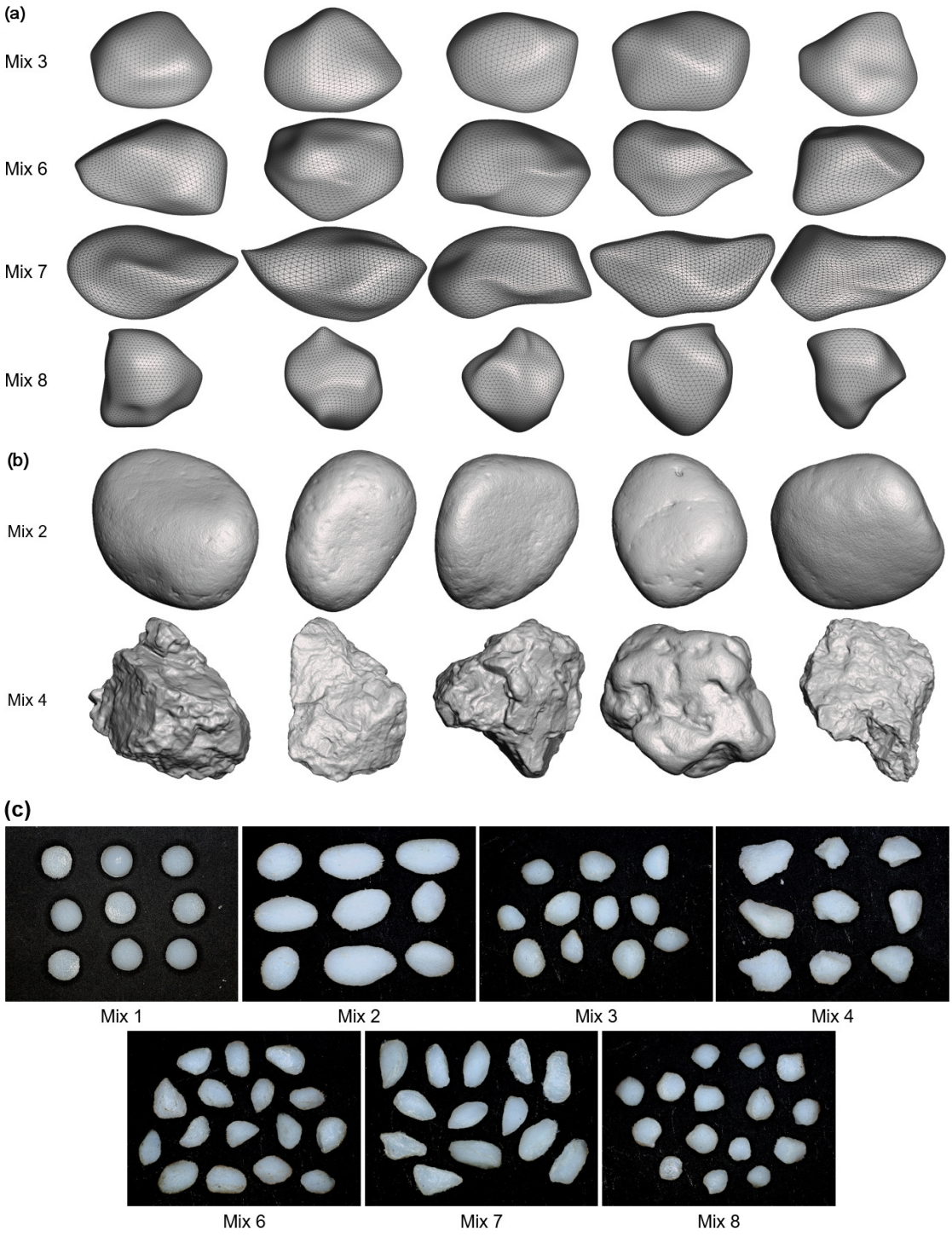

Figure 4.1: (a) 3D mesh of synthetic particles generated, (b) X-ray CT scans of mixes 2 and 4, and (c) 3D printed particles used in this study (not to scale). Note: mix 1 is composed of spheres; mixes 3, 6, 7 and 8 were created using spherical harmonics [after Wei et al., 2018]; and mixes 2 and 4 were generated from X-ray CT scans of rounded and angular sands, respectively.

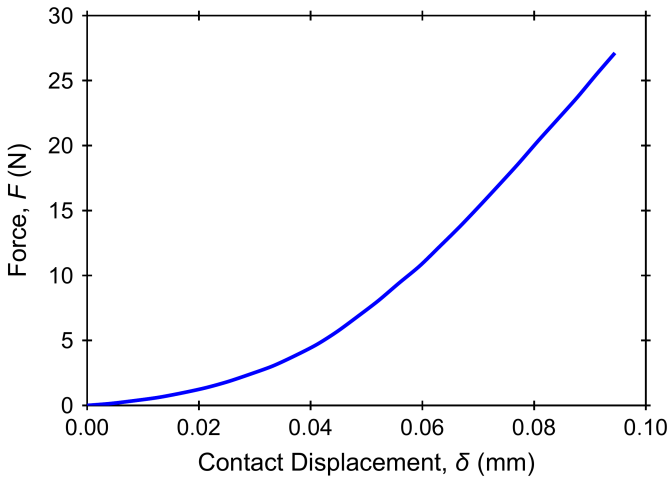

Figure 4.2: Uniaxial particle-particle compression test result on polyjet 3D printed equal-sized spheres.

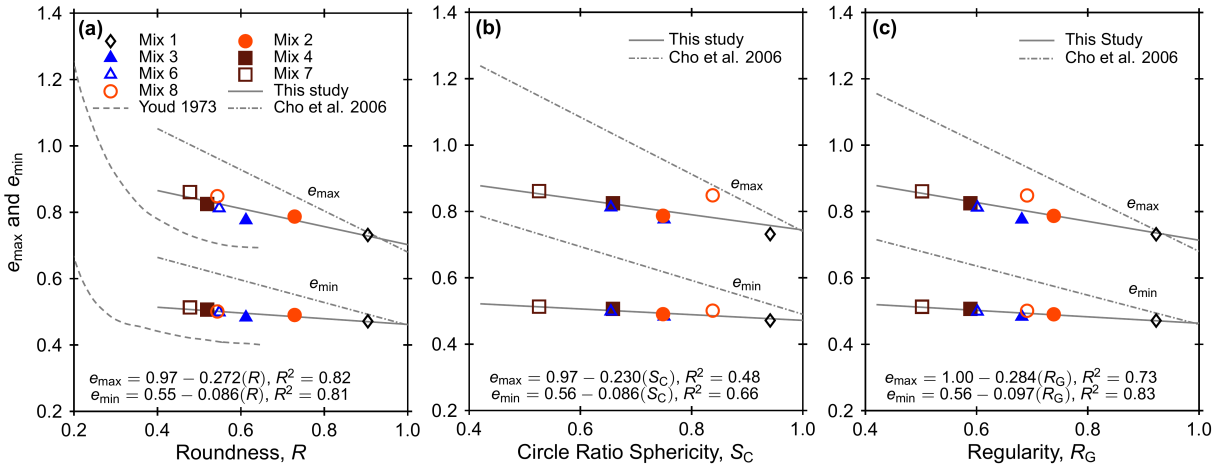

Figure 4.3: Variation of maximum and minimum void ratios of all the sand mixes with (a) roundness, (b) circle ratio sphericity, and (c) regularity.

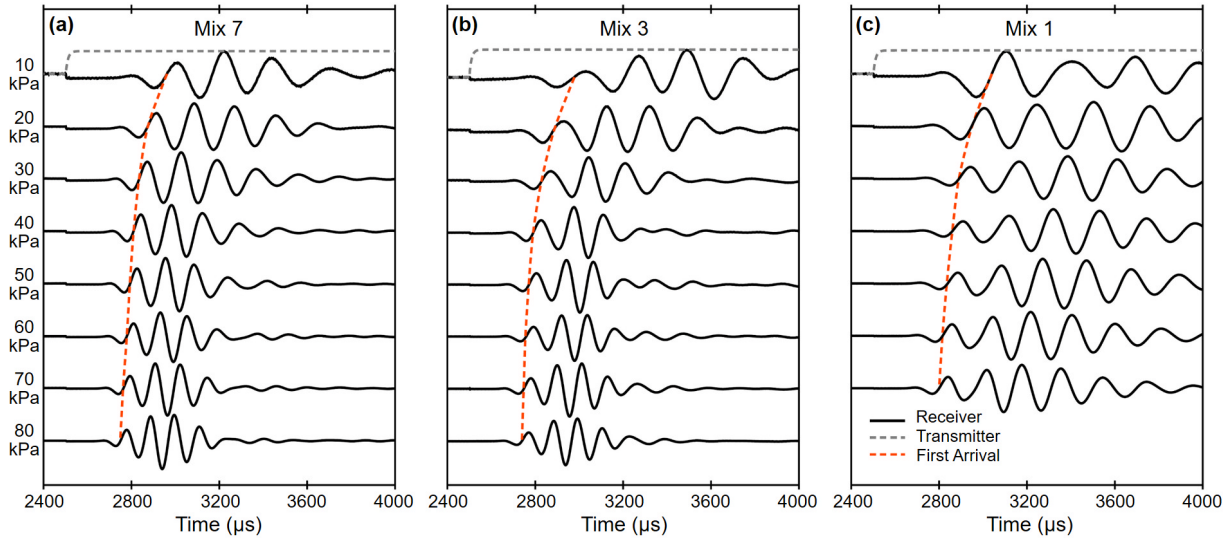

Figure 4.4: Receiver bender element signals for specimens of (a) mix 7 (initial height of 74.6 mm), (b) mix 3 (initial height of 72.2 mm) and (c) mix 1 (initial height of 67.8 mm) with $e_0 = 0.60 \pm 0.02$.

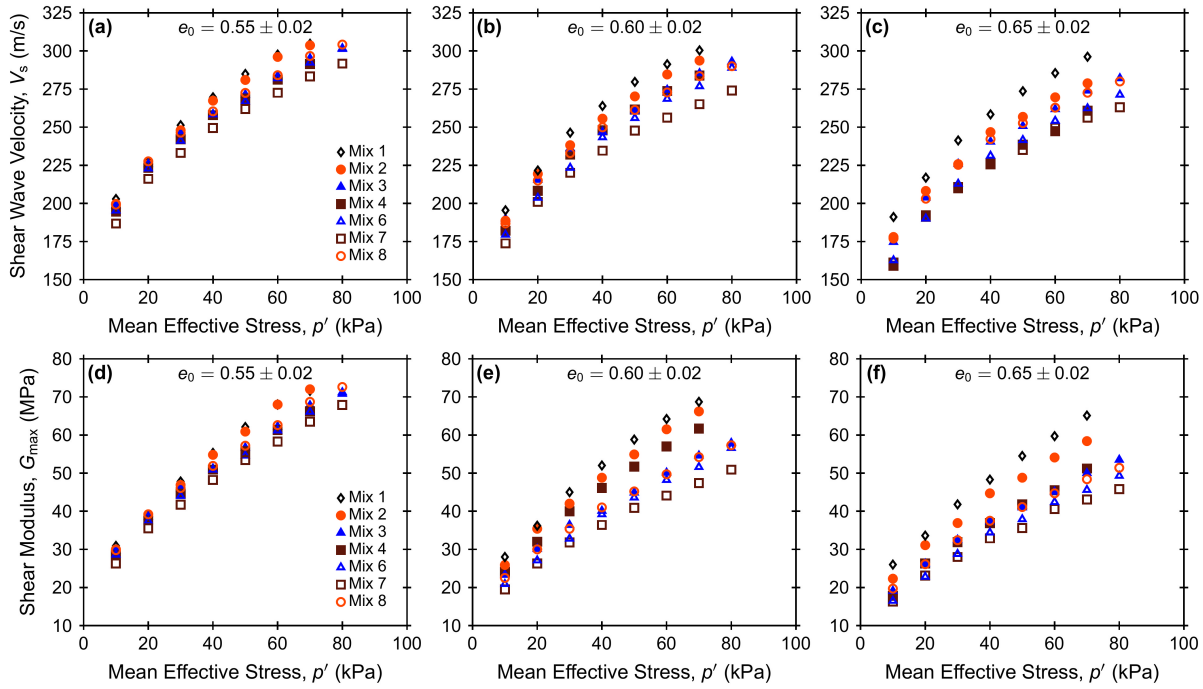

Figure 4.5: (a, b, c) Shear wave velocities and (d, e, f) shear moduli for all the specimens of 3D printed sands under isotropic confining pressures ranging from 10 to 80 kPa (power-law fits not shown for clarity).

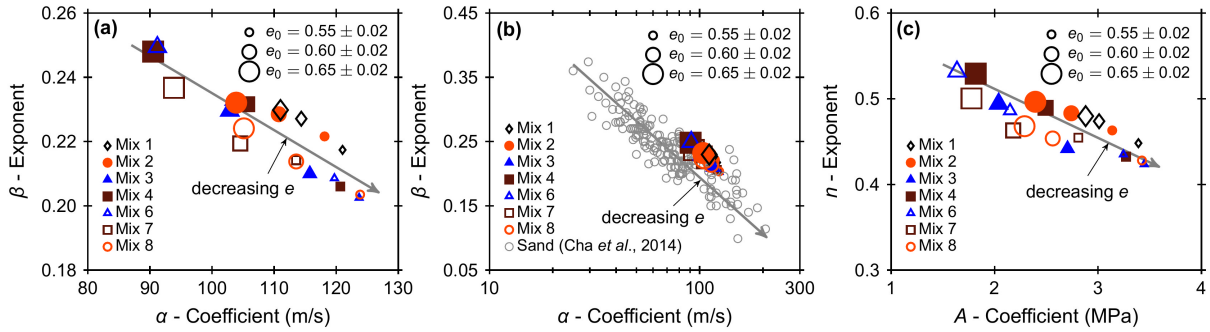

Figure 4.6: (a) Relationship between β-exponents and α-coefficients for all the specimens of 3D printed sands, (b) comparison of β-exponents and α-coefficients with database of natural sands and (c) relationship between n-exponents and A-coefficients for all the specimens of 3D printed sands.

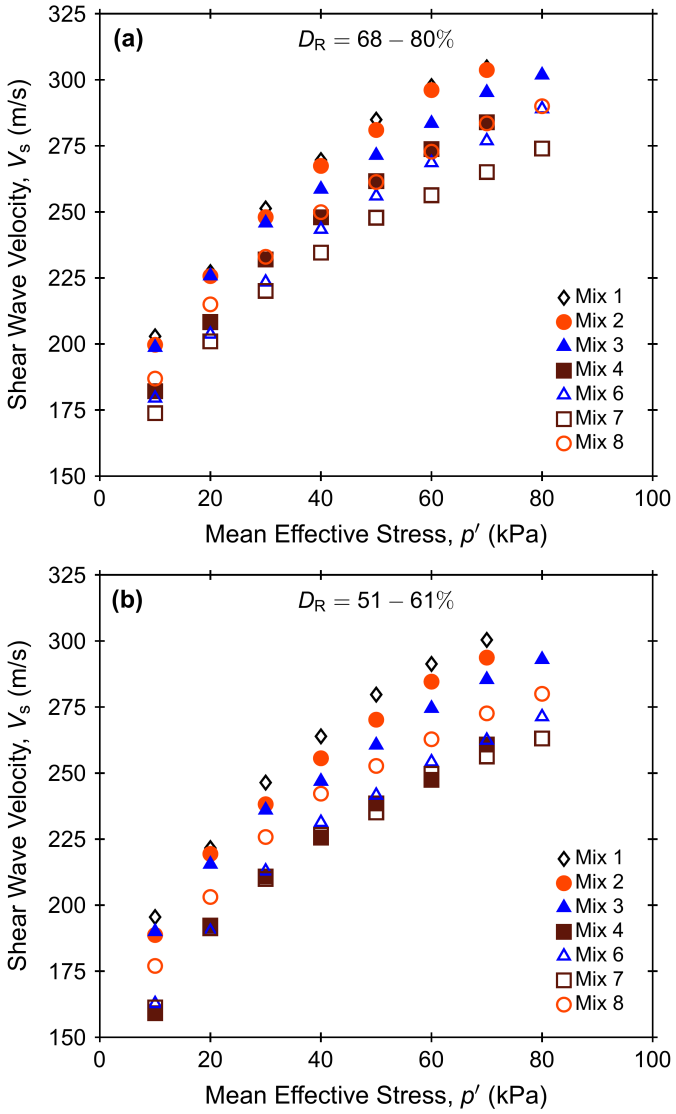

Figure 4.7: Shear wave velocities for all the specimens of 3D printed sands under isotropic confining pressures ranging from 10 to 80 kPa for (a) $D_R = 68 - 80\%$ and (b) $D_R = 51 - 61\%$ (power-law fits not shown for clarity).

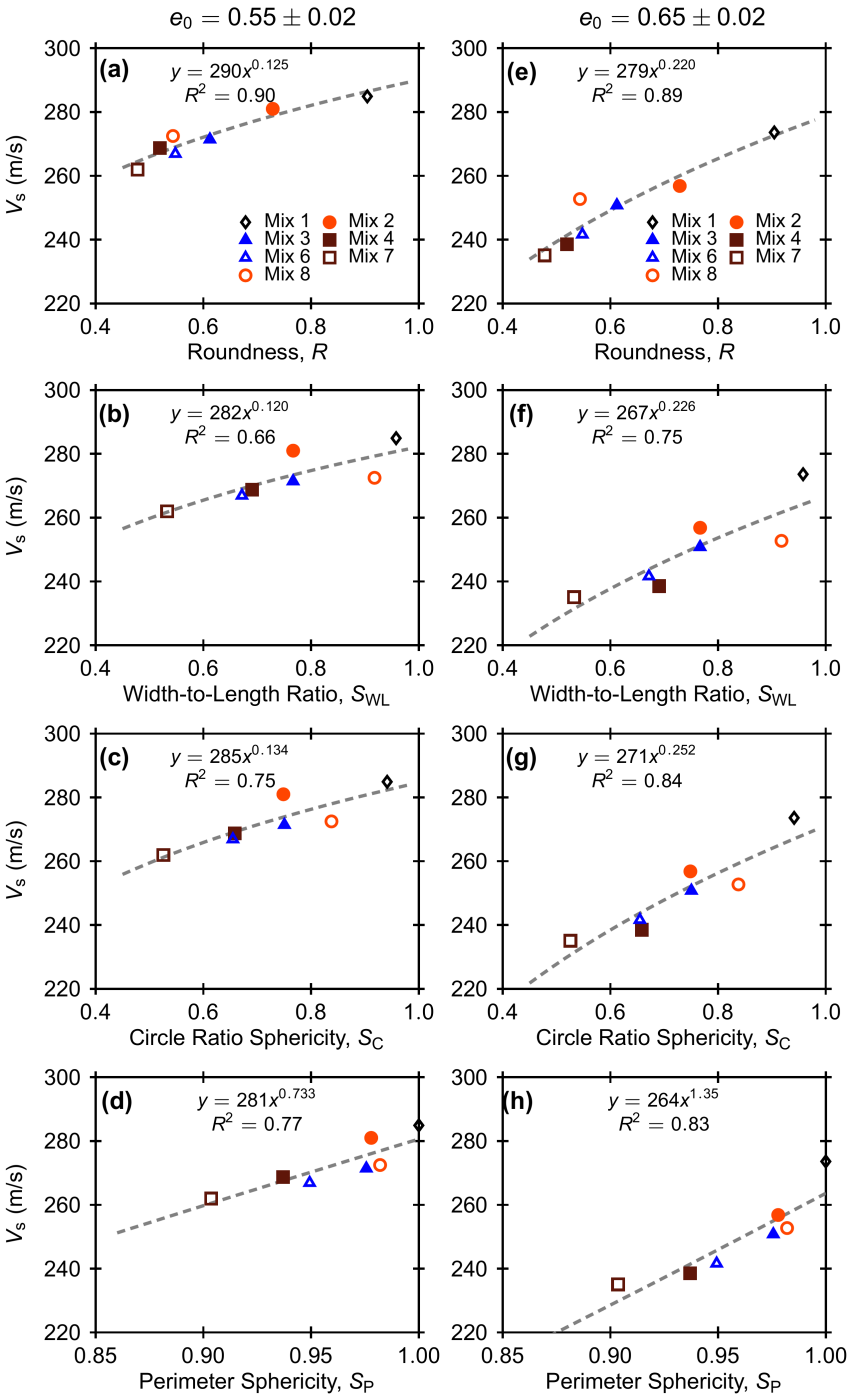

Figure 4.8: Variation of shear wave velocities with roundness, width-to-length ratio, circle ratio sphericity and perimeter sphericity, respectively for all the specimens at $p' = 50$ kPa with (a, b, c, d) $e_0 = 0.55 \pm 0.02$ and (e, f, g, h) $e_0 = 0.65 \pm 0.02$.

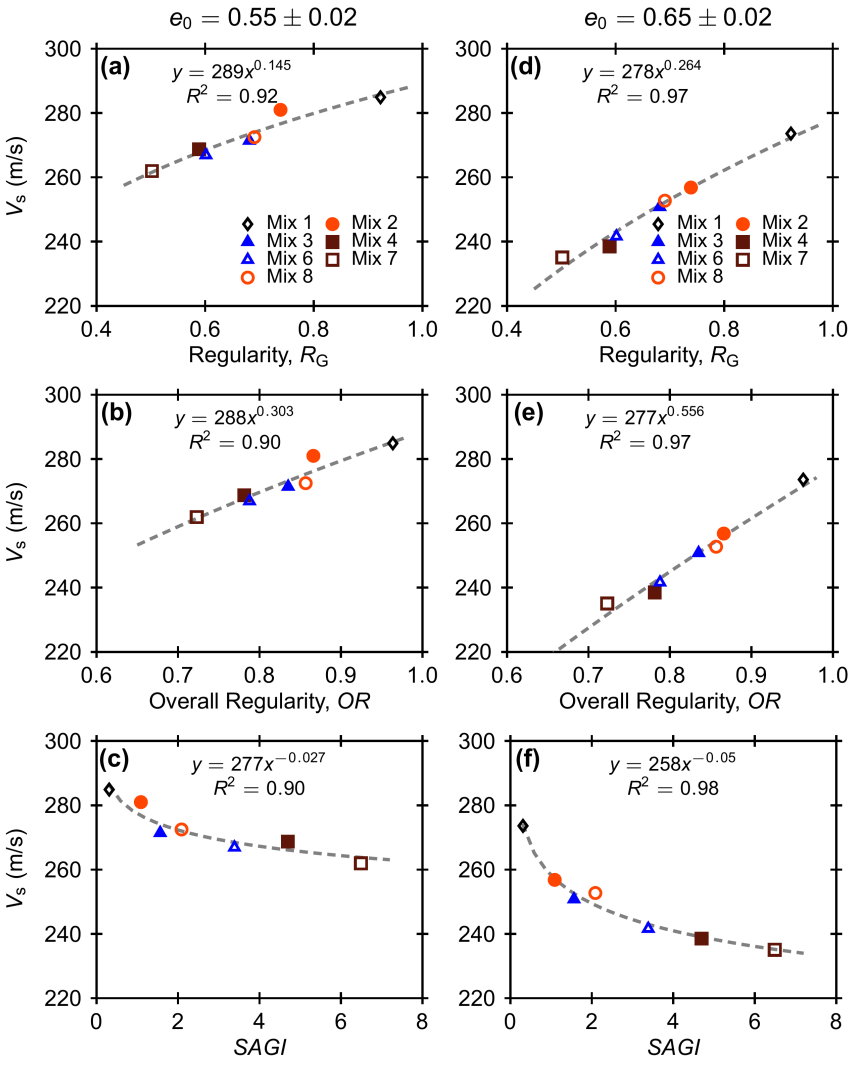

Figure 4.9: Variation of shear wave velocities with regularity, overall regularity and $SAGI$, respectively for all the specimens at $p' = 50$ kPa with (a, b, c) $e_0 = 0.55 \pm 0.02$ and (d, e, f) $e_0 = 0.65 \pm 0.02$.

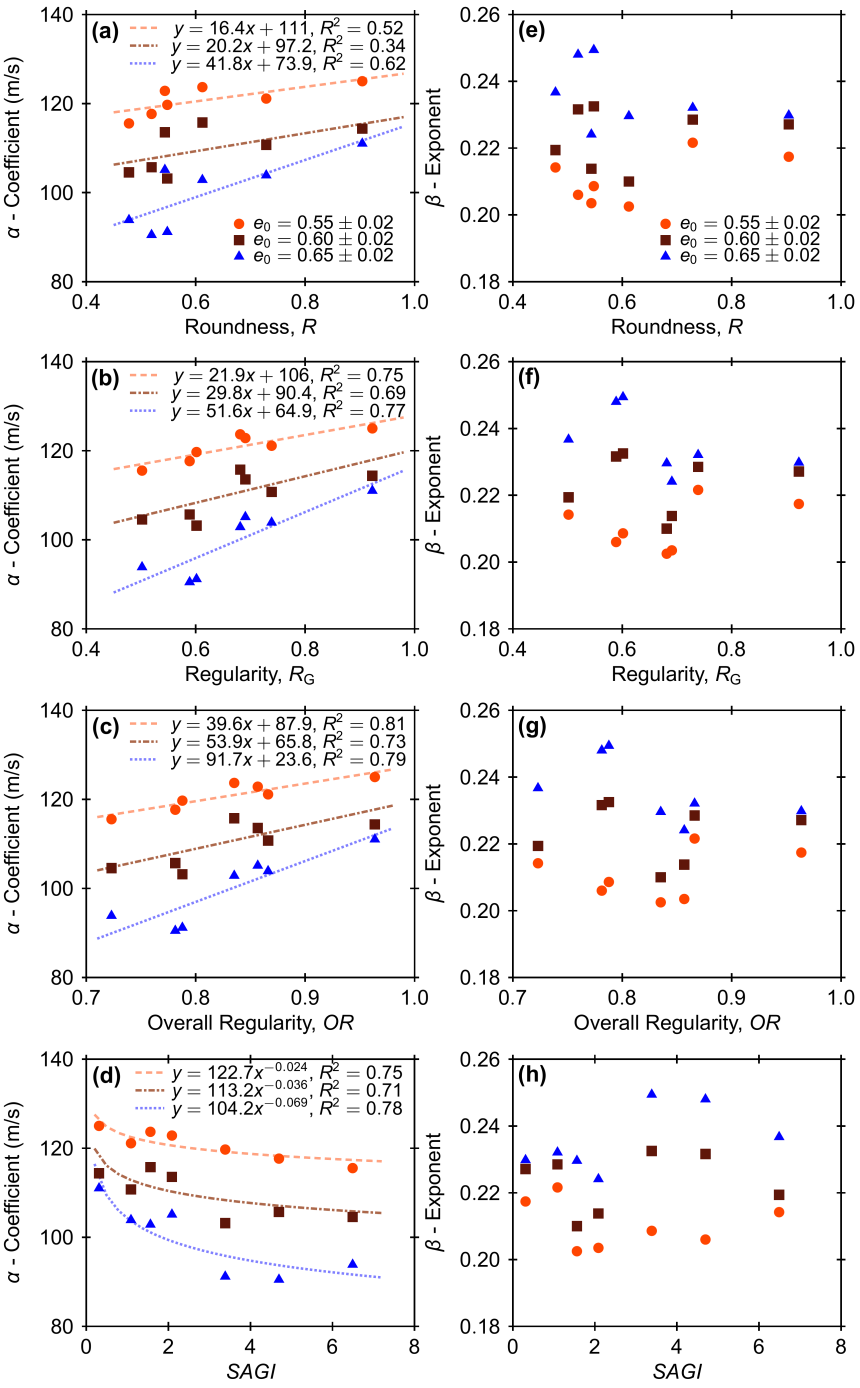

Figure 4.10: Variation of (a, b, c) α-coefficients and (d, e, f) β-exponents with regularity, overall regularity and $SAGI$, respectively, for all the specimens.

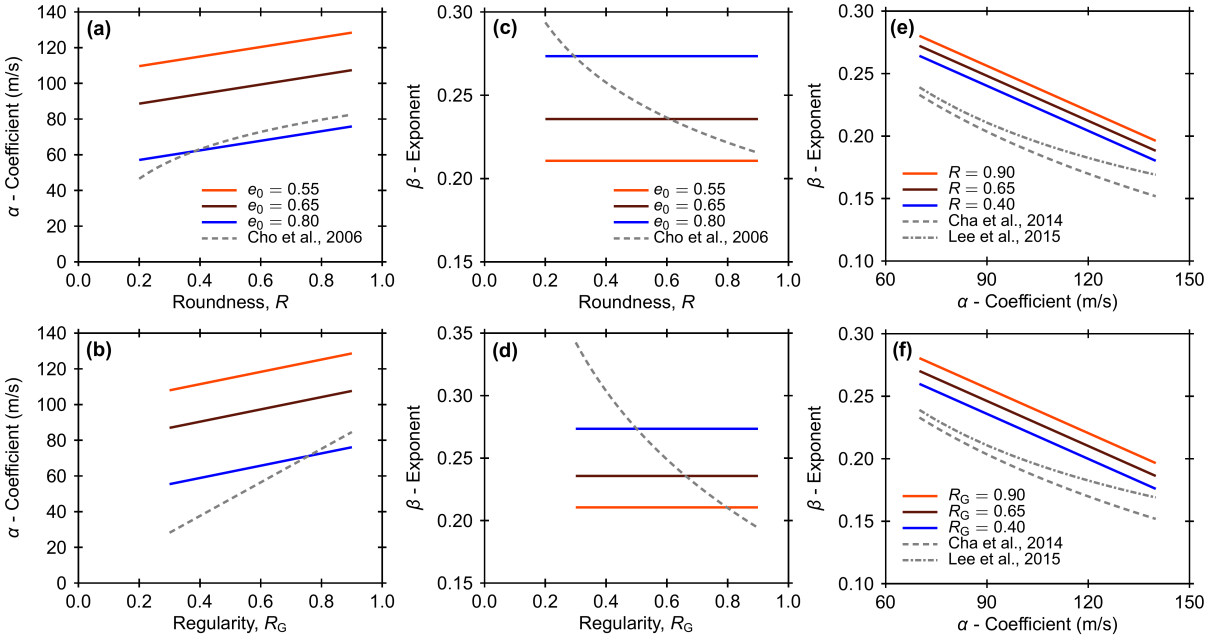

Figure 4.11: Comparison of (a, b) α-coefficients and (c, d) β-exponents relationships with roundness and regularity, and (e, f) relationships between α-coefficients and β-exponents for different roundness and regularity.

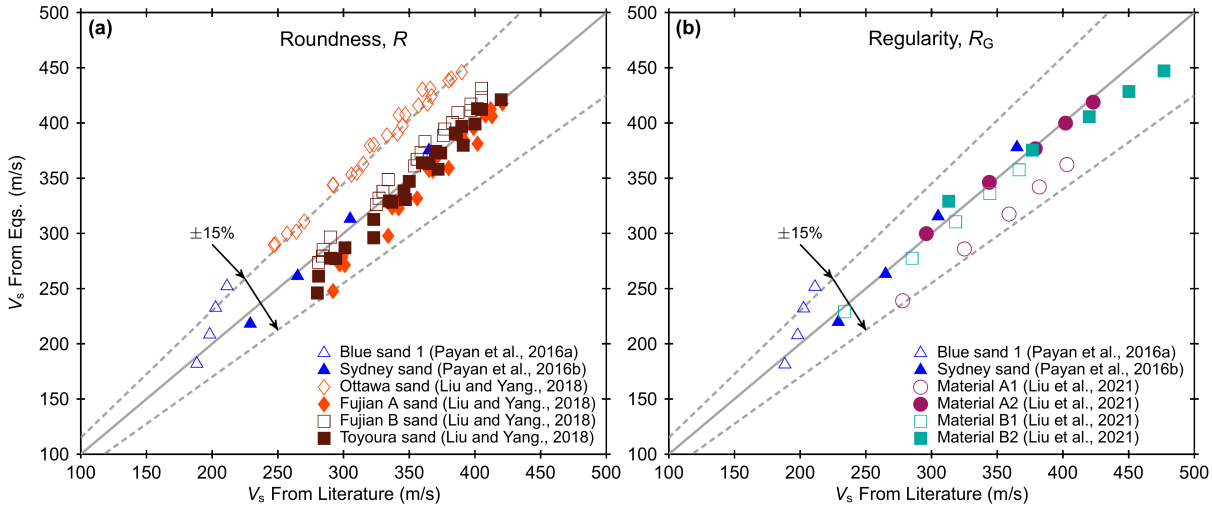

Figure 4.12: Comparison of shear wave velocities obtained from the regression analysis and literature based on: (a) roundness and (b) regularity.

4.9 Supplementary Information and Figures

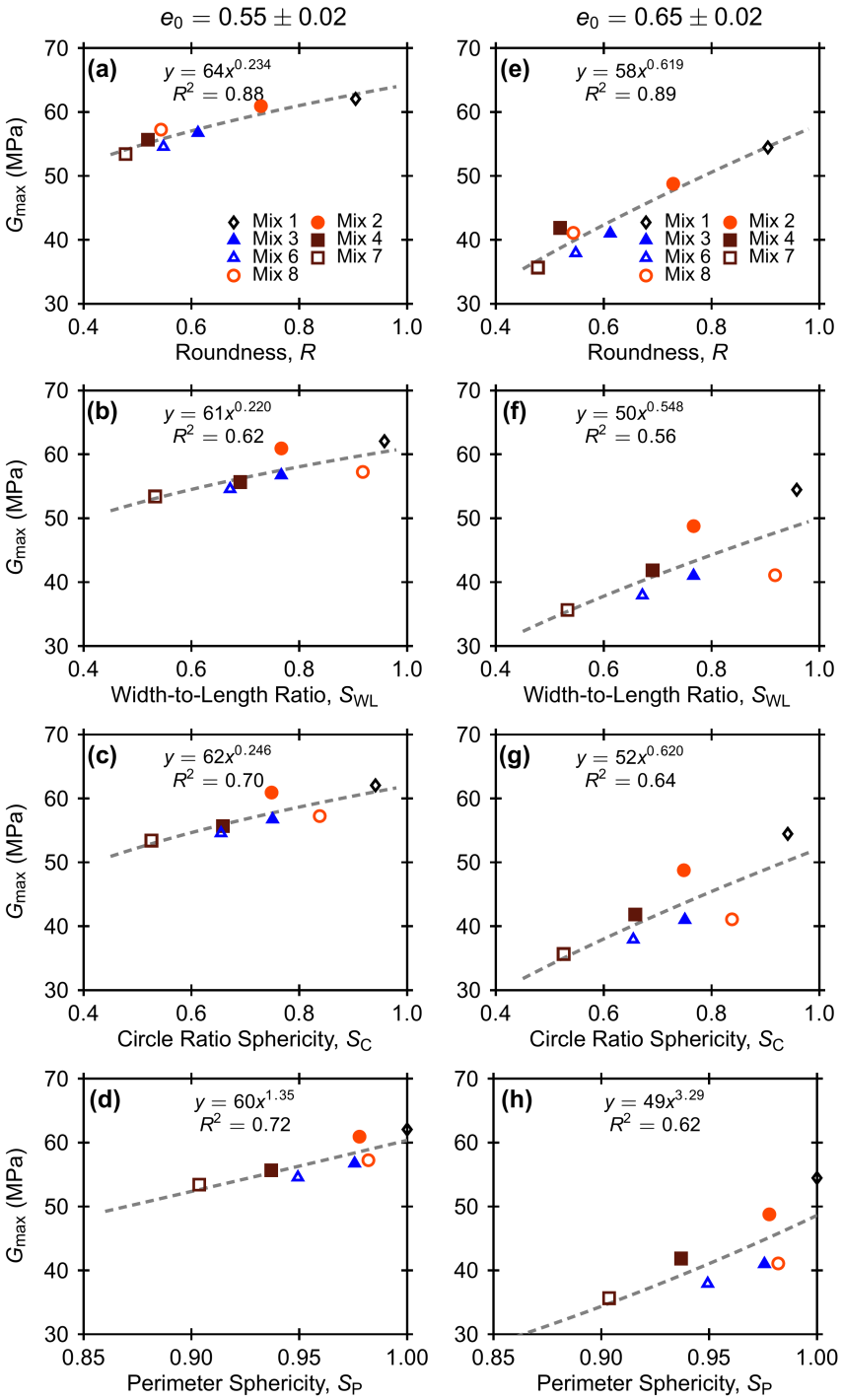

Figure 4.13: Variation of shear moduli with roundness, width-to-length ratio, circle ratio sphericity and perimeter sphericity, respectively, for all the specimens at $p' = 50$ kPa with (a, b, c, d) $e_0 = 0.55 \pm 0.02$ and (e, f, g, h) $e_0 = 0.65 \pm 0.02$.

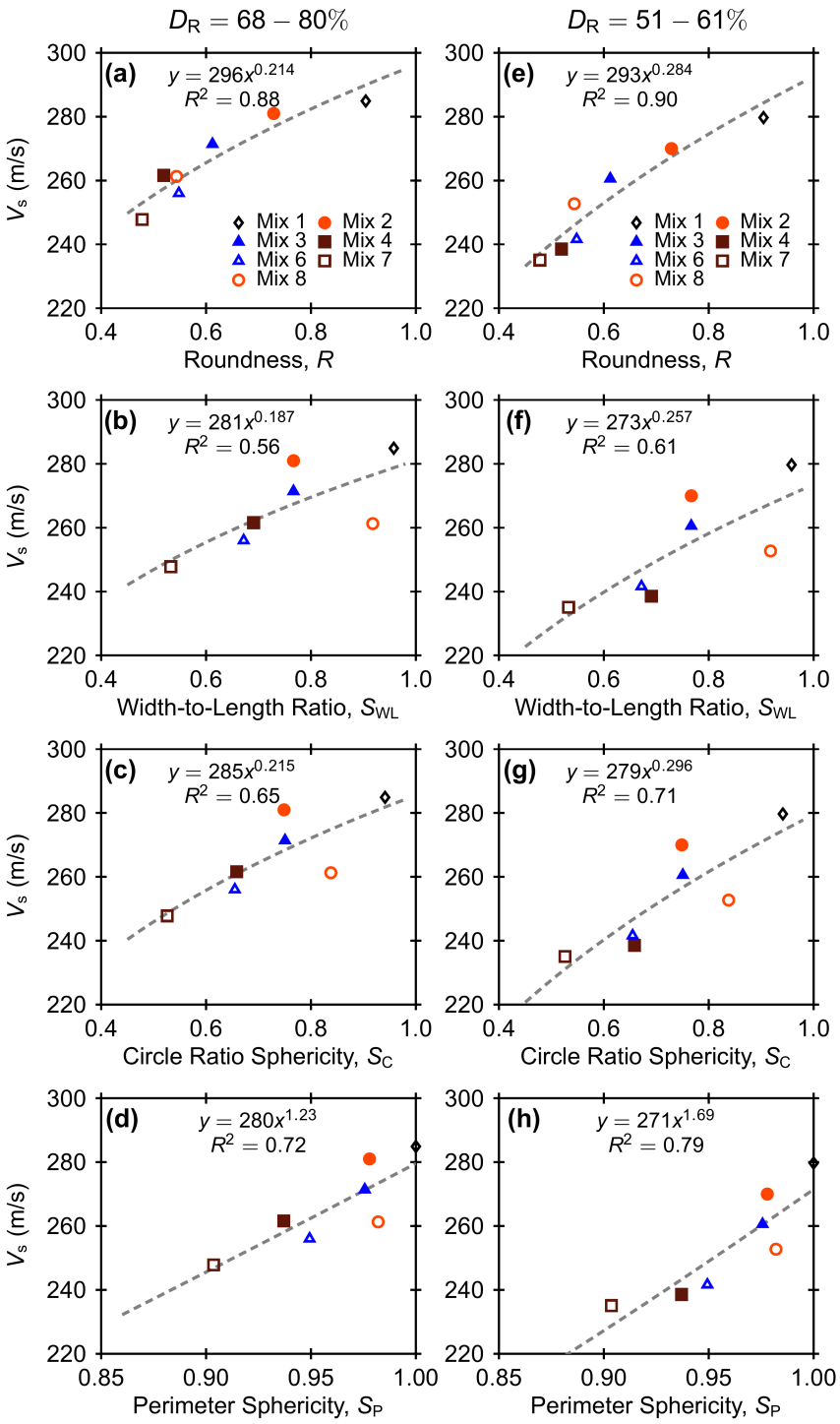

Figure 4.14: Variation of shear wave velocities with roundness, width-to-length ratio, circle ratio sphericity and perimeter sphericity, respectively, for all the specimens at $p' = 50$ kPa with (a, b, c, d) $D_R = 68 - 80\%$ and (e, f, g, h) $D_R = 51 - 61\%$.

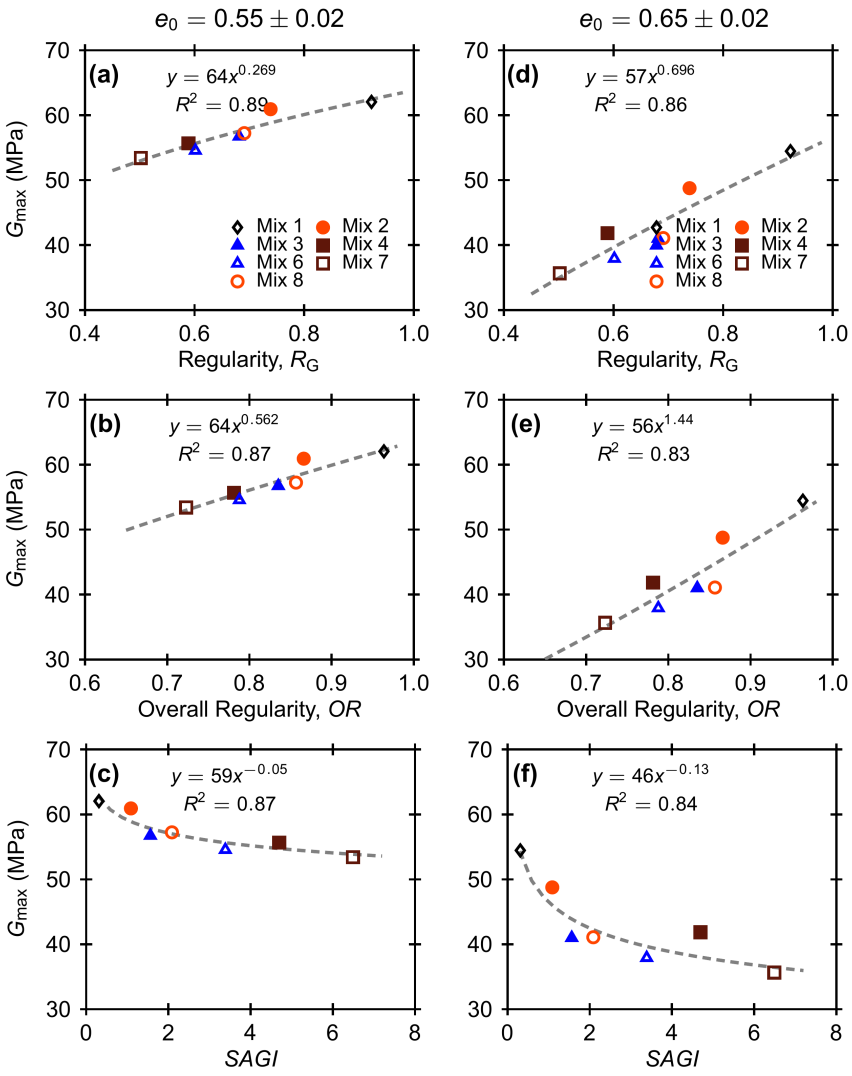

Figure 4.15: Variation of shear moduli with regularity, overall regularity and $SAGI$, respectively, for all the specimens at $p' = 50$ kPa with (a, b, c) $e_0 = 0.55 \pm 0.02$ and (d, e, f) $e_0 = 0.65 \pm 0.02$.

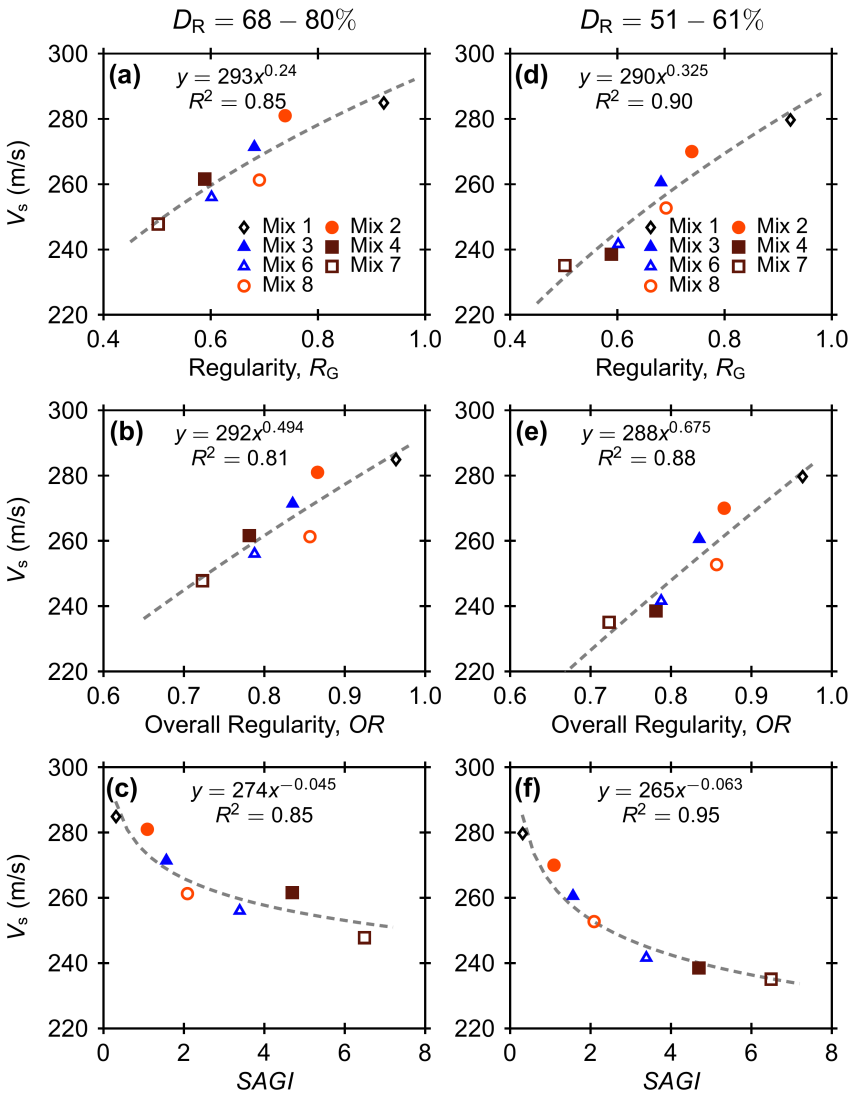

Figure 4.16: Variation of shear wave velocities with regularity, overall regularity and $SAGI$, respectively for all the specimens at $p' = 50$ kPa with (a, b, c) $D_R = 68 - 80\%$ and (d, e, f) $D_R = 51 - 61\%$.

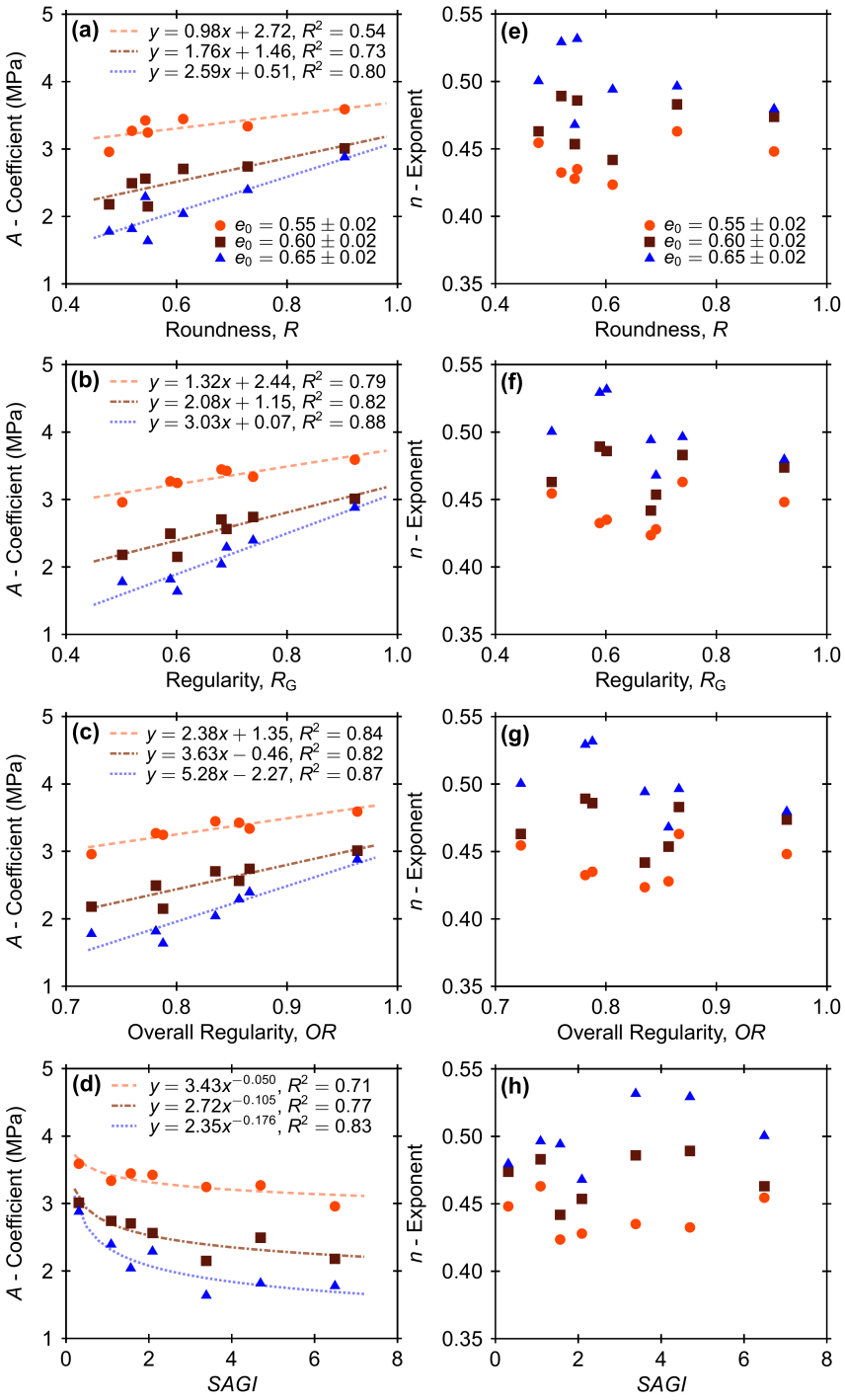

Figure 4.17: Variation of (a, b, c) A-coefficients and (d, e, f) n-exponents with regularity, overall regularity and $SAGI$, respectively, for all the specimens.

Chapter 5

Particle Shape Effects on the Triaxial Compression Behavior of 3D Printed Sand Analogs

5.1 Abstract

The shear behavior of granular soils is governed by particle morphology, gradation, surface roughness, and mineralogy. Experimental investigation of the effects of individual particle properties on the shear behavior of granular soils requires careful control over other properties which is a significant challenge with natural soils. Recent advances in 3D printing technology provide an alternative pathway of investigation by enabling the manufacturing of analog sand particles with independent control over particle shape and size. This study examines the effects of particle shape on the triaxial compression behavior of 3D printed sand analogs. Isotropically consolidated drained and undrained triaxial compression tests were performed on specimens of 3D printed sands with different shapes but similar particle size. The test results detail the significant effect that particle shape has on the shear behavior, wherein the specimens with more angular particles mobilize a greater critical state friction angle, and the slope of the critical state line in the void ratio-mean effective stress ($e - \log p'$) plane increases with increasing roundness. While the 3D printed sands capture some aspects of the particle shape effects on the shear behavior similar to those of natural sands (i.e., increase in friction angle with decreasing roundness), other aspects require further examination (i.e., increase in compressibility with increasing roundness).

5.2 Introduction

Inherent particle properties such as size, shape, gradation, surface roughness and mineralogy has significant influence on the mechanical behavior of granular soils [Santamarina, 2003]. Extending the understanding of the effects of individual particle properties on the mechanical behavior of coarse-grained soils poses a significant challenge in experimental studies since such an investigation requires careful control over the remaining particle properties, which is a pervasive challenge with natural soils. A number of previous studies attempted to investigate the effects of different particle properties on the engineering properties of coarse-grained soils, such as friction angle [e.g. Kirkpatrick, 1965; Marschi et al., 1972; Wang et al., 2013; Vangla and Latha, 2015; Xiao et al., 2019; Altuhafi et al., 2016], and shear wave velocity (V_s) and small-strain modulus (G_{max}) [e.g. Iwasaki and Tatsuoka, 1977; Chang and Ko, 1982; Menq, 2003; Sharifipour et al., 2004; Cho et al., 2006; Bartake and Singh, 2007; Bui, 2009; Patel et al., 2009; Wichtmann and Triantafyllidis, 2009; Senetakis et al., 2012; Yang and Gu, 2013; Hussien and Karray, 2015; Altuhafi et al., 2016; Payan et al., 2016b,a; Liu and Yang, 2018; Dutta et al., 2020; Liu et al., 2021]; however, some of these studies have reported contradictory trends, likely due to the aforementioned challenge.

3D printing technology offers the ability to create analog sand particles with independent control over particle size, shape and gradation [e.g. Hanaor et al., 2016; Adamidis et al., 2020]. Several recent studies have used 3D printing technology to generate analog particles of different sizes and shapes, showing the ability of these analogs to successfully replicate the morphology of natural particles [e.g. Miskin and Jaeger, 2013; Athanassiadis et al., 2014; Hanaor et al., 2016; Adamidis et al., 2020; Ahmed and Martinez, 2020; Su et al., 2020]. Results of triaxial tests on 3D printed particles show that they exhibit stress-dilatancy behavior similar to that typical of granular soils [e.g. Hanaor et al., 2016; Adamidis et al., 2020; Matsumura et al., 2017; Ahmed and Martinez, 2021], and the interpretation of their mechanical response can be captured with the critical state soil

mechanics framework [Ahmed and Martinez, 2021] (Chapter 3). Also, V_s and G_{max} of 3D printed particles obtained by bender element tests show mean effective stress, void ratio, and particle shape dependencies similar to those of natural sands [Ahmed and Martinez, 2020] (Chapter 2). These findings suggest that 3D printed analogs can be used to further explore the effects of individual particle properties on the engineering behavior of soil while controlling the remaining particle properties.

This study investigates the effect of particle shape on the shear behavior of 3D printed sands under triaxial compression. Six 3D printed sands with different particle shape parameters but similar gradations were generated based on spherical harmonics and X-ray CT scans of natural sands. Both drained and undrained triaxial compression tests on the specimens were performed. The specimens were prepared at initially loose state to obtain the critical state lines. The effect of particle shape on the critical state parameters obtained from the test results are discussed and compared to those of natural sands.

5.3 Materials and Methods

5.3.1 3D Printing Technology

3D printing technology has advanced rapidly in recent years, enabling the development of several 3D printing methods and materials. Modern 3D printers are capable of creating highly complex objects using materials such as polymers, metals, ceramics and concrete with a wide range of accuracy and cost. Specialized 3D printers can mix different materials to achieve the desired mechanical properties and aesthetics [e.g. Jiménez et al., 2019; Najmon et al., 2019]. However, more economic desktop 3D printers are typically constrained to printing using polymers with a printing resolution as low as 10 μm [Ngo et al., 2018].

A number of desktop 3D printing methods such as fused deposition modeling (FDM), polyjet, stereolithography (SLA), digital light processing (DLP), and selective laser sintering (SLS) are available that offer certain advantages and drawbacks. This study uses polyjet 3D

printing technology because it offers a relatively economic and fast manufacturing of small parts with high accuracy. Polyjet printers have two print heads to deposit different liquid photopolymer resins. One resin creates the desired object while the other resin acts as a support structure. Both resins are hardened by an ultraviolet laser. Once the printing is completed, the support structure is removed from the finished 3D object by water jetting and chemical treatment using a 2% sodium hydroxide solution. A more detailed description of the 3D printing process is provided in Chapters 2 and 3.

5.3.2 3D Printed Sand Analogs

The shape of a particle is typically described by roundness and sphericity, both of which can be defined in several ways [e.g. Mitchell et al., 2005; Guida et al., 2020]. This study considers the Wadell roundness, R [Wadell, 1932] and circle ratio sphericity, S_{C} [e.g. Mitchell et al., 2005; Zheng and Hryciw, 2015] to describe the particle shape. Four different 3D printed sand mixes with different roundness and sphericity were generated using the method proposed by Wei et al. [2018] that uses spherical harmonics to create random 3D shapes based on the desired shape features (mixes 3, 6, 7 and 8 in Figs. 5.1a and 5.1c, and Table 5.1). All these mixes are poorly-graded, with a median particle size (D_{50}) of 2.5 mm and coefficient of uniformity (C_{u}) of 1.26. In addition, two more 3D printed soil mixes (mixes 2 and 4 in Figs. 5.1b and 5.1c, and Table 5.1) were considered to extend the range of particle shape parameters. Mixes 2 and 4 were generated from the X-ray CT scans of randomly selected rounded and angular natural sand particles, respectively, as described by Ahmed and Martinez [2020] (Chapter 2). These two mixes are also poorly-graded, with a D_{50} of 3.2 mm and C_{u} of 1.47.

All the particles were generated using an *Objet Eden 260V* printer from Stratasys with *VeroWhitePlus* rigid acrylate-based polymer resin with a horizontal printing resolution of 30 μm. The hardened polymer resin has a Young's modulus of 2.4 GPa, Poisson's ratio of 0.3 and specific gravity of 1.18. The roundness and sphericities of the printed particles were

obtained from image analysis using the code by Zheng and Hryciw [2015]. The analysis of results also considered one combined shape parameter, regularity, R_{G}, which is the average of roundness, R, and circle ratio sphericity, S_{C} [Cho et al., 2006]. The maximum and minimum void ratios of all the mixes were determined using the methods outlined in Carey et al. [2020], which are similar to ASTM standards adapted for testing of smaller soil volumes, and are shown in Table 5.1.

5.3.3 Triaxial Tests

Both drained and undrained isotropically consolidated triaxial compression tests were performed to examine the effects of particle shape on the shear behavior of 3D printed sand analogs. In this study, an automated triaxial testing system with digital data acquisition capabilities was used. Cell and pore pressures, and volume change were controlled using two digital pressure volume controllers. The measured volume changes were used to determine the specimen volumetric strain, ε_{v}. Axial load was measured by an external load cell mounted on the load frame. Axial displacement was measured by an external linear variable differential transducer (LVDT) which was used to determine the specimen axial strain, ε_{a}. Pore pressure transducers were used to measure the specimen pore pressure as well as the triaxial confining pressure.

Tests were performed on loose specimens of 35 mm diameter and 71 mm height. This size gives a specimen diameter to D_{50} ratio of 14 and a specimen diameter to maximum particle diameter (D_{max}) ratio of 10. The specimens were prepared by pouring the particles from a small height into the mold in a single lift without any tamping. Once prepared, a small vacuum was applied to stabilize the specimen. The achieved initial relative density (D_{R}) of all the specimens before consolidation was around 10%. The specimen was then placed in the triaxial cell and the cell was filled with de-aired water. The specimen was saturated by applying back-pressure while maintaining a constant small difference between the cell and the back-pressure. The back-pressure was increased slowly until a B-value of 0.95

was obtained. After saturation, the specimen was consolidated isotropically to the target confining pressure; once the consolidation phase finished, the shearing phase commenced. Note that, the consolidation of all the specimens resulted in a significant reduction in void ratio and increase in relative density (D_{R}) which are discussed in the results and discussion section. All the specimens exhibited a bulging failure with no visible shear bands. The membrane penetration correction for the volume changes was found insignificant and not applied for all tests.

Table 5.2 summarizes the 38 triaxial tests performed. The testing ID convention is such that ID "M-AB-y" corresponds to type "AB" test on soil mix "M" at an effective confining pressure ($\sigma'_{3\mathrm{c}}$) of "y" kPa. For example, "3-CD-50" corresponds to "CD" (i.e. drained) test on soil mix "3" at $\sigma'_{3\mathrm{c}}$ of "50" kPa.

5.4 Results and Discussion

This section first discusses the isotropic consolidation and drained and undrained triaxial compression behavior of soil mixes 3, 6, 7 and 8. Then, the estimation of critical state lines in $q - p'$ space and $e - \log p'$ space is presented. Finally, the effects of particle shape on the critical state parameters are discussed and compared to those in literature. Note that, the drained test results for mixes 2 and 4 are discussed in Ahmed and Martinez [2021] (Chapter 3) and are not repeated here. However, the compressibility indices and critical state parameters for those two soil mixes are included in the discussion.

5.4.1 Triaxial Compression Behavior

Five drained and two undrained triaxial compression tests were performed on specimens of soil mixes 3, 6, 7 and 8 at different confining pressures to characterize their consolidation and shearing behavior. Figures 5.2a through 5.2d show the isotropic consolidation curves of mixes 3, 6, 7 and 8, respectively. The consolidation curves of all the specimens exhibited significant reduction in void ratios, and the reduction increased as the mean confining

pressure increased. Although the initial relative density of all the specimens was around 10% before the consolidation commenced, the reduction in void ratios resulted specimens with greater relative density for higher mean effective stress at the beginning of shearing (shown in Table 5.2). The consolidation curves of all the soil mixes tend to converge which is particularly evident in Fig. 5.2c. This behavior can be explained by the limiting compression curve (LCC) concept. Namely, the compression curves for natural granular soils with different initial densities tend to converge to a unique curve at high mean effective stress levels, referred to as the LCC [e.g. Coop and Lee, 1992; Pestana and Whittle, 1995]. At low stress levels, the volume changes of soils are due to elastic compression of the soil skeleton and particle rearrangement, while the LCC response is controlled by particle damage (i.e. asperity breakage and particle crushing) [Roberts, 1958]. The damage of particles is affected by particle shape, gradation and mineralogy. In this study, no crushing was observed in any of the specimens. However, damage of the 3D printed particles during consolidation occurred in the form of plastic yielding of the micro-asperities (as further discussed in Chapter 2), which could be analogous to the breakage of asperities in natural sands. Figure 5.3 shows the variation of compressibility indices (C_c) with roundness (R), circle ratio sphericity (S_C) and regularity (R_G) for soil mixes 3, 6, 7 and 8 including those for mixes 2 and 4 reported in Ahmed and Martinez [2021] (Chapter 3). The C_c values were calculated by taking the average of the slopes of the consolidation curves for mean effective stress range between 50 and 90 kPa. As shown, the values of C_c increase with increasing R, S_C and R_G, whereas for natural sands, the values of C_c decrease with increasing R, S_C and R_G [e.g. Cho et al., 2006]. As discussed above, the consolidation curves for the 3D printed particles tend to converge, indicating particle damage (i.e. breakage of micro-asperities). The particle damage might have led to greater contact slippage between the more rounded 3D printed particles, possibly explaining the greater C_c of the 3D printed particles with greater R, S_C and R_G.

The results of drained triaxial tests for mixes 3, 6, 7 and 8 are shown in Figs. 5.4, 5.5, 5.5 and 5.7, respectively. As shown, greater deviatoric stresses were developed at higher

confining pressure (σ'_{3c}) for all the soil mixes (Figs. 5.4a, 5.5a, 5.6a and 5.7a). The $q - \varepsilon_a$ curves for all the sand mixes exhibit strain hardening behavior with slight peak at a confining pressure of 90 kPa (Figs. 5.4b, 5.5b, 5.6b and 5.7b). The volumetric change response for the specimens of mix 3 at σ'_{3c} of 50, 70 and 90 kPa shows initial contraction followed by slight dilation at an axial strain greater than 30% (Fig. 5.4b) which is also shown by the stress paths in the $e - \log p'$ plane (Fig. 5.4d). The volumetric change response for the specimen of mix 8 at σ'_{3c} of 90 kPa also shows initial contraction followed by slight dilation at an axial strain greater than 30% (Fig. 5.7b) which is also shown by the stress paths in the $e - \log p'$ plane (Fig. 5.7d). All the other specimens exhibit an overall contractive behavior (Figs. 5.4b, 5.5b, 5.6b and 5.7b) with slight dilation at axial strains greater than about 15%. The overall contractive behavior with slight dilation is also shown by the stress paths in the $e - \log p'$ plane (Figs. 5.4d, 5.5d, 5.6d and 5.7d). Note that, as previously mentioned, the relative densities of the specimens at the beginning of shearing were different at different mean confining pressures as shown in Fig. 5.2 and Table 5.2. Hence, the trends in the volume change response are not as clear as one might expect if the relative densities at the beginning of shearing were constant and the confining pressure was changing.

The results of undrained tests for mixes 3, 6, 7 and 8 are shown in Figs. 5.8, 5.9, 5.10 and 5.11, respectively. Similar to the drained tests, greater deviatoric stresses were developed at higher confining pressure for all the soil mixes (Figs. 5.8a, 5.9a, 5.10a and 5.11a). Also, greater peak positive excess pore pressures (Δu) were developed at higher confining pressure for all the specimens (Figs. 5.8b, 5.9b, 5.10b and 5.11b). The excess pore pressures developed for all the sand specimens increase to a peak and then decreases indicating an initial volumetric contraction followed by a slight dilative tendency. The stress paths in the $q - p'$ plane initially tracked upward and then tracked rightward exhibiting no significant elbow or phase transformation indicating similar volumetric change tendency (Figs. 5.8c, 5.9c, 5.10c and 5.11c). Note that, the initial part of the stress paths for the specimens of mix 8 immediately tracked slightly rightward instead of tracking upward (Fig.

5.11c), as is typical for the initial part of elastic compression. The orientation of the path may however be due to anisotropic elasticity [Wood, 1990], though this cannot be confirmed at this point. As such, further investigation is required to figure out the cause and caution should be used in interpreting trends from the stress paths of the undrained tests presented in Figs. 5.8, 5.9, 5.10 and 5.11.

5.4.2 Critical State Lines

The critical state lines (CSL) in the $q - p'$ plane for all the soil mixes were estimated by taking the points at the end of shearing as the critical state points. The critical state points obtained from the tests can be fitted with a straight line passing through the origin with a slope of M. The slope M is the critical state stress ratio that can be used to estimate the critical state friction angle, ϕ'_{cs}. However, for the 3D printed sand mixes used in this study, the critical state points cannot be fitted with a single straight line in the $q - p'$ space. While the CSL may be curved, two straight lines are used here to define average friction angles for two σ'_{3c} ranges. A straight line fitted to the tests with σ'_{3c} smaller than 50 kPa has a higher M than that fitted to the tests with σ'_{3c} greater than 50 kPa for all the sands (shown in Figs. 5.12a-5.12d). The reason for the decrease in M with increasing σ'_{3c} could be due to the decrease in inter-particle friction coefficient of the 3D printed polymer as the normal stress is increased, as discussed in Ahmed and Martinez [2021] (Chapter 3).

The critical state lines in the $e - \log p'$ plane for all the soils are estimated by best fitting the critical state points obtained from both drained and undrained tests by extrapolating the end-of-test results following methods described in Zhang et al. [2018] and Torres-Cruz and Santamarina [2020], respectively. Examples of the extrapolation procedures can be found in Ahmed and Martinez [2021] (Chapter 3). The extrapolated points in the $e - \log p'$ plane for all the soil mixes are shown in Fig. 5.13. A logarithmic form of critical

state line is considered here that is presented by the following equation:

$$e_{cs} = e_{\Gamma} - \lambda \log p' \tag{5.1}$$

where, e_{cs} is the critical state void ratio at a mean effective stress p', e_{Γ} is the critical state void ratio at $p' = 1$ kPa, and λ is the slope of critical state line. The critical state line equations are also shown in Fig. 5.13 for all the soils.

5.4.3 Effects of Shape on Critical State Parameters

The effect of particle shape on the critical state parameters is examined considering the particle roundness, sphericity, and regularity as descriptions of particle shape. Figure 5.14 shows the variation of critical state parameters (M, e_{Γ} and λ) with particle roundness, sphericity and regularity. Note that, the results from Ahmed and Martinez [2021] (Chapter 3) are added in Fig. 5.14 for soil mixes 2 and 4. As shown, the M-values obtained for σ'_{3c} greater than 50 kPa decrease in a quasi-linear fashion as R, S_C and R_G are increased (Figs. 5.14a, 5.14e and 5.14i). Similarly, the M-values obtained for σ'_{3c} smaller than 50 kPa decrease in a similar manner as R, S_C and R_G are increased (Figs. 5.14b, 5.14f and 5.14j). The M-values for natural sands available in the literature (Table 5.3) exhibit a similar trend with decreasing M with increases in the shape parameters. However, the M-values for the 3D printed sand mixes are smaller than those for natural sands available in literature. The possible reasons could be either smaller inter-particle friction coefficient of the 3D printed polymer in the direction perpendicular to layer deposition compared to that of natural sands, or plastic deformation of the particles' asperities leading to decrease the interlocking between particles [Ahmed and Martinez, 2021] (Chapter 3).

Figure 5.15 shows the variation of critical state friction angles (ϕ'_{cs}) with particle roundness, sphericity, and regularity. In a similar fashion to M, ϕ'_{cs} decreases with increasing R, S_C and R_G, and the values of ϕ'_{cs} for the 3D printed sands are smaller than those of natural

sands. The variation of ϕ'_{cs} with particle roundness and regularity (Figs. 5.15a and 5.15c) shows stronger correlation than that with sphericity (Fig. 5.15b). Also, the general trends of ϕ'_{cs} with particle shape parameters for the 3D printed sands are almost parallel to that of natural sands suggesting that the effect of particle shape on ϕ'_{cs} is quite similar between the 3D printed sands and natural sands, while the difference in y-intercept could be due to the inter-particle friction coefficient as discussed above.

The CSLs in the $e - \log p'$ plane show a modest effect of R, S_C and R_G on e_Γ and a greater effect of the shape parameters on λ. As shown in Figs. 5.14c, 5.14g and 5.14k, e_Γ decreases slightly with increases in R, S_C and R_G, which is consistent with the trend reported in literature for natural sands (Table 5.3). In fact, the e_Γ-values obtained from the CSLs of the 3D printed soils are within the range of values for natural sands.

As shown in Figs. 5.14d, 5.14h and 5.14l, λ-values for the 3D printed sands are significantly higher than those of natural sands reported in literature. The lower stiffness of the 3D printed materials (i.e. Young's modulus of 2.4 GPa) compared to that of natural sand particles (i.e. Young's modulus of 76 GPa for quartz) is the likely reason for the higher λ-values of the 3D printed sands. The raito of Young's Moduli ($E_{\text{quartz}}/E_{\text{3DP polymer}}$) is 31.7, while the corresponding ratio of λ-values for natural and 3D printed sands ($\lambda_{\text{natural sand}}/\lambda_{\text{3DP sand}}$) is 0.41, indicating that, as expected, the differences in λ do not track linearly with the differences in E. The λ-values of the 3D printed sands appear to increase as R, S_C and R_G are increased, which is opposite to the trends for natural sands reported in literature (Figs. 5.14d, 5.14h and 5.14l). It is possible that this trend could be explained by the following mechanisms. At lower stress levels, particle damage is insignificant and more rounded natural sand particles have the ability to move more efficiently to form a denser packing during shearing than the angular particles, resulting in a less compressible packing. Hence, at lower stresses the λ-values of natural sands increase as R, S_C and R_G are increased. However, at higher stress levels, the particle breakage becomes significant and the values of λ generally increase [e.g. Been et al., 1991; Russell and Khalili, 2004;

Vilhar et al., 2013]. As discussed above, the damage of the 3D printed particles during the consolidation phase (i.e. breakage of micro-asperities) may have promoted greater slippage between the inter-particle contacts of the more rounded particles. This possible effect of particle shape on the inter-particle contact slippage, coupled with the small stiffness of the 3D printed materials, may have led to greater λ-values for sands with higher R, S_C and R_G. However, this hypothesis should be verified with Discrete Element Modeling simulations or with triaxial experiments on 3D printed particles that are less prone to suffer asperity damage.

5.5 Conclusion

This paper presents an investigation on the effects of particle shape on the shear behavior of 3D printed sands under triaxial compression. Both drained and undrained triaxial compression tests were conducted on specimens of six 3D printed sands with different particle shapes but similar gradations which were generated based on spherical harmonics and X-ray CT scans of natural sands. The effect of particle shape on the critical state parameters obtained from the test results were examined and compared to those of natural sands. The main findings of this study are summarized as follows:

- The 3D printed sands with higher particle roundness, sphericity and regularity exhibit greater compressibility during isotropic compression. However, this trend is opposite to that of natural sands. The damage of particles (i.e. breakage of micro-asperities) during consolidation might have led to greater contact slippage for the more rounded 3D printed particles, possibly giving rise to the greater compressibility measured in the experiments.
- Critical state lines (CSL) in both $q - p'$ and $e - \log p'$ plane can be approximated for the 3D printed sands similar to those of natural sands.
- Two different critical state stress ratios (M) can be obtained for each sand: one M for $\sigma'_{3c} < 50$ kPa and another for $\sigma'_{3c} > 50$ kPa. The M-values obtained for

$\sigma'_{3c} < 50$ kPa are higher than those for $\sigma'_{3c} > 50$ kPa. Both M-values decrease with an increase in particle roundness, sphericity and regularity which is consistent with literature. However, the M-values for the 3D printed sands are significantly smaller than those for the natural sands, possibly due to the plastic deformation of the particles' asperities leading to the decrease of any interlocking between particles and to the smaller inter-particle friction coefficient.

- The e_Γ obtained from the CSLs in $e - \log p'$ plane decreases slightly with increase in particle roundness, sphericity and regularity which is consistent with literature. Also, the e_Γ-values are within the range of those for natural sands.
- The λ-values obtained for the 3D printed sands are greater than those of natural sands; this is due to significantly smaller Young's modulus of the 3D printed polymer in comparison to the minerals in natural sands. The slope λ of the CSLs increases as particle roundness, sphericity and regularity are increased, which is opposite to the trend reported in the literature for natural sands. The damage of particles during consolidation and subsequent shearing may have caused greater inter-particle contact slippage, thus decreasing the interlocking for more rounded particles. This mechanism may lead to the greater λ-values for the soils with higher R, S_C and R_G. However, this should be further assessed using numerical simulations or experiments with less compressible 3D printed soils.

5.6 Acknowledgment

This material is based upon work supported in part by the National Science Foundation (NSF) under award No. 1735732. Any opinions, findings, and conclusions or recommendations expressed in this material are those of the author(s) and do not necessarily reflect those of the NSF.

Bibliography

Adamidis, O., Alber, S., and Anastasopoulos, I. (2020). Assessment of three-dimensional printing of granular media for geotechnical applications. *Geotechnical Testing Journal*, 43(3).

Ahmed, S. S. and Martinez, A. (2020). Modeling the mechanical behavior of coarse-grained soil using additive manufactured particle analogs. *Acta Geotechnica*, 15(10):2829–2847.

Ahmed, S. S. and Martinez, A. (2021). Triaxial compression behavior of 3d printed and natural sands. *Granular Matter*, 23(4):1–21.

Altuhafi, F. N., Coop, M. R., and Georgiannou, V. N. (2016). Effect of particle shape on the mechanical behavior of natural sands. *Journal of Geotechnical and Geoenvironmental Engineering*, 142(12):04016071.

Athanassiadis, A. G., Miskin, M. Z., Kaplan, P., Rodenberg, N., Lee, S. H., Merritt, J., Brown, E., Amend, J., Lipson, H., and Jaeger, H. M. (2014). Particle shape effects on the stress response of granular packings. *Soft Matter*, 10(1):48–59.

Bartake, P. and Singh, D. (2007). Studies on the determination of shear wave velocity in sands. *Geomechanics and Geoengineering*, 2(1):41–49.

Been, K. and Jefferies, M. (2004). Stress dilatancy in very loose sand. *Canadian Geotechnical Journal*, 41(5):972–989.

Been, K., Jefferies, M., and Hachey, J. (1991). The critical state of sands. *Geotechnique*, 41(3):365–381.

Been, K. and Jefferies, M. G. (1985). A state parameter for sands. *Géotechnique*, 35(2):99–112.

Bui, M. T. (2009). *Influence of some particle characteristics on the small strain response of granular materials*. PhD thesis, University of Southampton.

Carey, T. J., Stone, N., and Kutter, B. L. (2020). Grain size analysis and maximum and minimum dry density testing of ottawa f-65 sand for leap-ucd-2017. In *Model tests and numerical simulations of liquefaction and lateral spreading*, pages 31–44. Springer.

Castro, G. (1969). Liquefaction of sands. *ph. D. Thesis, Harvard Soil Mech.*

Cerato, A. B. and Lutenegger, A. J. (2006). Specimen size and scale effects of direct shear box tests of sands. *Geotechnical Testing Journal*, 29(6):507–516.

Chang, N.-Y. and Ko, H.-Y. (1982). Effects of grain size distribution on dynamic properties and liquefaction potential of granular soils. Research Report N R82-103.

Cho, G.-C., Dodds, J., and Santamarina, J. C. (2006). Particle shape effects on packing density, stiffness, and strength: Natural and crushed sands. *Journal of Geotechnical and Geoenvironmental Engineering*, 132(5):591–602.

Chu, J., Lo, S.-C., and Lee, I. K. (1993). Instability of granular soils under strain path testing. *Journal of Geotechnical Engineering*, 119(5):874–892.

Coop, M. and Lee, I. (1992). The behaviour of granular soils at elevated stresses. In *Predictive soil mechanics: Proceedings of the Wroth Memorial Symposium held at St Catherine's College, Oxford, 27-29 July 1992*, pages 186–198. Thomas Telford Publishing.

Cornforth, D. H. (1964). Some experiments on the influence of strain conditions on the strength of sand. *Geotechnique*, 14(2):143–167.

Cox, M. R. and Budhu, M. (2008). A practical approach to grain shape quantification. *Engineering Geology*, 96(1-2):1–16.

Dutta, T., Otsubo, M., Kuwano, R., and O'Sullivan, C. (2020). Evolution of shear wave velocity during triaxial compression. *Soils and Foundations*, 60(6):1357–1370.

Finno, R. J., Harris, W. W., Mooney, M. A., and Viggiani, G. (1996). Strain localization and undrained steady state of sand. *Journal of Geotechnical Engineering*, 122(6):462–473.

Gajo, A. and Muir Wood, D. (1999). A kinematic hardening constitutive model for sands: the multiaxial formulation. *International journal for numerical and analytical methods in geomechanics*, 23(9):925–965.

Ghafghazi, M., Shuttle, D., and DeJong, J. (2014). Particle breakage and the critical state of sand. *Soils and Foundations*, 54(3):451–461.

Guida, G., Viggiani, G. M., and Casini, F. (2020). Multi-scale morphological descriptors from the fractal analysis of particle contour. *Acta Geotechnica*, 15(5):1067–1080.

Hanaor, D., Gan, Y., Revay, M., Airey, D., and Einav, I. (2016). 3d printable geomaterials. *Géotechnique*, 66(4):323–332.

Hussien, M. N. and Karray, M. (2015). Shear wave velocity as a geotechnical parameter: an overview. *Canadian Geotechnical Journal*, 53(2):252–272.

Iwasaki, T. and Tatsuoka, F. (1977). Effects of grain size and grading on dynamic shear moduli of sands. *Soils and foundations*, 17(3):19–35.

Jiménez, M., Romero, L., Domínguez, I. A., Espinosa, M. d. M., and Domínguez, M. (2019). Additive manufacturing technologies: an overview about 3d printing methods and future prospects. *Complexity*, 2019.

Kirkpatrick, W. (1965). Effects of grain size and grading on the shearing behaviour of granular materials. In *Proceedings of the sixth International Conference on Soil Mechanics and Foundation Engineering*, pages 273–277.

Liu, X. and Yang, J. (2018). Shear wave velocity in sand: effect of grain shape. *Géotechnique*, 68(8):742–748.

Liu, X., Zou, D., Liu, J., Zheng, B., Zhou, C., and Bai, J. (2021). A gradation-dependent particle shape factor for characterizing small-strain shear modulus of sand-gravel mixtures. *Transportation Geotechnics*, 28:100548.

Maki, I. P., Boulanger, R. W., DeJong, J. T., and Jaeger, R. A. (2014). State-based overburden normalization of cone penetration resistance in clean sand. *Journal of Geotechnical and Geoenvironmental Engineering*, 140(2):04013006.

Marschi, N. D., Chan, C. K., and Seed, H. B. (1972). Evaluation of properties of rockfill materials. *Journal of the Soil Mechanics and Foundations Division*, 98(1):95–114.

Matsumura, S., Kobayashi, T., Mizutani, T., and Bathurst, R. J. (2017). Manufacture of bonded granular soil using x-ray ct scanning and 3d printing. *Geotechnical Testing Journal*, 40(6):1000–1010.

Menq, F.-Y. (2003). *Dynamic properties of sandy and gravelly soils*. PhD thesis.

Miskin, M. Z. and Jaeger, H. M. (2013). Adapting granular materials through artificial evolution. *Nature materials*, 12(4):326–331.

Mitchell, J. K., Soga, K., et al. (2005). *Fundamentals of soil behavior*, volume 3. John Wiley & Sons New York.

Najmon, J. C., Raeisi, S., and Tovar, A. (2019). Review of additive manufacturing technologies and applications in the aerospace industry. *Additive manufacturing for the aerospace industry*, pages 7–31.

Ngo, T. D., Kashani, A., Imbalzano, G., Nguyen, K. T., and Hui, D. (2018). Additive manufacturing (3d printing): A review of materials, methods, applications and challenges. *Composites Part B: Engineering*, 143:172–196.

Patel, A., Bartake, P., and Singh, D. (2009). An empirical relationship for determining shear wave velocity in granular materials accounting for grain morphology. *Geotechnical Testing Journal*, 32(1):1–10.

Payan, M., Khoshghalb, A., Senetakis, K., and Khalili, N. (2016a). Effect of particle shape and validity of gmax models for sand: A critical review and a new expression. *Computers and Geotechnics*, 72:28–41.

Payan, M., Khoshghalb, A., Senetakis, K., and Khalili, N. (2016b). Small-strain stiffness of sand subjected to stress anisotropy. *Soil Dynamics and Earthquake Engineering*, 88:143–151.

Pestana, J. M. and Whittle, A. (1995). Compression model for cohesionless soils. *Géotechnique*, 45(4):611–631.

Riemer, M. F. and Seed, R. B. (1997). Factors affecting apparent position of steady-state line. *Journal of geotechnical and geoenvironmental engineering*, 123(3):281–288.

Riemer, M. F., Seed, R. B., Nicholson, P. G., and Jong, H.-L. (1990). Steady state testing of loose sands: limiting minimum density. *Journal of Geotechnical engineering*, 116(2):332–337.

Roberts, J. (1958). The compressibility of sand. *Proc., Am. Soc. for Testing Mat.*, 58:1269–1277.

Robertson, P., Sasitharan, S., Cunning, J., and Sego, D. (1995). Shear-wave velocity to evaluate in-situ state of ottawa sand. *Journal of Geotechnical Engineering*, 121(3):262–273.

Russell, A. R. and Khalili, N. (2004). A bounding surface plasticity model for sands exhibiting particle crushing. *Canadian Geotechnical Journal*, 41(6):1179–1192.

Sadrekarimi, A. and Olson, S. M. (2010). Particle damage observed in ring shear tests on sands. *Canadian Geotechnical Journal*, 47(5):497–515.

Santamarina, J. C. (2003). Soil behavior at the microscale: particle forces. In *Soil behavior and soft ground construction*, pages 25–56.

Senetakis, K., Anastasiadis, A., and Pitilakis, K. (2012). The small-strain shear modulus and damping ratio of quartz and volcanic sands. *Geotechnical Testing Journal*, 35(6):964–980.

Sharifipour, M., Dano, C., and Hicher, P.-Y. (2004). Wave velocities in assemblies of glass beads using bender-extender elements. In *17th ASCE Engineering Mechanics Conference*.

Sladen, J., D'hollander, R., and Krahn, J. (1985). The liquefaction of sands, a collapse surface approach. *Canadian geotechnical journal*, 22(4):564–578.

Su, Y. F., Lee, S. J., and Sukumaran, B. (2020). Influence of particle morphology simplification on the simulation of granular material behavior. *Granular Matter*, 22(1):1–12.

Sukumaran, B. and Ashmawy, A. (2001). Quantitative characterisation of the geometry of discret particles. *Geotechnique*, 51(7):619–627.

Torres-Cruz, L. A. and Santamarina, J. C. (2020). The critical state line of nonplastic tailings. *Canadian Geotechnical Journal*, 57(10):1508–1517.

Tsomokos, A. and Georgiannou, V. (2010). Effect of grain shape and angularity on the undrained response of fine sands. *Canadian Geotechnical Journal*, 47(5):539–551.

Vangla, P. and Latha, G. M. (2015). Influence of particle size on the friction and interfacial shear strength of sands of similar morphology. *International Journal of Geosynthetics and Ground Engineering*, 1(1):6.

Verdugo, R. and Ishihara, K. (1996). The steady state of sandy soils. *Soils and foundations*, 36(2):81–91.

Vilhar, G., Jovičić, V., and Coop, M. R. (2013). The role of particle breakage in the mechanics of a non-plastic silty sand. *Soils and Foundations*, 53(1):91–104.

Wadell, H. (1932). Volume, shape, and roundness of rock particles. *The Journal of Geology*, 40(5):443–451.

Wang, J.-J., Zhang, H.-P., Tang, S.-C., and Liang, Y. (2013). Effects of particle size distribution on shear strength of accumulation soil. *Journal of Geotechnical and Geoenvironmental Engineering*, 139(11):1994–1997.

Wei, D., Wang, J., and Zhao, B. (2018). A simple method for particle shape generation with spherical harmonics. *Powder technology*, 330:284–291.

Wichtmann, T. and Triantafyllidis, T. (2009). Influence of the grain-size distribution curve of quartz sand on the small strain shear modulus g max. *Journal of geotechnical and geoenvironmental engineering*, 135(10):1404–1418.

Wood, D. M. (1990). *Soil Behaviour and Critical State Soil Mechanics*. Cambridge University Press.

Xiao, Y., Long, L., Matthew Evans, T., Zhou, H., Liu, H., and Stuedlein, A. W. (2019). Effect of particle shape on stress-dilatancy responses of medium-dense sands. *Journal of Geotechnical and Geoenvironmental Engineering*, 145(2):04018105.

Yang, J. and Gu, X. (2013). Shear stiffness of granular material at small strains: does it depend on grain size? *Géotechnique*, 63(2):165–179.

Yang, J. and Luo, X. (2015). Exploring the relationship between critical state and particle shape for granular materials. *Journal of the Mechanics and Physics of Solids*, 84:196–213.

Zelasko, J. S., Krizek, R. J., and Edil, T. B. (1975). Shear behavior of sands as a function of grain characteristics. *[No source information available]*, 1:55–64.

Zhang, H. and Garga, V. K. (1997). Quasi-steady state: a real behaviour? *Canadian Geotechnical Journal*, 34(5):749–761.

Zhang, J., Lo, S.-C. R., Rahman, M. M., and Yan, J. (2018). Characterizing monotonic behavior of pond ash within critical state approach. *Journal of Geotechnical and Geoenvironmental Engineering*, 144(1):04017100.

Zheng, J. and Hryciw, R. D. (2015). Traditional soil particle sphericity, roundness and surface roughness by computational geometry. *Géotechnique*, 65(6):494–506.

5.7 Tables and Figures

Table 5.1: Average and standard deviation (in parenthesis) of shape parameters and index properties of the 3D printed sand mixes

Soil Specimen	R	S_C	R_G	e_{max}	e_{min}	D_{50}	C_u	C_c
Mix 2	0.73 (0.09)	0.75 (0.10)	0.74 (0.08)	0.787 (0.036)	0.490 (0.004)	3.2	1.47	1.02
Mix 3	0.61 (0.12)	0.75 (0.04)	0.68 (0.07)	0.776 (0.008)	0.483 (0.008)	2.5	1.26	0.95
Mix 4	0.52 (0.13)	0.66 (0.10)	0.59 (0.08)	0.825 (0.008)	0.507 (0.006)	3.2	1.47	1.02
Mix 6	0.55 (0.13)	0.65 (0.05)	0.60 (0.07)	0.812 (0.013)	0.499 (0.011)	2.5	1.26	0.95
Mix 7	0.48 (0.12)	0.53 (0.04)	0.50 (0.06)	0.861 (0.012)	0.513 (0.005)	2.5	1.26	0.95
Mix 8	0.54 (0.11)	0.84 (0.04)	0.69 (0.07)	0.849 (0.027)	0.501 (0.009)	2.5	1.26	0.95

Note: R = roundness; S_C = circle ratio sphericity; R_G = regularity; e_{max} = maximum void ratio; e_{min} = minimum void ratio; D_{50} = median particle size; C_u = coefficient of uniformity; C_c = coefficient of curvature

Table 5.2: Summary of the triaxial tests performed

Soil specimen	Test ID	Test type	σ'_{3c} (kPa)	e_{eoc}	$D_{R(eoc)}$ (%)	e_f	ψ_0	$p'_{residual}$ (kPa)	$q_{residual}$ (kPa)	$(q/p')_{residual}$
Mix 2	2-CD-20	ICD	20	0.667	40%	0.654	-0.02	27	26	0.97
	2-CD-30		30	0.653	45%	0.634	0.00	40	34	0.85
	2-CD-50		50	0.624	55%	0.599	0.01	66	50	0.77
	2-CD-70		70	0.590	66%	0.571	0.00	91	68	0.75
	2-CD-90		90	0.556	78%	0.539	-0.01	116	81	0.70
Mix 3	3-CD-20	ICD	20	0.676	34%	0.681	-0.04	33	38	1.14
	3-CD-30		30	0.665	38%	0.665	-0.03	45	49	1.08
	3-CD-50		50	0.638	47%	0.641	-0.02	73	70	0.97
	3-CD-70		70	0.623	52%	0.613	-0.01	100	87	0.88
	3-CD-90		90	0.586	65%	0.593	-0.03	126	103	0.82
	3-CU-40	ICU	40	0.650	43%	0.650	-0.02	62	57	0.91
	3-CU-80		80	0.601	60%	0.601	-0.03	116	96	0.83
Mix 4	4-CD-20	ICD	20	0.703	38%	0.683	-0.01	28	29	1.03
	4-CD-30		30	0.688	43%	0.662	0.01	41	36	0.89
	4-CD-50		50	0.651	55%	0.627	0.01	67	52	0.78
	4-CD-70		70	0.628	62%	0.601	0.01	95	78	0.82
	4-CD-90		90	0.609	68%	0.581	0.01	119	90	0.75
Mix 6	6-CD-20	ICD	20	0.717	30%	0.701	-0.02	33	38	1.14
	6-CD-30		30	0.707	34%	0.692	-0.01	46	48	1.03
	6-CD-50		50	0.677	43%	0.668	-0.01	73	67	0.92
	6-CD-70		70	0.664	47%	0.656	0.00	98	85	0.86
	6-CD-90		90	0.619	62%	0.625	-0.03	128	109	0.85
	6-CU-40	ICU	40	0.687	40%	0.687	-0.01	55	46	0.84
	6-CU-80		80	0.633	57%	0.633	-0.02	91	72	0.79
Mix 7	7-CD-20	ICD	20	0.739	35%	0.729	-0.02	35	42	1.21
	7-CD-30		30	0.724	39%	0.711	-0.02	49	56	1.14
	7-CD-50		50	0.704	45%	0.696	-0.01	77	79	1.03
	7-CD-70		70	0.679	52%	0.671	-0.02	102	94	0.93
	7-CD-90		90	0.657	59%	0.656	-0.02	129	115	0.89
	7-CU-40	ICU	40	0.704	45%	0.704	-0.02	61	63	1.03
	7-CU-80		80	0.661	57%	0.661	-0.03	129	113	0.87
Mix 8	8-CD-20	ICD	20	0.716	38%	0.715	-0.03	33	40	1.21
	8-CD-30		30	0.697	44%	0.700	-0.03	45	45	0.99
	8-CD-50		50	0.678	49%	0.672	-0.02	72	63	0.88
	8-CD-70		70	0.652	57%	0.651	-0.02	98	83	0.85
	8-CD-90		90	0.637	61%	0.646	-0.02	124	100	0.81
	8-CU-40	ICU	40	0.694	45%	0.694	-0.01	55	53	0.97
	8-CU-80		80	0.649	57%	0.649	-0.02	106	86	0.82

Note: σ'_{3c} = effective confining pressure; e_{eoc} = void ratio at the end of consolidation; $D_{R(eoc)}$ = relative density at the end of consolidation; e_f = void ratio at the end of test; $p'_{residual}$ = end of test mean effective stress; $q_{residual}$ = end of test deviatoric stress

Table 5.3: Database compiled from literature

Soil	D_{50} (mm)	C_u	R	S_C	R_G	e_{max}	e_{min}	M	λ	e_Γ	References
Nevada sand	0.15	1.8	0.60	0.85	0.73	0.850	0.570	1.24	0.071	1.040	
Ticino sand	0.58	1.5	0.40	0.80	0.60	0.990	0.574	1.51	0.053	1.050	
Margaret river sand	0.49	1.9	0.70	0.70	0.70	0.870		1.33	0.051	0.840	
ASTM 20/30 sand	0.60	1.4	0.80	0.90	0.85	0.690		1.29	0.053	0.740	
Ponte Vedra sand	0.18	1.8	0.30	0.85	0.58	1.070		1.59	0.061	1.010	
8M8 crushed sand	0.38	3.3	0.20	0.70	0.45	0.970		1.64	0.138	1.160	
9C1 crushed sand	0.52	2.3	0.25	0.70	0.48	0.910		1.59	0.067	1.060	
Jekyll Island sand	0.17	1.7	0.30	0.85	0.58	1.040		1.64	0.053	0.980	Cho et al. [2006]
ASTM graded sand	0.35	1.7	0.80	0.90	0.85	0.820	0.500	1.20	0.080	0.869	
Blasting sand	0.71	1.9	0.30	0.55	0.43	1.025	0.698	1.37	0.069	1.099	
Glass beads	0.32	1.4	1.00	1.00	1.00	0.720	0.542	0.81	0.039	0.807	
Granite powder	0.09	6.2	0.40	0.24	0.32	1.296	0.482	1.37	0.070	1.124	
Ottawa 20/30 sand	0.72	1.2	0.90	0.90	0.90	0.742	0.502	1.07	0.047	0.802	
Ottawa F-110 sand	0.12	1.7	0.70	0.70	0.70	0.848	0.535	1.24	0.077	0.937	
7U7 crushed sand	0.30	3.2	0.20	0.80	0.50	0.790		1.51	0.064	1.060	
Brasted sand	0.26	2.4	0.67			0.790	0.480	1.30	0.051	0.912	Cornforth [1964]
Sand B	0.15	1.8	0.80			0.840	0.500	1.22	0.041	0.791	Castro [1969]
Sand C	0.28	2.3	0.27			0.990	0.660	1.37	0.088	0.988	
Leighton Buzzard sand	0.12	1.5	0.41			1.020	0.670	1.24	0.053	0.975	Been et al. [1991]
Erksak sand	0.33	1.8	0.65			0.810	0.610	1.24	0.044	0.875	
Masonry sand	0.32	1.3	0.68			0.880	0.600	1.16	0.041	0.900	Finno et al. [1996]
Ottawa C109	0.35	1.6	0.75	0.80	0.78	0.820	0.500	1.20	0.032	0.926	
Toyoura sand	0.17	1.7	0.42	0.65	0.54	0.970	0.640	1.32	0.060	1.048	
Lornex	0.30	2.0	0.22	0.70	0.46	1.080	0.680	1.42	0.115	1.100	Robertson et al. [1995]
Brenda	0.10	1.9	0.23	0.65	0.44	1.060	0.690	1.46	0.099	1.112	
Syncrude	0.17	2.4	0.81	0.70	0.76	0.930	0.550	1.20	0.039	0.847	
Kogyuk sand	0.35	1.7	0.42			0.780	0.520	1.24	0.064	0.845	Been and Jefferies [1985]
Nerkerk	0.23	2.0	0.43	0.75	0.59	0.940	0.620	1.20	0.069	0.885	Sladen et al. [1985]
Leighton Buzzard sand	0.86	1.2	0.42	0.82	0.62	0.820	0.540	1.20	0.053	1.030	
Reid Bedford sand	0.24	1.8	0.37			0.870	0.550	1.29	0.064	1.014	Been and Jefferies [2004]
Nevada sand	0.12	1.8	0.61	0.72	0.67	0.890	0.510	1.16	0.046	0.910	
Fraser River sand	0.25	1.7	0.28	0.50	0.39	1.000	0.600	1.40	0.067	1.110	Ghafghazi et al. [2014]
Toyoura sand	0.17	1.7	0.64	0.65	0.65	0.980	0.600	1.32	0.048	0.941	Verdugo and Ishihara [1996]
Hostun sand	0.32	1.8	0.42	0.62	0.52	1.000	0.660	1.35	0.069	0.969	Gajo and Muir Wood [1999]
Monterey sand	0.38	1.6	0.37	0.75	0.56	0.860	0.530	1.33	0.039	0.905	Riemer et al. [1990]
Crushed Unimin 2010	0.87	2.0	0.20			1.030	0.650	1.33	0.090	1.112	Zhang and Garga [1997]
Sydney sand	0.30	1.6	0.45	0.72	0.59	0.860	0.570	1.31	0.058	0.969	Chu et al. [1993]
Ottawa 20/40 sand	0.51	1.4	0.75	0.80	0.78	0.680	0.390	1.24	0.046	0.820	
Illinois River sand	0.50	2.5	0.25			0.760	0.460	1.33	0.113	0.920	Sadrekarimi and Olson [2010]
Mississippi River sand	0.10	5.0	0.40			1.040	0.560	1.37	0.081	0.820	

Table 5.3 Continued

Soil	D_{50} (mm)	C_u	R	S_C	R_G	e_{max}	e_{min}	M	λ	e_Γ	References
Ottawa 20-30	0.72	1.2	0.65	0.75	0.70	0.770	0.490	1.23			Zelasko et al. [1975]
Ottawa 35-45	0.42	1.2	0.60	0.75	0.68	0.820	0.480	1.31			
Ottawa 50-70	0.25	1.2	0.52	0.74	0.63	0.890	0.530	1.29			
Ottawa 70-100	0.18	1.2	0.50	0.73	0.62	0.920	0.540	1.29			
Ottawa 100-140	0.12	1.2	0.50	0.72	0.61	0.920	0.540	1.31			
Evanston Beach 20-30	0.72	1.2	0.44	0.71	0.58	0.920	0.550	1.32			
Evanston Beach 35-45	0.42	1.2	0.43	0.73	0.58	0.900	0.520	1.23			
Evanston Beach 50-70	0.25	1.2	0.41	0.73	0.57	0.920	0.540	1.32			
Evanston Beach 70-100	0.18	1.2	0.42	0.72	0.57	0.930	0.530	1.31			
Franklin Falls 20-30	0.72	1.2	0.36	0.52	0.44	1.010	0.620	1.38			
Franklin Falls 35-45	0.42	1.2	0.35	0.52	0.44	1.090	0.630	1.36			
Franklin Falls 50-70	0.25	1.2	0.34	0.52	0.43	1.100	0.640	1.38			
Brown Mortar	0.60	2.1	0.79	0.76	0.78	0.910	0.580	1.13			Cerato and Lutenegger [2006]
Ottawa	0.50	1.0	0.63	0.72	0.68	0.690	0.460	1.21			
Morie sand	1.30	1.8	0.24	0.75	0.50	0.780	0.590	1.46			
Gravel pack	2.80	2.1	0.29	0.73	0.51	0.830	0.670	1.48			
Ottawa 20	0.70	1.2	0.75	0.72	0.74	0.730	0.500	1.20			Cox and Budhu [2008]
Rillito River	0.56	2.0	0.50	0.65	0.58	0.730	0.420	1.37			
Silica 40	0.52	1.4	0.40	0.72	0.56	0.800	0.400	1.46			
Santa Cruz River	0.34	2.7	0.50	0.71	0.61	0.800	0.400	1.33			
Ticino sand	0.53	1.6	0.40	0.80	0.60	0.890	0.600	1.24	0.055	0.986	Maki et al. [2014]
Ottawa sand	0.53	1.5	0.75	0.80	0.78	0.790	0.490	1.13	0.028	0.754	
Hokksund sand	0.39	2.0	0.50			0.910	0.550	1.29	0.055	0.934	
Monterey sand	0.37	1.6	0.70			0.820	0.540	1.29	0.030	0.878	
Fontainebleau sand	0.20	1.4	0.55	0.69	0.62	0.870	0.540	1.24	0.069	0.980	Tsomokos and Georgiannou [2010]
Sacramento sand	0.30	1.7	0.65	0.65	0.65	0.870	0.530	1.34	0.039	0.905	Riemer and Seed [1997]
Fujian sand	0.51	1.2	0.49	0.75	0.62			1.21	0.039	0.890	Yang and Luo [2015]
Daytona Beach sand	0.23	1.4	0.62	0.70	0.66	1.000	0.640	1.30			Sukumaran and Ashmawy [2001]
Ottawa #20/70 sand	0.53	2.4	0.76	0.81	0.79	0.780	0.470	1.10			
Ottawa #45 sand	0.57	2.1	0.45	0.68	0.57	1.110	0.750	1.36			
Ottawa #60/80 sand	0.21	2.4	0.65	0.78	0.72	0.850	0.550	1.22			
Ottawa #90 sand	0.27	2.2	0.40	0.60	0.50	1.100	0.730	1.30			
Syncrude tailings	0.18	2.5	0.47	0.62	0.55	0.910	0.590	1.37			

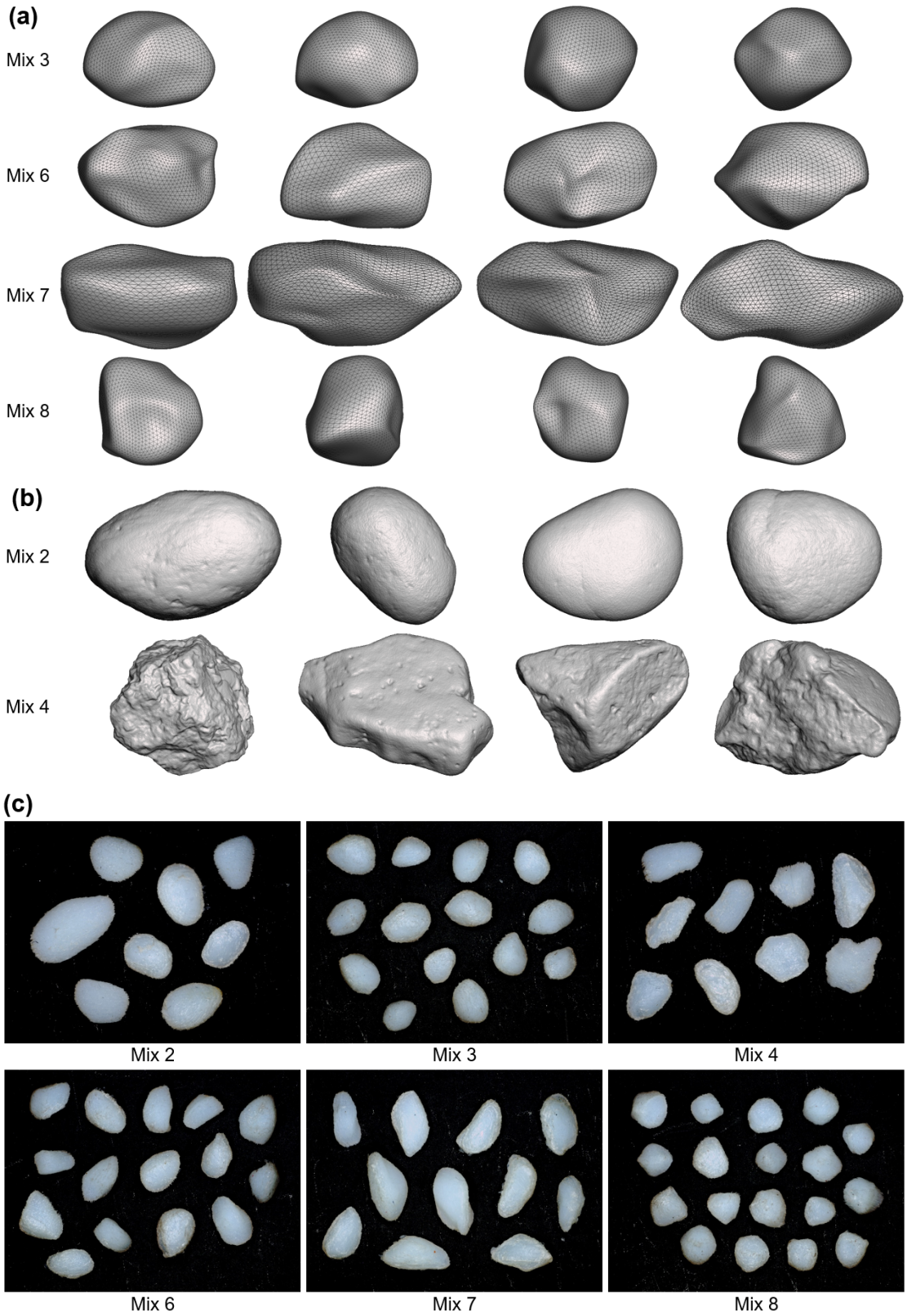

Figure 5.1: (a) 3D mesh of synthetic particles generated, (b) X-ray CT scans of mixes 2 and 4, and (c) 3D printed particles used in this study (not to scale). Note: mixes 3, 6, 7 and 8 were created using spherical harmonics [after Wei et al., 2018]; and mixes 2 and 4 were generated from X-ray CT scans of rounded and angular sands, respectively

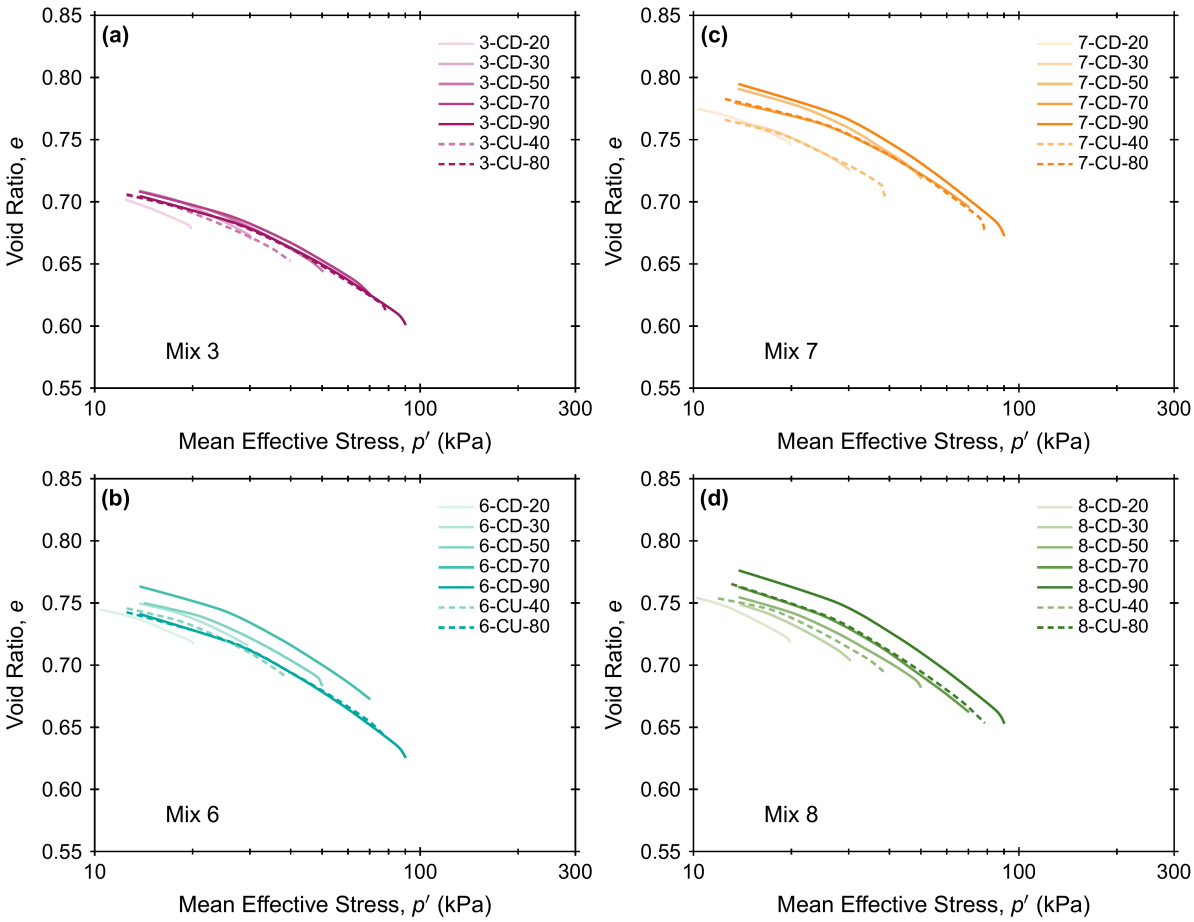

Figure 5.2: Isotropic consolidation curves for (a) sand mix 3, (b) sand mix 6, (c) sand mix 7, and (d) sand mix 8

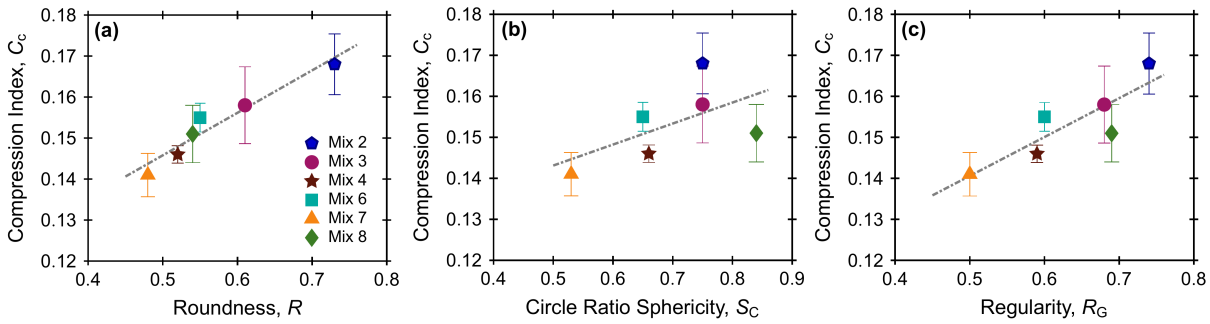

Figure 5.3: Variation of compressibility index (C_c) of all the sand mixes with (a) roundness, (b) circle ratio sphericity, and (c) regularity. Note: standard deviation of the average values are shown as error bars

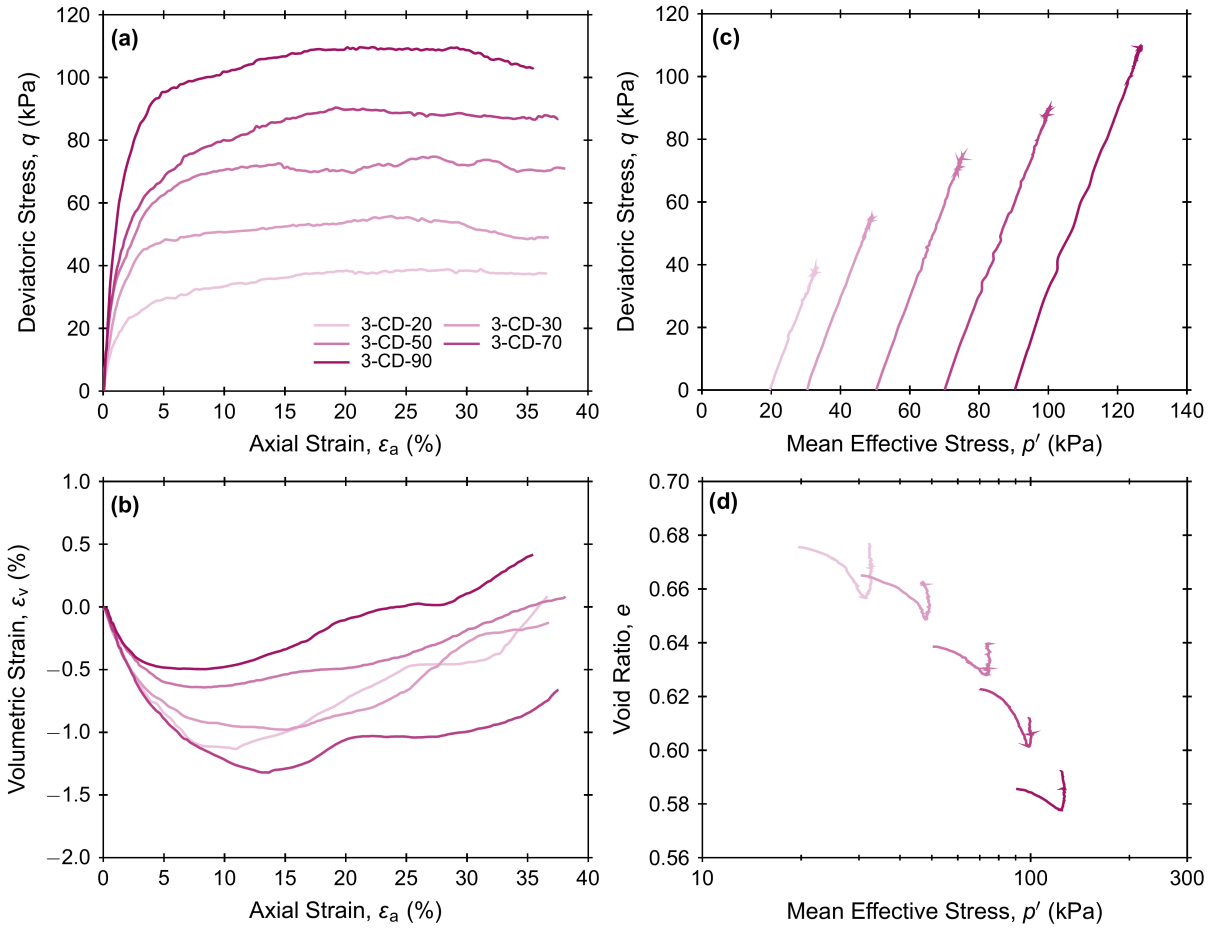

Figure 5.4: Drained triaxial test results on sand mix 3

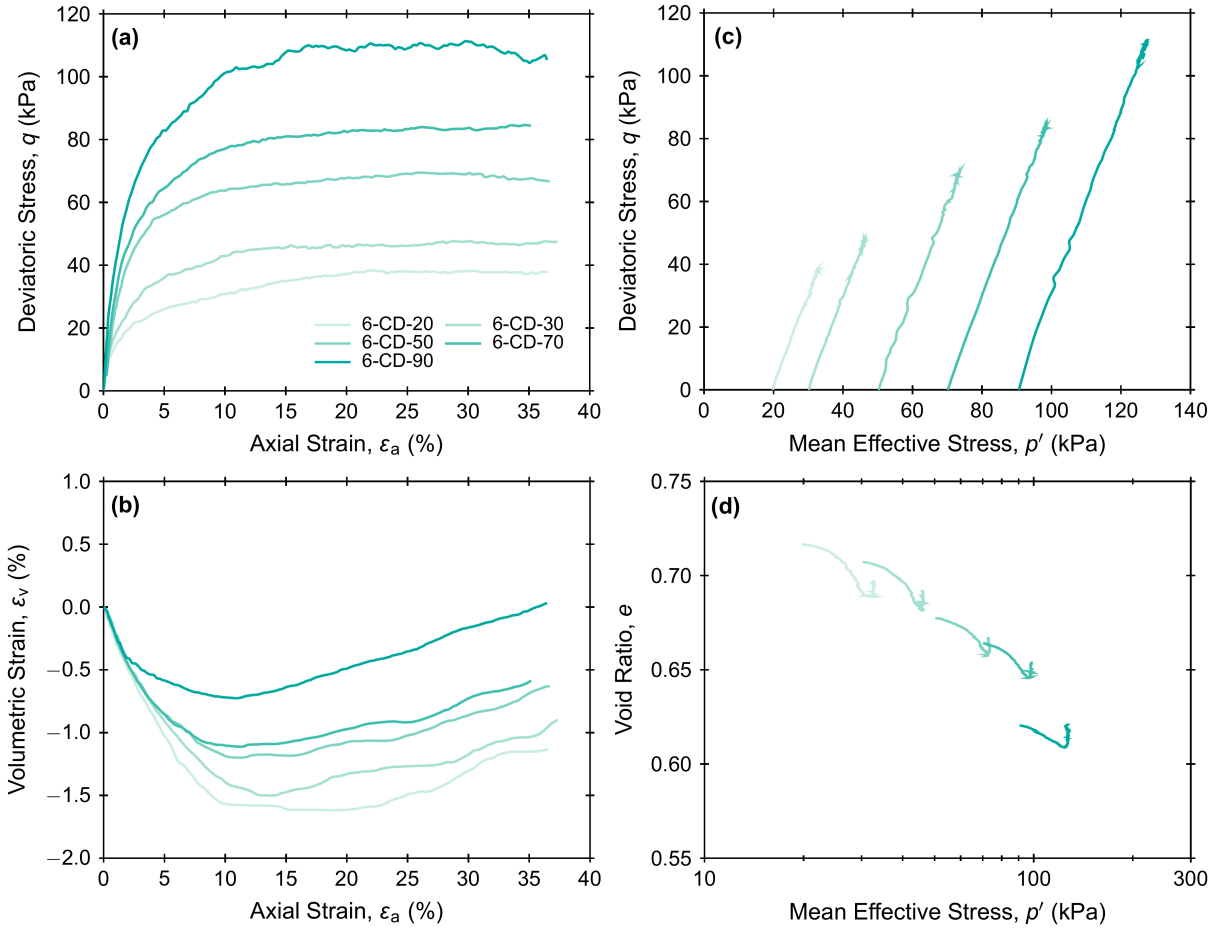

Figure 5.5: Drained triaxial test results on sand mix 6

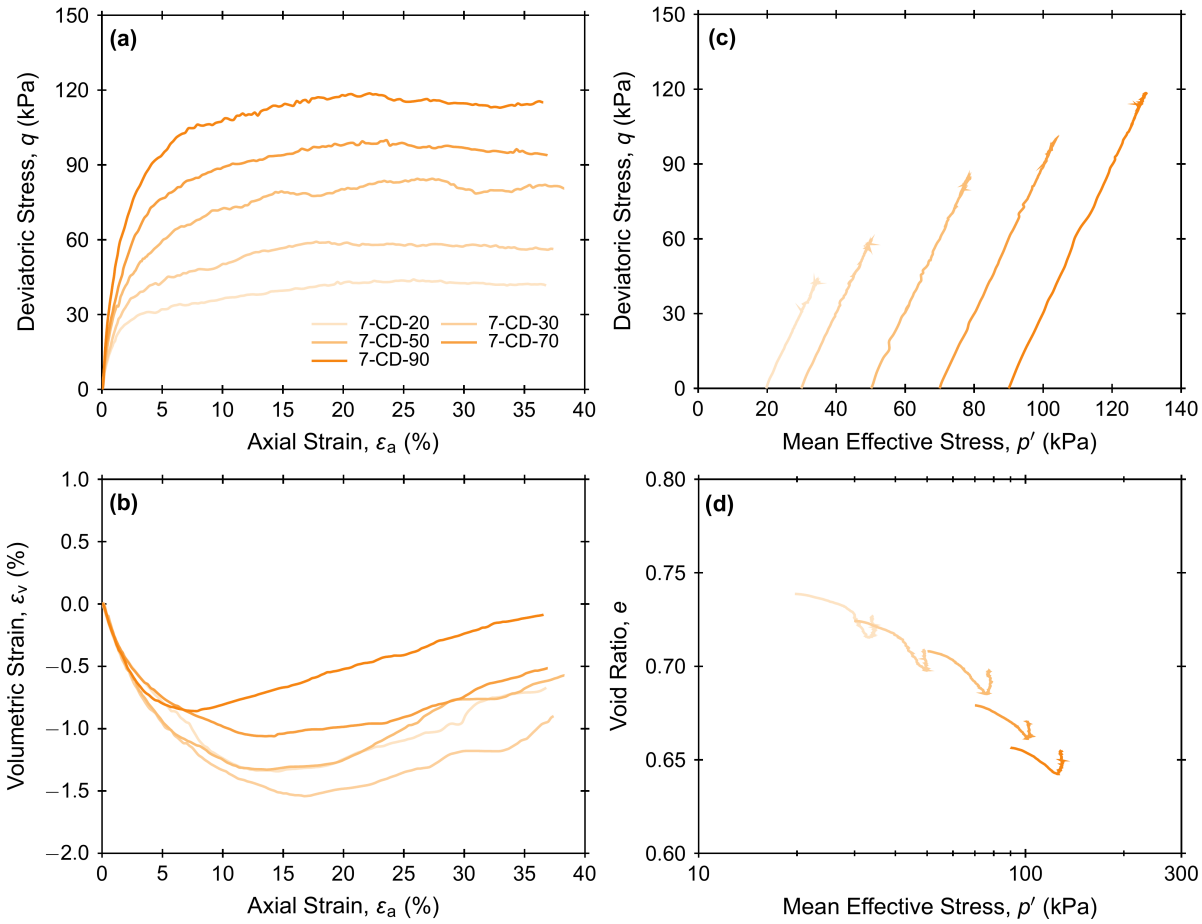

Figure 5.6: Drained triaxial test results on sand mix 7

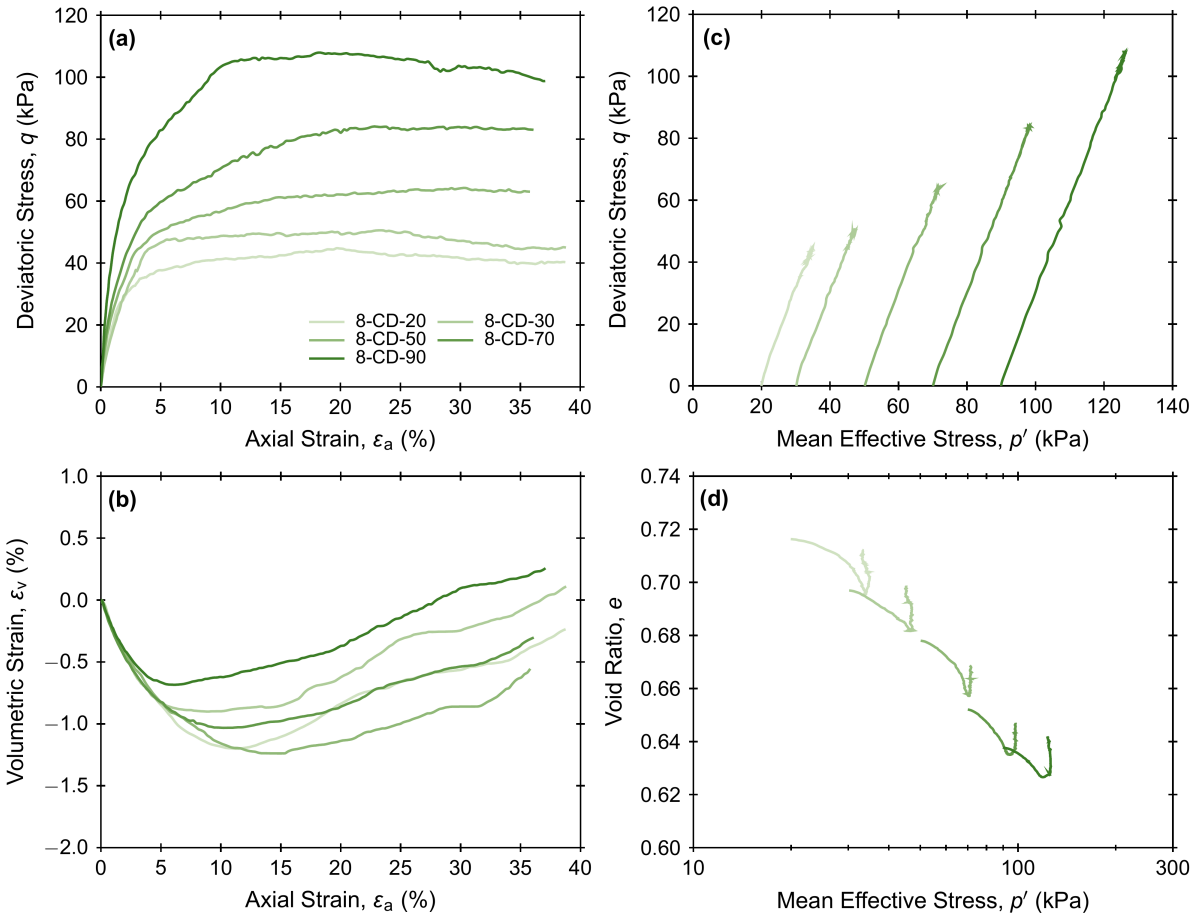

Figure 5.7: Drained triaxial test results on sand mix 8

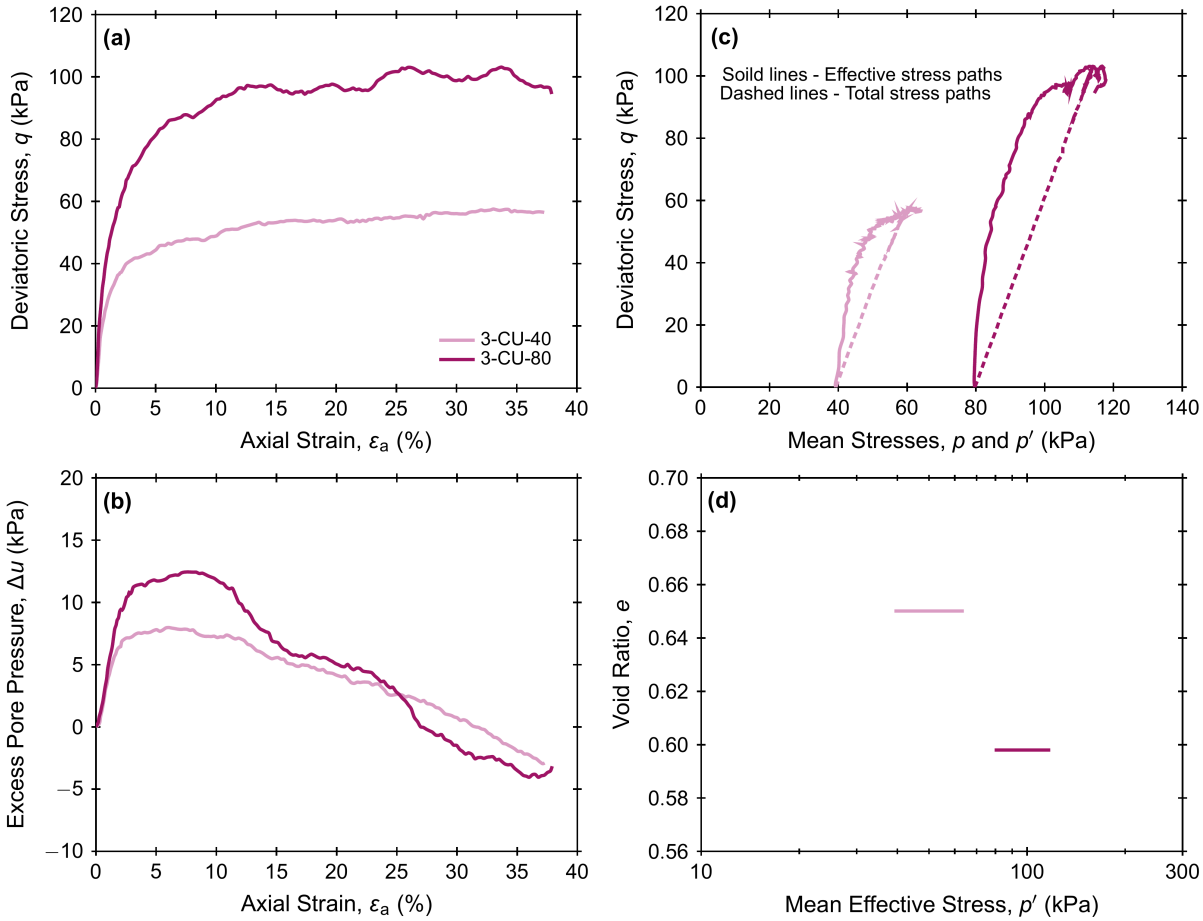

Figure 5.8: Undrained triaxial test results on sand mix 3

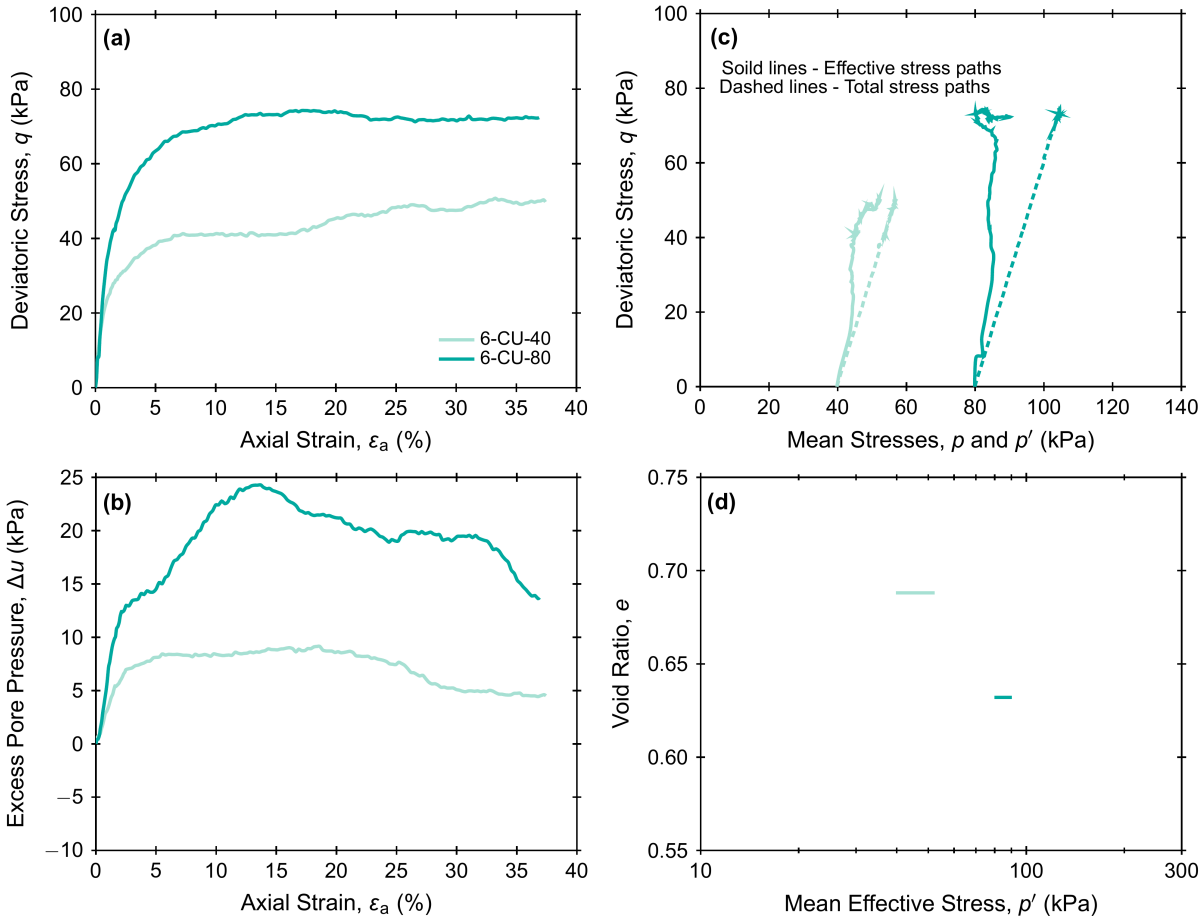

Figure 5.9: Undrained triaxial test results on sand mix 6

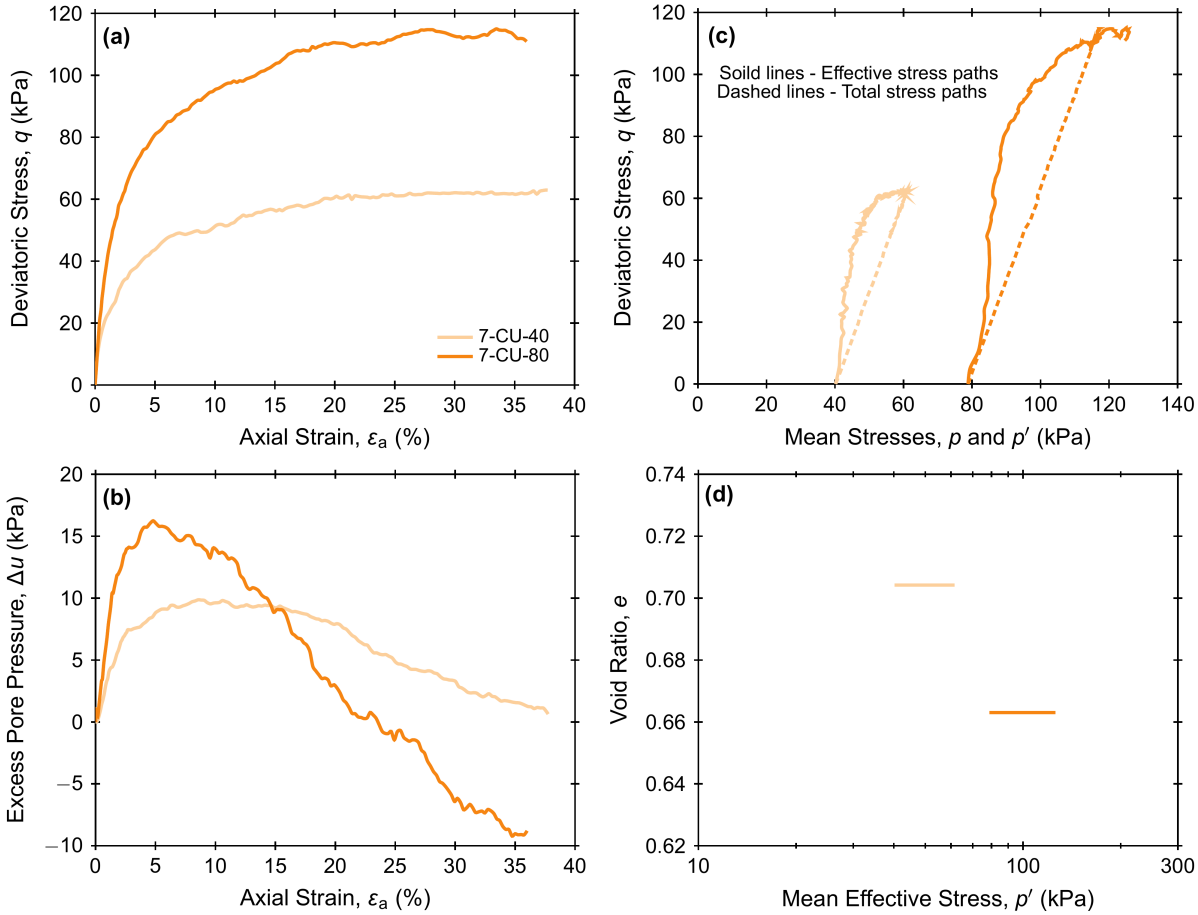

Figure 5.10: Undrained triaxial test results on sand mix 7

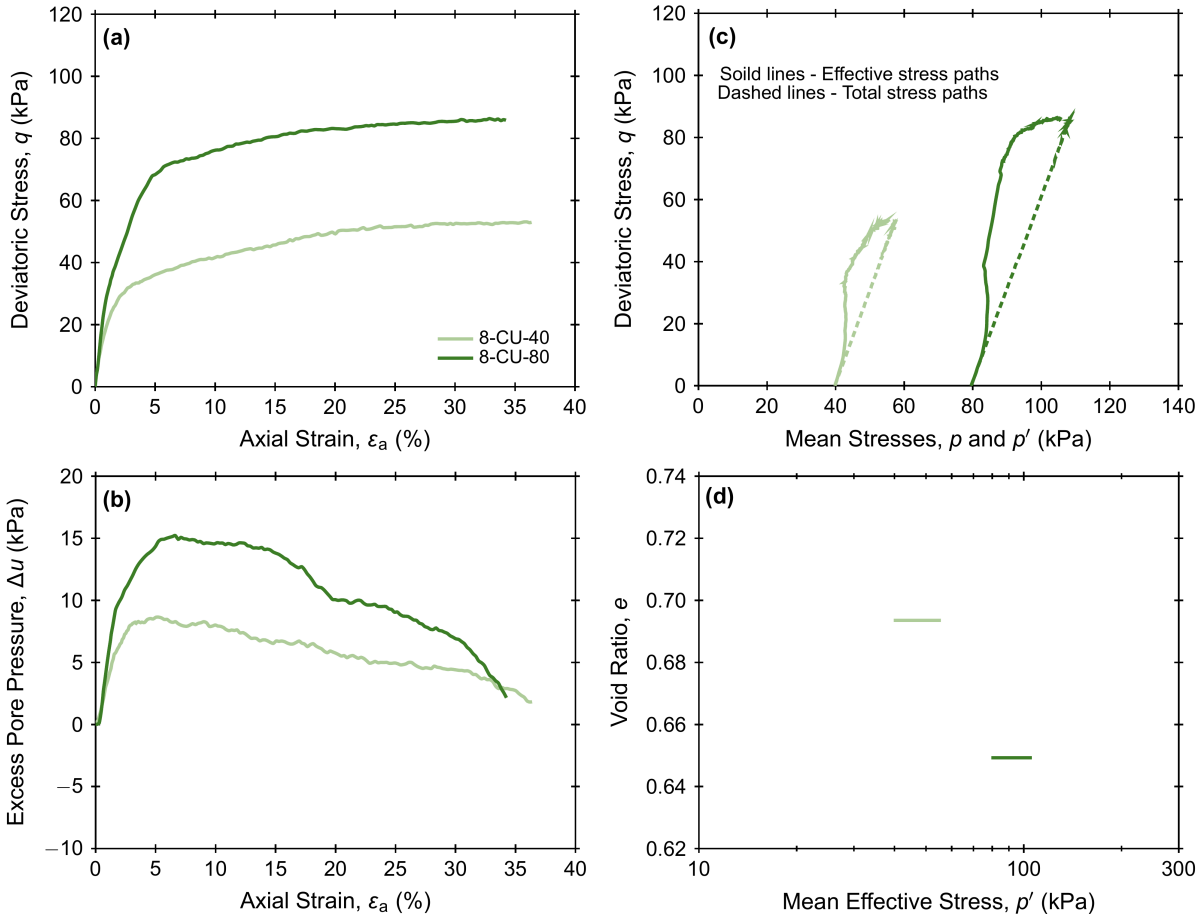

Figure 5.11: Undrained triaxial test results on sand mix 8

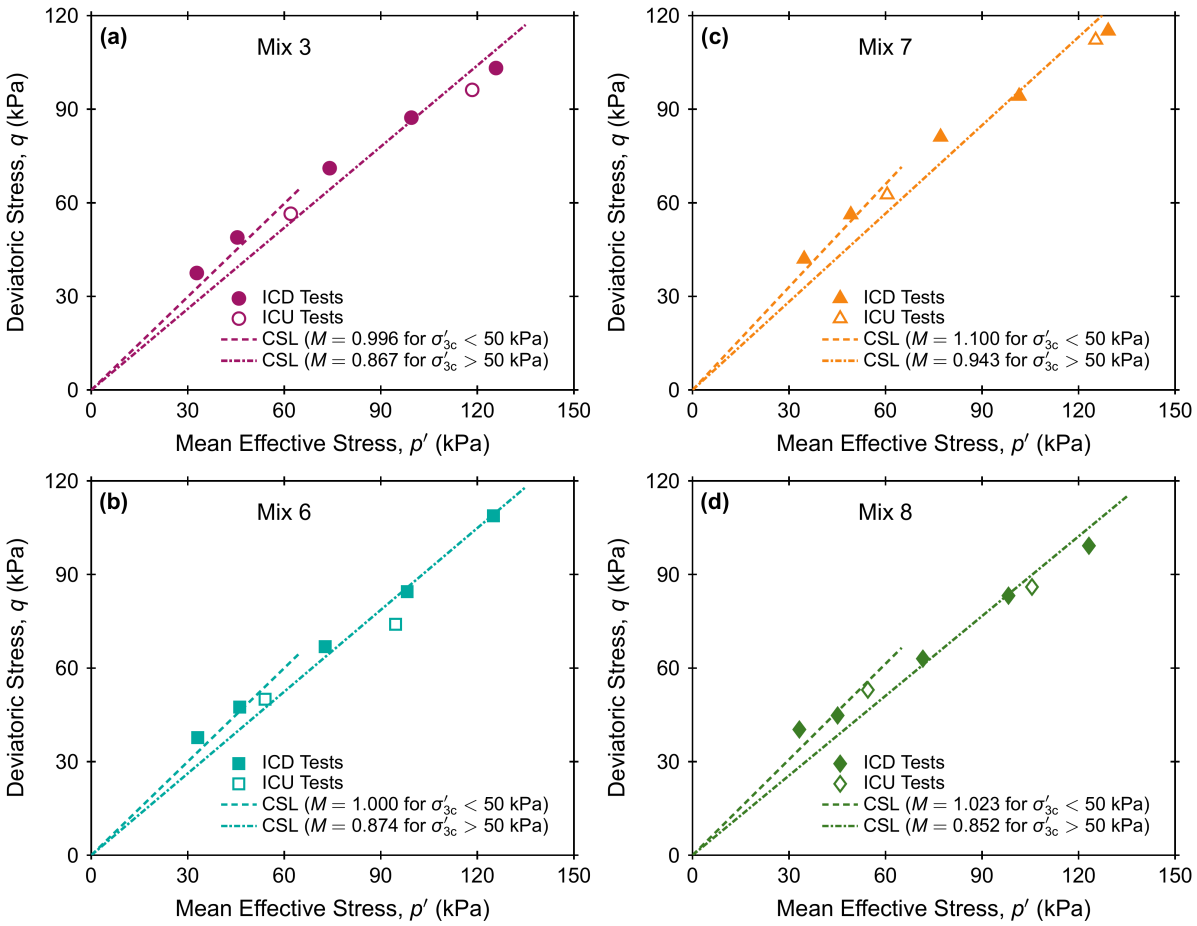

Figure 5.12: Critical state lines in $q - p'$ space approximated for (a) sand mix 3, (b) sand mix 6, (c) sand mix 7, and (d) sand mix 8

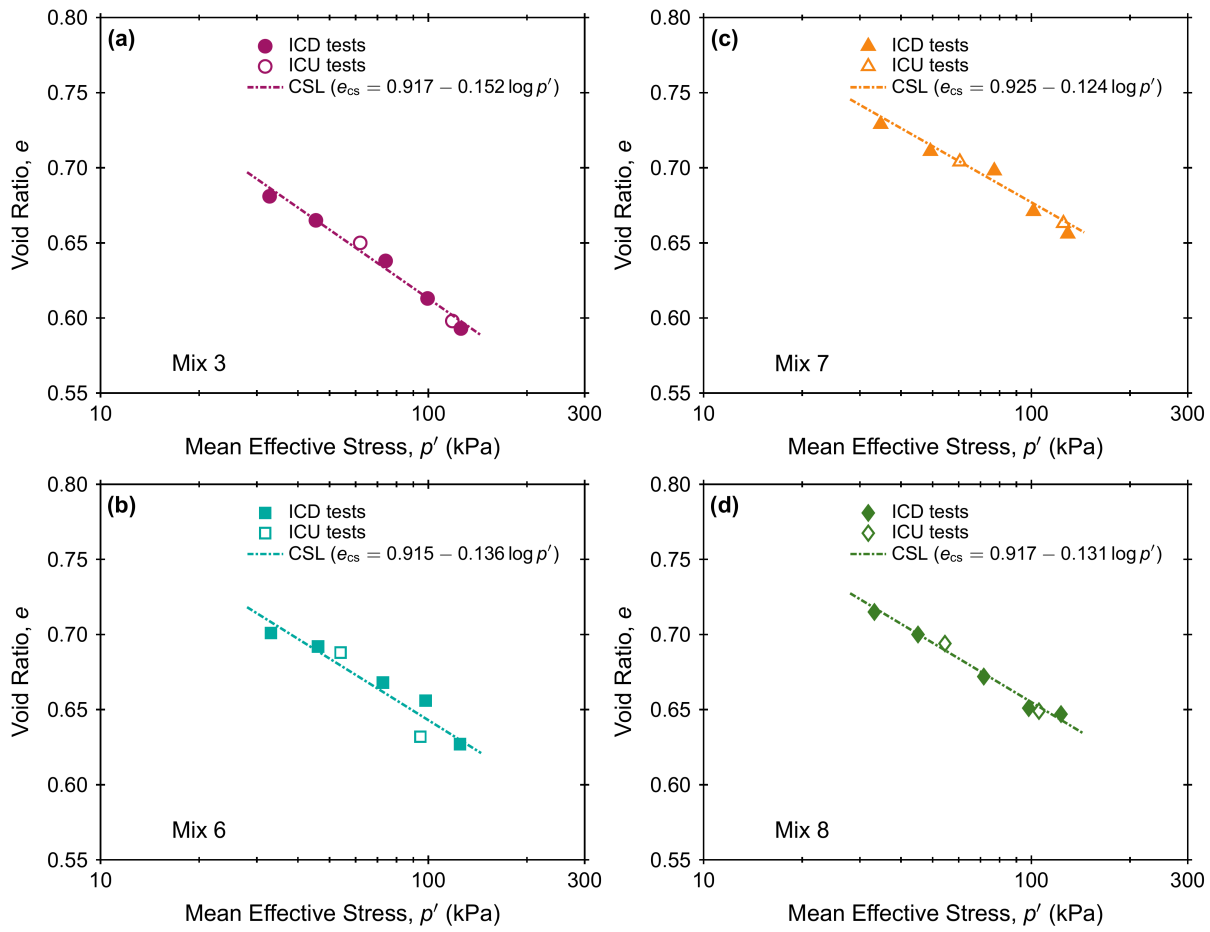

Figure 5.13: Critical state lines in $e - \log p'$ space approximated for (a) sand mix 3, (b) sand mix 6, (c) sand mix 7, and (d) sand mix 8

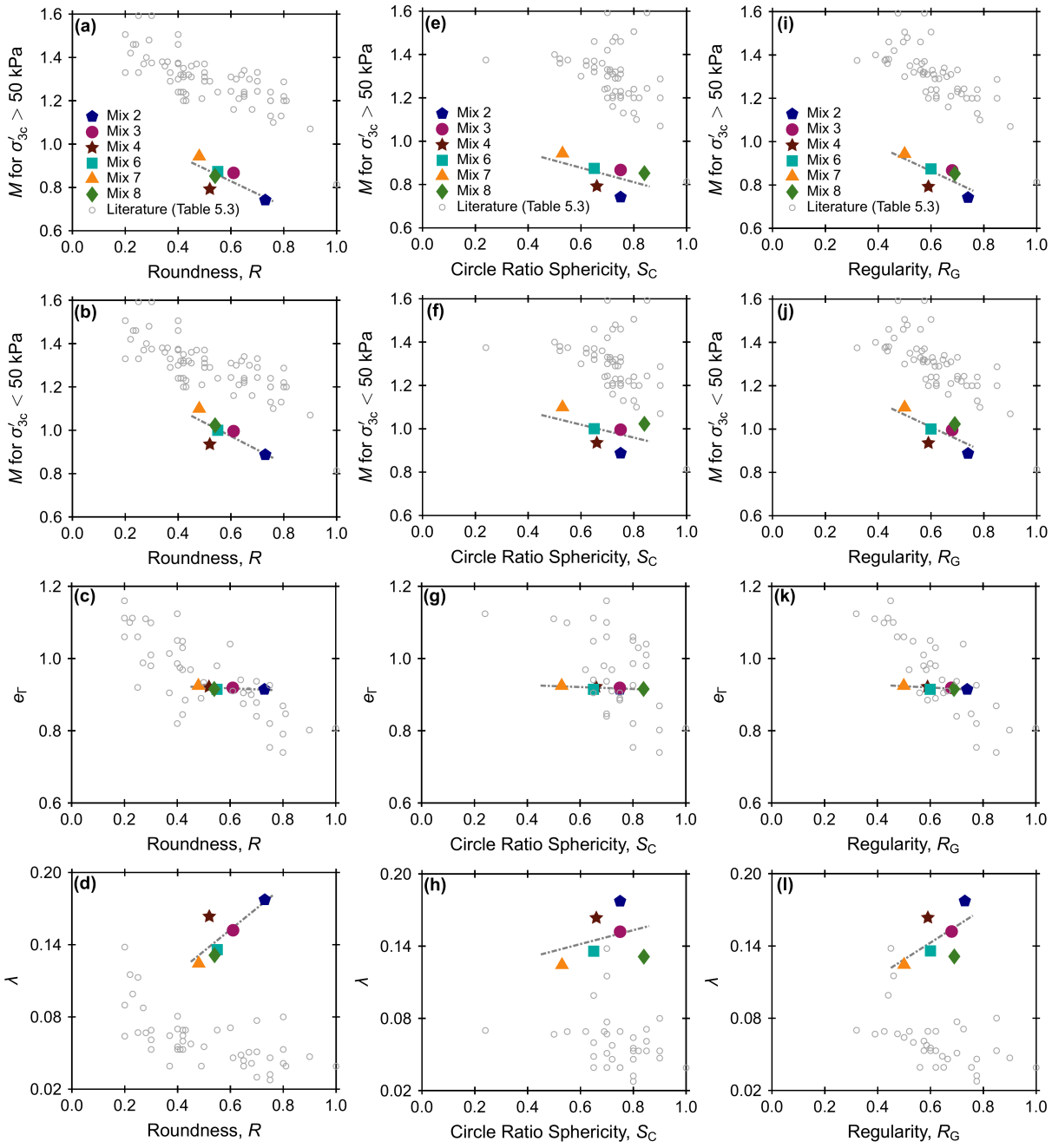

Figure 5.14: Variation of critical state parameters M for σ'_{3c} greater than 50 kPa, M for σ'_{3c} less than 50 kPa, e_Γ, and λ with (a, b, c, d) roundness, (e, f, g, h) sphericity, and (i, j, k, l) regularity

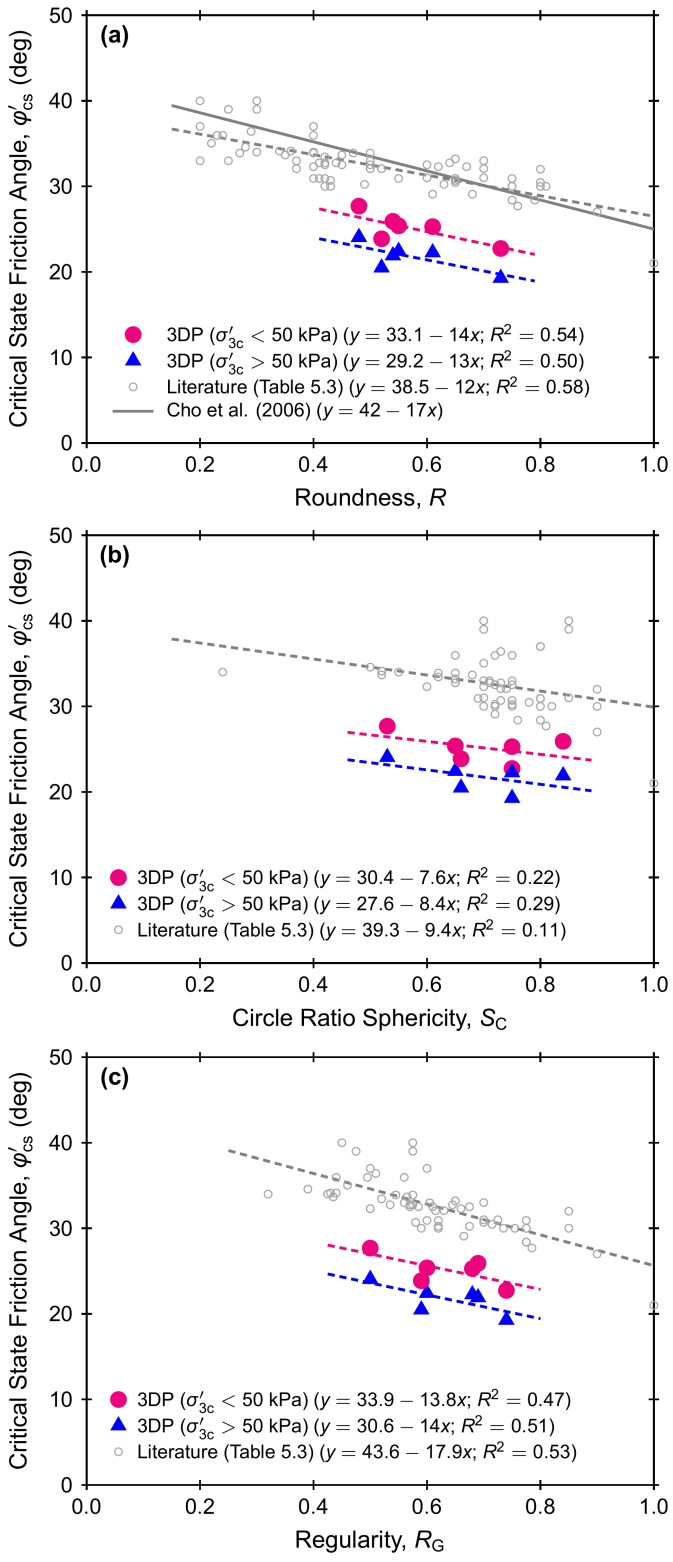

Figure 5.15: Variation of critical state friction angles (ϕ'_{cs}) with (a) roundness, (b) sphericity, and (c) regularity

Chapter 6

Drained and Undrained Triaxial Compression Behavior of Soils with Different Gradations and Particle Sizes

This chapter is prepared for submission in the *Journal of Geotechnical and Geoenvironmental Engineering (ASCE)* under the following citation and is presented herein with minor edits. Ahmed, S. S., Martinez, A. and DeJong, J. T. (2021). Drained and Undrained Triaxial Compression Behavior of Soils with Different Gradations and Particle Sizes. *Manuscript in Preparation.*

6.1 Abstract

The use of methods and relationships for estimating the behavior of widely-graded soils developed based on the behavior of clean, poorly-graded coarse-grained soils is common in geotechnical practice. The influence of gradation on the strength and stress-dilatancy behavior of coarse-grained soils is complex because it depends on the soil state, which is complicated by the use of parameters that can bias and obscure the effects of gradation (i.e. is void ratio, relative density or the state parameter an appropriate parameter?). This study examines the effect of gradation and particle size on the drained and undrained triaxial compression behavior of poorly-graded and widely-graded soils sourced and sieved from a single deposit. A series of 69 triaxial tests were performed on soil specimens with a range

of state parameters. The results indicate an increase in dilative tendencies and peak friction angles for soils with wider gradations. Wider gradations resulted in a reduction of the slope and intercept of the critical state line (CSL), while increasing particle size for poorly-graded soils resulted in an increase in the slope and intercept of the CSL. The results indicate that the increase in peak friction angle, and through that strength, with increasing gradation for any given state parameter is a consequence of the increase in dilatancy.

6.2 Introduction

The mechanical behavior of coarse-grained soils is governed by inherent particle properties such as shape, gradation, surface roughness, and mineralogy. The strength of these soils depends on their density and the magnitude of effective confining stress [e.g. Gudehus, 1996; Houlsby, 1991; Nakai, 1997; Vaid and Sasitharan, 1992; Wan and Guo, 1999]. Denser soils dilate more strongly, while higher confining pressures tend to suppress dilatancy. The combination of soil density and the magnitude of confining pressure is typically referred to as the soil state [Been and Jefferies, 1985]. While soil strength is a fundamental parameter for geotechnical engineering design, there is uncertainty in its estimation using both laboratory and in-situ testing methods. A number of knowledge gaps and limitations with existing studies remain due to the challenges associated with sampling and testing of widely-graded coarse-grained soils [e.g. Daniel et al., 2004; Goto et al., 1994; Kokusho and Tanaka, 1994; Yoshimi et al., 1994; Singh et al., 1982]. Widely-graded coarse-grained materials can exhibit a wide range of particle characteristics that can influence their behavior [e.g. Sturm, 2019]. For instance, the combination of differing effects of changing particle shape to size and gradation, or mixing materials of different depositional origins may produce ambiguous or conflicting results. Another complication in the study of these soils may arise while using different parameters to characterize the soil state, such as the void ratio (e), relative density (D_{R}), and the difference in void ratio between a given state and the critical state (termed as the state parameter, ξ, by Been and Jefferies [1985]. Hence, a systematic approach or framework

should be adopted for rational interpretation in the study of widely-graded coarse-grained soils.

Dilatancy of soils refers to the change in volume due to shear deformations [Reynolds, 1885]. The stress-dilatancy relationships capture the dependence of the soil strength on the dilation of coarse-grained soils. Since the early work of Taylor [1948], several stress-dilatancy frameworks have been proposed based on either theoretical [e.g. Skempton and Bishop, 1950; Skempton, 1954; Newland and Allely, 1957; Rowe, 1962, 1969; Schofield and Wroth, 1968; De Josselin de Jong, 1976] or experimental [e.g. Lee and Seed, 1967; Bolton, 1986; Negussey et al., 1988; Vaid and Sasitharan, 1992; Chakraborty and Salgado, 2010] studies. Rowe [1962] derived the saw blade stress-dilatancy model for an assembly of uncrushable particles based on the minimum energy principle, which was later validated by De Josselin de Jong [1976] with an alternative approach based on the laws of friction. Bolton [1986] derived stress-dilatancy correlations based on direct simple shear and triaxial compression test results on poorly-graded sands, and proposed a relative density index (I_{R}) that accounted for the effects of both relative density and effective confining stress. Further stress-dilatancy relations clearly demonstrated the effects of particle shape, stress history, density, fabric and confinement [e.g. Vermeer and De Borst, 1984; Pradhan et al., 1989; Houlsby, 1991; Gudehus, 1996; Nakai, 1997; Wan and Guo, 1998, 1999; Vaid and Sivathayalan, 2000; Guo and Su, 2007]. However, systematic evaluation of the effects of gradation and particle size warrants further investigation to assess whether exiting stress-dilatancy relations developed mostly based on experiments on poorly-graded sands are directly applicable to widely-graded materials.

In recent years, a number of researchers have attempted to capture the effects of gradation and particle size on the stress-dilatancy relations of coarse-grained soils from which some consistent trends can be summarized as follows: (i) generally, as particle gradation becomes wider (i.e. coefficient of uniformity, C_{u}, becomes larger), the maximum and minimum void ratios decrease, and the location of the critical state line (CSL) in e vs.

mean effective stress (p') space (i.e. $e - \log p'$ space) shifts downwards [e.g. Youd, 1973; Li et al., 2015; Liu et al., 2014; Wood and Maeda, 2008], (ii) the slope of the CSL decreases with increasing C_{u} for coarse-grained soils due to the increase in stiffness, but the soil may become more compressible if plastic fines are present [e.g. Li et al., 2015; Been and Jefferies, 1985], (iii) for the same initial void ratio, more widely-graded soils tend to exhibit a greater contractive behavior, lower undrained strengths, and higher susceptibility to liquefaction due to their increased distance from the CSL (i.e. increasing state parameter) [e.g. Liu et al., 2014; Li et al., 2015; Yan and Dong, 2011], (iv) in the absence of differences in particle shape, gradation and particle size exhibit no significant effect on the critical state friction angle [e.g. Yang and Luo, 2018; Jiang et al., 2018; Voivret et al., 2009; Harehdasht et al., 2017, 2019; Deng et al., 2021], (v) the small-strain stiffness generally increases with increasing C_{u} [e.g. Chang and Ko, 1982; Kokusho and Yoshida, 1997; Menq, 2003; Sturm, 2019], (vi) changes in the strength and index properties appear to saturate when C_{u} is greater than 10 [e.g. Liu et al., 2014], (vii) the behavior of soils with increasing gravels content (or wider gradation) is typically controlled by the interactions of the coarser particles [e.g. Fragaszy et al., 1990, 1992; Evans and Zhou, 1995], and (viii) increasing gradation results in an increase in contact numbers (i.e. coordination number) for the coarser particles of the assembly [e.g. Liu et al., 2021; Yi et al., 2011].

Despite the above insights, many of the previously published studies have been performed on the basis of fixed void ratio or have been concerned mainly with the critical state behavior. Because the CSL location and the maximum and minimum void ratios are affected by the gradation, adopting the void ratio as a reference state parameter when evaluating behaviors that depend on the volumetric response of the soil (i.e. mobilization of peak strengths and generation of excess pore pressures) can bias the interpretation and conclusions of a given study. Alternatively, a state parameter that incorporate the effects of gradation may be more appropriate. Namely, the use of D_{R} or ξ may provide a more robust interpretation for the effects of gradation on the stress-dilatancy behavior of coarse-grained

soils.

This study is aimed to systematically examine the role of D_{50} and C_u on the stress-dilatancy behavior of widely-graded coarse-grained soils by means of triaxial compression tests. To do so, a widely-graded natural sand was selectively sieved to produce different sands with similar particle shape parameters but with different gradation and D_{50}. A series of isotropically consolidated drained (ICD) and undrained (ICU) triaxial tests were performed on specimens with a range of initial D_R and effective confining stresses to define their CSLs and interpret the results based on the ξ corresponding to each specimen. The applicability of using poorly-graded sand-based method with widely-graded coarse-grained soils is evaluated through Bolton's [1986] empirical framework.

6.3 Materials and Methods

6.3.1 Soils of Varying Gradation and Particle Size

Six coarse-grained soils with different particle sizes and gradations were used in this study (6.1). All the soils are composed of quartz sand and gravel-sized particles sourced from the Cape May Formation near Mauricetown, New Jersey. The source soil was mechanically sieved into seven poorly-graded portions (100A, 100B, 100C, 100D, 100E, 100-140 and 140-200), ranging in median particle size, D_{50} from 0.13 to 4.20 mm. Three of these soils (100A, 100C and 100D) were selected to capture the effect of D_{50} on the behavior of poorly-graded soils, while minimizing variability regarding mineralogy, particle shape and gradation. To compare the behavior of these poorly-graded soils to that of widely-graded soils, three widely-graded sand-gravel mixtures (33ABC, 25ABCD and 12CU) were formed from those poorly-graded materials. Of the three widely-graded mixtures, 33ABC contains equal mass proportions of 100A, 100B and 100C, and 25ABCD contains equal mass proportions of 100A, 100B, 100C and 100D. However, 12CU contains all the seven poorly-graded soils in different mass proportions (5% 100-140, 140-200 and 100A, 19% 100B and 100C, and 24% 100D and 100E).

These seven soils capture a range in the coefficient of uniformity (C_u) of 1.53 to 12.34. A summary of the physical and index properties of the soils tested are presented in Table 6.1, with grain size distributions shown in Fig. 6.2a. The maximum (e_{max}) and minimum (e_{min}) void ratios of the test soils were determined by Sturm [2019] following Method A of ASTM [2016b] D4254-16 and Method 1B of ASTM [2016a] D4253-16, respectively. As shown in Fig. 6.2b, the poorly-graded soils (100A, 100C and 100D) have similar e_{max} $(0.812 - 0.881)$ and e_{min} $(0.540 - 0.579)$ values while both e_{max} and e_{min} significantly decreased with increasing C_u; these trends are consistent with those previously reported in literature [e.g. Youd, 1973]. The roundness and sphericity of the six tested soils were determined using the method and Matlab code proposed by Zheng and Hryciw [2015]. The tested soils all have similar particle shape parameters, with roundness in the range of 0.39 to 0.46 and sphericity in the range of 0.74 to 0.75. Based on the similar particle shape parameters, the differences in soil behavior observed throughout this investigation are attributed to the effects of gradation and particle size.

6.3.2 Triaxial Test

Monotonic drained and undrained isotropically-consolidated triaxial compression tests were performed to characterize the response of specimens of all six soil specimens. An automatic triaxial testing system with digital data acquisition capabilities, developed by Geotac Corporation (Houston, TX), was used in testing. Cell and pore pressures, and volume change were controlled using two digital pressure volume controllers. The measured volume changes were used to determine the specimen volumetric strain, ε_v. The applied axial load was measured by an external load cell mounted onto the load frame, while the axial displacement was measured by an external linear variable differential transducer (LVDT) which was used to determine the specimen's axial strain, ε_a. All the load and displacement results were corrected for piston friction and machine compliance. Pore pressure transducers were used to measure the specimen pore pressure as well as the triaxial confining pressure.

Tests were performed on specimens of 70 mm diameter and 150 mm height. This size gives a specimen diameter to D_{50} ratio of 27 for 100D specimens and a specimen diameter to maximum particle size, $D_{\max}$, ratio of 5.8 for 12CU specimens. Pluviation of dry particles from a constant height was used to prepare specimens; this sample preparation technique was employed in order to maximize specimen with uniform density [e.g. Miura and Toki, 1982; Vaid and Negussey, 1984; Vaid et al., 1999; Lagioia et al., 2006]. Specimens were prepared at target loose ($D_{\mathrm{R}} = 15 - 30\%$), medium dense ($D_{\mathrm{R}} = 40\%$), and dense ($D_{\mathrm{R}} = 65\%$) states. Once prepared, a small vacuum of 10 kPa was applied to stabilize the specimen. The specimen was then placed in the triaxial cell and the cell was filled with de-aired water. The specimen was then saturated by applying back-pressure while maintaining a constant small difference between the cell- and back-pressure (around 30 kPa). The back-pressure was increased slowly (to around 400 kPa) until a B-value of 0.95 was achieved. However, for the medium dense and dense specimens of 25ABCD and 12CU, a B-value of 0.91 was achieved (Table 6.3) indicating a saturation level of at least 99.5% [after Black and Lee, 1973]. After saturation, the specimen was consolidated isotropically to the target confining pressure. Once the consolidation phase up to the target confining pressure was completed, the shearing phase commenced at a strain rate of 10%/hr. Cavitation during undrained tests was not observed in any of the experiments. Appropriate membrane penetration correction for the volume changes was applied to the specimens of 100D and 12CU; the membrane penetration correction was found to be insignificant for the 100A, 100C, 33ABC, and 25ABCD soils.

In total, 33 drained and 36 undrained triaxial tests were performed at effective confining stresses ($\sigma'_{3\mathrm{c}}$) ranging from 50 to 500 kPa, as indicated in Tables 6.2 and 6.3, respectively. It was not expected that significant particle crushing took place at these stress levels, which was confirmed by visual inspection of the post-test soils. The testing ID convention is such that ID "P-x-Q-y" corresponds to soil "P" at "x"% relative density tested at "Q" condition at a $\sigma'_{3\mathrm{c}}$ of "y" kPa. For example, "100A-65-CD-500" corresponds to soil 100A at 65% relative density tested at drained condition at $\sigma'_{3\mathrm{c}}$ of 500 kPa.

6.4 Results

A total of 69 triaxial compression tests were performed on soils of varying gradation and particle size but with similar particle shapes. This section first describes the isotropic consolidation behavior of all the soils. The drained and undrained response of specimens of different initial D_R and subjected to different magnitudes of σ'_{3c} are discussed. Then, the results are used to estimate CSLs for all the soils. Finally, the trends in parameters that describe the specimens' response such as peak and critical state friction angles, maximum dilation angles, pore pressure generation magnitudes and rates are interpreted on the basis of the initial state parameter of the specimens.

6.4.1 Triaxial Compression Behavior

As shown throughout this section, the gradation of the soil influenced the strength and volume-change behavior observed during the triaxial tests. This section presents the results in terms of deviatoric stress (q)-axial strain (ε_a), volumetric strain (ε_v)-axial strain (ε_a), q-mean effective stress (p'), and $e - \log p'$ curves for tests performed on 100A, 100D, and 25ABCD soils. The corresponding results from tests on 100C, 33ABC, and 12CU soils are also provided in the supplementary figures at the end of this chapter. The discussion and analysis provided in the proceeding section includes the results from all six soils.

6.4.1.1 Isotropic Consolidation Response

The isotropic consolidation curves for all the sands with different initial relative densities and confining pressures are shown in Fig. 6.3. As shown, the decrease in void ratio with increasing mean effective stress is greater with greater median particle size for the poorly-graded sands (Figs. 6.3a, 6.3b and 6.3c). Also, the decrease in void ratio with increasing mean effective stress is greater as gradation becomes wider for the widely-graded soils (Figs. 6.3d, 6.3e and 6.3f). The variation of the average slopes of the consolidation curves (i.e. compressibility

index, C_c) with C_u and D_{50} for all the soils are shown in Figs. 6.4a and 6.4b, respectively. As shown, the C_c-values increase as both C_u and D_{50} are increased. However, the effect of D_{50} on C_c is greater than that of C_u.

6.4.1.2 Drained Response

The drained deviatoric stress and volumetric change responses for all the sands with different initial relative densities (i.e. $15-30\%$, 45%, 65%) at the same cell pressure ($\sigma'_{3c} = 100$ kPa) are shown in Figs. 6.5a-6.5l. As expected, greater peak deviatoric stresses and stiffer initial responses are exhibited by the specimens with higher initial relative density for all three soils (Figs. 6.5a, 6.5e, 6.5i and 6.5c, 6.5g, 6.5k). The $q-\varepsilon_a$ curves for all the dense ($D_R \approx 65\%$) specimens exhibit a distinct peak followed by strain softening (Figs. 6.5a, 6.5e and 6.5i), and they are accompanied by large dilative volumetric strains (Figs. 6.5b, 6.5f and 6.5j). The $q-\varepsilon_a$ curves for all the medium dense ($D_R \approx 40\%$) specimens exhibit a slight peak followed by strain softening and accompanied by dilative volumetric strains. Finally, $q-\varepsilon_a$ curves for all the loose ($D_R \approx 15-30\%$) specimens show strain hardening accompanied by initial volumetric contraction followed by slight dilation at axial strains greater than about 5%. As shown, for the dense and medium dense specimens, the peak in the $q-\varepsilon_a$ curves is more pronounced for the 25ABCD soil than for the 100A and 100D soils. As shown in Fig. 6.24 (in supplementary figures), the tests on 100C, 33ABC, and 12CU soils show the same trends. The curves in the $q-p'$ plane follow the expected stress paths for drained triaxial compression, while the stress paths in the $e-\log p'$ plane show the greater amount of dilation exhibited by the tests with greater initial D_R (i.e. smaller e). These stress paths also clearly show the smaller e values attained by the widely-graded 25ABCD soil. All the 100A and 100D specimens exhibited a barreling failure without clear shear bands. However, the "25ABCD-65-CD-100" specimen exhibited a shear band which may have been responsible for the large strain softening observed at ε_a between 3 and 7% (Fig. 6.5i) and the sharp reduction in dilative strains at greater ε_a values (Fig. 6.5j).

Figures 6.6a-6.6l show drained triaxial compression results of loose specimens sheared at different σ'_{3c}. As expected, greater deviatoric stresses were mobilized by the specimens at higher σ'_{3c} (Figs. 6.6a, 6.6e, 6.6i and Figs. 6.6c, 6.6g, and 6.6k). The $q - \varepsilon_a$ curves for all the sand specimens exhibit strain hardening under all σ'_{3c} considered. The volumetric strain response exhibits dependency on σ'_{3c}, with greater contratcive volumetric strains for specimens at greater σ'_{3c} for all three soils, and all the sand specimens exhibit overall contractive volumetric strains at σ'_{3c} of 500 kPa. The stress paths in the $e - \log p'$ plane clearly show the initial contraction observed in the tests performed at σ'_{3c} of 100 and 200 kPa as well as the overall contractive response of the tests performed at σ'_{3c} of 500 kPa.

6.4.1.3 Undrained Response

The deviatoric stress and excess pore pressure change responses during undrained shearing for soils 100A, 100D, and 25ABCD with different initial relative densities at a σ'_{3c} of 100 kPa are shown in Figs. 6.7a-6.7l. The dense ($D_R \approx 65\%$) specimens of all the soils mobilized the greatest deviatoric stresses while the loose ($D_R \approx 15 - 30\%$) specimens mobilized the smallest deviatoric stresses (Figs. 6.7a, 6.7e, 6.7i and Figs. 6.7c, 6.7g, and 6.7k). These trends in strength are a result of the negative excess pore pressures (Δu) generated by the dense specimens and the positive or slightly negative Δu generated by the loose specimens. In agreement with the drained test results shown in Fig. 6.5a-6.5l, the response of the dense specimens is dilative while that of the loose specimens is slightly contractive. The differences in the response can be seen in the stress paths in $q - p'$ space, showing an initial decrease in p' for the loose tests. In addition, it can be seen that the magnitudes of generated excess pore pressures are generally smaller for 100D soil than for 100A and 25ABCD.

Figures 6.8a-6.8l show the results of undrained tests performed on loose specimens at different σ'_{3c}. As shown, specimens under the highest σ'_{3c} mobilized the greatest deviatoric stress (Figs. 6.8a, 6.8e, 6.8i and Figs. 6.8c, 6.8g, and 6.8k) as well as the greatest positive excess pore pressures (Figs. 6.8b, 6.8f, and 6.8j). These trends are in agreement with the

greater contractive behavior observed at larger cell pressures in the drained tests (Figs. 6.6a to 6.6l). The excess pore pressures in the undrained tests reached a maximum positive value and then decreased to a lower positive value indicating overall contractive volumetric response. All the specimens under σ'_{3c} of 100 kPa generated small positive Δu which reduced to negative Δu values indicating small initial volumetric contraction followed by dilative response. On the other hand, all the specimens under σ'_{3c} of 500 kPa generated positive Δu. The stress paths in $q - p'$ space show that the 100A specimens exhibited a greater initial decrease in mean effective stress; however, all three soils mobilized almost similar q values at the end of the tests.

As pointed out earlier, the level of saturation achieved for the medium dense and dense specimens of 25ABCD soil was 99.5%. Black and Lee [1973] concluded that, for soft and medium stiff soils, a degree of saturation of 99.5% is acceptable. However, for stiff or very stiff soils a full 100% saturation is probably required to ensure adequate pore pressure response [Black and Lee, 1973]. These observations were based on clean Ottawa sand and may not be strictly applicable to the widely-graded sands used in this study. Hence, the undrained response of the widely-graded soils might have been affected by the level of saturation. Although the trend of generation of excess pore pressures during undrained shearing is consistent with the volume change response during drained shearing (i.e. greater positive excess pore pressure generation and volumetric contraction under greater confining stress), further studies are required to examine the adequacy of using a 99.5% saturation level in undrained triaxial tests of widely-graded soils.

6.4.2 Critical State Lines and the Effect of Particle Size and Gradation

The points at the end of shearing for the loose specimens of all six soils were considered to have reached the critical state, which were used to estimate the CSLs in the $q - p'$ plane. As shown in Figs. 6.9a-6.9f, the critical state points obtained from the tests on loose specimens can be fitted with a straight line passing through the origin with the slope M

that can be used to obtain the critical state friction angle, ϕ'_{cs}. The critical state points in $e - \log p'$ space for all the soils were approximated from both drained and undrained tests on loose specimens. These points were obtained for ICD and ICU tests by extrapolating the end-of-test results following the methods described in Zhang et al. [2018] and Torres-Cruz and Santamarina [2020]. Examples of the extrapolation procedures are presented in the supplementary information (Figs. 6.19a-6.19d), which consist of extrapolating the dilatancy to a value of 1.0 in drained tests and the rate of pore pressure change to a value of zero in undrained tests. The extrapolated points in the $e - \log p'$ plane for all the soils are shown in Figs. 6.10a-6.10f. The best fitting line is used to estimate the critical state line using a logarithmic function as follows:

$$e_{cs} = e_{\Gamma} - \lambda \log p' \tag{6.1}$$

where, e_{cs} is the critical state void ratio at a given p', e_{Γ} is the critical state void ratio at $p' = 1$ kPa, and λ is the slope of critical state line. The critical state line equations are shown in Fig. 6.10 for all the soils. It is noted that CSLs in the $e - \log p'$ plane could also be approximated using a power function which would appear curved in semi-log space, as presented by Wang et al. [2002]. However, due to the lack of clear curvature in the range of p' values considered in this study, a linear approximation was chosen for the interpretation.

The CSL parameters M, e_{Γ} and λ appear to be influenced by the soil gradation and particle size; the effect of these parameters is discussed here in terms of C_u and D_{50} (Figs. 6.11a-6.11f). All three poorly-graded soils (100A, 100C, and 100D) have almost similar M-values between 1.29 and 1.32 (ϕ'_{cs} = 32.1 and 32.8°) (Figs. 6.11a and 6.11d). On the other hand, the soils with wider gradations show a slight increase in M, with values of 1.33 (ϕ'_{cs} = 33.0°), 1.36 (ϕ'_{cs} = 33.7°), and 1.41 (ϕ'_{cs} = 34.8°) for soils 33ABC (C_u = 4.40), 25ABCD (C_u = 7.43), and 12CU (C_u = 12.34), respectively (Fig. 6.11a). Other studies [e.g. Yang and Luo, 2018; Jiang et al., 2018; Voivret et al., 2009; Harehdasht et al., 2017, 2019]

have reported either a negligible or a small influence of gradation on M or ϕ'_{cs}, which are in general agreement with the results presented here. The e_Γ parameter increases modestly with increasing particle size (Figs. 6.11b and 6.11e); however, it decreases sharply as the soil gradation becomes wider. The effect of gradation on e_Γ is readily explained by the decrease in e_{max} and e_{min} with increasing C_u, and is in agreement with previously published results [e.g. Li et al., 2015; Liu et al., 2014; Wood and Maeda, 2008]. The λ parameter is shown to increase with increasing particle size, suggesting an increase in compressibility (Figs. 6.11c and 6.11f). The λ parameter decreases as the C_u is increased (Fig. 6.11f), which is in general agreement with previously published results indicating an increase in shear stiffness for soils with a wider gradation [e.g. Altuhafi and Coop, 2011; Sturm, 2019; Zheng et al., 2017].

6.4.3 Interpretation of Test Results in Terms of the State Parameter

As previously described, Been and Jefferies [1985] proposed the state parameter (ξ) as an alternative definition of soil state. The state parameter offers the main advantage of combining the influence of confining pressure and void ratio, in a manner similar to Bolton's [1986] corrected relative density (I_R), and is defined as the difference of the void ratio between the initial and steady state conditions at the same p'. The steady state line (SSL) is defined as the locus of all steady state points in the compression plane at which the soil deforms under constant effective stress and volume (i.e. void ratio). In this study, no distinction between the CSL and SSL are made, and ξ is computed as the difference between the void ratio at the end of consolidation (e_{eoc}) and the critical state void ratio (e_{cs}) based on the fitted CSLs shown in Fig. 6.10a-6.10f. In this section, the effects of soil gradation and particle size are discussed in terms of ξ, while the results are also presented in the supplemental information in terms of D_R for the purposes of comparison.

6.4.3.1 Drained Response

The effect of initial state on the drained behavior of all the soils are examined by plotting test results for specimens within narrow ranges of ξ. Namely, for a loose state ($\xi = -0.03 \pm 0.01$), results for 100A, 33ABC, 25ABCD, and 12CU specimens at an σ'_{3c} of 100 kPa are presented in Figs. 6.12a-6.12d. For a dense state ($\xi = -0.16 \pm 0.02$), results for all six soils at an σ'_{3c} of 100 kPa are shown in Figs. 6.12e-6.12h. As shown by the $q - \varepsilon_a$ curves, all the loose specimens exhibit strain hardening behavior (Fig. 6.12a) accompanied by initial contractive volumteric strain response followed by slight dilative behavior (Fig. 6.12b). The 12CU specimen mobilized the greatest deviatoric stress, followed by the 25ABCD, 33ABC, and 100A specimens. The volumetic response is somewhat similar between all the soils, with the 100A specimen dilating more by the end of the test.

The dense specimens of 100A, 33ABC, 25ABCD and 12CU exhibit a distinct peak in q followed by significant strain softening (Fig. 6.12e) while the 100C and 100D specimens show only a slight peak. The greatest peak in q is mobilized by the 12CU specimen, followed by the 25ABCD, 33ABC, and 100A specimens, respectively. All specimens exhibited dilative volumetric strains, with the 12CU and 25ABCD exhibiting a greater rate of dilation at ε_a smaller than 5%, the 100C and 100D exhibiting the smallest rate of dilation, and the 100A specimen exhibiting the greatest volumetric strains by the end of the test (Fig. 6.12f).

6.4.3.2 Undrained Response

The effect of initial state on the undrained behavior of all the soils are examined by plotting the undrained test results of specimens at loose state ($\xi = -0.03 \pm 0.01$) and dense state ($\xi = -0.16 \pm 0.02$). Figures 6.13a-6.13d show the undrained test results of the 100A, 33ABC, 25ABCD, and 12CU specimens with a loose state. As shown by the $q - \varepsilon_a$ curves, all the specimens exhibit strain hardening behavior (Fig. 6.13a), and the specimens of 100A, 25ABCD and 12CU mobilized greater deviatoric stresses compared to that of 33ABC. At

smaller strains, the 12CU and 25ABCD specimens mobilized greater q due to the generation of smaller Δu which became negative at ε_a of about 5%. However, at ε_a greater than about 17%, the magnitude of Δu is greater for the 100A specimen, resulting in a slightly greater deviatoric stress. The effective stress paths for the 12CU and 25ABCD specimens show no or little decrease in p', while the specimens of 100A and 33ABC initially tracked leftward ($\Delta p' < 0$), then exhibited a phase transformation ($\Delta p' = 0$) after which the mean effective stress continued to increase (Fig. 6.13c).

The undrained test results on the dense 100A, 100B, 100C, 33ABC, and 25ABCD specimens are presented in Figs. 6.13e-6.13h. As shown by the $q-\varepsilon_a$ curves, all the specimens exhibit a strain hardening behavior (Fig. 6.13e), and the specimen of 25ABCD mobilized the greatest deviatoric stress. All the specimens generated a very small initial positive excess pore pressure followed by negative excess pore pressure. The specimens of 100A and 25ABCD generated the greatest negative excess pore pressures compared to those of other soils. Also, the effective stress paths of all the specimens tracked rightward exhibiting no phase transformation.

6.4.3.3 Mobilized Peak Friction Angle and Maximum Dilation Angle

The effect of gradation and median particle size on the peak friction angle (ϕ'_{peak}) and maximum dilation angle (ψ_{max}) are examined in terms of the state parameter. Here, the peak friction angle is calculated using the maximum stress ratio ($\eta_{max} = q/p'$) using the following equation:

$$\phi'_{peak} = \sin^{-1}\left(\frac{3\eta_{max}}{6+\eta_{max}}\right) \tag{6.2}$$

The maximum dilation angle is estimated following the equation proposed by Vaid and

Sasitharan [1992] as follows:

$$\psi_{\max} = \sin^{-1}\left(\frac{2}{\frac{3}{|d\varepsilon_{\mathrm{v}}/d\varepsilon_{\mathrm{a}}|_{\max}} - 1}\right) \tag{6.3}$$

where, $|d\varepsilon_{\mathrm{v}}/d\varepsilon_{\mathrm{a}}|_{\max}$ is the maximum rate of volume change or dilation.

Figures 6.14a and 6.14b show the variation of ϕ'_{peak} with ξ for drained and undrained tests, respectively. As expected, ϕ'_{peak} increases as ξ becomes more negative for all the soils. Also, greater ϕ'_{peak} is observed for the specimens of widely-graded soils (i.e. 33ABC, 25ABCD and 12CU) compared to those of poorly-graded soils (100A, 100C and 100D) at similar initial state parameters. This difference is due to the greater ϕ'_{cs} for the widely-graded soils as well as to the greater contribution from dilatancy (i.e. rate of dilation) at a given state parameter, as discussed in the following paragraph. The 100A soil exhibits greater ϕ'_{peak} for a given ξ among the poorly-graded soils, suggesting an effect of particle size. Combining the data of both drained and undrained tests, an empirical equation is developed by regression analysis to obtain ϕ'_{peak} as a function of ξ, C_{u} and D_{50} and is expressed as:

$$\begin{aligned} \phi'_{\mathrm{peak}} &= \phi'_{\mathrm{cs}} - k\xi \\ k &= 34(C_{\mathrm{u}})^{0.2845}(D_{50})^{-0.1145} \end{aligned} \tag{6.4}$$

As shown in Eq. 6.4, k is a parameter dependent on both C_{u} and D_{50}. The value of k increases if C_{u} is increased (when D_{50} is constant) and decreases if D_{50} is increased (when C_{u} is constant). However, if the coupling effect of both C_{u} and D_{50} on k is considered, the effect of C_{u} is more pronounced than that of D_{50} implying that C_{u} has a greater effect on ϕ'_{peak} than that of D_{50}.

The variation of maximum dilation angle ($\psi_{\max}$) with initial state parameter is shown in Fig. 6.15a. As shown, $\psi_{\max}$ increases as ξ becomes more negative for all the soil specimens.

Also, the 12CU and 25ABCD soils exhibit the greatest ψ_{max} at a given ξ in comparison to the poorly-graded soils. Of the poorly-graded soils, 100A exhibits the greatest ψ_{max} at a given ξ, in agreement with the ϕ'_{peak} results shown in Figs. 6.14a and 6.14b.

The variation of ϕ'_{peak} with D_R for drained and undrained tests are shown in Figs. 6.21a and 6.21b, while the variation of ψ_{max} with D_R for drained tests is shown in Fig. 6.22a (both figures are included in the supplementary information). As shown, ϕ'_{peak} generally increases as D_R is increased for all the soil specimens. However, no specific trend regarding the effects of C_u and D_{50} on ϕ'_{peak} is observed for the different soils at similar D_R. Similar observations can be made regarding the variation of ψ_{max} with D_R. This comparison indicates that while the D_R can capture the general trends in ϕ'_{peak} and ψ_{max}, it does not differentiate between soils of different gradation or particle size. This is likely because the D_R parameter contains no information regarding the influence of effective stress, which is an important consideration as shown for example in the differences in the intercept and slope of the CSL (Figs. 6.11b, 6.11c, 6.11e, and 6.11f).

Figure 6.15b shows the variation of $\phi'_{peak} - \phi'_{cs}$ with ξ along with the mean trend from Been and Jefferies [1985]. As shown, the test results exhibit relatively satisfactory agreement with the trends of Been and Jefferies [1985], indicating higher strengths and maximum dilation as ξ becomes more negative. While some scatter in the data exists, the results generally indicate smaller $\phi'_{peak} - \phi'_{cs}$ for the same ξ for soils with smaller C_u, which is consistent with the observations in Figs. 6.12a-6.12h and Figs. 6.14a and 6.14b. The variation of $\phi'_{peak} - \phi'_{cs}$ with D_R is shown in Fig. 6.22b. As shown, $\phi'_{peak} - \phi'_{cs}$ generally increases as D_R is increased. However, significant variability is observed at D_R smaller than 40% and the data shows no specific trend regarding the effects of C_u and D_{50} on $\phi'_{peak} - \phi'_{cs}$ for the specimens prepared at similar D_R.

6.4.3.4 Excess Pore Pressure and Maximum Normalized Shear Stress

The development of shear induced pore pressure during undrained shearing is related to the dilative or contractive tendencies of a soil specimen. The greatest magnitude of negative excess pore pressure ($\Delta u_{\min}$), which typically corresponded to the end of test condition, and the greatest rate of negative pore pressure generation ($[\delta u/d\varepsilon_a]_{\min}$) obtained from the undrained tests are shown in Figs. 6.16a and 6.16b, respectively, as a function of ξ. As shown, higher negative $\Delta u_{\min}$ was generated as ξ became more negative (Fig. 6.16a). With regards to the effect of particle size, the specimens with the smallest D_{50} (i.e. 100A) generated the greatest $\Delta u_{\min}$ while the specimens with the largest D_{50} (i.e. 100D) generated the smallest negative Δu at similar ξ. While the 100C and 100D poorly-graded soils generated smaller magnitudes of $\Delta u_{\min}$ at any given ξ, no systematic difference is observed for the 100A, 33ABC, 25ABCD, and 12CU soils. In a similar manner, greater magnitudes of $[\delta u/d\varepsilon_a]_{\min}$ are observed as ξ became more negative (Fig. 6.16b). Similar trends are observed with regards to the effect of particle size, where out of the poorly-graded soils 100A generated the greatest $[\delta u/d\varepsilon_a]_{\min}$ magnitude at any given ξ. The data suggests slightly greater $[\delta u/d\varepsilon_a]_{\min}$ at any given state parameter for the widely-graded soils than for the 100A soil; however, the differences are small and possibly subjected to the effects of experimental variability.

Figures 6.23a and 6.23b (in supplementary figures) show the variation of $\Delta u_{\min}$ and $[\delta u/d\varepsilon_a]_{\min}$, respectively as a function of D_R. As shown, greater negative $\Delta u_{\min}$ and $[\delta u/d\varepsilon_a]_{\min}$ are generated as D_R becomes higher for all the soil specimens. However, no systematic effect of gradation and particle size on $\Delta u_{\min}$ and $[\delta u/d\varepsilon_a]_{\min}$ is observed for the specimens prepared at similar D_R. These results further show that the relative density parameter captures the general trend in pore pressure generation and dilatancy behaviors; however, it does not capture the finer effects of gradation and particle size.

6.4.4 Stress-Dilatancy Behavior

Rowe [1962] developed a stress-dilatancy relationship which was later modified by Bolton [1986] with a scalar correction (b) that accounts for energy losses and adjusts for differences between various shearing modes. Rowe's [1962] stress-dilatancy relationship is expressed as:

$$R = D \tan^2 \left(\frac{\pi}{4} + \frac{\phi'_{\text{cs}}}{2} \right) \tag{6.5}$$

where, $R = \sigma'_1/\sigma'_3$ is the effective principal stress ratio and $D = 1 - d\varepsilon_{\text{v}}/d\varepsilon_{\text{a}}$ is the dilatancy factor. The Bolton [1986] expression is expressed as:

$$\phi'_{\text{peak}} - \phi'_{\text{cs}} = b\,\psi_{\max} \tag{6.6}$$

where a b-value of 0.8 for plane strain conditions was proposed based on 17 experimental datasets of poorly-graded sands with a narrow range of gradations ($C_{\text{u}} < 1.9$); others have proposed b-values in the range of 0.3 to 0.6 for triaxial compression conditions [e.g. Chakraborty and Salgado, 2010]. Bolton [1986] also stated that the effect of state is strongly correlated with soil strength, which is in turn related to potential effect of particle size, shape and gradation. As the current stress-dilatancy framework does not account for the effects of particle size and gradation, a discussion on the effect of these parameters is presented herein.

Figure 6.17 shows the stress-dilatancy ($R - D$) relationships for the drained test results on the specimens with similar ξ shown in Fig. 6.12b where the test data is compared with Rowe's stress-dilatancy relationship (Eq. 6.5). As shown, both the poorly-graded (100A, 100C and 100D) and widely-graded (33ABC, 25ABCD and 12CU) soils closely follow Rowe's relationship until the dilatancy factor (D) reaches a peak. Once D reaches a peak, the curves reverse and D drops to the critical state. As shown in Fig. 6.17a, the soil with the smallest D_{50} (i.e. 100A) exhibits the maximum dilatancy factor ($D_{\max}$) and the corresponding maximum principal stress ratio ($R_{\max}$). However, no specific effect of D_{50} on

D_{max} and R_{max} is observed. For the widely-graded soils, D_{max} and the corresponding R_{max} increase with an increase in C_u (Fig. 6.17b) supporting the observations from Figs. 6.14 and 6.15a.

Figure 6.18a shows the relationship between $\phi'_{peak} - \phi'_{cs}$ and ψ_{max} (the so-called stress-dilatancy relationship) for all the soils tested in this study, obtained from the drained tests. As shown, no significant effect of C_u and D_{50} is observed, suggesting that the contribution of dilation to the friction angle in excess of the critical state value is unaffected by these parameters. The fitted trend indicates an average b-value of 0.54, which is obtained by fitting the data for all soils. The b-value obtained here is within the typical range between 0.3 and 0.6 for triaxial compression reported in literature [e.g. Chakraborty and Salgado, 2010].

The drained test results for specimens of all soils are plotted in $\phi'_{peak} - \phi'_{cs}$ versus mean effective stress at failure (p'_f) in Fig. 6.18b to compare to the relationships proposed by Bolton [1986]. Empirical trend lines corresponding to relative densities (D_R) of 25, 40, 65 and 100% are also shown using Bolton's [1986] relationship, defined as:

$$I_R = D_R \left(10 - \ln p'_f\right) - 1 \tag{6.7}$$

where, I_R is the relative density index related to peak and critical state friction angle as: $\phi'_{peak} - \phi'_{cs} = 3I_R$ for triaxial strain condition, and p'_f is the mean effective stress at failure in kPa. The trend lines rotate upwards for denser soils, corresponding to a more dilative behavior that shift the mobilized peak friction angle further from the critical state. As shown, the specimens of all the soils prepared for a D_R less than 30% generally plotted between expected D_R values of 25 and 50% based on Bolton's [1986] relationship. The specimens prepared at a target D_R of 40% correspond to expected densities between 55 and 75% D_R based on Eq. 6.7. The specimens prepared at a target D_R of 65% plot at expected D_R values between 80 and 90% based on Eq. 6.7. The only very dense specimen of 12CU

prepared at a D_R of about 90% plotted above the $D_R = 100\%$ line. The disparity between the experimental results and those predicted by Eq. 6.7 may be attributed to the angular shape of the soil particles used in this study which would contribute to a more dilative soil response for a given D_R than the outwash and river sands evaluated in Bolton's [1986] framework.

The effect of D_{50} and C_u on the loose specimens ($D_R < 30\%$) is not clearly pronounced (Fig. 6.18b). However, for the medium dense ($D_R \approx 40\%$) and dense ($D_R \approx 65\%$) specimens, increasing D_{50} and C_u resulted in higher peak shear friction angles which further deviated from Bolton's stress-dilatancy framework. Using Bolton's relationship, the specimens of 100D prepared at a target D_R of 40% are predicted to have a D_R of 70% based on the measured $\phi'_{peak} - \phi'_{cs}$ value, which is greater than those predicted for 100C ($D_R \approx 63\%$) and 100A ($D_R \approx 58\%$) specimens. Also, the specimens of 12CU prepared at target D_R of 40% are predicted to have a D_R of 72%, which is greater than that for 25ABCD ($D_R \approx 61\%$) and for 33ABC ($D_R \approx 60\%$) specimens. Similar trends are observed for the specimens prepared at target D_R of 65%. Hence, the soil specimens with higher D_{50} and C_u exhibit greater peak friction angles and a more dilative soil response resulting in significant deviations from Eq. 6.7, in agreement with the results shown in Figs. 6.14a and 6.14b, and 6.15a and 6.15b.

6.5 Conclusions

A series of isotropically consolidated drained and undrained triaxial tests were conducted to systematically investigate the effects of median particle size and gradation on the triaxial compression behavior of widely-graded coarse-grained soils. The soils used in this study were sourced from a single deposit to eliminate the effects of particle shape and mineralogy. Tests were performed over a range of initial relative densities and confining pressures.

The results show that the index void ratio values (e_{max} and e_{min}) decrease as gradation becomes wider (i.e. C_u increases), whereas no significant effect of median particle size (D_{50}) on the index void ratios are observed. The critical state stress ratio (M) in the $q - p'$ plane

tends to increase as C_u is increased while the effect of D_{50} on M is negligible. The position (e_Γ) of the critical state line (CSL) in $e-\log p'$ space decreases as C_u is increased and the CSL shifts downwards in $e-\log p'$ space with increasing C_u. Also, e_Γ of the poorly-graded soils increases as D_{50} is increased. The slope (λ) of the CSL in $e-\log p'$ space tends to decrease as C_u is increased. However, λ of the poorly-graded soils increases as D_{50} is increased.

The effect of initial state parameter (ξ) on all the soil specimens is also evident from the test results. As ξ becomes more negative (i.e. specimens become denser), both the peak friction angle (ϕ'_{peak}) and maximum dilation angle (ψ_{max}) increase. At similar ξ, both ϕ'_{peak} and ψ_{max} increase as C_u is increased for the widely-graded soils. Of the poorly-graded soils, the soil with the smallest D_{50} (i.e. 100A) exhibits the greatest ϕ'_{peak} and ψ_{max}. The undrained test results show that higher negative excess pore pressure (Δu_{min}) was generated as ξ became more negative for all the soils. The soil with the smallest D_{50} (i.e. 100A) generated the greatest Δu_{min} while the soil with the largest D_{50} (i.e. 100D) generated the smallest Δu_{min} at similar ξ. However, no systematic effect of C_u on Δu_{min} is observed. Also, at similar ξ, $\phi'_{peak}-\phi'_{cs}$ tends to increase as C_u is increased across a range of ξ and confining pressures, and the data shows general agreement with the trends and bounds established by Been and Jefferies [1985]. With regards to the effects of C_u and D_{50} on ϕ'_{peak}, ψ_{max} and $\phi'_{peak}-\phi'_{cs}$ at similar relative density (D_R), no specific trend of the effect of C_u and D_{50} on ϕ'_{peak}, ψ_{max} and $\phi'_{peak}-\phi'_{cs}$ is observed suggesting the advantages of using ξ as reference parameter over D_R.

When the results are compared to Rowe's [1962] stress-dilatancy relation, the soils with wider gradation (i.e. higher C_u) exhibits greater principal stress ratio (R_{max}) and dilatancy (D_{max}). However, no specific trend regarding the effect of D_{50} on R_{max} and D_{max} is observed. The relationship between $\phi'_{peak}-\phi'_{cs}$ and ψ_{max} (the Bolton 1986 stress-dilatancy relationship) exhibit no significant effect of either C_u or D_{50}, and by fitting all the data a b-value of 0.54 is obtained which is within the typical range for triaxial compression reported in literature. In addition, a comparison of $\phi'_{peak}-\phi'_{cs}$ vs. p'_f data using Bolton's [1986] Eqs.

14 and 16 shows that $\phi'_{\text{peak}} - \phi'_{\text{cs}}$ values obtained from the test results are significantly higher than those predicted by Bolton's [1986] equations which may be attributed to the angular shape of the soil particles used in this study compared to the clean river sands evaluated in Bolton's [1986] framework. However, the difference among the measured and predicted values of $\phi'_{\text{peak}} - \phi'_{\text{cs}}$ becomes higher as both C_{u} and D_{50} are increased suggesting the effects of C_{u} and D_{50} on the stress-dilatancy behavior.

Both the state parameter, ξ [Been and Jefferies, 1985] and the relative density index, I_{R} [Bolton, 1986] combine the effects of density and confining pressure. Hence, considering either ξ or I_{R}, a clear dependency of $\phi'_{\text{peak}} - \phi'_{\text{cs}}$ on C_{u} is observed suggesting that a complete description of the stress-dilatancy behavior of coarse-grained soils should account for the effects of gradation.

6.6 Acknowledgment

The National Science Foundation (NSF) provided the funding for this work under grant No. CMMI-1916152 and also funded the Natural Hazards Engineering Research Infrastructure (NHERI) shared use centrifuge facility at the University of California at Davis under grant No. CMMI-1520581. The authors would also like to thank Rachel Reardon, Francisco Humire, Mandeep Singh Basson, Nathan Love, Trevor Carey, and Anna Chiaradonna for their insights and recommendations.

Bibliography

Altuhafi, F. and Coop, M. R. (2011). Changes to particle characteristics associated with the compression of sands. *Géotechnique*, 61(6):459–471.

ASTM (2016a). Standard test methods for maximum index density and unit weight of soils using a vibratory table. *D4253-16*.

ASTM (2016b). Standard test methods for minimum index density and unit weight of soils and calculation of relative density. *D4254-16*.

Been, K. and Jefferies, M. G. (1985). A state parameter for sands. *Géotechnique*, 35(2):99–112.

Black, D. K. and Lee, K. L. (1973). Saturating laboratory samples by back pressure. *Journal of the Soil Mechanics and Foundations Division*, 99(1):75–93.

Bolton, M. (1986). The strength and dilatancy of sands. *Géotechnique*, 36(1):65–78.

Chakraborty, T. and Salgado, R. (2010). Dilatancy and shear strength of sand at low confining pressures. *Journal of Geotechnical and Geoenvironmental Engineering*, 136(3):527–532.

Chang, N.-Y. and Ko, H.-Y. (1982). Effects of grain size distribution on dynamic properties and liquefaction potential of granular soils. Research Report R82-103, University of Colorado at Denver.

Daniel, C., Howie, J., Campanella, R., and Sy, A. (2004). Characterization of spt grain size effects in gravels. In *Proc., 2nd Int. Conf. on Site Characterization (ISC'2), Millpress, Rotterdam, Netherlands*.

De Josselin de Jong, G. (1976). Rowe's stress—dilatancy relation based on friction. *Géotechnique*, 26(3):527–534.

Deng, Y., Yilmaz, Y., Gokce, A., and Chang, C. S. (2021). Influence of particle size on the drained shear behavior of a dense fluvial sand. *Acta Geotechnica*, pages 1–18.

Evans, M. D. and Zhou, S. (1995). Liquefaction behavior of sand-gravel composites. *Journal of Geotechnical Engineering*, 121(3):287–298.

Fragaszy, R. J., Su, J., Siddiqi, F. H., and Ho, C. L. (1992). Modeling strength of sandy gravel. *Journal of Geotechnical Engineering*, 118(6):920–935.

Fragaszy, R. J., Su, W., and Siddiqi, F. H. (1990). Effects of oversize particles on the density of clean granular soils. *Geotechnical Testing Journal*, 13(2):106–114.

Goto, S., Nishio, S., and Yoshimi, Y. (1994). Dynamic properties of gravels sampled by ground freezing. In *Ground Failures under Seismic Conditions*, pages 141–157. ASCE.

Gudehus, G. (1996). A comprehensive constitutive equation for granular materials. *Soils and Foundations*, 36(1):1–12.

Guo, P. and Su, X. (2007). Shear strength, interparticle locking, and dilatancy of granular materials. *Canadian Geotechnical Journal*, 44(5):579–591.

Harehdasht, S. A., Hussien, M. N., Karray, M., Roubtsova, V., and Chekired, M. (2019). Influence of particle size and gradation on shear strength–dilation relation of granular materials. *Canadian Geotechnical Journal*, 56(2):208–227.

Harehdasht, S. A., Karray, M., Hussien, M. N., and Chekired, M. (2017). Influence of particle size and gradation on the stress-dilatancy behavior of granular materials during drained triaxial compression. *International Journal of Geomechanics*, 17(9):04017077.

Houlsby, G. T. (1991). How the dilatancy of soils affects their behaviour. In *Proceedings of the Tenth European Conference on Soil Mechanics and Foundation Engineering*, volume 4, pages 1189–1202.

Jiang, M., Yang, Z., Barreto, D., and Xie, Y. (2018). The influence of particle-size distribution on critical state behavior of spherical and non-spherical particle assemblies. *Granular Matter*, 20(4):1–15.

Kokusho, T. and Tanaka, Y. (1994). Dynamic properties of gravel layers investigated by in-situ freezing sampling. *Ground Failure under Seismic Condition*, pages 121–140.

Kokusho, T. and Yoshida, Y. (1997). Spt n-value and s-wave velocity for gravelly soils with different grain size distribution. *Soils and Foundations*, 37(4):105–113.

Lagioia, R., Sanzeni, A., and Colleselli, F. (2006). Air, water and vacuum pluviation of sand specimens for the triaxial apparatus. *Soils and Foundations*, 46(1):61–67.

Lee, K. L. and Seed, H. B. (1967). Drained strength characteristics of sands. *Journal of the Soil Mechanics and Foundations Division*, 93(6):117–141.

Li, G., Liu, Y.-J., Dano, C., and Hicher, P.-Y. (2015). Grading-dependent behavior of granular materials: from discrete to continuous modeling. *Journal of Engineering Mechanics*, 141(6):04014172.

Liu, D., O'Sullivan, C., and Carraro, J. A. H. (2021). Influence of particle size distribution on the proportion of stress-transmitting particles and implications for measures of soil state. *Journal of Geotechnical and Geoenvironmental Engineering*, 147(3):04020182.

Liu, Y.-J., Li, G., Yin, Z.-Y., Dano, C., Hicher, P.-Y., Xia, X.-H., and Wang, J.-H. (2014). Influence of grading on the undrained behavior of granular materials. *Comptes Rendus Mécanique*, 342(2):85–95.

Menq, F.-Y. (2003). *Dynamic properties of sandy and gravelly soils*. PhD thesis, The University of Texas at Austin.

Miura, S. and Toki, S. (1982). A sample preparation method and its effect on static and cyclic deformation-strength properties of sand. *Soils and Foundations*, 22(1):61–77.

Nakai, T. (1997). Dilatancy characteristics of geomaterials. In *Deformation and progressive failure in geomaterials, IS-Nagoya'97*, pages 899–906. Elsevier Science.

Negussey, D., Wijewickreme, W., and Vaid, Y. (1988). Constant-volume friction angle of granular materials. *Canadian Geotechnical Journal*, 25(1):50–55.

Newland, P. and Allely, B. (1957). Volume changes in drained taixial tests on granular materials. *Géotechnique*, 7(1):17–34.

Pradhan, T. B., Tatsuoka, F., and Sato, Y. (1989). Experimental stress-dilatancy relations of sand subjected to cyclic loading. *Soils and Foundations*, 29(1):45–64.

Reynolds, O. (1885). Lvii. on the dilatancy of media composed of rigid particles in contact. with experimental illustrations. *The London, Edinburgh, and Dublin Philosophical Magazine and Journal of Science*, 20(127):469–481.

Rowe, P. (1969). The relation between the shear strength of sands in triaxial compression, plane strain and direct. *Géotechnique*, 19(1):75–86.

Rowe, P. W. (1962). The stress-dilatancy relation for static equilibrium of an assembly of particles in contact. *Proceedings of the Royal Society of London. Series A. Mathematical and Physical Sciences*, 269(1339):500–527.

Schofield, A. N. and Wroth, P. (1968). *Critical State Soil Mechanics*. McGraw-hill London.

Singh, S., Seed, H. B., and Chan, C. K. (1982). Undisturbed sampling of saturated sands by freezing. *Journal of the Geotechnical Engineering Division*, 108(2):247–264.

Skempton, A. (1954). The pore-pressure coefficients a and b. *Géotechnique*, 4(4):143–147.

Skempton, A. and Bishop, A. (1950). The measurement of the shear strength of soils. *Géotechnique*, 2(2):90–108.

Sturm, A. P. (2019). *On the liquefaction potential of gravelly soils: Characterization, triggering and performance*. PhD thesis, University of California, Davis.

Taylor, D. W. (1948). *Fundamentals of soil mechanics*. John Wiley & Sons, New York, NY.

Torres-Cruz, L. A. and Santamarina, J. C. (2020). The critical state line of nonplastic tailings. *Canadian Geotechnical Journal*, 57(10):1508–1517.

Vaid, Y. and Sasitharan, S. (1992). The strength and dilatancy of sand. *Canadian Geotechnical Journal*, 29(3):522–526.

Vaid, Y. P. and Negussey, D. (1984). Relative density of pluviated sand samples. *Soils and Foundations*, 24(2):101–105.

Vaid, Y. P. and Sivathayalan, S. (2000). Fundamental factors affecting liquefaction susceptibility of sands. *Canadian Geotechnical Journal*, 37(3):592–606.

Vaid, Y. P., Sivathayalan, S., and Stedman, D. (1999). Influence of specimen-reconstituting method on the undrained response of sand. *Geotechnical Testing Journal*, 22(3):187–195.

Vermeer, P. A. and De Borst, R. (1984). Non-associated plasticity for soils, concrete and rock. *Heron*, 29(3).

Voivret, C., Radjai, F., Delenne, J.-Y., and El Youssoufi, M. S. (2009). Multiscale force networks in highly polydisperse granular media. *Physical Review Letters*, 102(17):178001.

Wan, R. and Guo, P. (1998). A simple constitutive model for granular soils: modified stress-dilatancy approach. *Computers and Geotechnics*, 22(2):109–133.

Wan, R. and Guo, P. (1999). A pressure and density dependent dilatancy model for granular materials. *Soils and Foundations*, 39(6):1–11.

Wang, Z.-L., Dafalias, Y. F., Li, X.-S., and Makdisi, F. I. (2002). State pressure index for modeling sand behavior. *Journal of Geotechnical and Geoenvironmental Engineering*, 128(6):511–519.

Wood, D. M. and Maeda, K. (2008). Changing grading of soil: effect on critical states. *Acta Geotechnica*, 3(1):3.

Yan, W. and Dong, J. (2011). Effect of particle grading on the response of an idealized granular assemblage. *International Journal of Geomechanics*, 11(4):276–285.

Yang, J. and Luo, X. (2018). The critical state friction angle of granular materials: does it depend on grading? *Acta Geotechnica*, 13(3):535–547.

Yi, L., Dong, K. J., Zou, R., and Yu, A. (2011). Coordination number of the packing of ternary mixtures of spheres: Dem simulations versus measurements. *Industrial & Engineering Chemistry Research*, 50(14):8773–8785.

Yoshimi, Y., Tokimatsu, J., and Ohara, A. (1994). In situ liquefaction resistance of clean sands over a wide density range. *Géotechnique*, 44(3):479–494.

Youd, T. (1973). Factors controlling maximum and minimum densities of sands. In *Evaluation of relative density and its role in geotechnical projects involving cohesionless soils*. ASTM International.

Zhang, J., Lo, S.-C. R., Rahman, M. M., and Yan, J. (2018). Characterizing monotonic behavior of pond ash within critical state approach. *Journal of Geotechnical and Geoenvironmental Engineering*, 144(1):04017100.

Zheng, J. and Hryciw, R. D. (2015). Traditional soil particle sphericity, roundness and surface roughness by computational geometry. *Géotechnique*, 65(6):494–506.

Zheng, J., Hryciw, R. D., and Ventola, A. (2017). Compressibility of sands of various geologic origins at pre-crushing stress levels. *Geotechnical and Geological Engineering*, 35(5):2037–2051.

6.7 Tables and Figures

Table 6.1: Properties of the soils used in this study (standard deviations are in parenthesis for roundness and sphericity)

Soil	D_{10} (mm)	D_{30} (mm)	D_{50} (mm)	D_{60} (mm)	C_{u}	C_{c}	$e_{\max}$	$e_{\min}$	Roundness	Sphericity	G_{s}
100A	0.12	0.16	0.18	0.20	1.74	1.04	0.881	0.579	0.39 (0.11)	0.74 (0.13)	2.62
100C	0.91	1.13	1.31	1.39	1.53	1.01	0.839	0.557	0.42 (0.12)	0.75 (0.12)	2.61
100D	1.79	2.21	2.58	2.74	1.53	1.00	0.812	0.540	0.45 (0.09)	0.75 (0.12)	2.60
33ABC	0.15	0.26	0.51	0.66	4.40	0.68	0.622	0.397	0.40 (0.11)	0.75 (0.12)	2.61
25ABCD	0.23	0.53	0.80	1.71	7.43	0.71	0.544	0.303	0.41 (0.12)	0.75 (0.12)	2.61
12CU	0.18	0.66	1.55	2.20	12.34	1.11	0.450	0.276	0.46 (0.12)	0.75 (0.12)	2.61

Table 6.2: Details of drained triaxial tests

Soil	Test ID	σ'_{3c} (kPa)	e_{eoc}[1]	$D_{R(eoc)}$ (%)[2]	State Parameter, ξ
100A	100A-LOOSE-CD-100	100	0.812	23	-0.04
	100A-LOOSE-CD-200	200	0.806	25	-0.03
	100A-LOOSE-CD-500	500	0.788	31	-0.02
	100A-40-CD-100	100	0.757	41	-0.10
	100A-65-CD-100	100	0.684	65	-0.17
100C	100C-LOOSE-CD-100	100	0.800	14	-0.10
	100C-LOOSE-CD-200	200	0.771	24	-0.08
	100C-LOOSE-CD-500	500	0.764	27	-0.02
	100C-LOOSE-CD-700	700	0.753	30	-0.01
	100C-40-CD-100	100	0.729	39	-0.17
	100C-65-CD-100	100	0.655	65	-0.24
100D	100D-LOOSE-CD-100	100	0.766	17	-0.09
	100D-LOOSE-CD-200	200	0.751	23	-0.04
	100D-LOOSE-CD-500	500	0.720	34	0.00
	100D-40-CD-100	100	0.693	44	-0.16
	100D-65-CD-100	100	0.623	69	-0.23
33ABC	33ABC-LOOSE-CD-100	100	0.572	22	-0.04
	33ABC-LOOSE-CD-200	200	0.562	27	-0.03
	33ABC-LOOSE-CD-500	500	0.574	21	0.00
	33ABC-LOOSE-CD-700	700	0.572	22	0.01
	33ABC-40-CD-100	100	0.530	41	-0.09
	33ABC-65-CD-100	100	0.476	65	-0.14
25ABCD	25ABCD-LOOSE-CD-100	100	0.506	16	-0.03
	25ABCD-LOOSE-CD-200	200	0.506	16	-0.01
	25ABCD-LOOSE-CD-500	500	0.498	19	0.00
	25ABCD-40-CD-100	100	0.449	39	-0.08
	25ABCD-65-CD-100	100	0.387	65	-0.15
12CU	12CU-LOOSE-CD-100	100	0.420	17	-0.03
	12CU-LOOSE-CD-200	200	0.413	21	-0.02
	12CU-LOOSE-CD-500	500	0.409	24	-0.01
	12CU-40-CD-100	100	0.373	44	-0.07
	12CU-65-CD-100	100	0.334	66	-0.11
	12CU-90-CD-100	100	0.293	90	-0.15

[1]Void ratio at the end of the consolidation phase; [2]Relative density at the end of the consolidation phase

Table 6.3: Details of undrained triaxial tests

Soil	Test ID	σ'_{3c} (kPa)	e_{eoc}[1]	$D_{R(eoc)}$ (%)[2]	State Parameter, ξ	B-Values
100A	100A-LOOSE-CU-50	50	0.811	23	-0.07	0.97
	100A-LOOSE-CU-100	100	0.819	21	-0.04	0.97
	100A-LOOSE-CU-200	200	0.815	22	-0.02	0.98
	100A-LOOSE-CU-500	500	0.795	28	-0.01	0.96
	100A-40-CU-100	100	0.754	42	-0.10	0.96
	100A-65-CU-100	100	0.688	64	-0.17	0.96
100C	100C-LOOSE-CU-50	50	0.793	16	-0.15	0.97
	100C-LOOSE-CU-100	100	0.787	18	-0.11	0.97
	100C-LOOSE-CU-200	200	0.776	22	-0.07	0.96
	100C-LOOSE-CU-500	500	0.757	29	-0.03	0.97
	100C-40-CU-100	100	0.729	39	-0.17	0.96
	100C-65-CU-100	100	0.654	66	-0.24	0.96
100D	100D-LOOSE-CU-50	50	0.777	13	-0.14	0.97
	100D-LOOSE-CU-100	100	0.767	17	-0.09	0.96
	100D-LOOSE-CU-200	200	0.757	20	-0.04	0.97
	100D-LOOSE-CU-500	500	0.724	32	0.01	0.96
	100D-40-CU-100	100	0.692	44	-0.16	0.97
	100D-65-CU-100	100	0.630	67	-0.22	0.97
33ABC	33ABC-LOOSE-CU-50	50	0.602	9	-0.03	0.96
	33ABC-LOOSE-CU-100	100	0.597	11	-0.02	0.96
	33ABC-LOOSE-CU-200	200	0.585	17	-0.01	0.97
	33ABC-LOOSE-CU-500	500	0.567	25	0.00	0.95
	33ABC-40-CU-100	100	0.530	41	-0.09	0.96
	33ABC-65-CU-100	100	0.473	66	-0.14	0.95
25ABCD	25ABCD-LOOSE-CU-50	50	0.515	12	-0.03	0.95
	25ABCD-LOOSE-CU-100	100	0.506	16	-0.03	0.95
	25ABCD-LOOSE-CU-200	200	0.502	17	-0.02	0.95
	25ABCD-LOOSE-CU-500	500	0.497	20	0.00	0.95
	25ABCD-40-CU-100	100	0.442	42	-0.09	0.91
	25ABCD-65-CU-100	100	0.389	64	-0.14	0.91
12CU	12CU-LOOSE-CU-50	50	0.432	11	-0.03	0.95
	12CU -LOOSE-CU-100	100	0.428	12	-0.02	0.95
	12CU -LOOSE-CU-200	200	0.420	17	-0.01	0.96
	12CU -LOOSE-CU-500	500	0.407	25	-0.01	0.95
	12CU -40-CU-100	100	0.374	44	-0.07	0.91
	12CU -65-CU-100	100	0.335	66	-0.11	0.91

[1]Void ratio at the end of the consolidation phase; [2]Relative density at the end of the consolidation phase

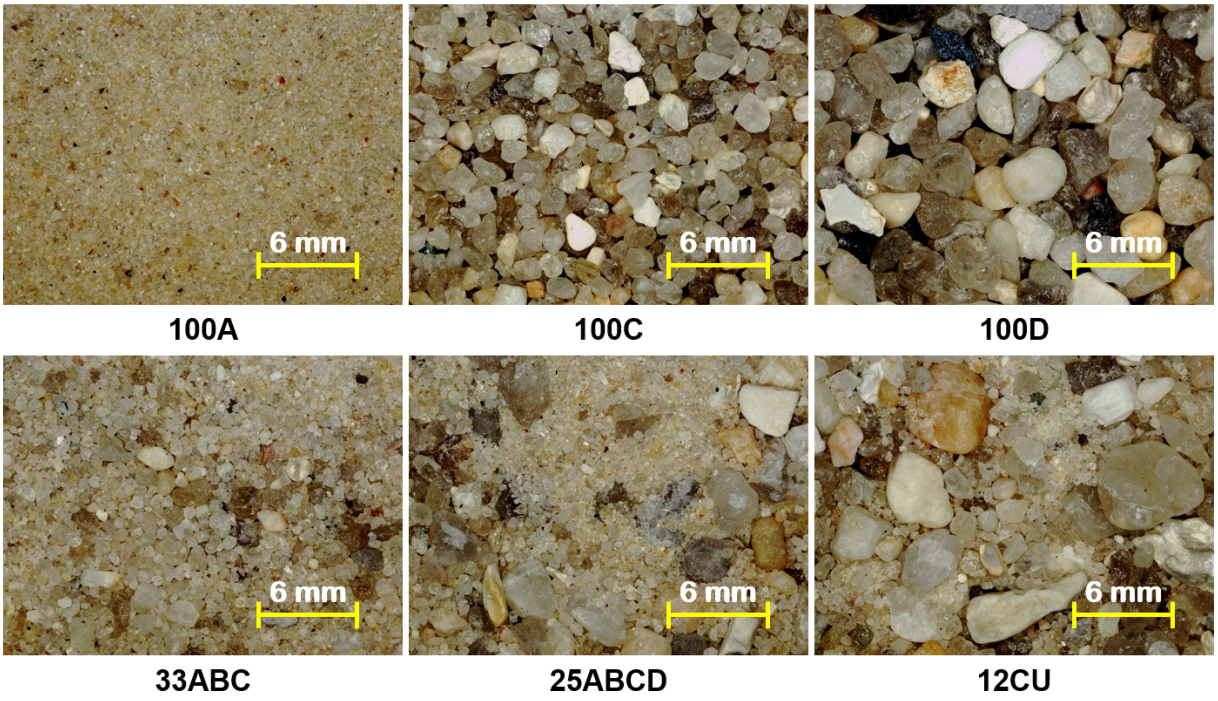

Figure 6.1: Sands used in this study

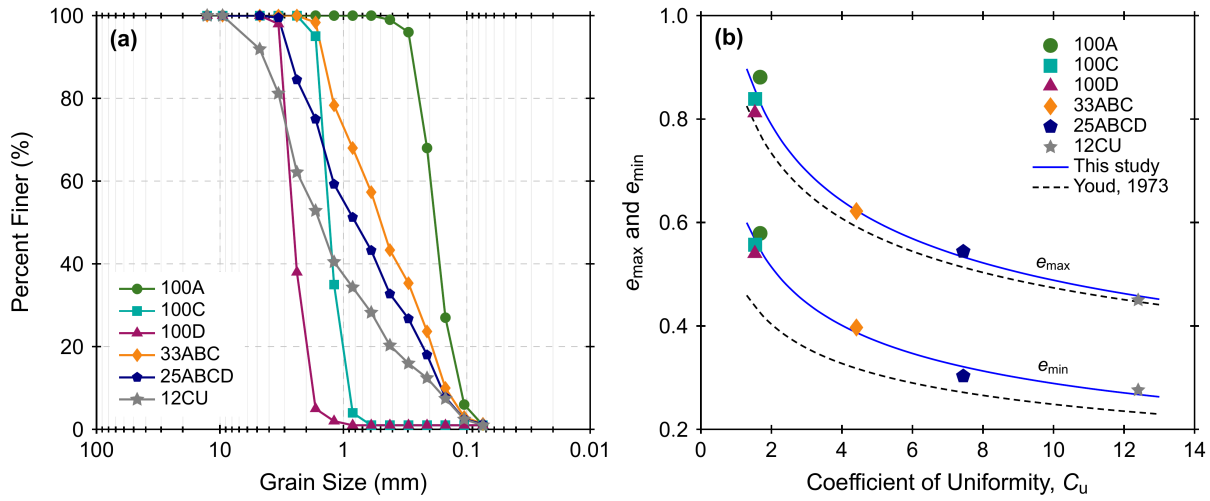

Figure 6.2: (a) Gradation of the soils used in this study and (b) variation of maximum and minimum void ratios with coefficient of uniformity

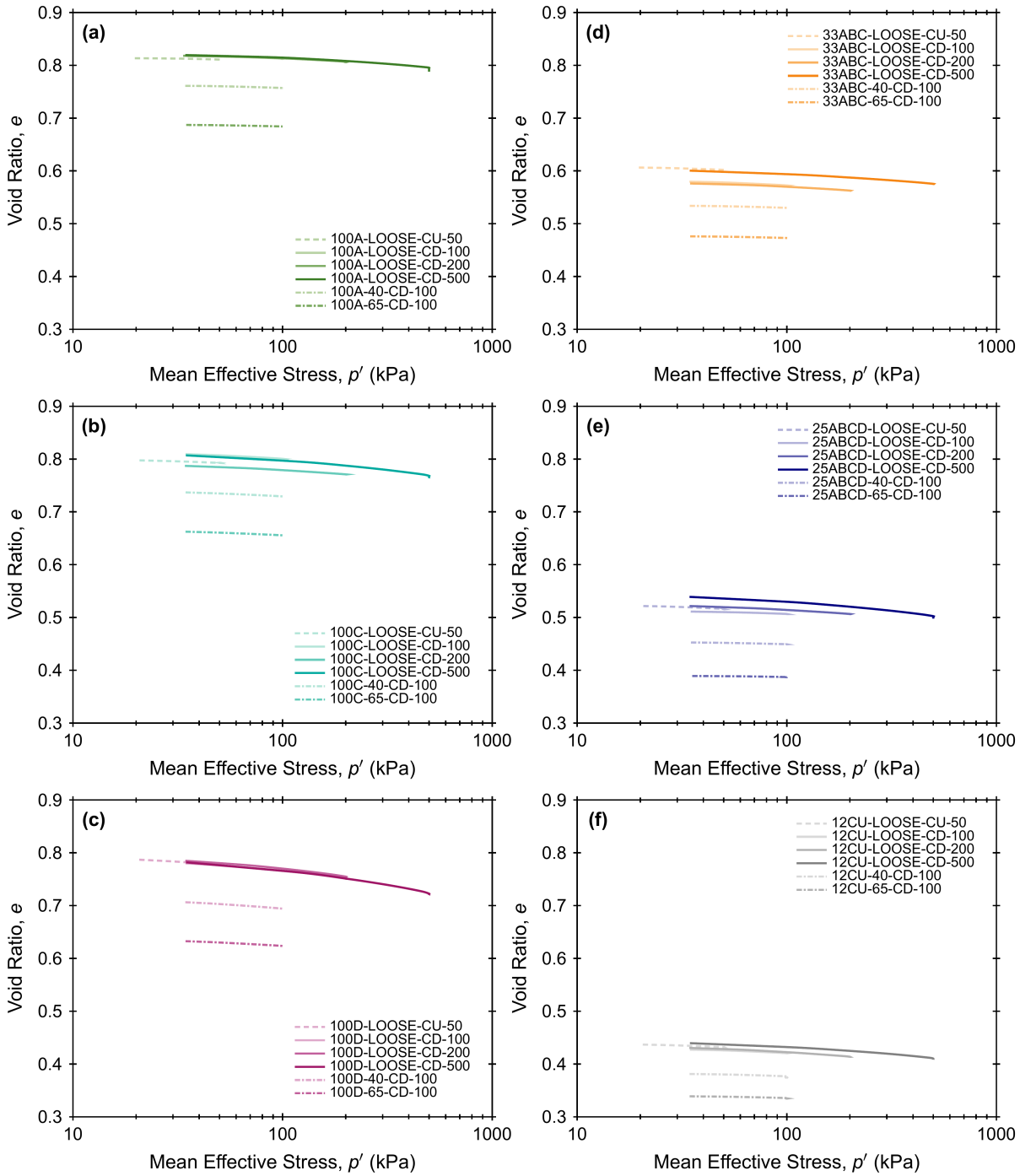

Figure 6.3: Isotropic consolidation curves for specimens of (a) 100A, (b) 100C, (c) 100D, (d) 33ABC, (e) 25ABCD, and (f) 12CU

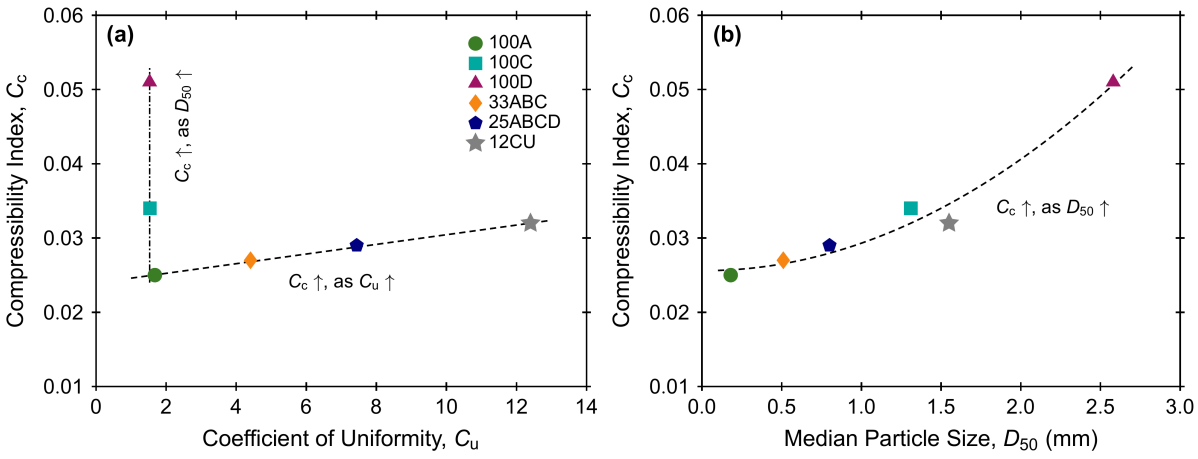

Figure 6.4: Variation of compression index, C_c with (a) C_u and (b) D_{50}

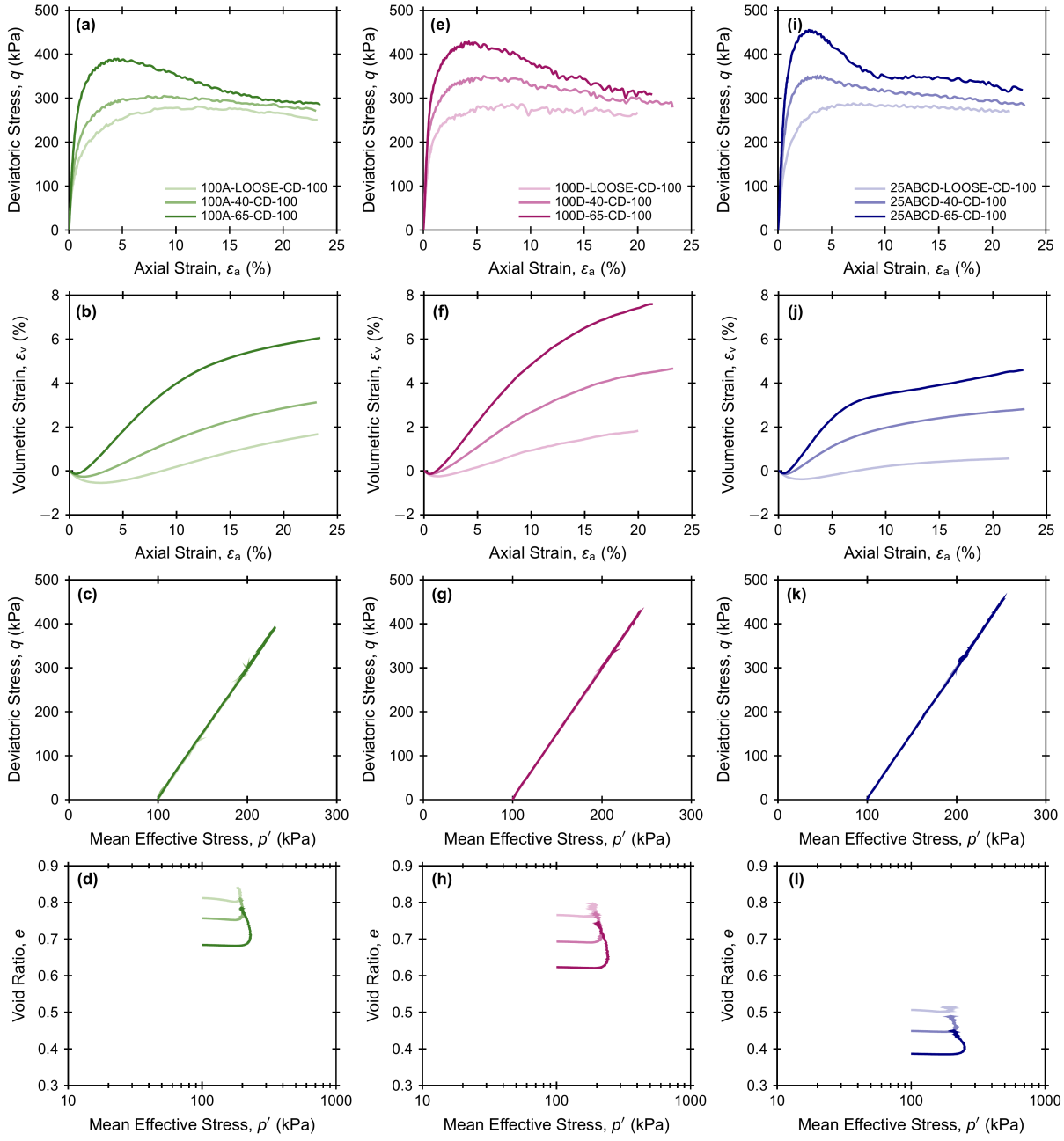

Figure 6.5: ICD test results for specimens of (a, b, c, d) 100A, (e, f, g, h) 100D, and (i, j, k, l) 25ABCD at different D_{R} and $\sigma'_{3\mathrm{c}} = 100$ kPa

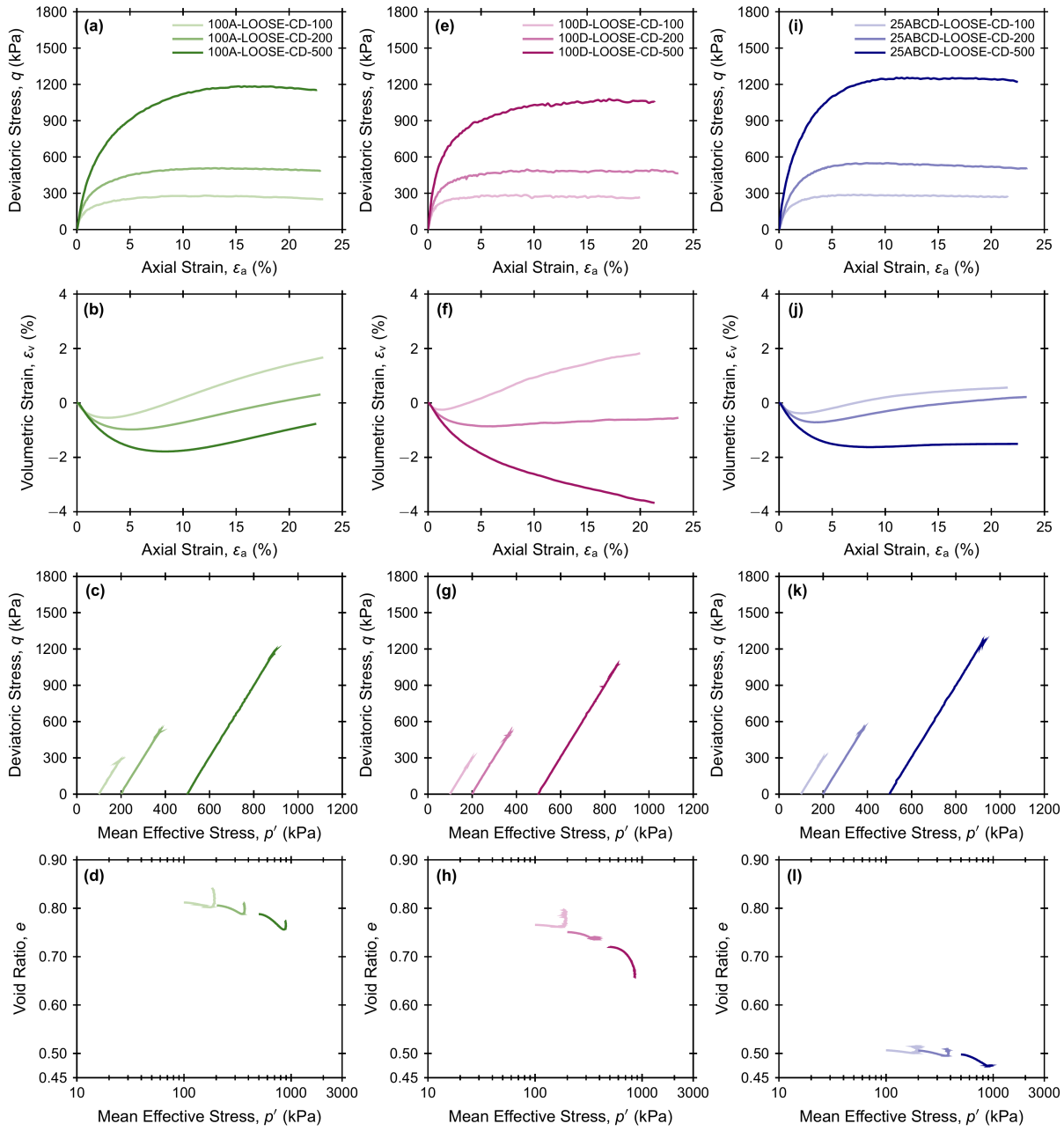

Figure 6.6: ICD test results for loose specimens of (a, b, c, d) 100A, (e, f, g, h) 100D, and (i, j, k, l) 25ABCD at different σ'_{3c}

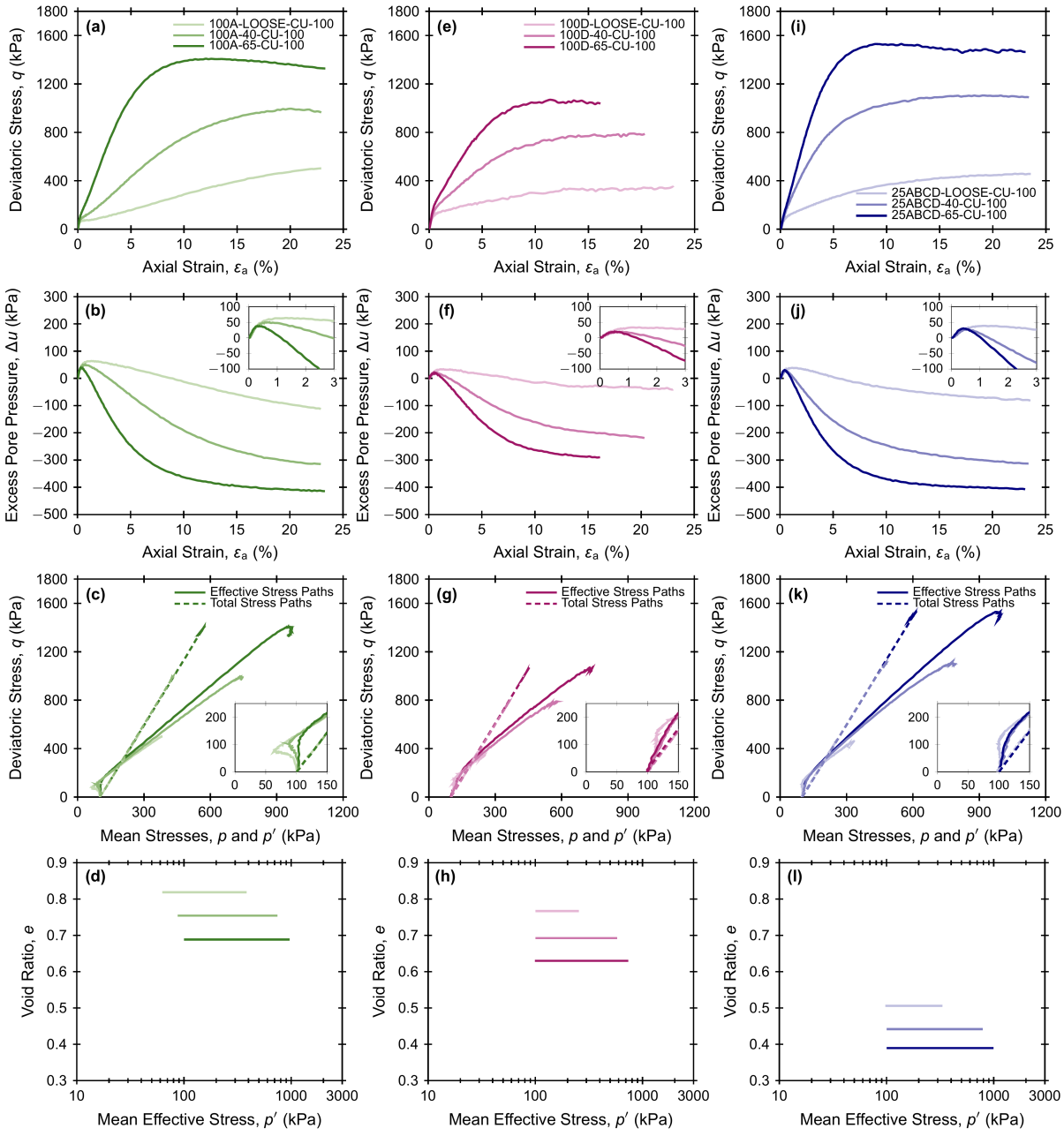

Figure 6.7: ICU test results for specimens of (a, b, c, d) 100A, (e, f, g, h) 100D, and (i, j, k, l) 25ABCD at different D_{R} and $\sigma'_{3\mathrm{c}} = 100$ kPa

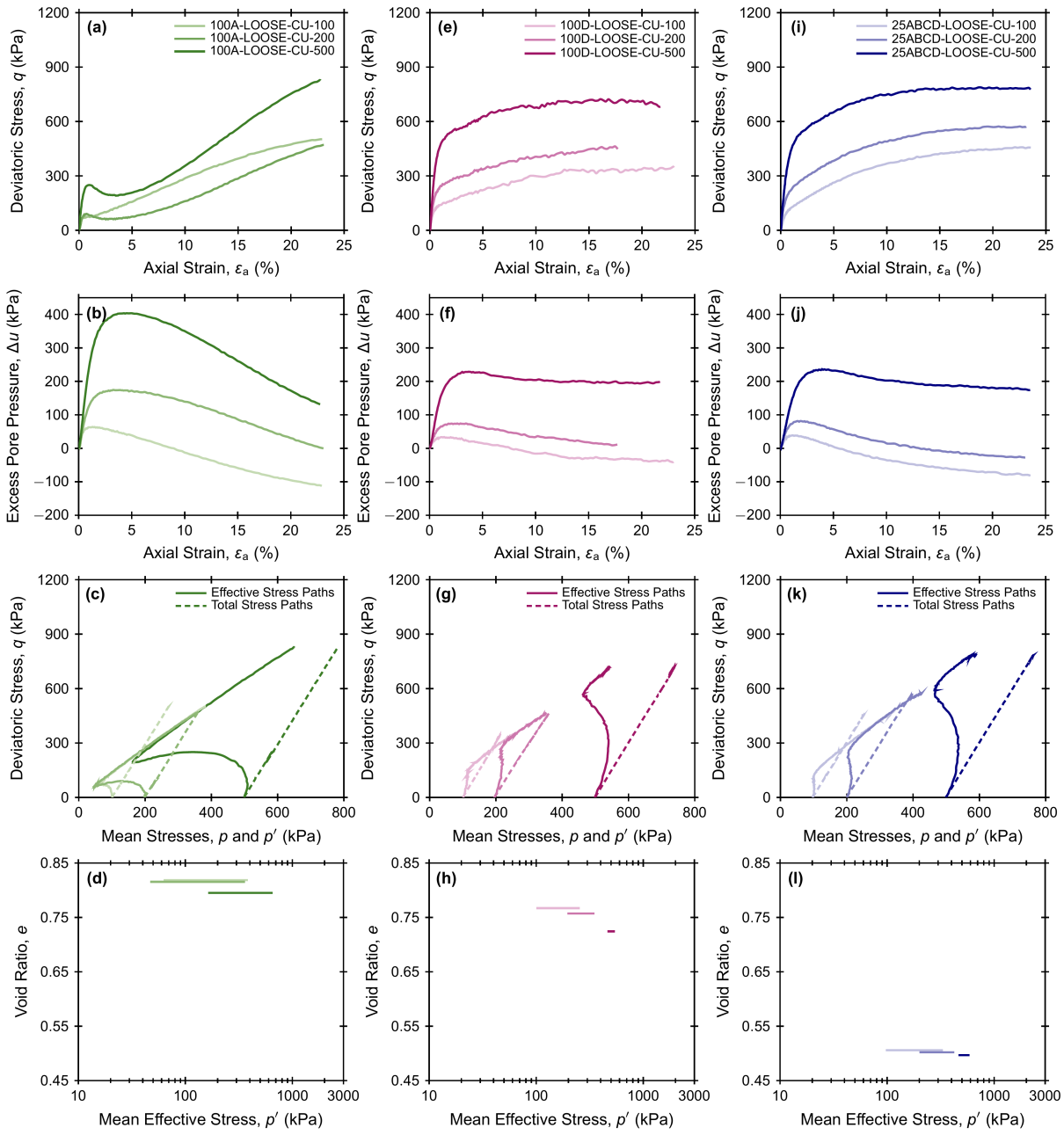

Figure 6.8: ICU test results for loose specimens of (a, b, c, d) 100A, (e, f, g, h) 100D, and (i, j, k, l) 25ABCD at different σ'_{3c}

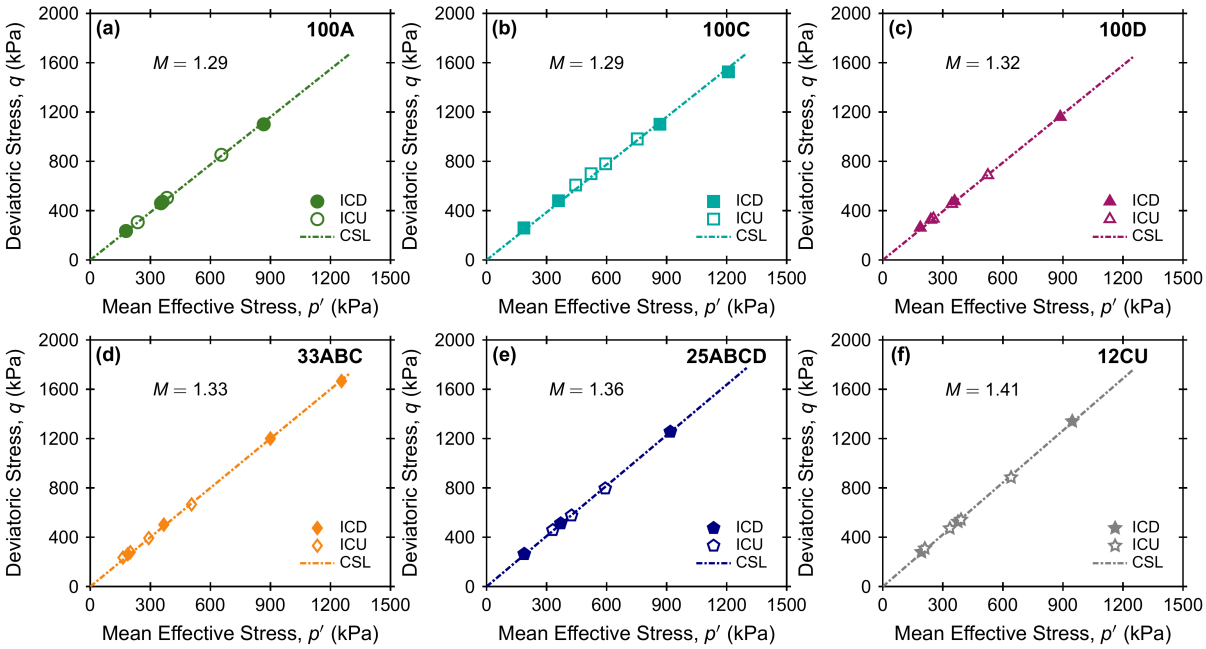

Figure 6.9: Critical state lines in $q - p'$ space

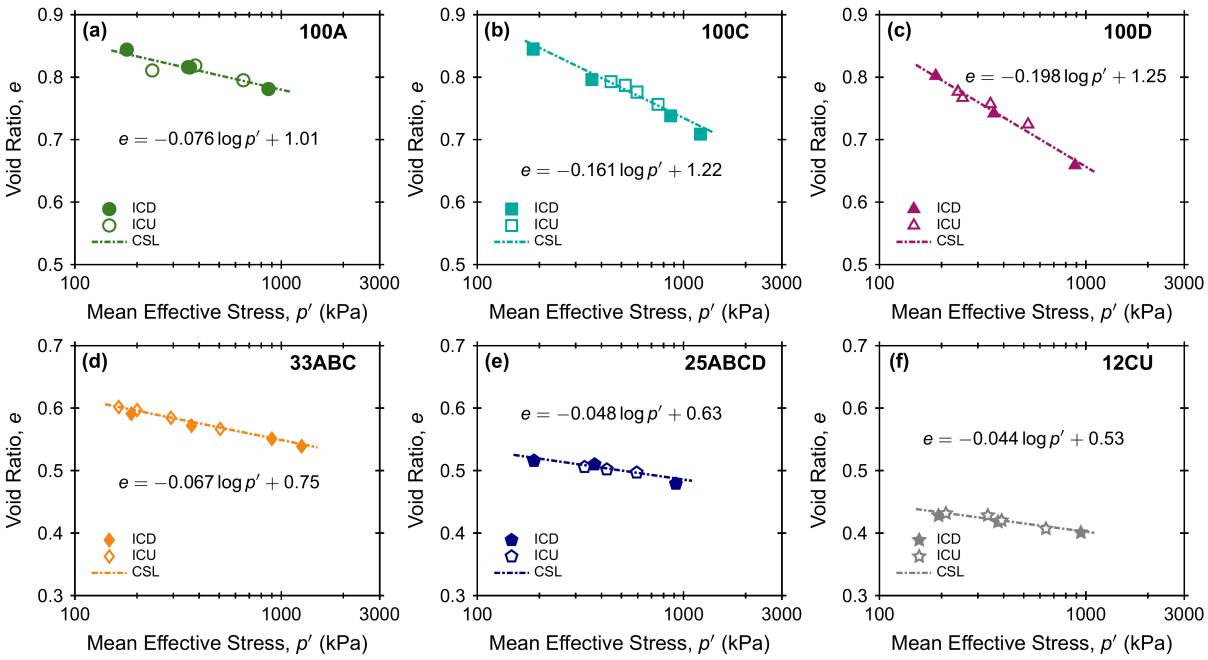

Figure 6.10: Critical state lines in $e - \log p'$ space

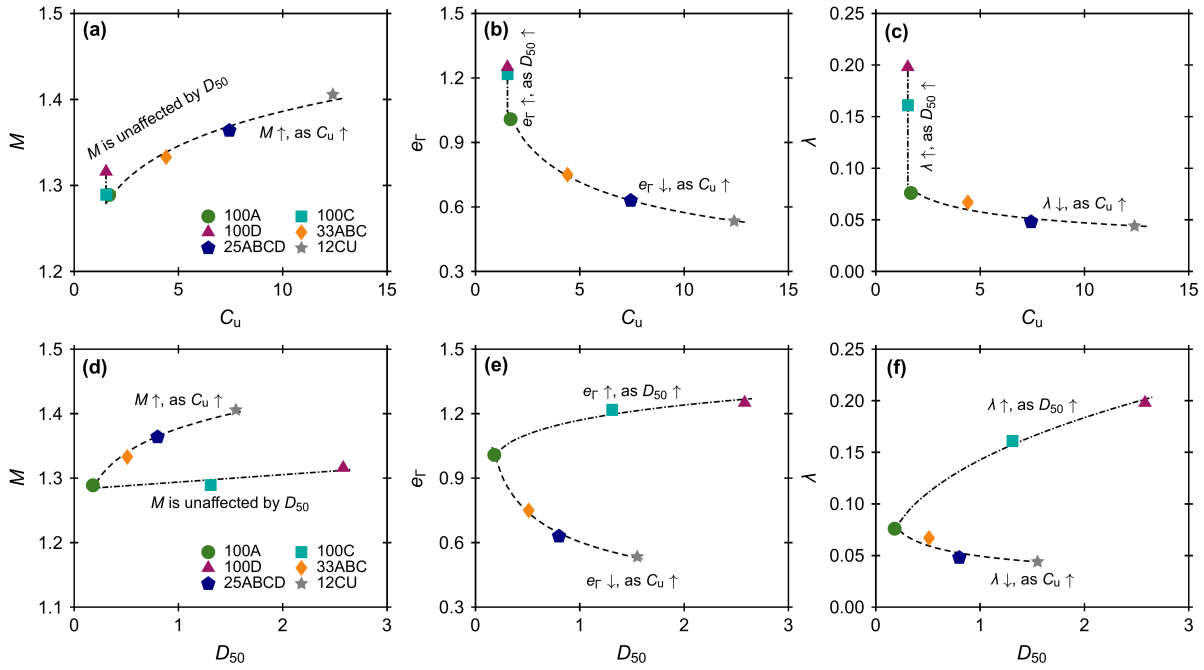

Figure 6.11: Variation of M, e_Γ and λ with (a, b, c) C_u and (d, e, f) D_{50}

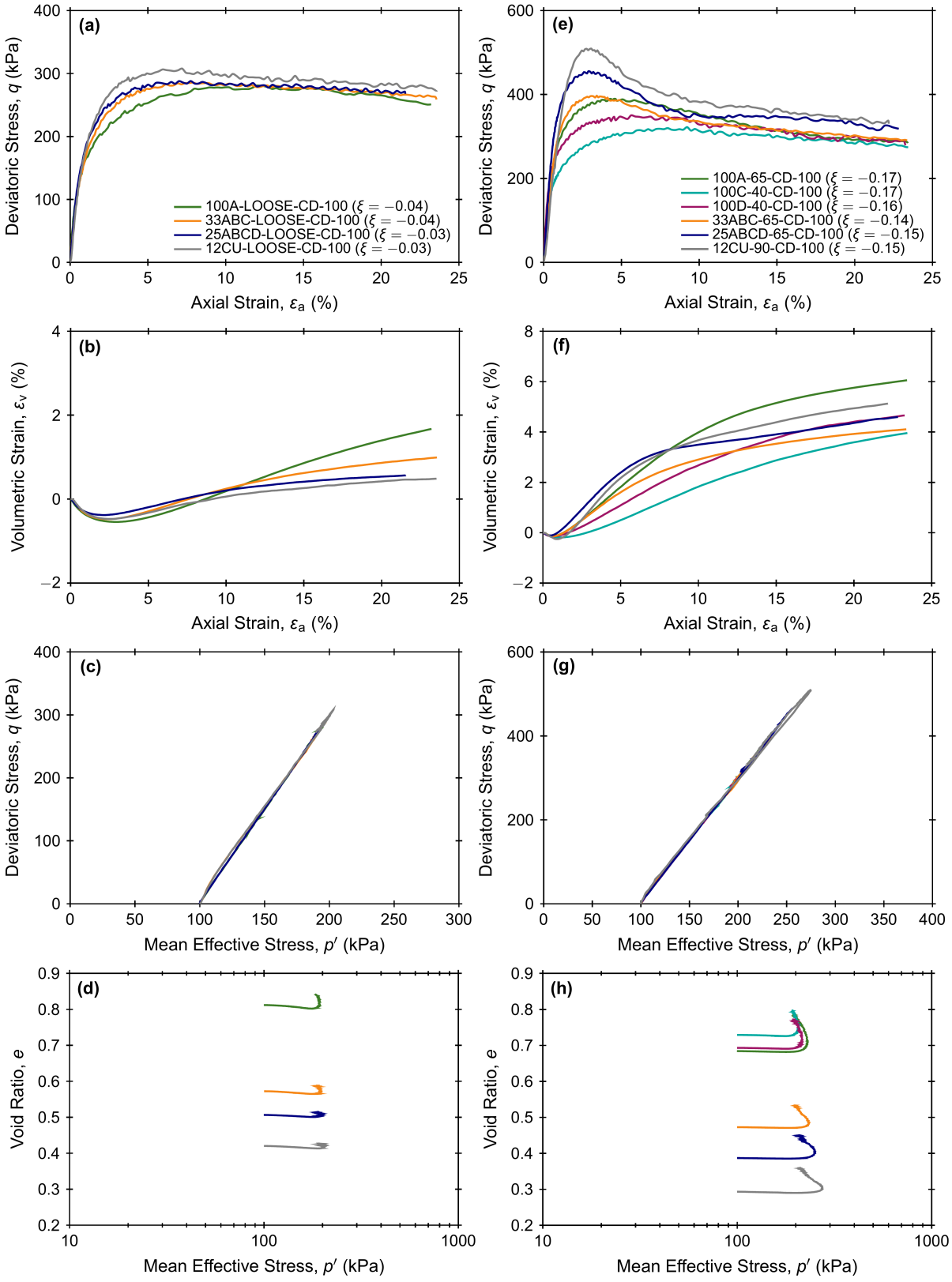

Figure 6.12: Drained test results for (a, b, c, d) $\xi = -0.03 \pm 0.01$, and (e, f, g, h) $\xi = -0.16 \pm 0.02$

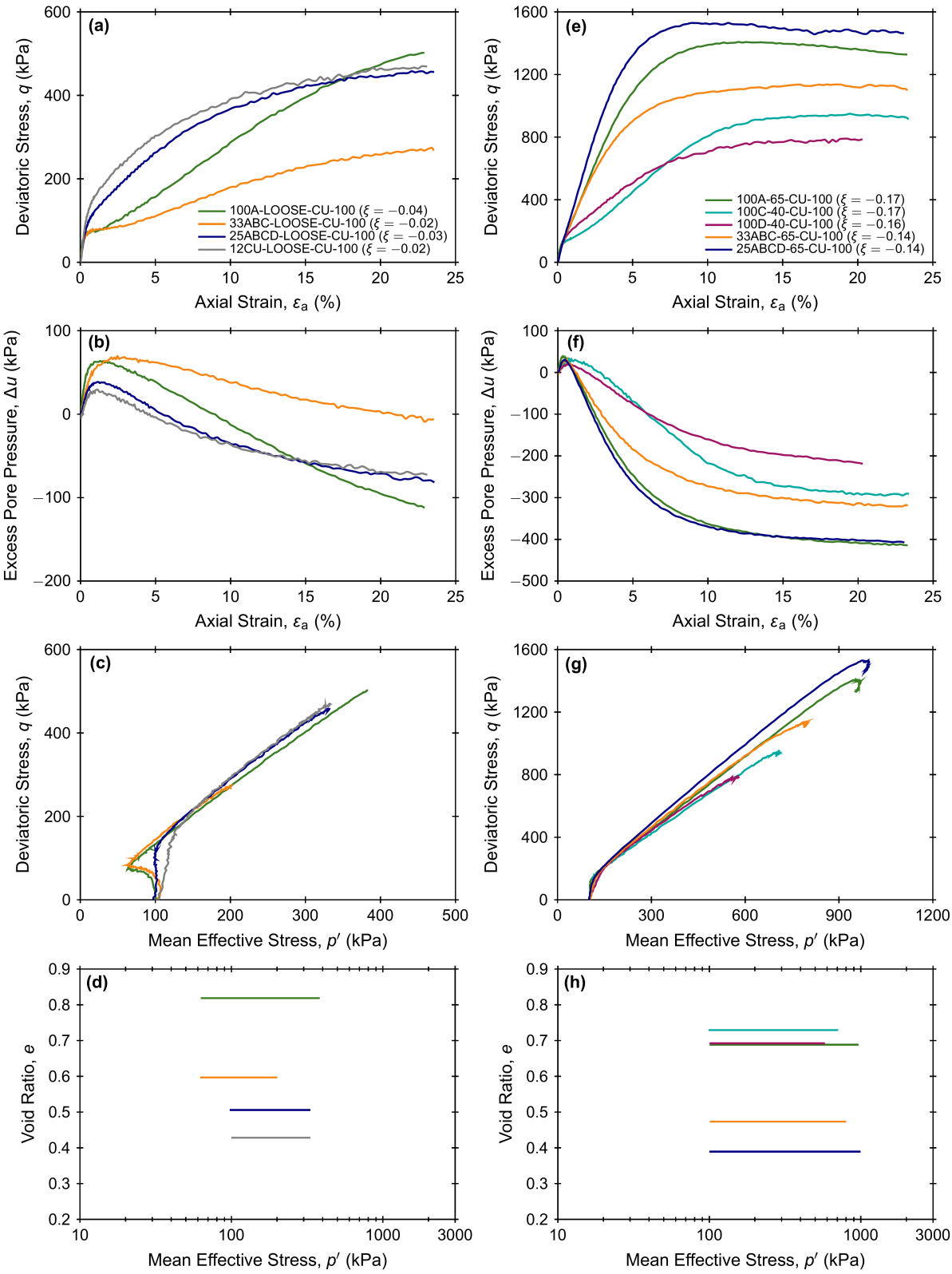

Figure 6.13: Undrained test results for (a, b, c, d) $\xi = -0.03 \pm 0.01$, and (e, f, g, h) $\xi = -0.16 \pm 0.02$

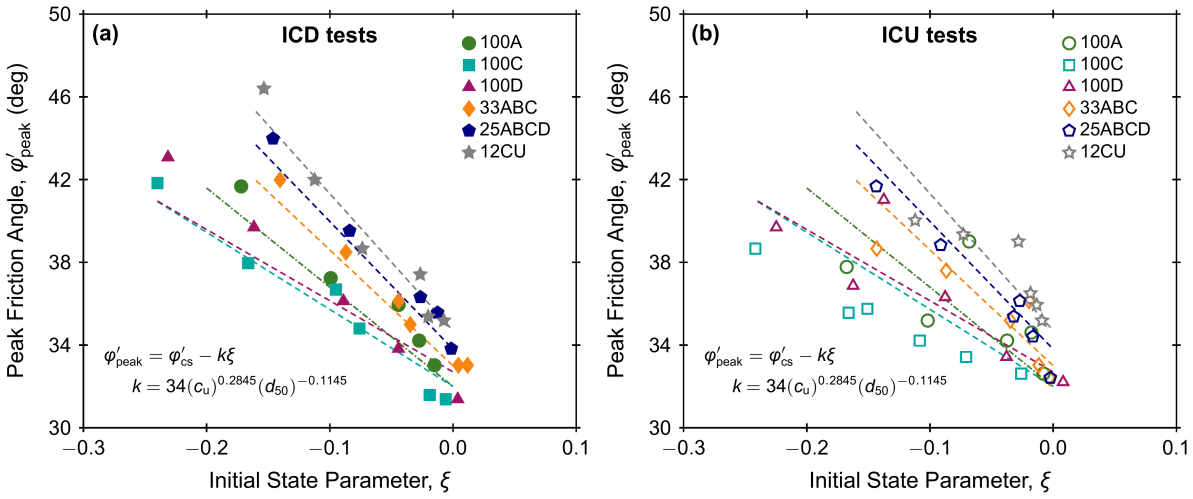

Figure 6.14: Variation of ϕ'_{peak} with ξ for (a) drained tests and (b) undrained tests

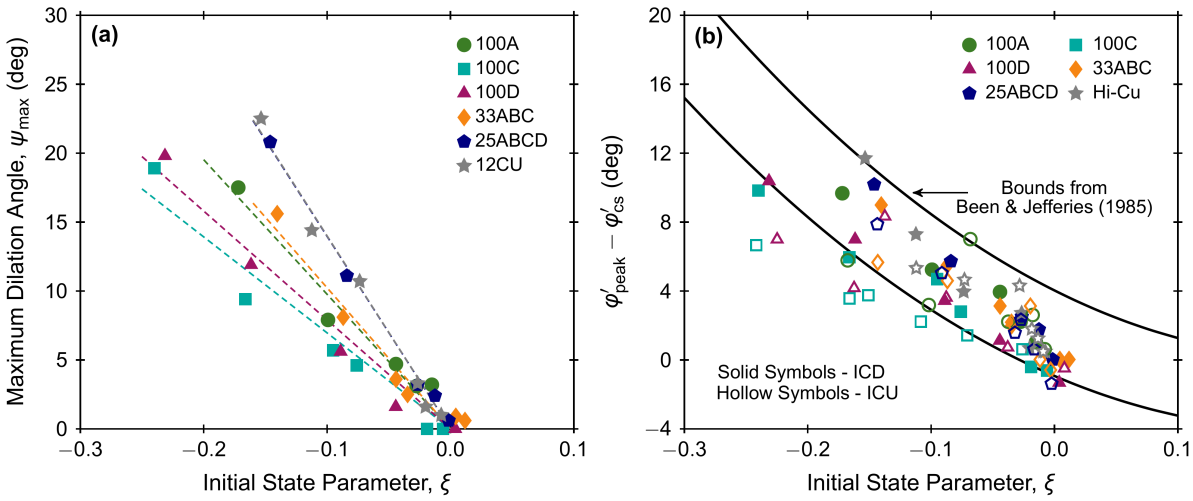

Figure 6.15: (a) Variation of $\psi_{\max}$, and (b) $\phi'_{\text{peak}} - \phi'_{\text{cs}}$ with ξ

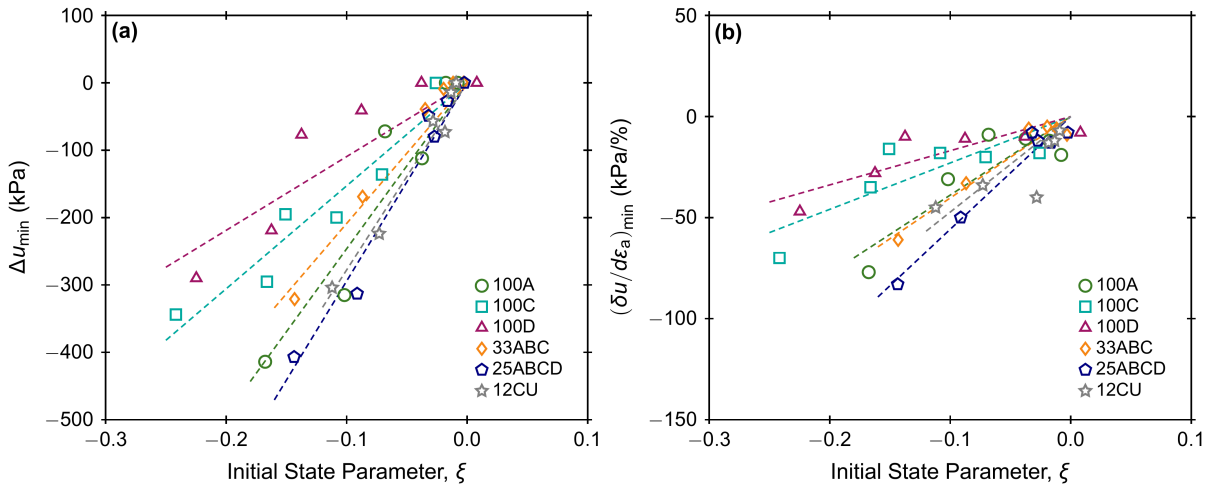

Figure 6.16: Variation of (a) Δu and (b) minimum rate of change of pore pressure with ξ

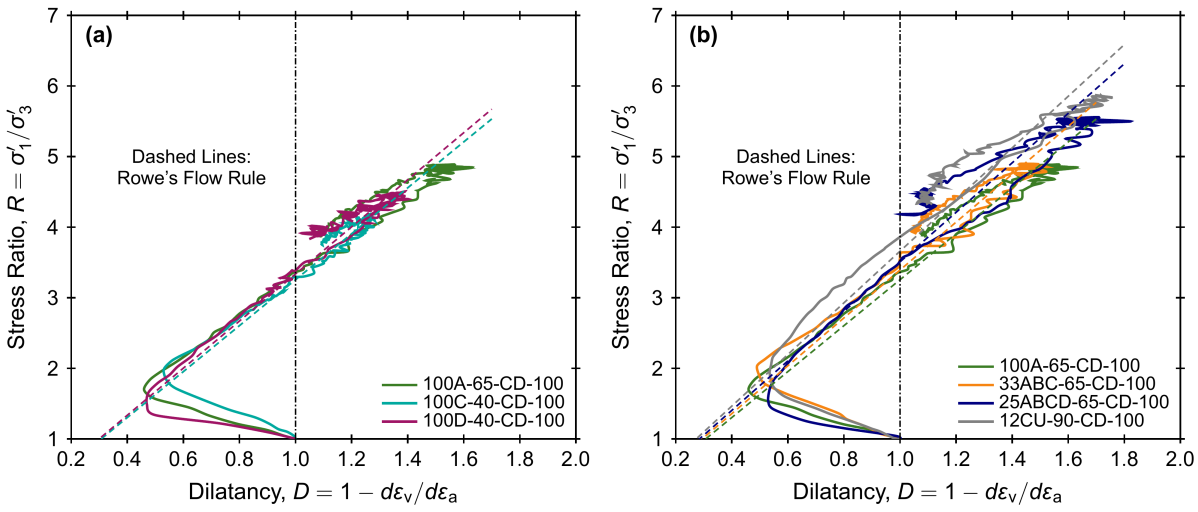

Figure 6.17: Relation between stress ratio and dilatancy for $\xi = -0.16 \pm 0.02$ for (a) poorly-graded, and (b) widely-graded soils

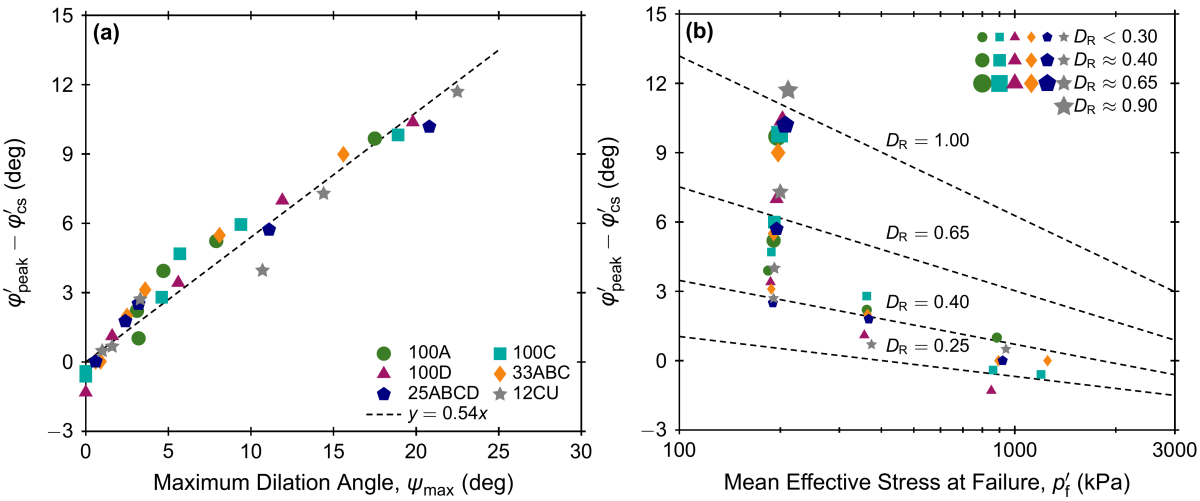

Figure 6.18: Relation between (a) $\phi'_{\text{peak}} - \phi'_{\text{cs}}$ and ψ_{max} and (b) $\phi'_{\text{peak}} - \phi'_{\text{cs}}$ and p'_{f}

6.8 Supplementary Information and Figures

The extrapolation procedure to obtain the critical state (CS) parameters (final void ratio, e_{f}, and stress ratio, R_{f}) from drained (ICD) tests is based on the assumption that dilatancy, D, converges to a value of 1 at the critical state (Zhang et al. 2018). The procedure is exemplified taking test "100D-LOOSE-CD-100" as the reference. First, void ratio, e, and stress ratio, R, are plotted against dilatancy, D, as shown in Figs. 6.19a and 6.19b, respectively. Then, the $e-D$ and $R-D$ curves are extrapolated linearly to a value of $D = 1$, and the intercepts are considered as e_{f} and R_{f}, respectively. Since σ'_3 remains constant in drained tests, q_{f} and p'_{f} can be calculated from the extrapolated R_{f}. The extrapolated CS data of "100D-LOOSE-CD-100" are $e_{\mathrm{f}} = 0.802$, $R_{\mathrm{f}} = 3.62$, $q_{\mathrm{f}} = 262$ kPa, and $p'_{\mathrm{f}} = 187$ kPa.

The CS points from the undrained (CU) tests are obtained assuming that the rate of change of excess pore pressure ($\delta u/\delta\varepsilon_{\mathrm{a}}$) converges to 0 at the critical state [Torres-Cruz and Santamarina, 2020]. As shown in Fig. 6.19c, stress ratio ($\eta = q/p'$) is plotted against $\delta u/\delta\varepsilon_{\mathrm{a}}$ for the test "100D-LOOSE-CU-100", and $\eta_{\mathrm{f}} = 1.36$ by linear extrapolation when $\delta u/\delta\varepsilon_{\mathrm{a}} = 0$. Then, the data obtained from the test are plotted in $q - p'$ plane space and, assuming that the critical state stress ratio $\eta_{\mathrm{f}} = 1.36 = M$, the critical state line (CSL) is plotted. The $q-p'$ curve is then extrapolated to the CSL (Fig. 6.19d), and values of $q_{\mathrm{f}} = 327$ kPa and $p'_{\mathrm{f}} = 240$ kPa are obtained with $e_{\mathrm{f}} = 0.777$, which remains constant during undrained shearing.

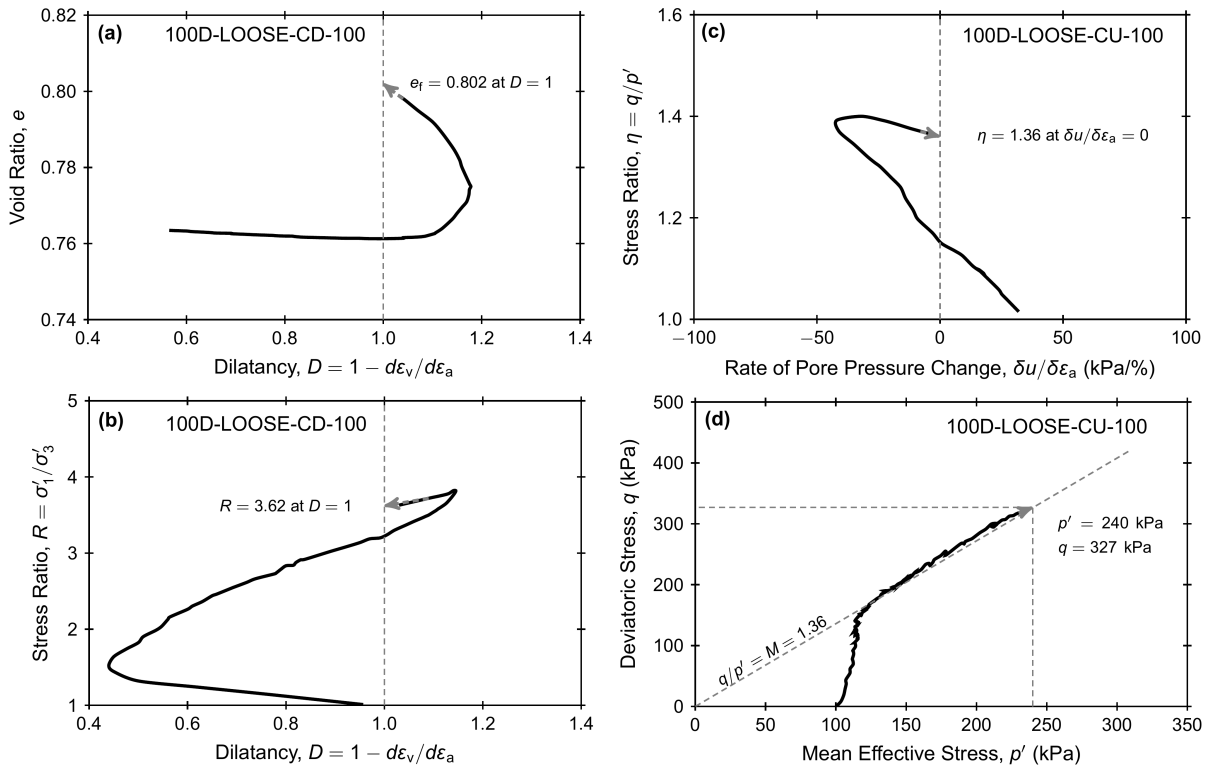

Figure 6.19: Example of extrapolation procedure to obtain the final void ratio and stress ratio from (a, b) ICD tests and (c, d) ICU tests

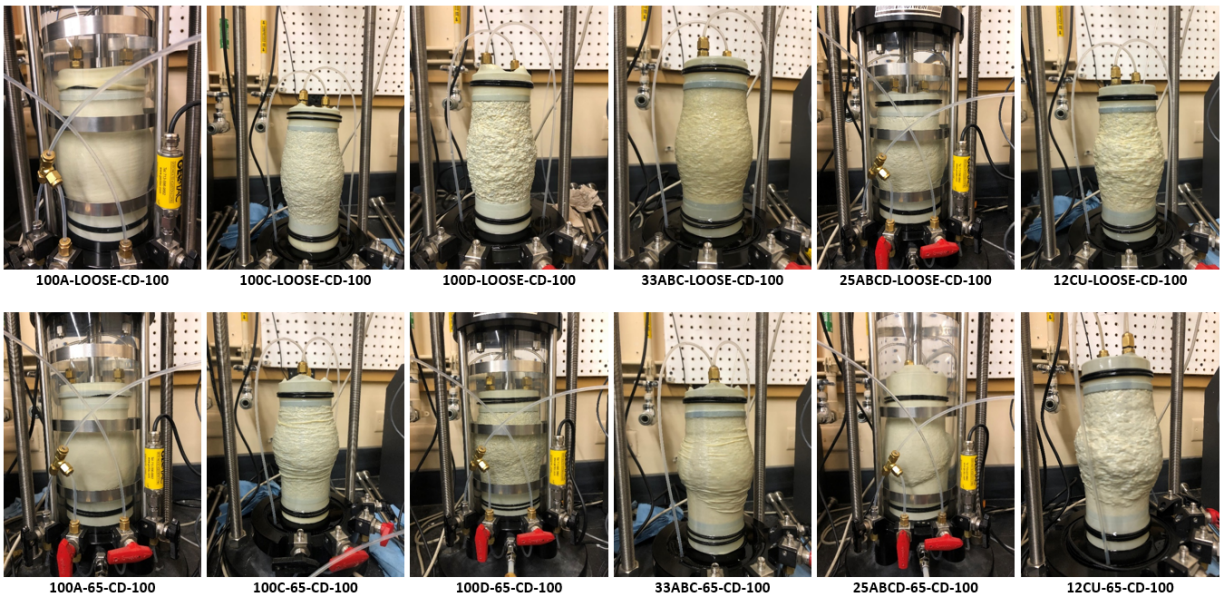

Figure 6.20: Photographs of failed specimens

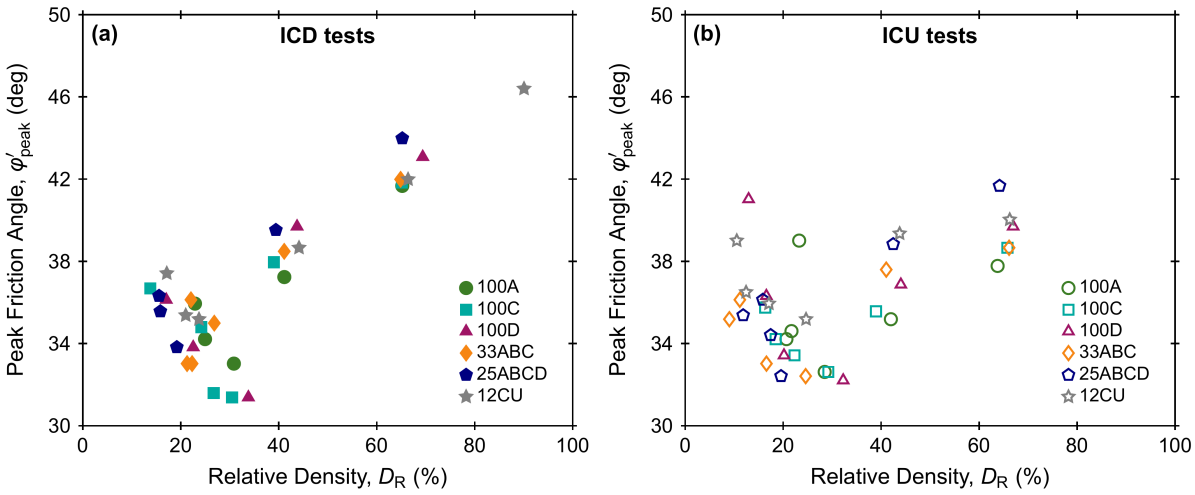

Figure 6.21: Variation of ϕ'_{peak} with D_{R} for (a) drained tests and (b) undrained tests

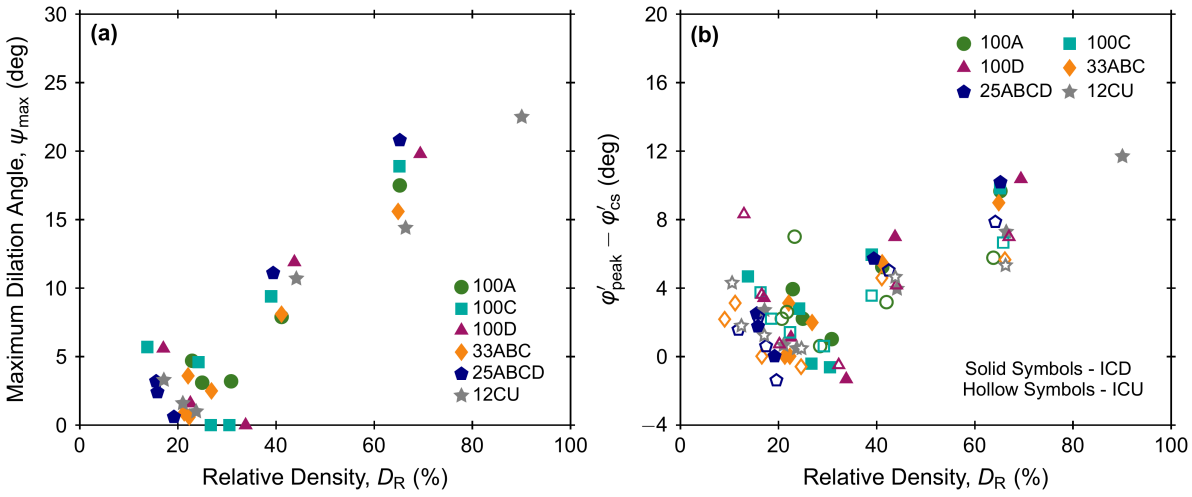

Figure 6.22: Variation of (a) $\psi_{\max}$, and (b) $\phi'_{\text{peak}} - \phi'_{\text{cs}}$ with D_{R}

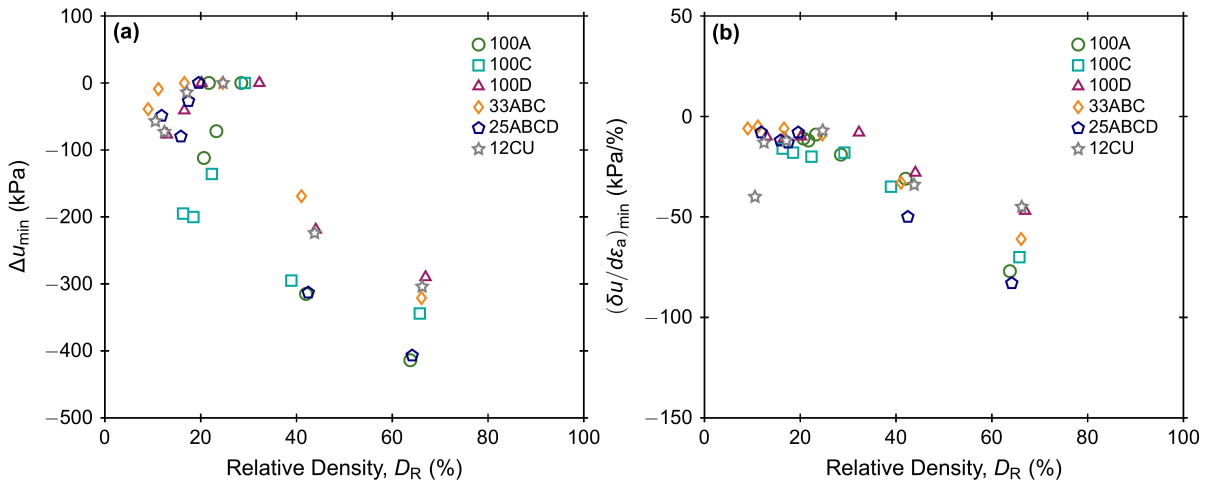

Figure 6.23: Variation of (a) Δu and (b) minimum rate of change of pore pressure with D_R

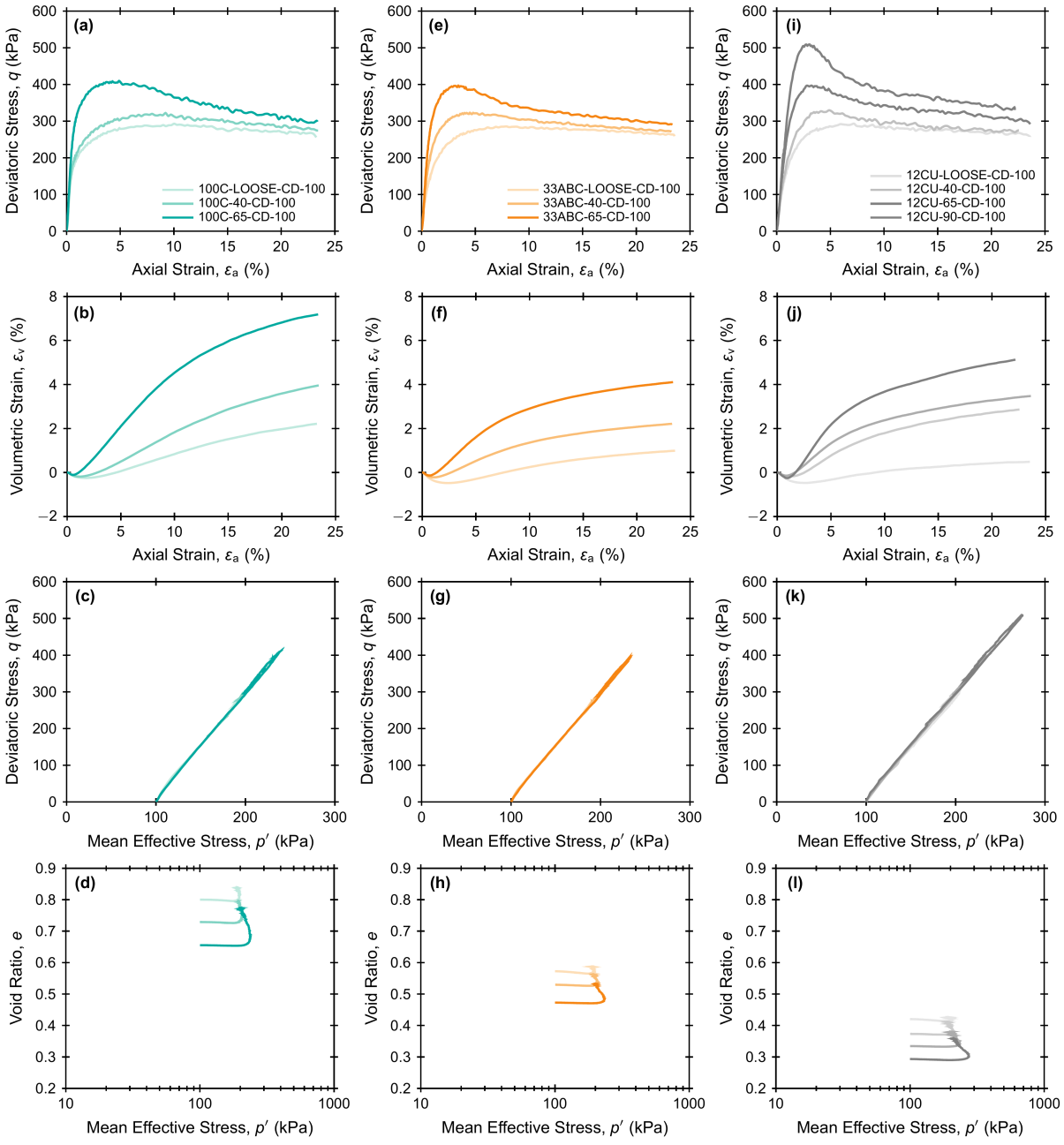

Figure 6.24: ICD test results for specimens of (a, b, c, d) 100C, (e, f, g, h) 33ABC, and (i, j, k, l) 12CU at different D_{R} and $\sigma'_{3\mathrm{c}} = 100$ kPa

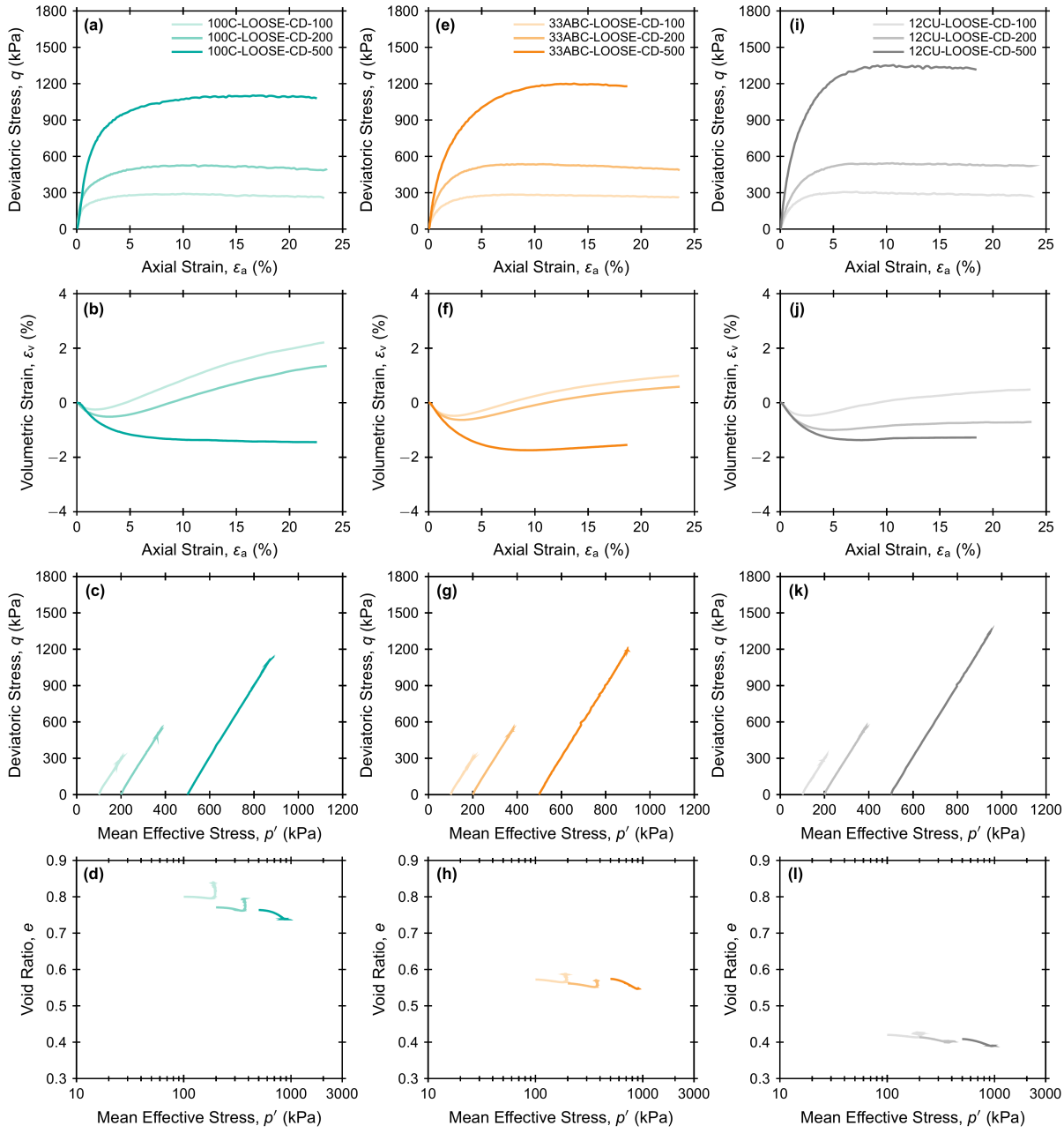

Figure 6.25: ICD test results for loose specimens of (a, b, c, d) 100C, (e, f, g, h) 33ABC, and (i, j, k, l) 12CU at different σ'_{3c}

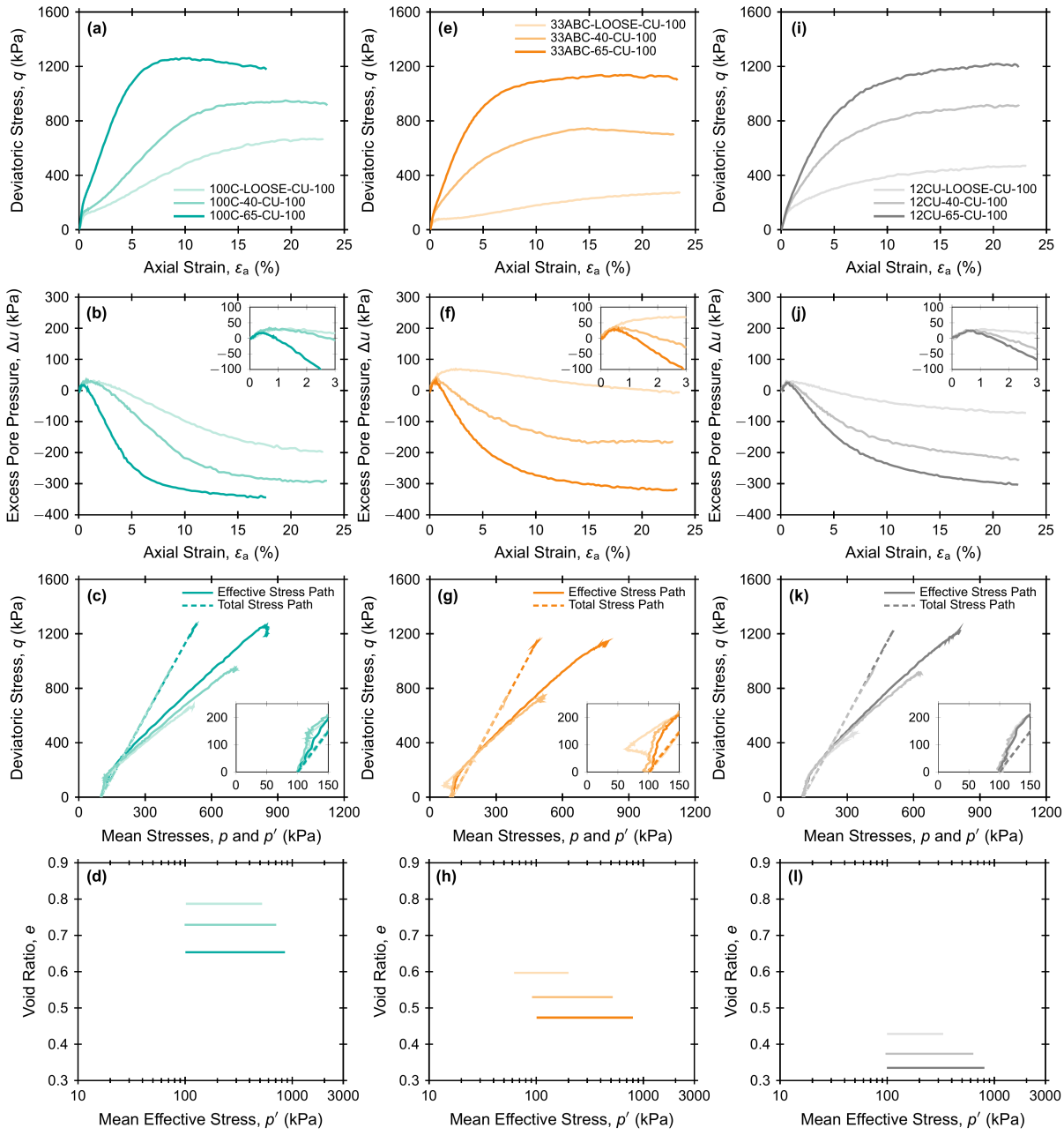

Figure 6.26: ICU test results for specimens of (a, b, c, d) 100C, (e, f, g, h) 33ABC, and (i, j, k, l) 12CU at different D_{R} and $\sigma'_{3\mathrm{c}} = 100$ kPa

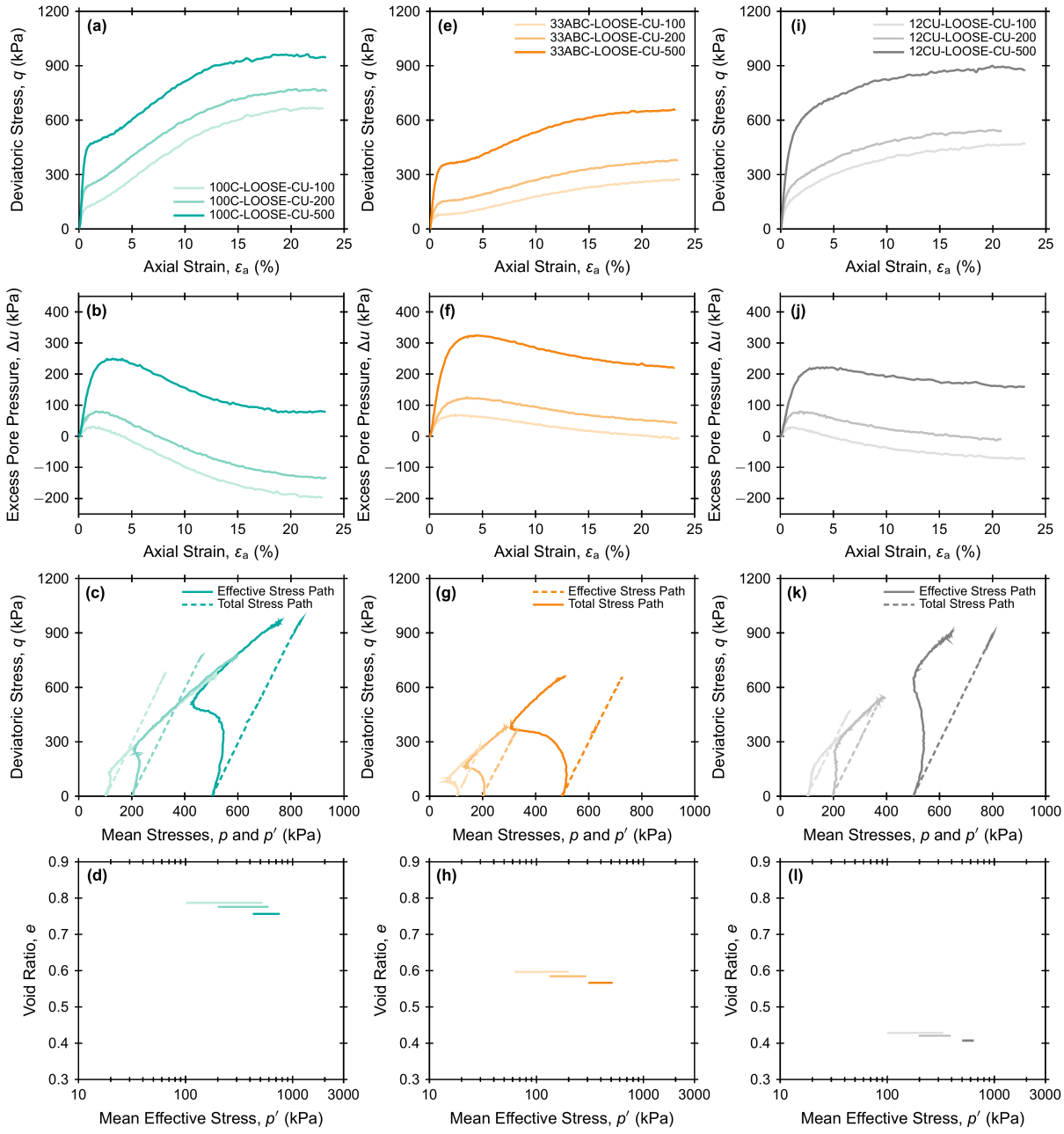

Figure 6.27: ICU test results for loose specimens of (a, b, c, d) 100C, (e, f, g, h) 33ABC, and (i, j, k, l) 12CU at different σ'_{3c}

Chapter 7

Conclusions and Future Directions

7.1 Background

This dissertation presented a collection of research manuscripts addressing topics related to the effects of particle size, shape, and gradation on the mechanical behavior of coarse-grained soils.

In Chapter 2, the feasibility of using 3D printing technology to create sand particle analogs to model the mechanical behavior of coarse-grained soils was investigated. Two different 3D printing technologies, stereolithography (SLA) and polyjet, were used to generate analog particles and equal-sized spheres. Uniaxial inter-particle compression, oedometric compression, and shear wave transmission behaviors of 3D printed analogs were examined, and were compared to those of natural sands.

In Chapter 3, the viability of using 3D printed analog particles with two different shapes (i.e. angular and rounded) to model the triaxial compression behavior of coarse-grained soils was examined. Also, the existence of critical states for the 3D printed sands in the stress and compression planes was investigated. Both drained and undrained behaviors of 3D printed analogs are investigated and compared to those of natural angular and rounded particles.

In Chapter 4, an investigation on the effects of particle shape on the shear wave transmission behavior of sands using seven 3D printed soils with different particle shapes was presented. The artificial particles were designed based on spherical harmonics and on

X-ray CT images from natural sands, allowing for careful control of the materials' particle shape parameters.

In Chapter 5, the effects of particle shape on the shear behavior of 3D printed sands under triaxial compression using was investigated. Six 3D printed sands with different shape parameters were tested under both drained and undrained triaxial compression.

In Chapter 6, the effects of gradation and median particle size on the strength and stress-dilatancy behavior of natural widely-graded coarse-grained soils were investigated by conducting a series of drained and undrained triaxial tests. Tests were performed with a range of initial relative densities and confining stresses with the goal of attaining different state parameters. The applicability of using poorly-graded sand based method to characterize the stress-dilatancy behavior of widely-graded coarse-grained soils was evaluated through Bolton's [1986] framework.

The primary findings of this work are summarized and recommendations for future research are provided herein.

7.2 Modeling the Mechanical Behavior of Granular Soils Using 3D Printed Analog Particles

7.2.1 Conclusions

Both the stereolithography (SLA) and polyjet 3D printing technologies can be used to accurately reproduce the shape of natural coarse-grained soil particles. However, the surface texture of the 3D printed particles is determined by the specific manufacturing process that can result in different surface roughnesses affecting the inter-particle contact behavior. The contact response of the polyjet particles under uniaxial inter-particle compression was significantly influenced by the deformation of micro-asperities at small loads leading to an initially softer response compared to that of SLA particles. A comparison of the oedometric compression behavior of the polyjet particles to that of the natural particles showed greater

compressibility of the polyjet particles. However, the shear wave transmission behavior of the polyjet particles exhibited dependency on the mean effective stress and void ratio which is typical of natural sands.

A further investigation on the surface texture of the polyjet 3D printed particles exhibited dependency on the printing layer direction resulting in different surface roughness that affects the inter-particle friction coefficient. It was observed that the frictional resistance tends to decrease with increasing normal stress, possibly due to greater plastic deformation of micro-asperities when the normal load is increased.

The results of isotropically consolidated drained and undrained triaxial tests on the polyjet 3D printed sands exhibited greater compressibility compared to that of natural sands which was also observed in oedometric compression. The likely reason of this greater compressibility is the lower Young's Modulus of the polyjet polymer and plastic yielding of micro-asperities on the surface of the 3D printed material. During shearing, this greater compressibility likely causes larger initial volumetric contraction (or positive excess pore pressure generation) followed by skeletal shear deformation that begins at a higher axial strain compared to that of natural sand. Analysis of the drained test results using Rowe's [1962] stress-dilatancy relation shows that the 3D printed sands can replicate the stress-dilatancy behavior observed in natural sands. Also, the interpretation of their shear response can be captured with the critical state soil mechanics framework, i.e. critical state lines (CSL) appear to exist for the 3D printed sands in both deviatoric stress-mean effective stress ($q - p'$) and void ratio-mean effective stress ($e - \log p'$) planes.

The results of a series of additional isotropically consolidated drained and undrained triaxial tests on the polyjet 3D printed sands with different particle shapes showed that the sands with greater particle roundness exhibited greater compressibility. Two different critical state stress ratios (M) can be obtained for each sands: one M for a confining stress (σ'_{3c}) < 50 kPa and another for $\sigma'_{3c} > 50$ kPa. The M-values obtained for $\sigma'_{3c} < 50$ kPa are higher than those for $\sigma'_{3c} > 50$ kPa. Both M-values decrease with increase in particle

roundness which is consistent with literature. However, the M-values for the 3D printed sands are smaller than those for the natural sands probably due to plastic deformation of the particles' asperities leading to decrease the interlocking between particles and the smaller inter-particle friction coefficient. Also, the intercept (e_Γ) obtained from the CSLs in $e - \log p'$ plane tends to decrease with increase in particle roundness which is consistent with literature, and the e_Γ-values are within the range of those for natural sands. In addition, the slope λ of the CSLs increases as particle roundness is increased. The values of λ are significantly higher than those for natural sands due to higher compressibility of the 3D printed polymer.

The results of a series of bender element tests on the polyjet 3D printed sands with different particle shapes indicated an increase in shear wave velocity (V_s) and small-strain modulus (G_{max}) with increasing mean effective stress (p') and decreasing void ratio (e), which is in agreement with trends reported for natural sands. Both V_s and G_{max} were found to increase with increases in particle roundness, sphericity, and regularity for a given void ratio, relative density and mean effective stress. The relation between V_s and p' can be fitted with a power law as $V_s = \alpha(p')^\beta$. The test results were used to develop equations for the α-coefficient and β-exponent that consider their dependency on particle shape and void ratio. A comparison between the published V_s values of natural sands and those estimated by those developed equations showed that the V_s values of natural sands can be predicted with an error smaller than or equal to 15%.

7.2.2 Future Recommendations

3D printing technology is a strong tool to manufacture artificial analog particles while independently controlling the particle size, shape and gradation. This dissertation has shown that the effects of particle shape on the behavior of 3D printed analogs are similar to those of natural sands. However, the following future research directions may help resolve key knowledge gaps and limitations associated with the present study:

- 3D printing technology is rapidly evolving and manufacturing processes are becoming

faster and more precise, allowing for better representation of particle properties. Also, new materials are being developed, some of which have properties that are closer to natural minerals such as quartz. While the technology is readily available to manufacture artificial sand particles, it is suggested for each manufacturing process and material to be evaluated carefully to optimize its efficiency, cost, and capability to model the behavior of natural sands.

- The particle-scale contact response of granular soils can be investigated by using 3D printed analogs with different shapes and sizes that may give insights on the effects of particle properties on the micro-scale behavior of sands.

- The use of 3D printed analogs can be extended to investigate the effects of particle gradation and size on the behavior of granular soils. Spherical harmonics can be used to describe particles with similar shape but different size and can be printed using 3D printing.

- The dynamic response of 3D printed analogs under cyclic shear can be investigated and compared to that of natural sands by performing cyclic undrained triaxial or direct simple shear tests. This investigation can be further extended to examine the effects of different particle properties (e.g. shape, gradation, size) on the dynamic response.

- 3D printed particles can be used to investigate the soil-structure interaction behavior in laboratory or centrifuge experiments and a comparison of that with natural sand may give insights for further investigation.

- As shown in this dissertation, the constituent material stiffness of the 3D printed analogs can be much lower than that of natural sands leading to higher compressibility at particle-scale contacts and soil skeleton. Hence, a scaling law to take into account the effects of constituent material stiffness or Young's modulus can be developed by utilizing available contact laws (e.g. Hertz theory).

7.3 Effect of Gradation and Particle Size on the Strength and Stress-Dilatancy Behavior of Widely-Graded Coarse-Grained Soils

7.3.1 Conclusions

A series of isotropically consolidated drained and undrained triaxial tests with a range of initial relative density and confining stresses were performed to examine the effects of median particle size and gradation on the strength and stress-dilatancy behavior of natural widely-graded coarse-grained soils. The results showed that the index void ratio values (e_{max} and e_{min}) decreased as the gradation became wider (i.e. coefficient of uniformity, C_u increases), whereas no significant effect of median particle size (D_{50}) on the index void ratios were observed.

While evaluating the strength and stress-dilatancy behavior of the tested soils, two separate parameters were considered to define the soil state: initial state parameter (ξ) and relative density (D_R). As shown by the results, both the peak friction angle (ϕ'_{peak}) and maximum dilation angle (ψ_{max}) increased as ξ became more negative (i.e. specimens became denser). At similar ξ, both ϕ'_{peak} and ψ_{max} increased for the soils with wider gradation. Of the poorly-graded soils, the soil with the smallest D_{50} exhibited the greatest ϕ'_{peak} and ψ_{max}. However, no systematic effect of D_{50} on ϕ'_{peak} and ψ_{max} was observed. Also, at similar ξ, the difference between peak and critical state friction angles ($\phi'_{peak} - \phi'_{cs}$) generally increased as the gradation became wider across a range of ξ and confining pressures, and the data showed general agreement with the trends and bounds established in literature [e.g. Been and Jefferies, 1985]. In addition, as shown by the undrained test results, negative excess pore pressure with greater magnitudes (Δu_{min}) was generated as ξ became more negative for all the soils. At similar ξ, the magnitude of Δu_{min} decreased as D_{50} was increased for the poorly-graded soils. Also, as suggested by the test data, the magnitude of Δu_{min} generally increased as the gradation became wider. With regards to the effects of C_u and D_{50} on ϕ'_{peak}, ψ_{max} and $\phi'_{peak} - \phi'_{cs}$ at similar relative density (D_R), no specific trend of the effect of C_u and

D_{50} on those was observed suggesting the advantages of using ξ as reference parameter over D_{R} to define the soil state.

Analysis of the test results showed that both gradation and median particle size affected the critical state parameters. The critical state stress ratio (M) in the $q - p'$ plane increased slightly as gradation became wider while the effect of D_{50} on M was found to be negligible. The position of the critical state line (CSL) in $e - \log p'$ space (e_Γ) moved towards smaller void ratio values for wider gradations. Also, e_Γ of the poorly-graded soils increased as D_{50} was increased. The slope (λ) of the CSL in $e - \log p'$ space decreased as gradation became wider. However, λ of the poorly-graded soils increased as D_{50} was increased.

When the test results were analyzed using Rowe's [1962] stress-dilatancy relation, the soils with wider gradation exhibited greater principal stress ratio ($R_{\max}$) and dilatancy ($D_{\max}$); although no specific trend regarding the effect of D_{50} on $R_{\max}$ and $D_{\max}$ was observed. Analysis of the test results using Bolton's [1986] stress-dilatancy relationship ($\phi'_{\mathrm{peak}} - \phi'_{\mathrm{cs}}$ vs. $\psi_{\max}$) exhibited no significant effect of either C_{u} or D_{50}, suggesting that dilation contributes in the same way across all soils to the friction angle in excess of the critical state value. A comparison of $\phi'_{\mathrm{peak}} - \phi'_{\mathrm{cs}}$ vs. mean effective stress at failure (p'_{f}) data using Bolton's [1986] Eqs. 14 and 16 showed that $\phi'_{\mathrm{peak}} - \phi'_{\mathrm{cs}}$ values obtained from the test results were higher for any given relative density than those predicted by Bolton's [1986] equations, which may be attributed to the angular shape of the soil particles used in this study compared to the clean river sands evaluated in Bolton's [1986] framework. However, the difference between the measured and predicted $\phi'_{\mathrm{peak}} - \phi'_{\mathrm{cs}}$ values increased as both C_{u} and D_{50} were increased.

Both the state parameter, ξ [Been and Jefferies, 1985] and the relative density index, I_{R} [Bolton, 1986] combine the effects of density and confining pressure. Hence, considering either ξ or I_{R}, a clear dependency of $\phi'_{\mathrm{peak}} - \phi'_{\mathrm{cs}}$ on soil gradation was observed, suggesting that a complete description of the stress-dilatancy behavior of coarse-grained soils should consider the dependencies on gradation and state.

7.3.2 Future Recommendations

The following research directions may be useful to gain further insights which are limited in this study:

- Both the peak and critical state strengths are dependent on loading condition even for the same initial states. A series of monotonic drained and undrained triaxial extension tests on the six test soils can be performed to examine the effect of gradation on the strength anisotropy.

- A series of cyclic undrained triaxial and direct simple shear tests on the test soils can be conducted to examine the effect of gradation and particle size on the dynamic response of the test soils.

- The effects of gradation and particle size on the small-strain modulus at a similar state may be evaluated by conducting a series of bender element tests at different confining pressures on the test soils. The coupled effect of stress anisotropy, and gradation and particle size can also be examined.

- By taking advantage of powerful numerical simulation tools such as Discrete Element Method (DEM), a DEM model can be developed and calibrated to the triaxial test results presented in this dissertation. To take into account the particle shape effects, cluster of spheres can be used to change the particle shape parameters. The calibrated DEM model can then be utilized to examine further the aspects of micro-mechanics (e.g. contact numbers, force chains, shear bands) on the strength and stress-dilatancy behavior. The DEM technique can also be utilized to simulate the behavior under direct simple shear or plane strain condition.

- The widely-graded soil mixes consisted of three or more different poorly-graded soils with different particle sizes. It can be interesting to investigate which poorly-graded soil at what proportion actually dominates the behavior of a particular widely-graded

soil. Also, if the boundary condition (e.g. triaxial compression, plane strain) has any effect on the dominant soil portion can be examined. This investigation may help to choose the right proportions of poorly-graded soils to create a widely-graded soil for further research on the effect of gradation.

Bibliography

Been, K. and Jefferies, M. G. (1985). A state parameter for sands. *Géotechnique*, 35(2):99–112.

Bolton, M. (1986). The strength and dilatancy of sands. *Géotechnique*, 36(1):65–78.

Rowe, P. W. (1962). The stress-dilatancy relation for static equilibrium of an assembly of particles in contact. *Proceedings of the Royal Society of London. Series A. Mathematical and Physical Sciences*, 269(1339):500–527.